Modulation of Amyloid Aggregation and Cancer Theranostic Using Luminescent Conjugate Materials

A Dissertation Submitted for the Degree of

Doctor of Philosophy

By

Sayan Roy Chowdhury

Roll No. 126122041

Department of Chemistry

Indian Institute of Technology Guwahati

January 2018

Department of Chemistry
IIT Guwahati

PhD Thesis

Modulation of Amyloid Aggregation and Cancer Theranostic Using Luminescent Conjugate Materials

By

Sayan Roy Chowdhury

Supervisor

Prof. Parameswar Krishnan Iyer

January, 2018

PhD
Thesis

Modulation of Amyloid Aggregation and Cancer Theranostic Using Luminescent Conjugate Materials

Sayan
Roy
Chowdhury

Indian Institute of Technology Guwahati
Department of Chemistry

Certificate

This is to certify that Sayan Roy Chowdhury has been working under my supervision since December, 2012 as a regular registered PhD student. His thesis entitled "Modulation of Amyloid Aggregation and Cancer Theranostic Using Luminescent Conjugate Materials" is an authentic record of the results obtained from the research work at Department of Chemistry, Indian Institute of Technology Guwahati, Assam, India. I am forwarding his dissertation for the award of the degree of Doctor of Philosophy, from this institute. I certify that he has fulfilled all the requirements according to the rules of this institute regarding the investigations embodied in his thesis and this work has not been submitted elsewhere for a degree.

January 2018

IIT Guwahati

Prof. Parameswar Krishnan Iyer

Thesis Supervisor

Department of Chemistry

IIT Guwahati

Guwahati-781039

Assam, India.

Indian Institute of Technology Guwahati
Department of Chemistry

Statement

I do hereby declare that herein is five years of work at the department of chemistry, Indian Institute of Technology Guwahati presented under supervision of Professor Parameswar Krishnan Iyer.

In keeping with the general practice of reporting my observations, due acknowledgements have been made wherever the work described is based on the findings of other investigators.

January 2018

IIT Guwahati

Sayan Roy Chowdhury

Dedicated to My Mamma

Contents

Acknowledgments

First of all, I would like to thank my supervisor Prof. Parameswar Krishnan Iyer (PKI) who took me in as a PhD-student and during this time has given me the means needed to secure the results presented herein.

One of my smarter decisions ever was to tell PKI that I wanted to work with Dr. Muthuraj on part of his PhD-project on detection and modulation of amyloid aggregates. During this time you were in your final year of your Ph.D. and I was just a beginner. I was introduced to this part of misfolding because of you but our collaboration was terminated due to personal issues. You always have a different perspective on life and work and I really enjoyed working with you.

Niranjan Meher (Meher), you came in as a Ph.D. student just after Muthuraj left for postdoc and have always taken time to improve my work. Efforts of our sleepless nights helped me to put tons of results and few ideas finally into a manuscript. Later you took the aggregating pathway for your Ph.D. work. All the best for your future. I really look forward to our future collaborations!!!

Mahesh Agarwal, you are the first one to give biological perspective on my work. I would also like to thank Prof. Biplab Bose to improve my manuscript and allowing Mahesh to involve in my project for a long time and make it a success.

Dr. Sudip Mukherjee and especially your supervisor, Dr. Chitta Ranjan Patra for the work on Chapter 2b and other collaborations. We have had several collaborations after that and will successfully continue those. You are really an inspiration and no words are enough to summarize events and people like you.

Subrata Mondal, you joined initially as an M.Sc. project and later joined as a Ph.D. under PKI. I will never forget how we got stuck with our results and finally came out of it. Without you, this chapters might have taken a different path. I really look forward to finding out what we can accomplish in future projects. Soon we will let the world know what we know!

Dr. S N Balaji, you have finished all my BBB experiments like a superman and introduced me to one of your smart design. During this period you were about to graduate but managed to find time for me to finish my ongoing projects. I would also like to thank your supervisor Dr. Vishal Trivedi for his continuous help and suggestions in terms of improving my manuscripts and other biological experiments performed almost in all the chapters.

Ajeet Singh, your passion for work and always find a smart solution will be missed by the scientific community. I have learned a lot about misfolding from you and the experiments we have performed together may not be publishable but most exciting for my spirits.

Sudesna Chakravarty, life without you knowing all the things others don't bother knowing would be a mess.

Would be Dr. Manash Jyoti Deka, you are a foundation for PhD-students at distress, always willing to listen and truly passionate about life.

The PKI group members, Dr. Atul, Dr. Muthuraj, Dr. Radhakrishna, Dr. Sameer, Dr. Suresh, Dr. Bheem, Dr. Akhtar, Arvin, Dr. Gopu, Dr. Ana K, Dr. Ana D, Dr. Ashish, Dr. Dip, Rahul, Indrani, Maimur, Subrata, Meher, Raman, Adil, Ritesh, Nasima, Anwesha, Biki, Ramesh, Retwik, Rabindra, Dr. Ekta, Dr. Himani, Dr. Priyanka, Dr. Jupitara, and Debasish, I have enjoyed working next to all of you. M. Sc. and B. tech. project staffs over the years Nayan, Raj, Suraj, Sudipta, Siraj, Tanay, Samprita, and Tamal; others hanging in the lab, Prashant, Nystha, and Debojeet. All of you have contributed to this work by being who you are.

My doctoral committee members, Prof. Mohd. Qureshi, Dr. Manabendra Sarma, and Dr. A. S. Achalkumar for their precious time, suggestions over the past five years.

I would also like to thank Dr. Chitralekha Gogoi, Jr. Consultant, Pathology & Microbiology, GNRC Sixmile, for her precious time and helping me to get CSF samples throughout this period.

All fictional characters who helped to get slots in CIF during tough times (Prof. G. Krishnamoorthy's tenure)!

Others at chemistry and other departments making life at and outside work better: Dr. Saty, Dr. Krapa, Dr. Babulal, Dr. Arghya, Dr. Satavisha, Garima, Dr. Ananya, Dr. Ashim, Rajat, Tanmay, Shilaj, Bandhan, Dhriti, Hiranya, Suranjan, and Soumen.

All proud and amazing members of "chemistry cricket association" and "joy football hok football" for many memorable days.

The rest of Chemistry at IITG, my family, and friends.

To all of you forgotten, deserving acknowledgment.

Synopsis

Alzheimer's disease (AD) is pathologically highlighted by the aggregation of intracellular neurofibrillary tangles shaped by tau proteins and extracellular feeble torment by amyloid β-proteins (Aβ) in the patient brain. Aβ39–43 residues are typically created by successive cleavage of the amyloid precursor protein (APP) by both β- and γ-secretases. Numerous studies have demonstrated that the aggregation of Aβ into amyloid fibrils containing trademark cross-β-sheet structure in the brains of AD patients is firmly connected to the pathogenesis of AD. Moreover, it is by and large acknowledged that dissolvable Aβ oligomers or protofibrils are the most poisonous species, in charge of neuron dysfunction and death. A few methodologies have been endeavored averting Aβ oligomerization into fibrils in vitro. Among them, nanoparticle-based hindrance is the most productive, and has gotten more consideration in the therapeutics of AD because of their special auxiliary prevalence, for example, size, high dependability, simplicity of surface functionalization and tunable physicochemical properties of nanoparticle. Nanoparticles are small to the point that they can get to all aspects of the human body, notwithstanding going through the blood brain barrier. Consequently, if nanoparticles can hinder the procedure of fibrillogenesis or disaggregate amyloid fibrils, they can possibly be utilized as medications to control neurodegenerative amyloid diseases like Alzheimer's. In the meantime, itemized data about the associations in the middle of nanoparticles and amyloid proteins could help to illustrate the system of fibril formation at the molecular level, a territory which still stays tricky. Most studies demonstrate that it is the composition of nanoparticles and their surface qualities, instead of surface curvature or surface concentration, which focus their effect on fibrillogenesis. From the information got from in vitro tests, it is difficult to foresee the conduct of nanoparticles in the human body. Further, an extensive number of different proteins could rival Aβ peptide for interaction with nanoparticles, which would lessen the availability of the nanoparticles to Aβ peptide and diminish the probability of creating a high surface concentration of the amyloidogenic peptide. In this research, the intriguing aggregation prospect of amyloid fibrils were conferred using luminescent conjugate materials technique as a scaffold for polymer-protein hybrid materials as this technique provides a direct link between spectral signal and protein conformation and can be used to gain more information concerning the morphology of the protein deposits and facilitate a greater understanding of the conformational phenotype encoded in the native protein aggregates.

The amyloid hypothesis has now been the backbone of therapeutic research in Alzheimer's disease for over two decades. In several studies amyloid plaques does not correlate to cognitive decline. However, other investigations have established a much stronger correlation between soluble Aβ oligomers level and severity of cognitive decline. The difficulty in isolating the specific neurotoxic species of Aβ and characterizing its effects makes research problematic. Although aggregation of Aβ is vital for the cytotoxic effects of Aβ but in vitro preparations does not result in unique potencies of the peptide that leads to fibrillar aggregates. Studies based on transgenic mouse models of AD does not recapitulate human conditions due to lack of human-like inflammatory response and tau protein which also plays a pivotal role in disease progression. Type 2 diabetes and AD are believed to be two associated pathological commonness of misfolded proteins and an assumption that such diseases may share intricate downstream of events. For example increase in activity of GSK-3 and thus its inhibition is recognized as another promising strategy. It can interact with presenilin and regulate Aβ production by activating γ secretase complex.

Current developments are directed at metal ion chelators, γ-secretase, β-secretase, statins, and associated cholesterol dropping agents, other drugs targeting Aβ production, and synthetic pharmaceutical and plant extracts and their derivatives which have been revealed to tweak excess production of Aβ peptides in various ways and thus lowering the levels in order to decrease the burden. But soluble Aβ oligomers are considered as a major molecular culprit in AD. Development of biomarkers or drugs that target these soluble aggregates may open a prevention window well before the symptoms appear. This thesis is mainly focused on luminescent materials viz both small molecules, polymeric nanoparticles and conjugates that can either modulate or inhibit early amyloid aggregates. Interaction interface between small molecule/polymer-protein has been explored with an intention to find structural variations that can interact with the hydrophobic core of the amyloid and interrupt pathogenic aggregation. Therefore the main objective of the thesis was to modulate the robust amyloid by targeting them selectively and making luminescent materials that can preclude amyloid aggregation which lead to final fibrillation found in plaques and extract optical information on protein aggregation. Importantly, some of these materials may help in the advancement of drugs for early or 'pre-clinical' stages of AD that may reverse neurodegeneration well before symptoms prevail of this progressively incapacitating disease. Apart from that, one of the luminescent polymeric material was also explored as multi-color bio-imaging and drug delivery for cancer treatment.

In addition the details of the thesis work is summarized in a nut shell,

Chapter 1. Details about the already existing developments and strategies to inhibit production, aggregation and clearance of Aβ along with other indirect strategies taken to fight against AD and a sneak peak of the objective of this thesis.

Chapter 2a. Modulation of amyloid aggregates by a conjugate polymeric material (PF-HQ) that shows an amyloid like surface motif in aqueous medium due to aggregation. It also formed a co-aggregate in presence of early amyloid aggregates and stops final fibril formation.

Chapter 2b. Multifunctional (3-in-1) cancer theranostics applications of hydroxyquinoline appended polyfluorene nanoparticles. PF-HQ is further utilized to design and fabricate a drug delivery system (PF-HQ-DOX) that successfully inhibits the cancer cell proliferation and tumor growth in mice melanoma tumor model. Mechanistic studies reveal inhibition of Ki-67 and subsequent apoptosis in PF-HQ-DOX treated the tumor.

Chapter 3. Modulation of early amyloid aggregates using a polymeric conjugate that crosses blood brain barrier efficiently. A polyfluorene derivative is functionalized with chitosan and utilized as an oligo-modulator.

Chapter 4. Two perylenebisimide isomers are designed that inhibits amyloid fibrillation by blocking the early amyloid aggregates. A mutual aggregation directs amyloid aggregation into an 'off-pathway'. Less aggregation prone isomer is able to target the oligomers more selectively and able to cross blood brain barrier efficiently compared to its sibling.

Chapter 5. The perylenebisimide twins are explored to modulate insulin amyloid. More aggregation prone isomer is able to target the early aggregates of insulin amyloid and inhibits fibrillation.

A sneak peek into the future toward theranostic developments in order to predict and slow/reverse the neurodegeneration.

Chapter 1. Introduction

Recent developments and strategies were discussed in this chapter. This chapter also includes an overview of all the chapters and objective of the work presented in this thesis (Scheme 1). An advantage over the current available strategies were also discussed in detail. Luminescent conjugate materials have significant advantage over all classes of probes and presently used methods in multiple aspects of reducing the toxicity by forming co-aggregates even with early stage amyloid elements, blood brain barrier crossing ability, self-indicator and prevent

recurring of aggregation, and formation of final fibrillar amyloid network, all of which are very unique to these materials. Thus complimentary aggregation, formation of co-aggregates with appropriately designed bio probes is an important approach to diminish toxic amyloid structures for pre-senile therapeutics.

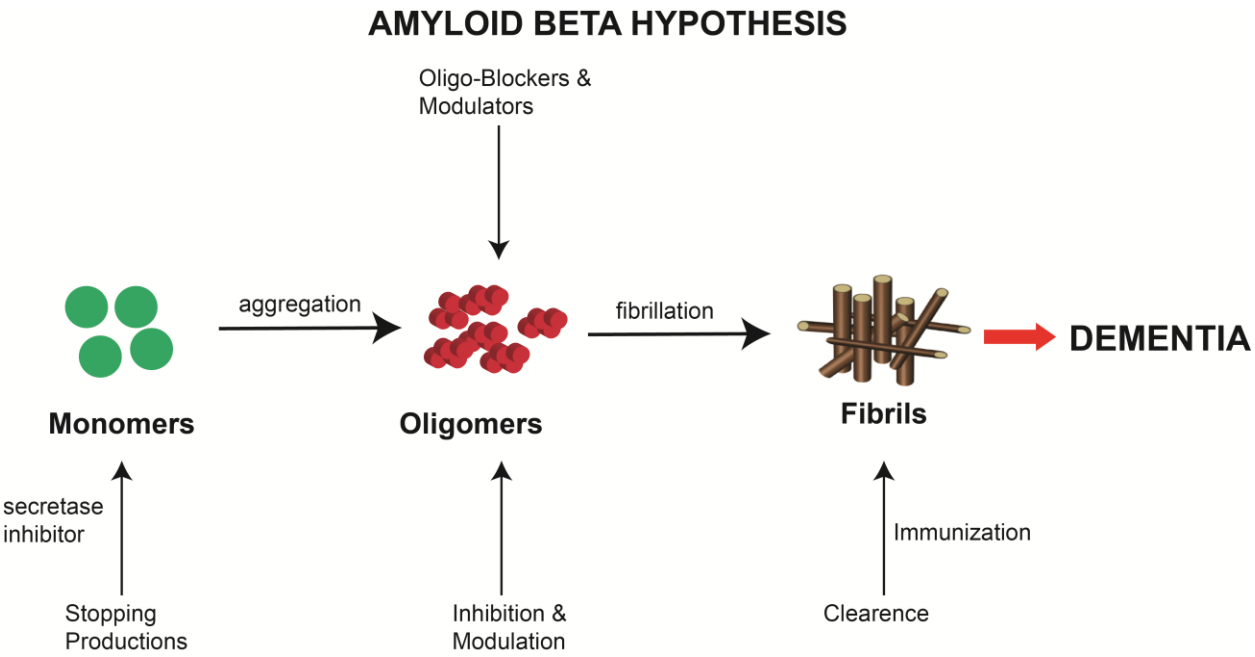

Scheme 1. Amyloid β hypothesis and strategies based on production, clearance and inhibition of amyloid aggregation.

Small molecule and polymer based Aβ aggregation inhibitors and modulators have been developed and the corresponding interface was delineated in the respective chapters.

Chapter 2a. Amyloid-like Polymeric Template to Trigger Toxic Amyloid Aggregate into Nontoxic Co-aggregates

Inhibitory modulation towards de novo protein aggregation is likely to be a vital and promising therapeutic strategy for understanding the molecular etiology of amyloid related diseases such as Alzheimer's disease (AD). The building up of toxic oligomeric and fibrillar amyloid aggregates in the brain plays host to a downstream of events, causing damage to axons, dendrites, synapses, signaling, transmission and finally cell death. Herein, a conjugated polymer (CP), hydroxyquinoline appended polyfluorene (PF-HQ) was introduced.

PF-HQ has typical 'amyloid like' surface motif and exhibits inhibitory modulation effect on amyloid β (Aβ) aggregation. Inhibitory effects of PF-HQ was delineated based on Thioflavin T (ThT) fluorescence; atomic force microscopy (AFM), circular dichroism (CD) and Fourier transform infrared (FTIR) studies. The amyloid-like PF-HQ forms nano co-aggregates by templating with toxic amyloid intermediates and displays improved inhibitory impacts towards Aβ fibrillation and diminishes amyloid cytotoxicity (Scheme 2). CP based modulation strategy was developed for the first time, which demonstrates beneficiary amyloid-like surface motif to interact efficiently with the protein, the pendant side groups to trap the toxic amyloid intermediates as well as optical signal to acquire the mechanistic insight.

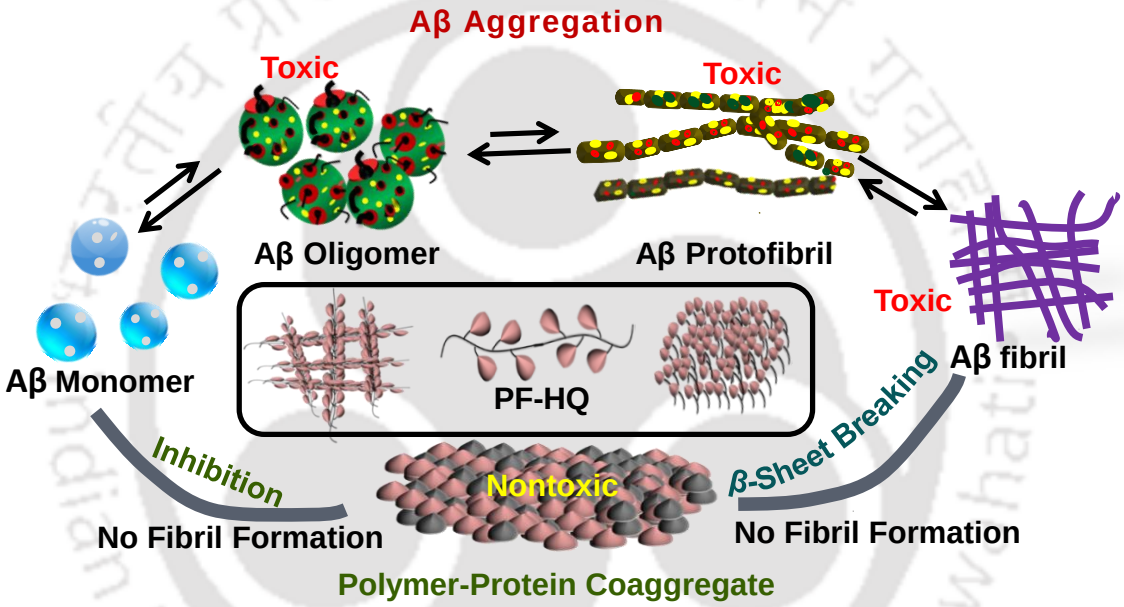

Scheme 2. Amyloid-β modulation by PF-HQ and formation of nontoxic polymer-protein co-aggregates avoiding formation of toxic fibrillar aggregates.

Chapter 2b. Multifunctional (3-in-1) Cancer Theranostics Applications of Hydroxyquinoline Appended Polyfluorene Nanoparticles

The accumulation of fluorescent hydroxyquinoline affixed polyfluorene (PF-HQ) nanoparticles and their utility for multi-color bio-imaging and drug delivery for cancer treatment is reported. The formation of nanoparticles (PF-HQ) containing hydrophobic pockets via three-dimensional growth of polymeric backbone in higher water fraction (THF:

H2O = 1:9) was observed. The nanoparticles showed incredible dual state optical and fluorescence properties, which were further explored in multi-color cell imaging in both cancer and normal cells. The cell viability assay in various normal cells confirmed the biocompatible nature of PF-HQ, which was further supported by ex vivo (Chick Chorioallantoic Membrane assay) model. This encouraged us to fabricate PF-HQ based new drug delivery systems (DDS: PF-HQ-DOX) upon conjugation with FDA approved anticancer drug doxorubicin (DOX) by filling the hydrophobic pockets of the polymer nanoparticles. The enhanced anticancer activity of DDS (PF-HQ-DOX) compared with free DOX was observed in mouse melanoma cancer cells (B16F10) and subcutaneous mouse (C57BL6/J) melanoma tumor model upon administration of PF-HQ-DOX. Ex vivo biodistribution studies using fluorescence quantification method demonstrated the enhanced accumulation of DOX in tumor tissues in the PF-HQ-DOX treated group compared to free drug signifying the drug delivery efficacy of the delivery system by passive targeting manner. Based on the above biological data (in vitro and in the pre-clinical model), this robust and versatile fluorescent hydroxyquinoline annexed polyfluorene nanoparticles (PF-HQ) could be effectively utilized for multifunctional biomedical applications (biocompatible, bio-imaging and drug delivery vehicle).

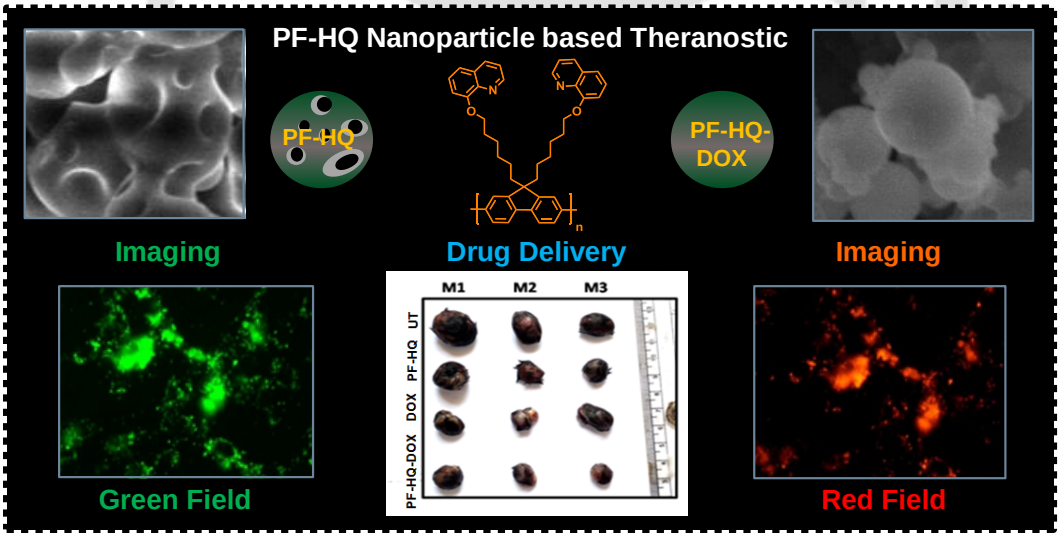

Chapter 3. Polymer-Polymer Scaffold Tweaks Early Amyloid Aggregates and Crosses Blood Brain Barrier Efficiently

Amyloid oligomers are recently considered as the prime suspect in Alzheimer's dementia. In order to address materials of diagnostic or therapeutic value must cross the blood-brain barrier (BBB) efficiently and target the toxic aggregate among other heterogenic amyloid aggregates which may present in equilibrium. Successful modulation of early aggregates may open a new approach toward presenile dementia. In this study, polyfluorene nanoparticle was coated with chitosan as an additive which can cross BBB efficiently and employed as an amyloid oligomer modulator. The polymer conjugate, PC shows no toxicity in MTT assay and precludes self-aggregation of Aβ1-40 and human cerebrospinal fluid (CSF) oligomers to final fibril formation. This modulation strategy is supported by Thioflavin T (ThT) assay, atomic force microscope (AFM) images, circular dichroism (CD), and Fourier transforms infrared (FTIR) studies. Polymer-protein interface exhibits the presence of co-aggregates and responded with a stable optical response (Scheme 3). The straightforward synthesis in desired shapes and photophysical properties, biocompatibility, non-toxicity and BBB permeability make this polymer conjugate highly attractive for modulation of amyloid oligomers and as well as developing next generation nano-theranostic materials toward pre-senile dementia.

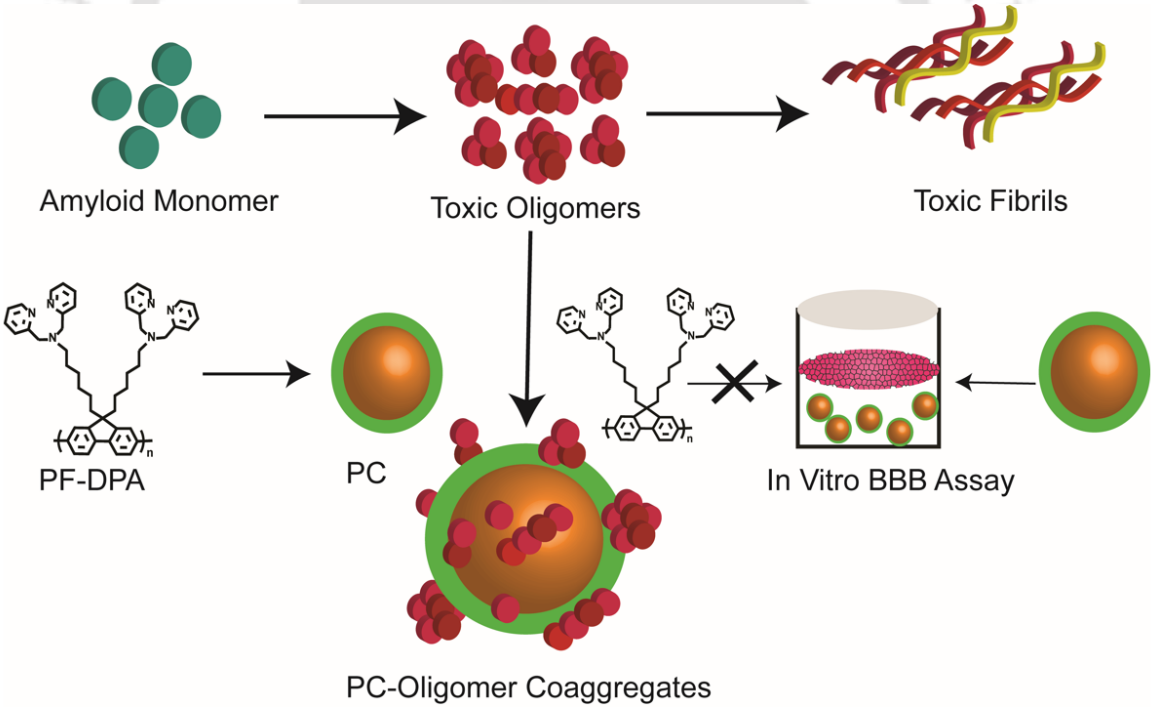

Scheme 3. Polymeric conjugate, PC acts as a self-indicator and oligo-modulator as well. It was shown to pass through BBB unlike the precursor polyfluorene derivative.

Chapter 4. Modulating Early Stage Amyloid Aggregates by Dipeptide Linked Perylenebisimides: Structure Activity Relationship, Inhibition of fibril formation in Human CSF and Aβ1-40

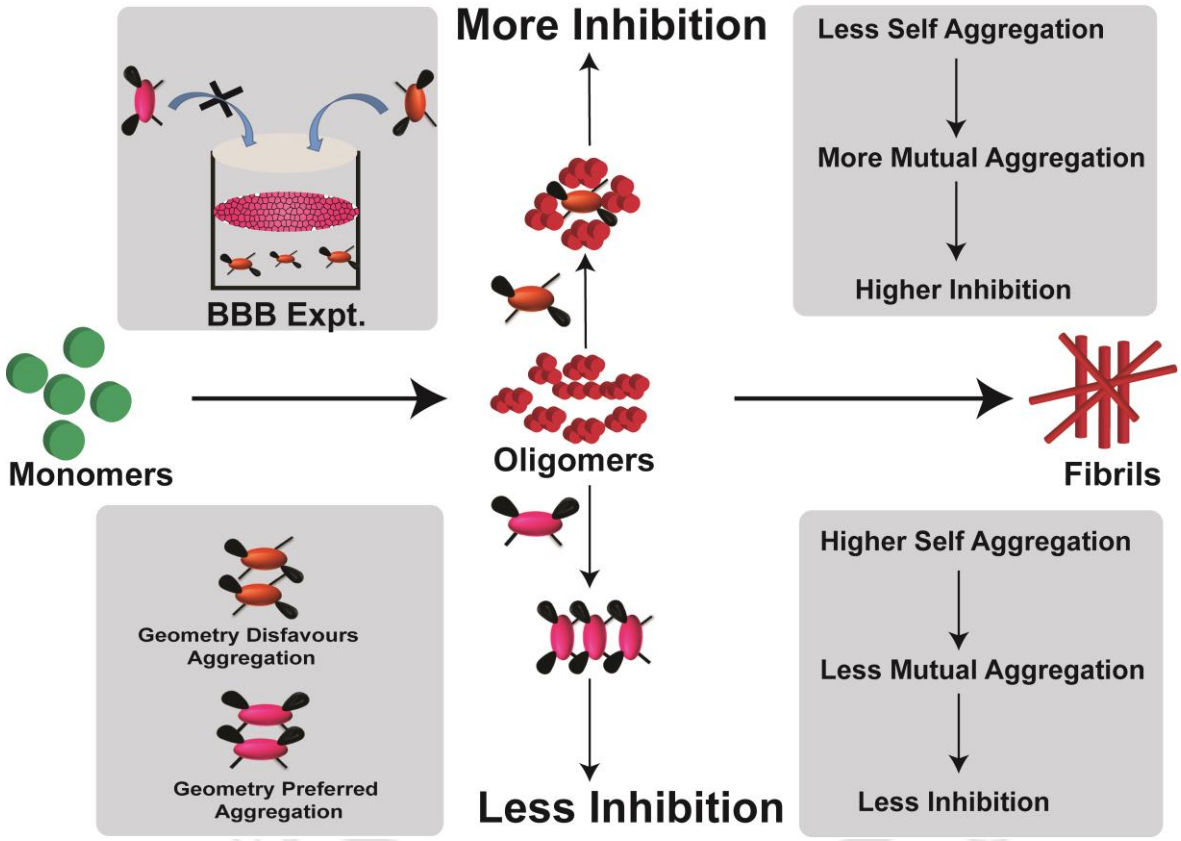

Scheme 4. Schematic presentation of oligo-modulators PAPAP and APPPA. Structural dissimilarity eases BBB permeability due to different self-aggregation and mutual aggregation predominates over self-aggregation which finally results in modulation.

Amyloid aggregation is observed in many neurodegenerative diseases but the formation of final plaque seldom correlates to the disease severity. Early and intermediate structures such as soluble oligomers are considered as primary toxic species in protein misfolding diseases specifically linked to Aβ in Alzheimer's disease (AD). Two peptides linked perylenebisimide isomers (PAPAP and APPPA) were developed to study the structure-activity relationship with toxic Aβ oligomer in commercial Aβ as well as in human cerebrospinal fluid (CSF), diminish and inhibit them and prevent them to form toxic amyloid fibrils from an early stage. Self-

aggregation of perylenebisimides enables to form nano/micro-objects that is used to interact with the hydrophobic regions of peptide and direct the peptide aggregation into an 'off-pathway' preventing mature fibril formation. Remarkably, one of the Ala-Phe dipeptides linked perylenebisimide isomer (APPPA) showed high selectivity toward Aβ oligomer and could also cross endothelial monolayer barrier (blood-brain barrier-BBB) efficiently than the other derivative (PAPAP). Kinetic ThT studies and AFM imaging pro-vided strong proof of both the isomers being able to inhibit fibrillation of prefibrillar and oligomeric Aβ in both commercial Aβ1-40 peptide as well as in real human CSF sample. Further, a correlation has been built using pristine fluorescence of perylenebisimides, showing modulation and 'oligo-blocking' (Scheme 4). The obtained data provides clear evidence that the mutual aggregation between the modulator and amyloid aggregate becomes predominant compared to their individual aggregation. These results reinforce the development of structural platform design to diminish toxic oligomers, inhibit them and prevent forming toxic amyloid fibrils at an early stage.

Chapter 5. Inhibition of Insulin Amyloid using Synthetic Perylenebisimide Twins

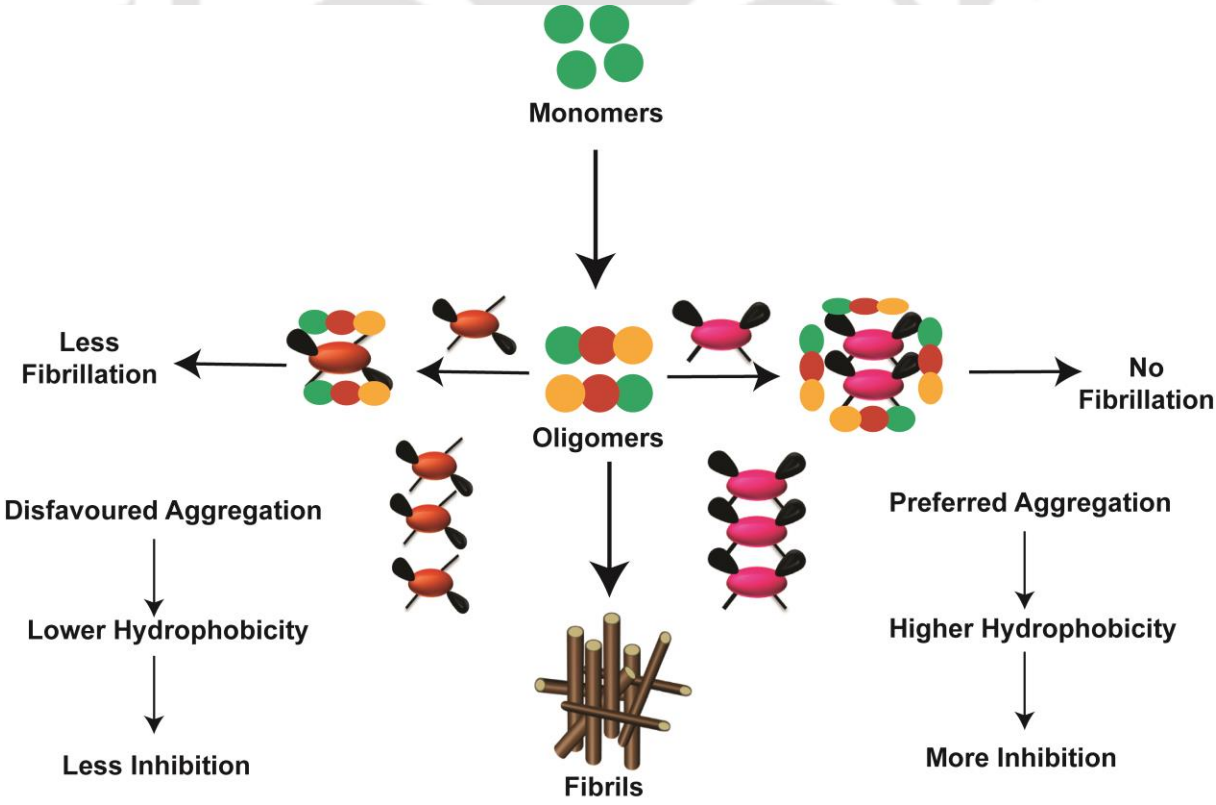

Scheme 5. Inhibitory effects of PAPAP and APPPA on insulin aggregation and fibril formation.

Perylenebisimide interferes with amyloid fibrillation. Mutual aggregation happens in presence of these structural motifs and nucleation on the particle surface leads to inhibition of the fibrillization process. Oligomers are the primary toxic species that initiate pathogenic aggregation. In this study, two perylenebisimide isomers (PAPAP and APPPA) were shown as modulators of insulin fibrillization. Early insulin aggregates are adsorbed into the modulator surface and result in an increase in lag phase. Fibrillation was monitored by Thioflavin T (ThT) fluorescence measurement in presence and absence of both the isomers, PAPAP and APPPA (Scheme 5). Conformational modulation using far UV circular dichroism studies also highlighted their role as an aggregation inhibitor via reduction of α-helix into β-sheet along with increased random coil contents. Moreover, the inhibitory effects were more pronounced with the more aggregation prone derivative due to higher chances of a hydrophobic encounter between protein and the small molecule modulator.

Future Aspect and Thesis Overview

Alzheimer's disease is genetically complex irreversible neurodegenerative disease in the brain. A succinct future prospective was highlighted in this chapter to achieve better treatment response or monitoring disease progression with high sensitivity and specificity before clinical integration.

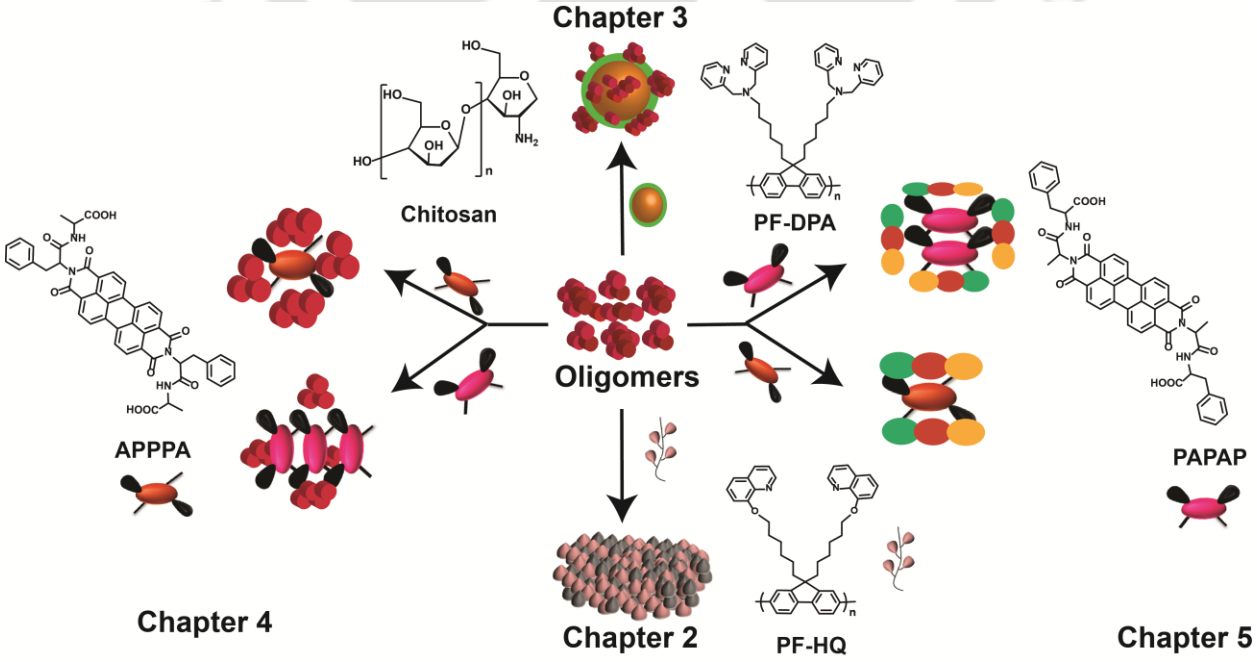

Scheme 6. Thesis overview: Development of polymer and small molecule based luminescent Aβ modulator.

In this thesis, I have focused on small molecule and polymer based luminescent materials on amyloid aggregation in order to modulate amyloid aggregates with an additional feature of self-indication. Mutual aggregation between amyloid and modulator becomes predominant compared to self-aggregation due to oligo-blocking and/or formation of co-aggregates. An overview of my observations (Scheme 6) was also presented in this final chapter. Briefly, in second chapter PF-HQ showed an amyloid surface motif and hence, due to this similar interacting interface, it showed an excellent in vitro inhibition of amyloid aggregation by forming polymer-protein co-aggregates. Further, this polymeric nanoparticle showed excellent dual emission in aqueous and as well as organic solvent and thus utilized as for multi-color bio-imaging and drug delivery for cancer treatment. But unfortunately, these polymer nanoparticles were not able to cross blood brain barrier (BBB) due to its hydrophobic nature. To overcome this, in the next chapter, a polymeric conjugate using polyfluorene (PF-DPA) and chitosan was developed. It can cross BBB and traps oligomers in Aβ and CSF. The similar interacting interface provided the adsorption and further inhibition to fibril formation. To achieve better optical correlation on protein aggregation, perylenebisimide isomers (PAPAP and APPPA) were designed with a hydrophobic dipeptide tail. As expected they showed a distinct aggregation pattern in presence of oligomers of Aβ and insulin amyloid. These observations were discussed in chapter four and five. Interestingly, less aggregation prone derivative (APPPA) was able to cross BBB more proficiently and found efficient in modulating oligomers in Aβ and CSF whereas the other sibling, PAPAP was consistent with insulin amyloid. These findings may not directly involve in clinical trials but definitely, provide guidance taking molecules to clinical trials in order to achieve early diagnosis and prevention of neurodegeneration.

Chapter 1

Introduction

Malik, A. H.; Hussain, S.; **Chowdhury, S. R**.; Iyer, P. K. Conjugate polymer for disease diagnosis and theranostic medicine. Book Chapter. John Wiley & Sons (In print).

1. Introduction

1.1. Protein Aggregation and Neurodegenerative Diseases

The last decade has provided significant achievements in the field of protein folding, misfolding and aggregation. By and by, protein folding and protein aggregation are considered in close competition to each other due to the same physicochemical basis. Protein achieves its well defined three-dimensional native state via protein folding. Proteins attain its functional state undergoing post-translational modification after they are produced on the ribosome through amino acid linking.[1,2] Although protein quality control framework in living organism has developed over years to defense proper protein folding, trafficking and degradation of misfolded proteins,[3] a large number of proteins leads to misfolding.[4] The unfurled protein has high free energy and entropy.[5] Misfolding is driven by several reasons viz., (1) transcriptional or translational errors (2) erroneous post-translational modifications or trafficking of proteins and (3) structural modification due to environmental changes (4) ageing, (5) somatic or genetic mutations, (6) changes in intracellular environment such as temperature, pH, oxidative stress and presence of metal ions.[6]

Aggregation occurs when folding intermediates bare their hydrophobic amino acid residues or regions that are deeply hidden in the native state and the aggregation is mainly boosted by hydrophobic forces that results in the formation of amorphous aggregates, oligomers and amyloid fibrils. The leading aspects that have been documented as important factors of the transformation of a native protein into these aggregates are hydrophobicity, low net charge and propensity to form β-sheets.[7,8] Reverse turns are broadly delineated as those regions of the polypeptide where chain reversal happens and are known to play important role in protein folding and stability.[9] They play crucial role in protein folding because of their innate stability, topological features and hydrophobic areas within the protein's structure. The onset or progression of disease that occurs due to formation of protein aggregates is called as protein aggregation diseases. Most common among them is neurodegenerative disorder in which the protein abnormally aggregate and deposit in specific regions of the brain and hampers its function.

Neurodegeneration covers a wide spectrum of neurological disorders with many different symptoms, including cognitive impairment, speech difficulties, and motor dysfunction. Each neurodegenerative disorder has its unique features, these diseases can look somewhat similar at the end stage with patients becoming bed bound, mute, and unable to care for self. The

underlying pathological hallmark is the loss of neuronal populations in the brain and/or spinal cord.[10] The particular areas of the brain and spinal cord in which neuronal loss occurs dictate the clinical features of a given neurodegenerative disorder. The most common and uncommon Neurodegenerative disorders include Alzheimer's disease (AD), Parkinson's disease (PD), Huntington's disease (HD), amyotrophic lateral sclerosis (ALS), other polyglutamine diseases (DRPLA, SCA1-3, SBMA), frontotemporal dementia with Parkinsonism (FTD) and prion diseases (kuru, CJD, GSS, fatal familial insomnia, new variant CJD). Interestingly, all of them share common histopathological features. All of this diseases are increasingly being realized to have common cellular and molecular mechanisms including protein aggregation and inclusion body formation.[11] The progression of these diseases is supposed to be caused by the misfolding of specific proteins, resulting in aggregation and fibril formation. In many cases the highly soluble protein are gradually converted into these insoluble aggregated protein having a very ordered structure and exhibit characteristics of so called amyloid-like protein assemblies.[12] The structure and biophysical properties of these fibrillar networks are very similar across different amyloid diseases, despite the fact that each disease involve amyloidogenic aggregation of one or several distinct proteins.[13,14] Furthermore, amyloid fibril formation has been reported to be associated with the loss of protein function,[15] a toxic gain of function,[16] or even functional reversible amyloid assembling.[17] AD is the most common progressive dementia among other neurodegenerative diseases and current estimation of affected 36 million worldwide population will triple by 2050. Neuronal death in AD happens mainly in the hippocampus, amygdala, and cortex regions of brain that are involved in memory and thinking.[18] PD is categorized by neuronal loss in the substantia nigra and depletion of dopamine in the striatum.[19] HD is categorized by severe neuronal loss in the striatum and cerebral cortex.[20] ALS is categorized by the degeneration of lower motor neurons in the spinal cord and brainstem and loss of neurons in the motor cortex.[21] The protruding feature of pathogenesis in TSEs is the spongiform degeneration of brain tissue. The location and extent of neuronal loss is variable in case of TSEs.[22]

1.2. Alzheimer's Disease

Alzheimer's dementia (AD) is the most common among debilitating neurodegenerative diseases that have a worldwide unmet need due to socioeconomic burden and increase in aging population. Currently 46 million AD is registered and the amount will triple worldwide by 2050 in light of predictions. AD was first identified by Alois Alzheimer in 1906.[23] Early detection of AD is not yet reliable and preventative treatments in prodromal AD (pre-senile

dementia) are not available. Memory tests involving psychiatric appraisals are the standard diagnostic tool. Neural imaging is used as a supplementary diagnostic tool along with memory tests.[24,25] Till date there is no existing technology to detect this disease as sympotoms may require a decade to manifest after the onset of pathophysiology in AD.[26]

1.3. Amyloid Beta (Aβ) Hypothesis

This hypothesis is the most widely accepted among several other theories which have been proposed to explain disease progression. It describes the amassing of Aβ within neural tissue as the initial key event that initiates the disease.[27] According to this theory soluble Aβ oligomers are the primary toxic species which causes the primary neurological insult. Aβ accumulation is responsible for an imbalance between its production and clearance, which leads to the formation of plaques which, in turn, triggers the formation of neurofbrillary tangles.[28] Aβ monomers are formed by the cleavage of trans-membrane amyloid precursor protein (APP) by β and γ secretases.[25] Aβ monomers then misfold to form toxic β-sheet oligomers and eventually aggregate toform larger fibrils and plaques (scheme 1.1). This misfolding is seemed to happen through side chain interactions creating a hairpin structure with residues in the central region and N-terminus developing intermolecular hydrogen bonds with other monomers.[29] Aggregation is considered to follow a nucleation pathway i.e., monomeric binding sides appear on the outside of the budding oligomer, turning into nucleation sites for further evolution into toxic oligomers, protofibrils, and eventually mature fibrils.

Recent reports suggest that oligomers are the most toxic among other aggregated species and non-specific interactions with the cell membrane is considered to play a significant role in cytotoxicity.[27,30] Effects on the cell membrane caused by amyloid oligomers may be more subtle, including: receptor protein distribution, modification of signaling pathways, and change in synaptic plasticity prior to the occurrence of more severe deformations.[31,32]

Although Aβ is produced in all humans, irrespective of age or disease but the natural role of these amyloid are largely unidentified. Few reports describe the role of Aβ monomer in important signaling pathways in the brain[33] and is expected to have neuroprotective properties and physiological roles at low concentrations.[34] It seems that healthy individuals are not vulnerable to amyloid induced cytotoxicity and can clear amyloid from the brain before it grasps neurotoxic levels by balancing amyloid production and clearance.[35]

1.4. Therapeutic Strategies

Aβ is a 4-kDa peptide derivative of the larger APP[36] and it was first revealed as part of senile plaques in AD patients in 1983.[37] The transmembrane protein, APP was first identified in 1987 as a ~700 residue. Since it has no known physiological purpose except as the precursor to Aβ, it was simply labelled as APP. The APP gene is positioned on chromosome 21, resulting in overexpression of APP in patients with trisomy 21.[38] This clarifies the Aβ overproduction and early development of AD in individuals with Down's syndrome.[36] APP is known to undergo cleavage in three different sites: (1) β-secretase cleaving at the N-terminal of the Aβ domain; (2) γ-secretase cleaving at the C-terminal of the Aβ domain; and (3) α-secretase cleaving within the Aβ domain. Since proteolytic cleavage by α-secretase does not produce complete Aβ and, therefore, does not lead to the development of AD. The length of the two most prevalent isoforms of Aβ are composed of 40 and 42 amino acids and they vary at the C terminal, where length is decided by the cleavage site of γ-secretase.[39] As mentioned before, once the amyloid plaques are formed, it triggers the hyperphosphorylation of microtubule-associated tau protein. This causes the tau protein to accumulate and form neurofbrillary tangles, which cause synaptic dysfunction and contribute considerably to AD symptoms.[40,41] Although two parallel belief exist over the initial occurrence it is speculated that it may be possible to slow disease progression if amyloid burden can be reduced. Very recent progresses are considering both proteinopathies.

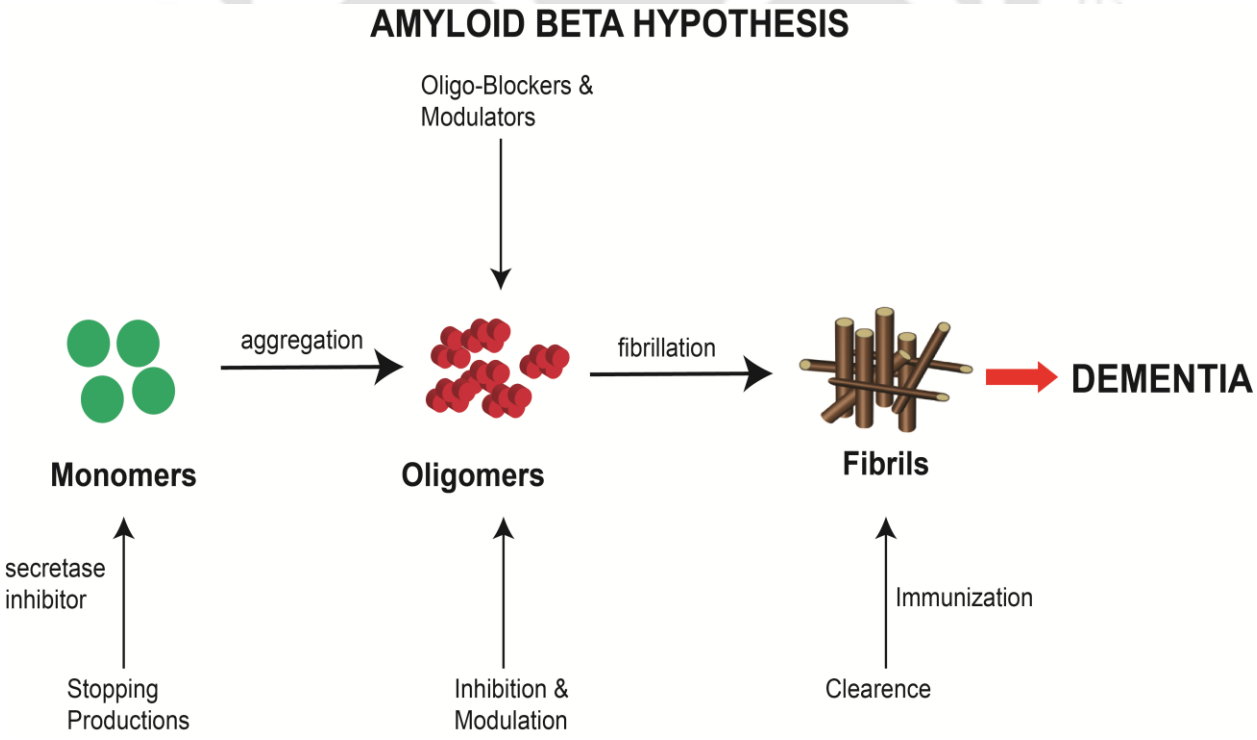

Scheme 1.1. Amyloid β hypothesis and strategies based on production, clearance and inhibition of amyloid aggregation.

1.4.1. α-secretase based strategy

Since α-secretase processing of APP involves cleavage within the Aβ domain, stopping Aβ formation, activation α -secretase cleavage of APP is considered as an obvious potential treatment for AD.[42] Such activation would be supposed to both and increase levels of the neuroprotective sAPPα and lower levels of Aβ.[43] Another physiologically relevant enzyme is ADAM 10 which is essential for constitutive α-secretase cleavage of APP among other 30 substrates.[43] Increasing the activity of α-secretases via the activation of associated signaling cascades has been considered as one of the best therapeutic approach to design drugs against AD.[44] A number of drugs intended as direct or indirect α-secretase activators have progressed to the clinical trials stage for AD (Figure 1.1). Selegiline (monoamine oxidase inhibitor),[45,46] etazolate (GABA receptor modulator),[47] PRX-03140 (5HT4 agonist),[48] epigallocatechin gallate (PKC pathway),[49] bryostatin (PKC modulator)[50] are known to increase or stimulate sAPPα production and undergoing clinical trials.

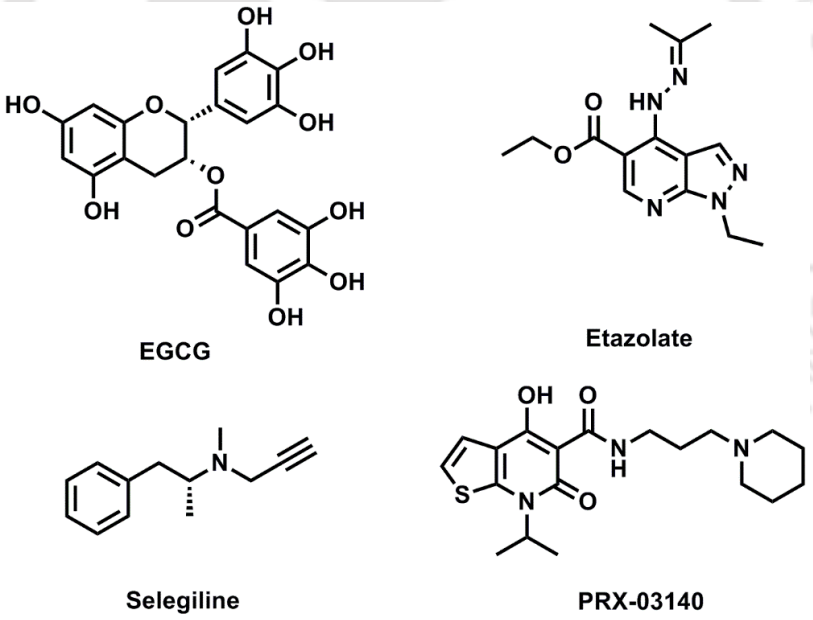

Figure 1.1. α-secretase activators designed to increase levels of the neuroprotective sAPPα.

1.4.2. β-secretase based strategy

Transmembrane aspartic protease, BACE1 is about 500 residues in length with two active sites located on the lumenal side of the membrane.[51,52] It is a highly sequence specific β site APP cleaving enzyme which was considered as a likely candidate for β-secretase. BACE1 activity has been shown to be preeminent in cases of sporadic AD. Although it is not exclusively active

in AD instead it appears to be producing more Aβ by favoring β-secretase cleavage. BACE1 inhibition was the most likely choice for the scientific community in the last decade. Development of the most successful inhibitors include CTS-21166, LY-2886721, E2601, HPP854, RG7129, MK-8931, AZD3293 which have provided initial reduction of Aβ levels by following BACE1 inhibition but failed to pass safety evaluation in clinical trials (Figure 1.2).[53-57] Due to the large active site of BACE1, two factors become really challenging to achieve: first sufficient selectivity over BACE2 which possess approximate 64% identity of BACE1 and second crossing the blood brain barrier due to large molecular weight of the inhibitors. Encouragingly, it was recently shown by Steinberg et al that a single residue mutation within the APP gene which decreases the ability of β-secretase to cleave APP deliberates a strongly protective effect against both AD and general cognitive impairment in human.[58] These findings boosts further sustenance of the amyloid hypothesis and of BACE1 as a therapeutic target in AD.

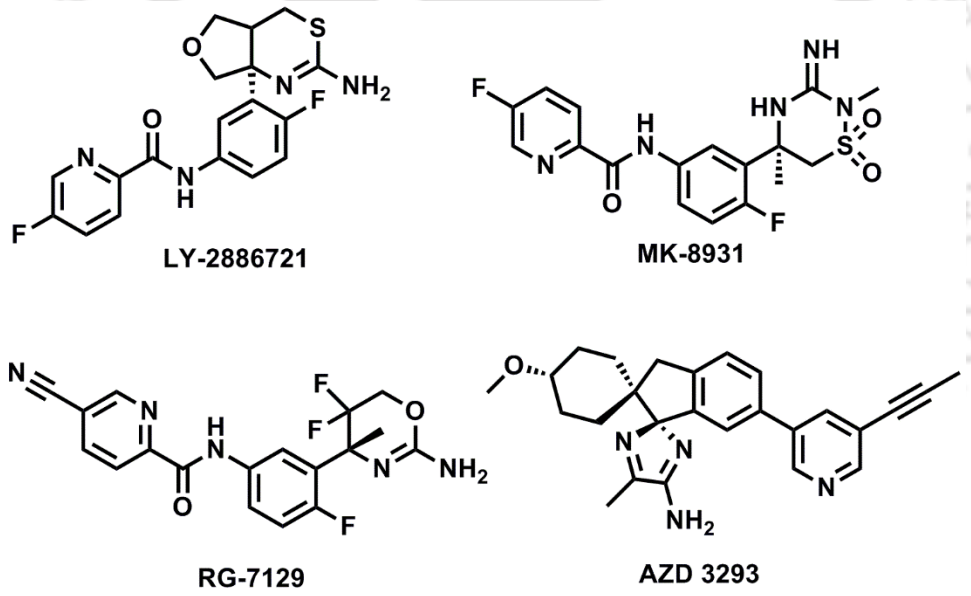

Figure 1.2. BACE inhibitors that are designed as a therapeutic target for AD.

1.4.3. γ-secretase based strategy

γ secretase cleaves the C terminal of APP and releases its cytoplasmic domain. It is also influenced by presenilin 1 and 2 (PS-1 and PS-2), which seemed to determine where at the C-terminal cleavage of Aβ occurs by γ-secretase. However, γ-secretase had been shown to cleave a wide range of substrates, the most important one is Notch, a cell surface signaling receptor that is indispensable for many facets of cell development and differentiation.[59] γ-secretase has

been the most commonly studied including semagacestat, avagacestat did not work well due to Notch inhibition with symptoms of worsening cognition and skin cancer.[60,61] The future of γ secretase inhibitors are notch sparing inhibitions capable of lowering Aβ without disturbing the processing of Notch and producing non-pathogenic isoforms of Aβ. Following this new developments come up including ELND006, Begacestat, Tarenflurbil, CHF-5074, NIC5-15 showed initial positive results on cognition and lowering Aβ levels but ultimately discontinued due to liver toxicity, poor results and for some unknown reasons in some cases (Figure 1.3).[62-66]

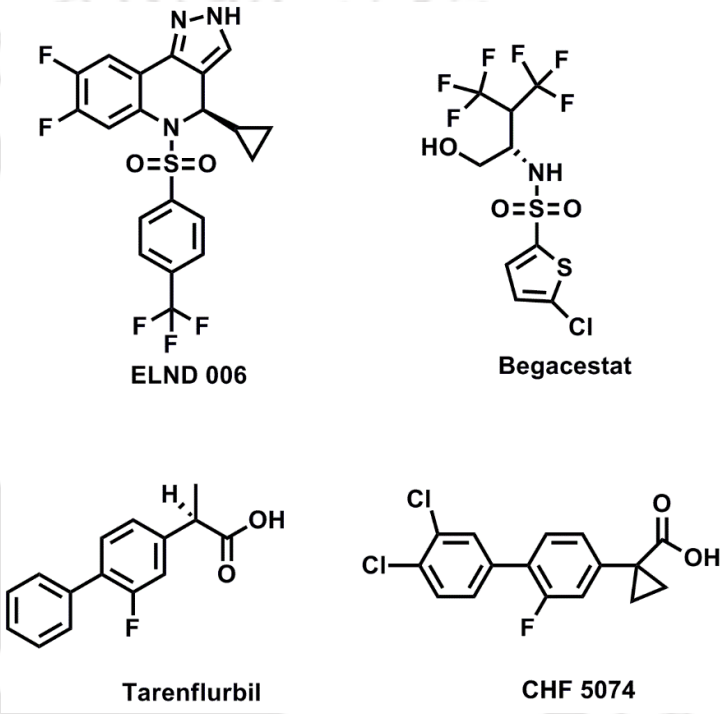

Figure 1.3. γ secretase inhibitors that showed initial positive therapeutic response for AD.

1.4.4. Inhibition of AChE

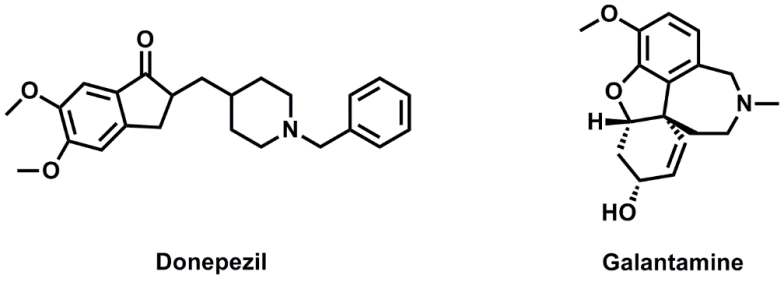

Figure 1.4. AChE inhibitors for anti-AD therapy.

The most common pharmacological approach of non Aβ targeting is inhibition of AChE that inactivates acetylcholine in AD brain. Therefore the inhibitors can transiently increase acetylcholine concentration supporting cholinergic neurotransmission. Hence, it compensates for the deficit of acetylcholine in AD due to cholinergic neuronal loss.[67] Donepezil, galantamine are selective AChE inhibitors and rivastagmine can inhibit both acetyl and butylcholinesterase activities (figure 1.4). Despite of several other neurological complications donepezil hydrochloride and rivastagmine are the drug of choice worldwide and still prescribed in India for anti-AD therapy.[68]

1.4.5. NMDA receptor antagonist

The over-stimulation of N-methyl D-aspartate (NMDA) receptors by glutamate up-regulates excitatory signal transduction resulting in neural dysfunction and progressive neurodegeneration. Dysfunction of glutamatergic neurotransmission manifests neuronal excitotoxicity and is seemed to be linked with AD etiology.[69] To block the effects of excess glutamate NMDA receptor antagonists have been strategically framed and thereby physiological signal neurotransmission is restored. Memantine has been used clinically as it possesses atropinic, cholinergic, dopaminergic and serotonergic pharmacological effects[68] but it has been stopped due to limited clinical effectiveness and high cost-to-benefit ratios.[70] Combinatorial AChE-glutamatergic drug strategies, NMDA receptor antagonist alone have shown equally disappointing results in clinical trials.

1.4.6. Anti-cholesterol drugs and cholesterol lowering agents

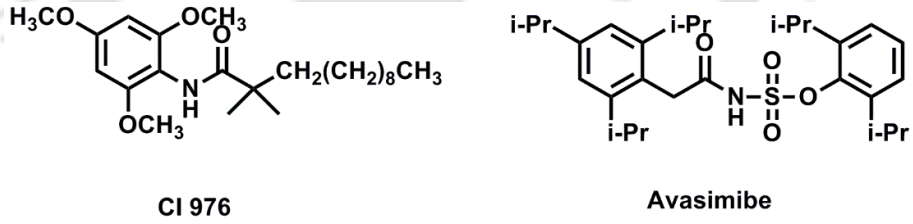

CI 976 Avasimibe

Figure 1.5. ACAT inhibitors that suppress cholesterol levels and have shown an indirect positive therapeutic effects in patients who are at AD risk.

Statins are well known inhibitors of 3-hydroxy-3-methylglutaryl coenzyme A. They reduce plasma cholesterol and hence increase the risk of stroke, cerebrovascular and cardiovascular disease which are often present in AD subjects.[71] In addition to their primitive role of reducing cholesterol and blood plasma lipids they have been shown to increase βAPP/Aβ ratio. Thus it acts as anti Aβ modulator and due to several other pleiotropic effects viz. endothelial-vascular

function, increased myocardial and microcapillary perfusion, enhancement of the bioavailability of nitric oxide, inhibition of biosynthesis of isoprenoids, and decreasing protein isoprenylation, it contributes to cell to tissue specific anti-inflammatory and immunomodulatory effects. Lovastatin, simvastatin, pravastatin and fluvastatin are the most prescribed statins that show an 'off-target' 'pleiotrophic' effects. Acyl-coenzyme A cholesterol acyltransferase (ACAT) catalyzes the formation of cholesterol esters from cholesterol and fatty acyl-coenzyme A. Inhibitors of this intracellular enzyme are known to suppress the APP containing lipoproteins. They are known to reduce plasma low density lipoproteins, either alone or in combination with statins. Selective estrogen receptor modulators are also known to reduce serum cholesterol in patients who are at increased AD risk. 2,2-methyl-N-(2,4,6,-trimethoxyphenyl dodecanamide (CI-976) and avasimibe are ACAT inhibitors that have following three key positive effects: first on multiple membrane trafficking pathways in eukaryotic cells, second decrease excessive hepatic apolipoprotein secretion into plasma, and third significantly increasing clearance of triglyceride-rich lipoprotein from the systemic circulation (Figure 1.5).[72] Despite these positive facts, Concerns about clinical outcomes, safety, and efficacy in various combinations still remain poorly understood in development of cholesterol absorption and transport inhibitors, ACAT inhibitors and estrogen modulators.

1.4.7. Metal ion chelators

Neurotoxic metal ions and their role in AD first came to limelight after the discovery of antioxidant desferrioxamine, a trivalent ion chelator that can eliminate excessive iron and aluminum from the body. It was also reported to slow the progression of AD.[73] Copper, iron, zinc, and aluminum are known to bind βAPP and Aβ under psychological conditions and increasing evidence supports the idea that trace amounts of neurotoxic metal ions are essential for Aβ peptide aggregation. Formation of insoluble fibrillar network from Aβ peptide monomers is accelerated in presence of these metal ions. Metal-ion catalyzed inflammatory signaling and oxidative stress precede amyloid aggregation and plaques formation. Therefore strategies based on anti-oxidant and metal-ion chelation have been developed for the management of AD. 'Molecular shuttle chelation' in presence of desferrioxamine, clioquinol, PBT2, FI, PHQ, Feralex-G and silicon approve antioxidant-chelation and reduce metal mediated burden by disrupting amyloid aggregates (Figure 1.6).[74-77] But none of them proceed further as they face competition between free metals and metals trapped within amyloid aggregates.

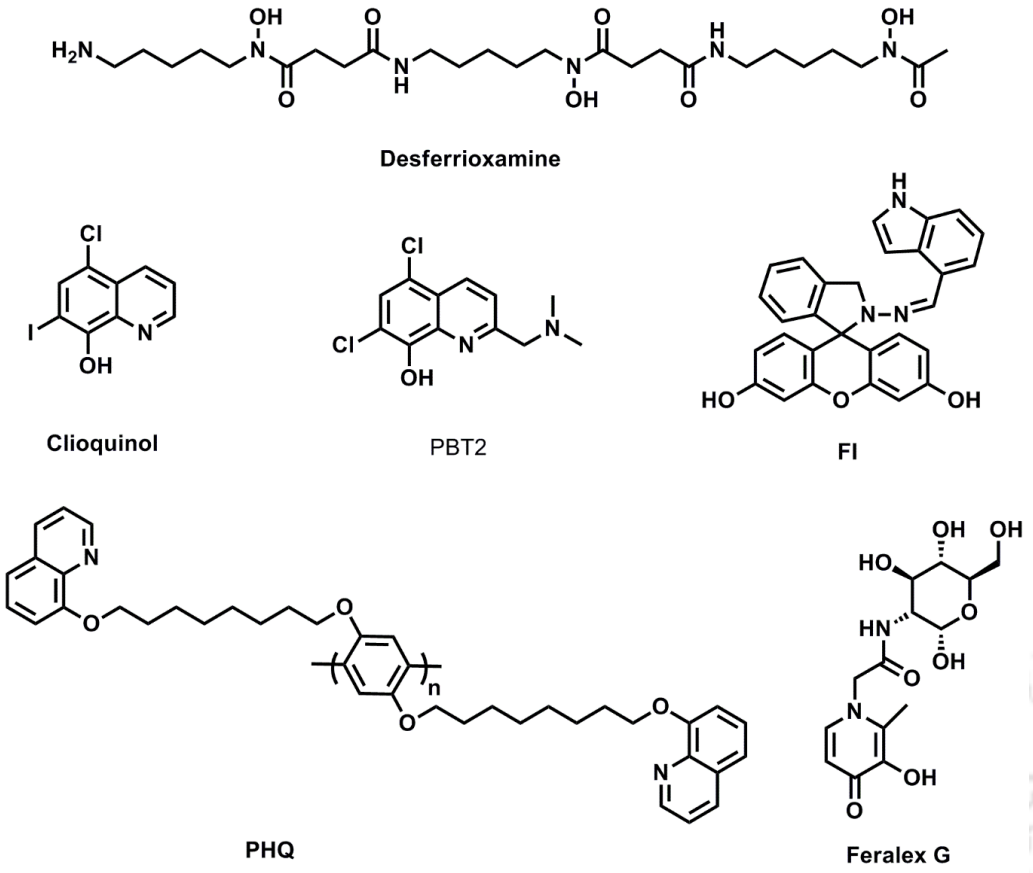

Figure 1.6. Metal chelators that are known to decrease the metal mediated amyloid burden.

1.4.8. Modulation of Aβ

Immunization against Aβ-peptides is proposed to be highly effective in reducing excessive amounts of Aβ-peptides in the AD brain, and hence expected to be useful in lowering Aβ-peptide-triggered pathogenic change. Humanized monoclonal anti Aβ antibody Bapineuzumab, Solanezumab, and Aducanumab showed positive response in prodromal or mild AD.[78-80] As described by Alzheimer himself, amyloid plaques are one of the key pathological hallmarks of the disease. Therefore amyloid β-derived-diffusible ligands (oligomers formed by variable number of Aβ polypeptide chains) are developed to distinguish the soluble aggregate known as oligomers from other heterogenic forms of protein.[81] But their exact conformation and aggregation state are still unclear. Many studies reveal that dimers and trimers are most synaptotoxic. Proposed mechanism of cellular dysfunction and neuronal death is triggered by activating several signaling pathways due to their preferential binding

with postsynaptic receptors viz. p75 neurotrophin receptor, neuroligin-1 (NL-1), the α7-nicotinic acetylcholine receptor (α7-nAChR), the cellular prion protein (PrPc), and glutamatergic receptors.[82]

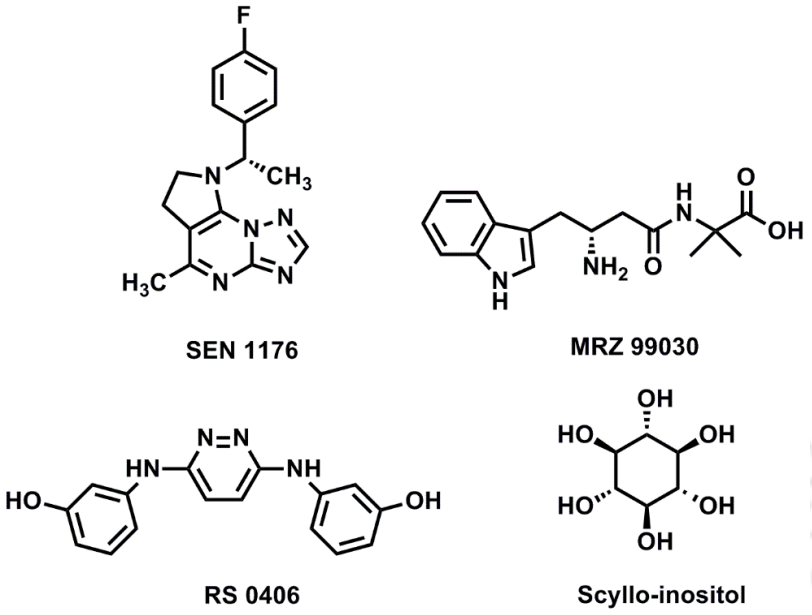

Figure 1.7. Aβ modulators that are known to interrupt amyloid aggregation and inhibits fibrillation.

Scyllo-inositol is reported to reduce Aβ1-42 level in CSF but an increase in brain ventricular volume is observed in patients.[83] Some natural molecules including curcumin, grape seed extract, and (–)-epigallocatechin-3-gallate (EGCG) are also reported in literature that attenuate Aβ toxicity.[84] SEN-1176, SEN-1276, and BGC20-0406 (RS-0406) are initially reported as small molecule inhibitors of early amyloid oligomerization with no recent updates (Figure 1.7). Acumen developed a number of small molecule based oligomer inhibitors using screening cascade: first a fluorescence resonance energy transfer based assay and second checked inhibitory modulation using synaptic spines of hippocampal neurons in primary culture.[85] EG30 (MRZ99030) was first characterized as a modulator of Aβ aggregation by promoting aggregation into nontoxic, off-pathway MRZ-99030/Aβ assemblies.[86] MRZ-99030 also prohibited the twofold increase in resting Ca^{2+} levels in pyramidal neuron dendrites and spines caused by Aβ1–42 oligomers. Exebryl-1 and pepticlere were developed earlier in 2008 and 2009, as Aβ inhibitors but no further developments are reported since then. Polymer and inorganic nanoparticles also have shown promising results due to their large surface to volume ratio, polypeptides get adsorbed into its surface resulting the formation of protein corona and aggregation takes an off-route pathway. Nano-bio interface has been a growing interest due to its colloidal forces and biophysicochemical interactions.[87] Polymeric nanoparticles

fabricated with the central hydrophobic core is developed to preclude amyloid aggregation and fibril formation. Gold nanoparticles, molybdenum disulfide nanoparticles have gained significant attention as inhibitors of amyloid aggregation.[88]

1.4.9. Other strategies

Apart from the strategies discussed above there are some additional compounds that are developed to reduce amyloid load in animal studies and as well as in human. Among them non-steroidal anti-inflammatory drugs and medicinal plant extracts are proved to be the most promising due to their anti-oxidant, anti-inflammatory, anti-apoptotic, anti-angiogenic and immune-stimulatory activities. Most beneficial therapeutic effects are achieved from *Salvia officinalis*, *Melissa officinalis*, and the Chinese concoctions *Ba Wei Di Huang Wan* and *Yi-Gan San* in case of mild to moderate AD. Neutraceuticals, herbal medicines, phytochemicals, and ethnobotanicals are being developed to achieve effective symptomatic treatments.[89,90] Recently, Tsai et al developed a light based therapy for AD. They used optogenetics to correct gamma rhythm in the hippocampus by stimulating neurons at 40 Hz range at the optimal gamma rhythm amplitude. They were able to lower the Aβ level and senile plaques by activating microglia.[91]

1.5. Blood-Brain Barrier

Targeting the robust amyloid fibril and crossing the blood-brain-barrier is the key to fight against these diseases. Hence biomolecules were the initial choices for the scientific community. The blood brain barrier (BBB) is a highly selective and efficient barrier that defends the brain from undesirable molecules and pathogens. In order to transport potential therapeutic and diagnostic agents to the brain, BBB is the most difficult hurdle to overcome. The lack of therapeutics for the treatment of Alzheimer's and other brain diseases is due to their inability to cross BBB.[92] Endothelial cells are glued together with the help of binding proteins. A large portion of brain homeostasis is controlled by BBB through junctions made by endothelium and binding proteins known as tight junction and adherin junction. It has the authority to prevent entry of unwanted molecules or pathogens inside brain. There is no known one-size-fits-all drug delivery system for delivery of drugs/pathogens to brain diseases. There are different routes for molecules to pass through this barrier viz (1) paracellular and transcellular routes, (2) lipophilic and transport protein pathways (influx/efflux), (3) receptor mediated transcytosis, and (4) absorptive mediate transcytosis. Nanoparticle based delivery systems have a reputation of passing through this barrier efficiently and therefore, delivery of

therapeutics to brain can be improved using nanoparticles. But safety and efficacy of these models are time taking and still under progress.

1.6. Luminescent Conjugate Materials

An ideal luminescent material have high absorbance, quantum yield, specific and selective excitation and emission to diminish background fluorescence. Toxicity and solubility under psychological conditions also played a key role *in vivo* or live cell staining. Both small molecules and polymers are well known conjugate systems that have been utilized to study biological events due to their excellent light harvesting ability (Figure 1.8). Although these molecules have been successfully involved in detection schemes in numerous biological instances, reports on protein interactions are rare. The following sections will focus on luminescent materials based on small molecule and polymer, as these materials have proven useful for studying modulation, inhibition of protein-protein interaction, thus opening a new interface not only toward disease diagnosis but also theranostic medicine.

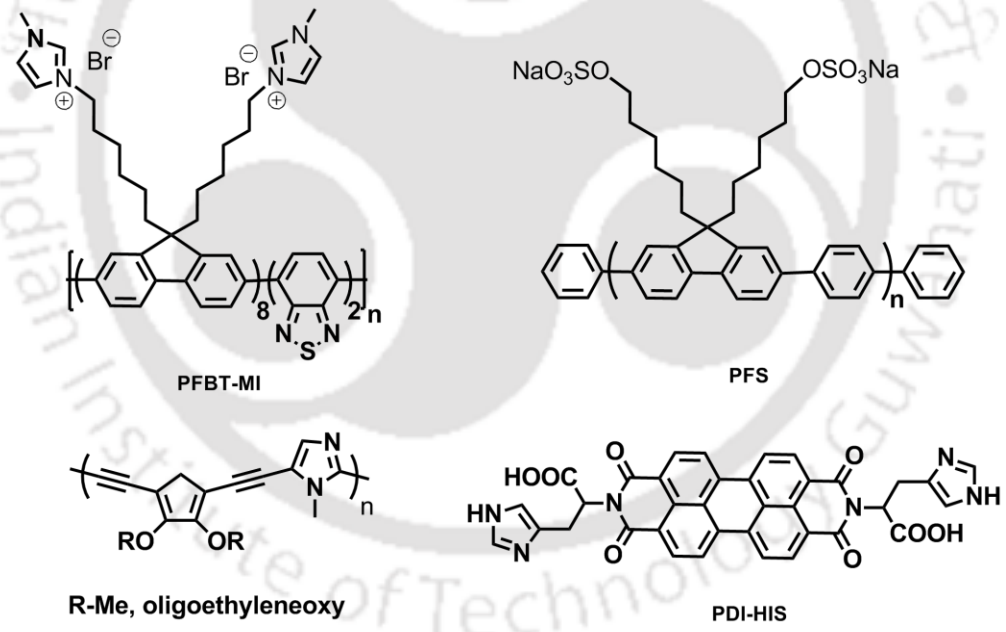

Figure 1.8. Polymeric and perylene based conjugate materials that are known to interrupt amyloid aggregation, detect biomarkers (for early diagnosis) and biomedical imaging applications.

Molecular recognition based on conjugate polymer nanoparticles and small molecule approach to selective molecular imaging in biological systems is a rapidly increasing field that can develop the study of life processes with specific chemical detail. Fundamental organic, and inorganic reactivity ideologies, combined with a taste towards biological finding, have given rise to a variety of new chemical outfits for probing the complex roles of conjugated materials

and biomarkers in physiology and pathology. Equally important in terms of new reaction design and development is fundamental biology; the ultimate impact of chemical tools will be in the discovery and understanding of new biological processes.[93] Here, both the choice of an important biological problem and the development of chemical tools to address such questions are essential for pushing the boundaries of the field. A host of enticing opportunities awaits. The greatest challenge is the discovery and identification of selective, bioorthogonal reactions that form the basis for new detection schemes.[94] Many well-designed chemical schemes for fluorescence detection continue to be reported and are essential for building the foundation for molecular imaging applications. But subcellular delivery still remains a challenge using these materials. Conjugate polyelectrolytes were designed as a DNA specific marker and the idea was to use Förster resonance energy transfer (FRET), where the added chromophore served as an acceptor, and the LCP was the donor.[95] Similarly, it can be tuned to produce an efficient strategy to predict disease occurrence based on biomarkers detection and reading elevated levels optically.[96-99] Conformational flexibility of proteins and peptides is the key in their associated pathological connections and therefore successful detection and diagnosis based on luminescent materials offers unlimited possibilities to visualize and understand disease etiology, and it indicates an exciting future for diagnosis and theranostic medicine.

1.7. Objective of the Thesis Work

The amyloid hypothesis has now been the backbone of therapeutic research in Alzheimer's disease for over two decades. In several studies amyloid plaques does not correlate to cognitive decline.[100] However, other investigations have established a much stronger correlation between soluble Aβ oligomers level and severity of cognitive decline.[101] The difficulty in isolating the specific neurotoxic species of Aβ and characterizing its effects makes research problematic. Although aggregation of Aβ is vital for the cytotoxic effects of Aβ but *in vitro* preparations does not result in unique potencies of the peptide that leads to fibrillar aggregates.[102] Studies based on transgenic mouse models of AD does not recapitulate human conditions due to lack of human-like inflammatory response and tau protein which also plays a pivotal role in disease progression. Type 2 diabetes and AD are believed to be two associated pathological commonness of misfolded proteins and an assumption that such diseases may share intricate downstream of events.[103] For example increase in activity of GSK-3 and thus its inhibition is recognized as another promising strategy. It can interact with presenilin and regulate Aβ production by activating γ secretase complex.

Current developments are directed at metal ion chelators, γ-secretase, β-secretase, statins, and associated cholesterol dropping agents, other drugs targeting Aβ production, and synthetic pharmaceutical and plant extracts and their derivatives which have been revealed to tweak excess production of Aβ peptides in various ways and thus lowering the levels in order to decrease the burden. But soluble Aβ oligomers are considered as a major molecular culprit in AD. Development of biomarkers or drugs that target these soluble aggregates may open a prevention window well before the symptoms appear. This thesis is mainly focused on luminescent materials viz both small molecules, polymeric nanoparticles and conjugates that can either modulate or inhibit early amyloid aggregates. Interaction interface between small molecule/polymer-protein has been explored with an intention to find structural variations that can interact with the hydrophobic core of the amyloid and interrupt pathogenic aggregation. Therefore the main objective of the thesis was to modulate the robust amyloid by targeting them selectively and making luminescent materials that can preclude amyloid aggregation which lead to final fibrillation found in plaques and extract optical information on protein aggregation. Importantly, some of these materials may help in the advancement of drugs for early or 'pre-clinical' stages of AD that may reverse neurodegeneration well before symptoms prevail of this progressively incapacitating disease.

In addition the details of the thesis work is summarized in a nut shell,

Chapter 1. Details about the already existing developments and strategies to inhibit production, aggregation and clearance of Aβ along with other indirect strategies taken to fight against AD and a sneak peak of the objective of this thesis.

Chapter 2. Modulation of amyloid aggregates by a conjugate polymeric material (PF-HQ) that shows an amyloid like surface motif in aqueous medium due to aggregation. It also formed a co-aggregate in presence of early amyloid aggregates and stops final fibril formation.

Chapter 3. Modulation of early amyloid aggregates using a polymeric conjugate that crosses blood brain barrier efficiently. A polyfluorene derivative is functionalized with chitosan and utilized as an oligo-modulator.

Chapter 4. Two perylenebisimide isomers are designed that inhibits amyloid fibrillation by blocking the early amyloid aggregates. A mutual aggregation directs amyloid aggregation into an 'off-pathway'. Less aggregation prone isomer is able to target the oligomers more selectively and able to cross blood brain barrier efficiently compared to its sibling.

Chapter 5. The perylenebisimide twins are explored to modulate insulin amyloid. More aggregation prone isomer is able to target the early aggregates of insulin amyloid and inhibits fibrillation.

Chapter 6. A sneak peek into the future toward theranostic developments in order to predict and slow/reverse the neurodegeneration.

Reference

(1) Ellis, R. J.; Minton, A. P. *Biol. Chem.* **2006**, *387*, 485-97.

(2) van den Berg, B.; Wain, R.; Dobson, C. M.; Ellis, R. J. *EMBO J.* **2000**, *19*, 3870–3875.

(3) Kim, Y. E.; Hipp, M. S.; Bracher, A.; Hayer-Hartl, M.; Hartl, F. U. *Annu. Rev. Biochem.* **2013**, *82*, 323-55.

(4) Balch, W. E.; Morimoto, R. I.; Dillin, A.; Kelly, J. W. *Science* **2008**, *319*, 916-9.

(5) Naz, H.; Shahbaaz, M.; Bisetty, K.; Islam, A.; Ahmad, F.; Hassan, I. *Biochem. Cell Biol.* **2016**, *94*, 221-228.

(6) Herczenik, E.; Gebbink, M. F. *FASEB J.* **2008**, *22*, 2115-33.

(7) Chiti, F.; Stefani, M.; Taddei, N.; Ramponi, G.; Dobson, C. M. *Nature* **2003**, *424*, 805-8.

(8) Tartaglia, G. G.; Pawar, A. P.; Campioni, S.; Dobson, C. M.; Chiti, F.; Vendruscolo, M. *J. Mol. Biol.* **2008**, *380*, 425-36.

(9) Santiveri, C. M.; Santoro, J.; Rico, M.; Jiménez, M. A. *Protein Sci.* **2004**, *13*, 1134-47.

(10) Brettschneider, J.; Tredici, K. D.; Lee, V. M.-Y.; Trojanowski, J. Q. *Nat Rev Neurosci.* **2015**, *16*, 109–120.

(11) Ross, C. A.; Poirier, M. A. *Nat. Med.* **2004**, S10-7.

(12) Uversky, V. N. *Curr. Alzheimer Res* **2008**, *5*, 260–287.

(13) Dobson, C. M. *Nature* **2003**, *426*, 884-890.

(14) Baker, D. *Nature* **2000**, *405*, 39-42.

(15) Paine, H. *Biosci. Horiz.* **2015**, *8*, 1-9.

(16) Cowan, C. M.; Mudher, A. *Front Neurol.* **2013**, *4*, 1-13.

(17) Maji, S. K.; Perrin, M. H.; Sawaya, M. R.; Jessberger, S.; Vadodaria, K.; Rissman, R. A.; Singru, P. S.; Nilsson, K. P.; Simon, R.; Schubert, D.; Eisenberg, D.; Rivier, J.; Sawchenko, P.; Vale, W.; Riek, R. *Science* **2009**, *325*, 328-32.

(18) Hyman, B. T.; Hoesen, G. W. V. *Neurobiol. Aging* **1987**, *8*, 555-556.

(19) Forno, L. S. *J. Neuropathol. Exp. Neurol.* **1996**, *55*, 259-72.

(20) Myers, R. H.; Vonsattel, J. P.; Paskevich, P. A.; Kiely, D. K.; Stevens, T. J.; Cupples, L. A.; Richardson, E. P. Jr.; Bird, E. D. *J. Neuropathol. Exp. Neurol.* **1991**, *50*, 729-42.

(21) Hughes, J. T. *Adv. Neurol.* **1982**, *36*, 61-74.

(22) Gray, F.; Chrétien, F.; Adle-Biassette, H.; Dorandeu, A.; Ereau, T.; Delisle, M. B.; Kopp, N.; Ironside, J. W.; Vital, C. *J. Neuropathol. Exp. Neurol.* **1999**, *58*, 321-8.

(23) Alzheimer, A. Über eine eigenartige Erkrankung der Hirnrinde. Allgemeine Zeitschrift für Psychiatrie **1907**, 64.

(24) Ong, K. T.; Villemagne, V. L.; Bahar-Fuchs, A.; Lamb, F.; Langdon, N.; Catafau, A. M.; Stephens, A. W.; Seibyl, J.; Dinkelborg, L. M.; Reininger, C. B.; Putz, B.; Rohde, B.; Masters, C. L.; Rowe, C. C. *J. Neurol. Neurosurg. Psychiatry* **2015**, *86*, 431-6.

(25) Querfurth, H. W.; LaFerla, F. M. *N. Engl. J. Med.* **2010**, *362*, 329-44.

(26) Sperling, R. A.; Aisen, P. S.; Beckett, L. A.; Bennett, D. A.; Craft, S.; Fagan, A. M.; Iwatsubo, T.; Jack, C. R. Jr.; Kaye, J.; Montine, T. J.; Park, D. C.; Reiman, E. M.; Rowe, C. C.; Siemers, E.; Stern, Y.; Yaffe, K.; Carrillo, M. C.; Thies, B.; Morrison-Bogorad, M.; Wagster, M. V.; Phelps, C. H. *Alzheimers Dement.* **2011**, *7*, 280-92.

(27) Cecchi, C.; Stefani, M. *Biophys. Chem.* **2013**, *182*, 30-43.

(28) Drolle, E.; Gaikwad, R. M.; Leonenko, Z. *Biophys. J.* **2012**, *103*, L27-9.

(29) Shitaka, Y.; Mitani, Y.; Nagakura, A.; Miyake, A.; Matsuoka, N. *Nihon Yakurigaku Zasshi.* **2010**, *136*, 15-20.

(30) Petkova, A. T.; Ishii, Y.; Balbach, J. J.; Antzutkin, O. N.; Leapman, R. D.; Delaglio, F.; Tycko, R. *Proc. Natl. Acad. Sci. U.S.A.* **2002**, *99*, 16742-7.

(31) Matsuzaki, K. *Acc. Chem. Res.* **2014**, *47*, 2397–2404.

(32) Arispe, N.; Pollard, H. B.; Rojas, E. *Proc. Natl. Acad. Sci. U.S.A.* **1993**, *90*, 10573–10577.

(33) Plant, L. D.; Boyle, J. P.; Smith, I. F.; Peers, C.; Pearson, H. A. *J. Neurosci.* **2003**, *23*, 5531-5.

(34) Giuffrida, M. L.; Caraci, F.; Pignataro, B.; Cataldo, S.; De Bona, P.; Bruno, V.; Molinaro, G.; Pappalardo, G.; Messina, A.; Palmigiano, A.; Garozzo, D.; Nicoletti, F.; Rizzarelli, E.; Copani, A. *J. Neurosci.* **2009**, *29*, 10582-7.

(35) Hardy, J.; Selkoe, D. J. *Science* **2002**, *297*, 353-6.

(36) Kang, J.; Lemaire, H. G.; Unterbeck, A.; Salbaum, J. M.; Masters, C. L.; Grzeschik, K. H.; Multhaup, G.; Beyreuther, K.; Müller-Hill, B. *Nature* **1987**, *325*, 733-6.

(37) Allsop, D.; Landon, M.; Kidd, M. *Brain Res.* **1983**, *259*, 348-52.

(38) Beyreuther, K.; Pollwein, P.; Multhaup, G.; Mönning, U.; König, G.; Dyrks, T.; Schubert, W.; Masters, C. L. *Ann. N. Y. Acad. Sci.* **1993**, *695*, 91-102.

(39) Younkin, S. G. *J Physiol Paris.* **1998**, *92*, 289-92.

(40) Brion, J. P. *Eur. Neurol.* **1998**, *40*, 130-40.

(41) Bierer, L. M.; Hof, P. R.; Purohit, D. P.; Carlin, L.; Schmeidler, J.; Davis, K. L.; Perl, D. P. *Arch. Neurol.* **1995**, *52*, 81-8.

(42) Kuhn, P. H.; Wang, H.; Dislich, B.; Colombo, A.; Zeitschel, U.; Ellwart, J. W.; Kremmer, E.; Rossner, S.; Lichtenthaler, S. F. *EMBO J.* **2010**, *29*, 3020-32.

(43) Lichtenthaler, S. F. *J. Neurochem.* **2011**, *116*, 10-21.

(44) Hong-Qi, Y.; Zhi-Kun, S.; Sheng-Di, C. *Transl. Neurodegener.* **2012**, 1:21.

(45) Yang, H. Q.; Sun, Z. K.; Ba, M. W.; Xu, J.; Xing, Y. *Eur J Pharmacol.* **2009**, *610*, 37-41.

(46) Filip, V.; Kolibás, E. *J. Psychiatry Neurosci.* **1999**, *24*, 234–243.

(47) Marcade, M.; Bourdin, J.; Loiseau, N.; Peillon, H.; Rayer, A.; Drouin, D.; Schweighoffer, F.; Désiré, L. *J. Neurochem.* **2008**, *106*, 392-404.

(48) NCT00693004. Study of PRX-03140 monotherapy in subjects with Alzheimer's disease. http://clinicaltrials.gov/show/NCT00693004.

(49) Rezai-Zadeh, K.; Shytle, D.; Sun, N.; Mori, T.; Hou, H.; Jeanniton, D.; Ehrhart, J.; Townsend, K.; Zeng, J.; Morgan, D.; Hardy, J.; Town, T.; Tan, J. *J. Neurosci.* **2005**, *25*, 8807-14.

(50) Khan, T. K.; Nelson, T. J.; Verma, V. A.; Wender, P. A.; Alkon, D. L. *Neurobiol. Dis.* **2009**, *34*, 332–339.

(51) Yan, R.; Bienkowski, M. J.; Shuck, M. E.; Miao, H.; Tory, M. C.; Pauley, A. M.; Brashier, J. R.; Stratman, N. C.; Mathews, W. R.; Buhl, A. E.; Carter, D. B.; Tomasselli, A. G.; Parodi, L. A.; Heinrikson, R. L.; Gurney, M. E. *Nature* **1999**, *402*, 533-7.

(52) Vassar, R.; Bennett, B. D.; Babu-Khan, S.; Kahn, S.; Mendiaz, E. A.; Denis, P.; Teplow, D. B.; Ross, S.; Amarante, P.; Loeloff, R.; Luo, Y.; Fisher, S.; Fuller, J.; Edenson, S.; Lile, J.; Jarosinski, M. A.; Biere, A. L.; Curran, E.; Burgess, T.; Louis, J. C.; Collins, F.; Treanor, J.; Rogers, G.; Citron, M. *Science* **1999**, *286*, 735-41.

(53) NCT01561430. Study of LY2886721 in mild cognitive impairment due to Alzheimer's disease or mild Alzheimer's disease.

(54) NCT01511783. Evaluation of the safety, pharmacokinetics, and pharmacodynamics of multiple doses of E2609 in healthy subjects. http://clinicaltrials.gov/ct2/show/NCT01511783?term=E260 9&rank=3.

(55) NCT01739348. An effcacy and safety trial of MK-8931 in mild to moderate Alzheimer's disease (P07738) (EPOCH). https://clinicaltrials.gov/ct2/show/NCT01739348.

(56) NCT02245737. An effcacy and safety study of AZD3293 in early Alzheimer's disease (AMARANTH)). https://clinicaltrials.gov/ct2/show/NCT02245737.

(57) NCT00621010. Safety study of CTS21166 to treat Alzheimer disease. http://clinicaltrials.gov/ct2/show/ NCT00621010?term=CTS-21166&rank=1

(58) Jonsson, T.; Atwal, J. K.; Steinberg, S.; Snaedal, J.; Jonsson, P. V.; Bjornsson, S.; Stefansson, H.; Sulem, P.; Gudbjartsson, D.; Maloney, J.; Hoyte, K.; Gustafson, A.; Liu, Y.; Lu, Y.; Bhangale, T.; Graham, R. R.; Huttenlocher, J.; Bjornsdottir, G.; Andreassen, O. A.; Jönsson, E. G.; Palotie, A.; Behrens, T. W.; Magnusson, O. T.; Kong, A.; Thorsteinsdottir, U.; Watts, R. J.; Stefansson, K. *Nature* **2012**, *488*,96-9.

(59) Artavanis-Tsakonas, S.; Rand, M. D.; Lake, R. J. *Science* **1999**, *284*, 770-6.

(60) Doody, R. S.; Raman, R.; Farlow, M.; Iwatsubo, T.; Vellas, B.; Joffe, S.; Kieburtz, K.; He, F.; Sun, X.; Thomas, R. G.; Aisen, P. S.; Alzheimer's Disease Cooperative Study Steering Committee, Siemers, E.; Sethuraman, G.; Mohs, R.; Semagacestat Study Group. *N. Engl. J. Med.* **2013**, *369*, 341-50.

(61) Coric, V.; van Dyck, C. H.; Salloway, S.; Andreasen, N.; Brody, M.; Richter, R. W.; Soininen, H.; Thein, S.; Shiovitz, T.; Pilcher, G.; Colby, S.; Rollin, L.; Dockens, R.; Pachai, C.; Portelius, E.; Andreasson, U.; Blennow, K.; Soares, H.; Albright, C.; Feldman, H. H.; Berman, R. M. *Arch. Neurol.* **2012**, *69*, 1430–1440.

(62) Hopkins, C. R. *ACS Chem. Neurosci.* **2011**, *2*, 279–280.

(63) Green, R. C.; Schneider, L. S.; Amato, D. A.; Beelen, A. P.; Wilcock, G.; Swabb, E. A.; Zavitz, K. H.; Tarenflurbil Phase 3 Study Group. *JAMA*. **2009**, *302*, 2557-64.

(64) NCT01928420. A single site, randomized, double-blind, placebo controlled trial of NIC5–15 in subjects with Alzheimer's disease. www.clinicaltrials.gov/ct2/show/NCT01928420.

(65) NCT01303744. Evaluation of safety & tolerability of multiple dose regimens of CHF 5074 and exploration of effects on potential markers of clinical effcacy in patients with mild cognitive impairment (CT04). www.clinicaltrials.gov/ct2/show/NCT01303744.

(66) NCT00959881. Study evaluating the coadministration of begacestat and donepezil. https://clinicaltrials.gov/ct2/show/NCT00959881.

(67) Reitz, C.; Mayeux, R. *Biochem. Pharmacol.* **2014**, *88*, 640–651.

(68) Herrmann, N.; Chau, S. A. Lanctôt, K. L. *Drugs* **2011**, *71*, 2031-65.

(69) Yanagisawa K. *Brain Nerve* **2011**, *63*, 863–868.

(70) Iliffe, S. *CNS Drugs* **2007**, *21*, 177-84.

(71) Santos, D. B.; Peres, K. C.; Ribeiro, R. P.; Colle, D.; dos Santos, A. A.; Moreira, E. L.; Souza, D. O.; Figueiredo, C. P.; Farina, M. *Exp. Neurol.* **2012**, *233*, 767-75.

(72) Parri, H. R.; Hernandez, C. M.; Dineley, K. T. *Biochem. Pharmacol.* **2011**, *82*, 931-42.

(73) Percy, M. E.; Kruck, T. P. A.; Pogue, A. I.; Lukiw, W. J. *J. Inorg. Biochem.* **2011**, *105*, 1505–1512.

(74) Kruck, T. P.; Cui, J-G.; Percy, M. E.; Lukiw, W. J. *Cell Mol. Neurobiol.* **2004**, *24*, 443–459.

(75) Roberts, B. R.; Ryan, T. M.; Bush, A. I.; Masters, C. L.; Duce, J. A. *J. Neurochem.* **2012**, *120*, 149-66.

(76) Muthuraj, B.; Layek, S.; Balaji, S. N.; Trivedi, V.; Iyer, P. K. *ACS Chem. Neurosci.* **2015**, *6*, 1880–1891.

(77) Muthuraj, B.; Hussain, S.; Iyer, P. K. *Polym. Chem.* **2013**, *4*, 5096–5107.

(78) Panza, F.; Frisardi, V.; Solfrizzi, V.; Imbimbo, B. P.; Logroscino, G.; Santamato, A.; Greco, A.; Seripa, D.; Pilotto, A. *Immunotherapy* **2012**, *4*, 213-38.

(79) Imbimbo, B. P.; Ottonello, S.; Frisardi, V.; Solfrizzi, V.; Greco, A.; Seripa, D.; Pilotto, A.; Panza, F. *Expert Rev. Clin. Immunol.* **2012**, *8*, 135-49.

(80) Sevigny, J.; Chiao, P.; Bussière, T.; Weinreb, P. H.; Williams, L.; Maier, M.; Dunstan, R.; Salloway, S.; Chen, T.; Ling, Y.; O'Gorman, J.; Qian, F.; Arastu, M.; Li, M.; Chollate, S.; Brennan, M. S.; Quintero-Monzon, O.; Scannevin, R. H.; Arnold, H. M.; Engber, T.; Rhodes, K.; Ferrero, J.; Hang, Y.; Mikulskis, A.; Grimm, J.; Hock, C.; Nitsch, R. M.; Sandrock, A. *Nature* **2016**, *537*, 50–56

(81) Selkoe, D. J. *Nat. Med.* **2011**, *17*, 1060-5.

(82) Dinamarca, M. C.; Ríos, J. A.; Inestrosa, N. C. *Front. Physiol.* **2012**, *3:464*, 1-7.

(83) Salloway, S.; Sperling, R.; Keren, R.; Porsteinsson, A. P.; van Dyck, C. H.; Tariot, P. N.; Gilman, S.; Arnold, D.; Abushakra, S.; Hernandez, C.; Crans, G.; Liang, E.; Quinn, G.; Bairu, M.; Pastrak, A.; Cedarbaum, J. M.; ELND005-AD201 Investigators. *Neurology* **2011**, *77*, 1253–1262.

(84) Mandel, S. A.; Amit, T.; Weinreb, O.; Reznichenko, L.; Youdim, M. B. *CNS Neurosci. Ther.* **2008**, *14*, 352-65.

(85) Look, G. C.; Jerecic, J.; Cherbavaz, D. B.; Pray, T. R.; Breach, J. C.; Crosier, W. J.; Igoudin, L.; Hironaka, C. M.; Lowe, R. M.; McEntee, M.; Ruslim-Litrus, L.; Wu, H. M.; Zhang, S.; Catalano, S. M.; Goure, W. F.; Summa, D.; Krafft, G. A. *Curr. Alzheimer Res.* **2007**, *4*, 562-7.

(86) Frydman-Marom, A.; Rechter, M.; Shefler, I.; Bram, Y.; Shalev, D. E.; Gazit, E. *Angew. Chem. Int. Ed. Engl.* **2009**, *48*, 1981-6.

(87) Nel, A. E.; Mädler, L.; Velegol, D.; Xia, T.; Hoek, E. M. V.; Somasundaran, P.; Klaessig, F.; Castranova, V.; Thompson, M. *Nat. Mater.* **2009**, *8*, 543 – 557.

(88) Gao, N.; Sun, H.; Dong, K.; Ren, J.; Qu, X. *Chemistry* **2015**, *21*, 829-35.

(89) Mazza, M.; Capuano, A.; Bria, P.; Mazza, S. *Eur. J. Neurol.* **2006**, *13*, 981-5.

(90) Kim, H. G.; Oh, M. S. *Curr. Pharm. Des.* **2012**, *18*, 57-75.

(91) Iaccarino, H. F.; Singer, A. C.; Martorell, A. J.; Rudenko, A.; Gao, F.; Gillingham, T. Z.; Mathys, H.; Seo, J.; Kritskiy, O.; Abdurrob, F.; Adaikkan, C.; Canter, R. G.; Rueda, R.; Brown, E. N.; Boyden, E. S.; Tsai, L-H. *Nature* **2016**, *540*, 230-235.

(92) Chen, Y.; Liu, L. *Adv. Drug Deliv. Rev.* **2012**, *64*, 640-65.

(93) Chan, J.; Dodani, S. C.; Chang, C. J. *Nat. Chem.* **2012**, *4*, 973–984.

(94) Malik, A. H.; Hussain, S.; Iyer, P. K. *Anal. Chem.* **2016**, *88*, 7358–7364.

(95) Muthuraj, B.; Mukherjee, S.; Chowdhury, S. R.; Patra, C. R.; Iyer, P. K. *Biosens Bioelectron.* **2017**, *89*, 636-644.

(96) Sun, M.; Müllen, K.; Yin, M. *Chem. Soc. Rev.* **2016**, *45*, 1513-1528.

(97) Görl, D.; Zhang, X.; Würthner, F. *Angew. Chem. Int. Ed. Engl.* **2012**, *51*, 6328-48.

(98) Tuncel, D.; Demir, H. V. *Nanoscale* **2010**, *2*, 484-494.

(99) Repenko, T.; Rix, A.; Ludwanowski, S.; Go, D.; Kiessling, F.; Lederle, W.; Kuehne, A. J. C. *Nat. Commun.* **2017**, *8*, doi: 10.1038/s41467-017-00545-0.

(100) Holtzman, J. L. *Clin. Pharmacol. Ther.* **2010**, *88*, 563–565.

(101) McLean, C. A.; Cherny, R. A.; Fraser, F. W.; Fuller, S. J.; Smith, M. J.; Beyreuther, K.; Bush, A. I.; Masters, C. L. *Ann. Neurol.* **1999**, *46*, 860-6.

(102) Pike, C. J.; Walencewicz, A. J.; Glabe, C. G.; Cotman, C. W. *Brain Res.* **1991**, *563*, 311-4.

(103) Kim, I.; Lee, J.; Hong, H. J.; Jung, E. S.; Ku, Y. H.; Jeong, I. K.; Cho, Y. M.; So, I.; Park, K. S.; Mook-Jung, I. *J. Alzheimers Dis.* **2010**, *19*, 1371-6.

Chapter 2a

Amyloid-like Polymeric Template to Trigger Toxic Amyloid Aggregate into Nontoxic Co-aggregates

Chowdhury, S. R.; Agarwal, M.; Meher, N.; Muthuraj, B; Iyer, P. K. Modulation of Amyloid Aggregates into Nontoxic Coaggregates by Hydroxyquinoline Appended Polyfluorene. *ACS Appl. Mater. Interfaces* **2016**, *8*, 13309-13319.

Abstract

Inhibitory modulation towards de novo protein aggregation is likely to be a vital and promising therapeutic strategy for understanding the molecular etiology of amyloid related diseases such as Alzheimer's disease (AD). The building up of toxic oligomeric and fibrillar amyloid aggregates in the brain plays host to a downstream of events, causing damage to axons, dendrites, synapses, signaling, transmission and finally cell death. Herein, a conjugated polymer (CP), hydroxyquinoline appended polyfluorene (PF-HQ) which has a typical 'amyloid like' surface motif was introduced and explored as an inhibitory modulator of amyloid β (Aβ) aggregation. Inhibitory effects of PF-HQ was outlined based on Thioflavin T (ThT) fluorescence; atomic force microscopy (AFM), circular dichroism (CD) and Fourier transform infrared (FTIR) studies. The amyloid-like PF-HQ forms nano co-aggregates by templating with toxic amyloid intermediates and displays improved inhibitory impacts towards Aβ fibrillation and diminishes amyloid cytotoxicity. CP based modulation strategy have been developed for the first time, that demonstrates beneficiary amyloid-like surface motif to interact efficiently with the protein, the pendant side groups to trap the toxic amyloid intermediates as well as optical signal to acquire the mechanistic insight.

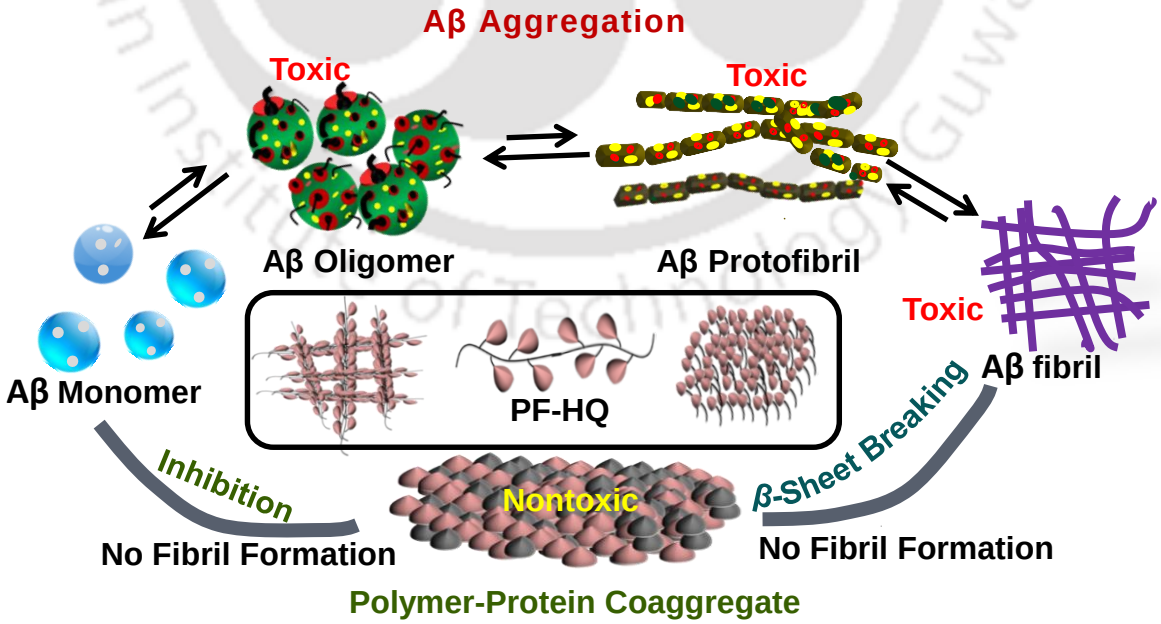

2a.1. Introduction

Alzheimer's disease (AD) has emerged as the most prevalent neurodegenerative disease amongst others and considered to be one of the leading cause of dementia.[1,2] The likelihood of developing this disease increases with age, effecting progressive attrition of cognition, task performance ability, memory, etc.[3] In the subsequent decades, AD is expected to increase at an alarming rate particularly due to the fast growth of the elderly population in developing countries, thus effecting their economy and public health.4 Advancement of precursor biomarkers either to distinguish preclinical AD or to attenuate debilitating cognitive symptoms in future clinical trials turns into a need of this century to make a noteworthy progress.[5–8]

The extracellular deposits of amyloid fibrils as senile plaques is considered to be one of the most essential hallmarks of Alzheimer's disease.[9] Amyloid protein aggregation is triggered by Aβ through a cascade of events leading to a fibrillar self-assembly process represented by a nucleation dependent polymerization and several of these accumulated forms of amyloid, oligomeric and protofibrillar aggregates are recognized as most neurotoxic agents by broad studies.[10–14] Albeit, Aβ fibrils and intermediates in AD brain display key contrasts from those fibrils in vitro,[15] a wide number of presynthesized conglomeration inhibitors that forestall Aβ fibril formation and improve cytotoxicity of these aggregates were developed and mulled over as potential medication competitors.[16–21] Numerous endeavors including small molecule,[18,22–24] peptides,[25,26] nucleic acid,[27,28] antibody,[29] and nanomaterials (NMs) based inhibitors like inorganic nanoparticles (NPs),[30,31] polymer NMs,[32–36] carbon NMs,[37,38] biomaterial aggregates[39] have been accounted for of late for reducing amyloid cytotoxicity.

In the present study, 8-hydroxyquinoline appended polyfluorene derivative (PF–HQ) was designed to investigate the effect of PF-HQ towards Aβ fibrillization. Previous studies with CPs have focused mainly on the sensitive detection of amyloid deposits and prion strains[40–45] and few elegant studies using CPs exhibited inhibitory modulation towards metal mediated amyloid fibrillation[46,47] whereas, few others accentuate faster protein clustering to exacerbate the risk for amyloidoses.[48] Wisely chosen pendant hydroxyquinolines are endowed with metal-chelating,[49,50] neuroprotective and antioxidant[51] properties and therefore few hydroxyquinoline scaffolds previously have been shown sequestering Cu(II) and Zn(II) from both amyloid plaques and the synaptic cleft and acting as Cu(II) ionophores to compensate

the AD-related Cu(II) dyshomeostasis.[52,53] Recent work confirms that 8-hydroxyquinolines (CQ and PBT2) hinder Aβ aggregation by targeting intermediate critical nuclei, responsible for Aβ fibrillation and both are at preclinical and phase II clinical advancement for the treatment of AD.[54] Polyfluorene derivatives have been previously investigated for a variety of antimicrobial and sensing applications as well as for organic semiconductor and light emitting devices.[55–65] Although CPs are well documented as amyloid biomarkers[66] due to their highly conjugated morphology and tailoring with desired side groups, several fluorescence sensing effects have been achieved,[67] yet their interaction with amyloid are rarely explored.[68]

Herein, Aβ1-40 aggregation was monitored in the presence of PF-HQ and envisioned that low dimensionality of the CP surface enhances the probability of the target proteins coming into frequent contact, leading to complex formation between protein and a CP, and conformational changes in the protein bound to either aggregated polymeric backbone or to the pendant hydroxyquinolines occurs, resulting an alteration in optical properties of PF-HQ, and providing a direct link between spectral signal and protein conformation and a mechanistic insight towards disease etiology. Further the role of PF-HQ was explored in preformed Aβ1-40 fibrils (10 μM) containing other neurotoxic intermediates and as well as in real human cerebrospinal fluid containing fibrillar amyloid aggregates (11.5 μM). Thioflavin T (ThT) fluorescence, atomic force microscopy (AFM), circular dichroism (CD), Fourier transform infrared (FT-IR) studies confirm that PF-HQ inhibits Aβ fibrillization. Besides, MTT studies demonstrate that Aβ aggregates intervened by PF-HQ ameliorates Aβ cytotoxicity. This molecular recognition was based on the premise that the hydrophobic core of the PF-HQ and a suitable functionality over its side chain gives rise to easy modification of particle surfaces for controlling physio-chemical properties and abundant binding sites for protein interactions and thus PF-HQ and related analogues may have therapeutic potentials to prevent amyloid related diseases.

2a.2. Experimental Section

2a.2.1. Materials

All the reagents and chemicals were purchased from Aldrich Chemicals, Merck or Ranbaxy (India) and were used as received. Milli-Q water and HPLC grade solvents were used in all the experiments. Solvents were degassed using three freeze thaw cycles or flushed with nitrogen for at least 1 h prior to use when necessary. β-Amyloid (1-40), human was purchased from G L Biochem Ltd., Shanghai, China.

2a.2.2. Instrumentation

UV–Vis absorption spectra were recorded on a Perkin Elmer Lambda–25 spectrometer. Fluorescence spectra were carried out on a Varian Cary Eclipse Spectrometer. A 10 mm x 10 mm quartz cuvette was used for solution spectra and emission was collected at 90° relative to the excitation beam. FT–IR spectra were recorded on a Perkin Elmer spectrophotometer with samples prepared as KBr pellets. A fresh glass slide was used for every experiment. Deionized water was obtained from Milli–Q system (Millipore). Atomic force microscopy (AFM) was recorded on Agilent, Model 5500 series with non-contact mode. The PF-HQ NPs were examined using an ultrahigh resolution transmission electron microscope (TEM; JEM 2100; Jeol, Peabody, MA, USA). DLS and Zeta Potentials were measured by Malvern Zetasizer Nano series Nano-ZS90 instrument. ^{1}H and ^{13}C NMR spectra were recorded on a Bruker AscendTM 600 MHz spectrometer using chloroform-d as solvent.

2a.2.3. Synthesis of PF-HQ

Fluorene (2 g, 12.032mmol), 50% aq. NaOH and a catalytic amount of tetra-butyl ammonium Iodide (TBAI) (0.888 g, 2.406 mmol) were added to a 100 mL round bottom flask and then degassed 3 times by applying freeze-thaw cycles. 1,6- dibromohexane (20.632 g, 84.227mmol) was added through a syringe (degassed) and the mixture was stirred continuously for 6 hours at 70°C. The reaction mixture was cooled to room temperature and extracted with chloroform. The organic layer was washed with water and dried over anhydrous sodium sulphate. The solvent was removed under vacuum and excess 1, 6- dibromohexane was removed through shortpath distillation and the crude was purified using Column Chromatography over a pad of silica gel using hexane as an eluent to get the desired doubly alkylated product as yellow oil (4.8 g, 81%).^{1}H NMR (600MHz, $CDCl_3$), δ (ppm): 7.7(m, 2H), 7.32(m, 6H), 3.26(t, 4H), 1.96(m, 4H), 1.64(m, 4H), 1.18(m, 4H), 1.07(m, 4H), 0.62(m, 4H);^{13}C NMR (150MHz, $CDCl_3$), δ (ppm): 150.5, 141.3, 127.3, 127.1, 123, 119.9, 55.1, 40.4, 34.1, 32.8, 29.3, 28, 23.7.

Anhydrous ferric chloride (FeCl3) (1.30g, 8.12 mmol) and 9, 9-Bis-(6-bromohexyl)-9H-fluorene (2.0 g, 4.06 mmol) were dissolved in 15 mL nitrobenzene in a 100 mL three-necked round-bottom flask equipped with a nitrogen inlet. The reaction mixture was stirred at room temperature for 36 hours, followed by precipitation from methanol. The resulting polymer, poly 9, 9-Bis-(6-bromohexyl)-9H-fluorene was dried under reduced vacuum to obtain 1.3 g (65%) as dark brown powder.

^{1}H NMR (600MHz, $CDCl_3$), δ (ppm): 7.74(bp), 7.31(bp), 3.29(bp), 2.1(bp), 1.64(bp), 1.25(bp), 0.88(bp); bp: broad peak.

To synthesize PF-HQ, PF-Br (0.1 g, 0.203 mmol), 8-hydroxyquinoline (0.14 g, 1.01 mmol) and K_2CO_3 (0.28 g, 2.03mmol) were dissolved in 20 mL dry DMF and heated at 100°C for 48 hours in a 50 mL round bottom flask. Then the solvent was removed through a rotavapor under reduced vacuum and dried under a high vacuum, followed by precipitated from methanol and acetone to obtain the final polymer (57 mg, ~60%). 1H NMR (600 MHz, CDCl3), δ (ppm): 0.8–1.0(–CH2), 1.2–1.3(–CH2–), 1.4–1.6(–CH2–), 1.6–1.8 (–CH2–), 2–2.1(–CH2–), 4.0 (–CH2-O–), 6.9–7.1(ArH), 7.2–7.3(ArH), 7.7–8.1(ArH), 8.9(ArH). 13C NMR (150 MHz, CDCl3), δ (ppm): 155.0, 149.4,143.0, 140.6, 136.0, 135.4, 130.0, 129.6, 126.8, 124.2, 123.7, 121.6, 119.5, 116.1, 114.3, 108.8, 40.6, 34.5, 31.8, 29.4, 25.9, 24.2, 24.1, 22.9, 14.3, 11.6. ArH: aromatic hydrogen.

FT-IR (KBr pelettes), wavenumber (cm^{-1}): 3432.09, 2930.65, 2853.24, 1724.16, 1630.77.

The weight average molecular weight (Mw) of PF-HQ was found to be 40.2 kDa with polydispersity 1.8.

2a.2.4. Preparation stock solution

PF-HQ stock solution was prepared at the concentration of 1.0 X 10^{-3} mL^{-1} in 10 mL THF. This stock solution was diluted to desire concentration for each titration in 1mL cuvette. All the experiments like UV-Visible, FT-IR and fluorescence titrations were performed in 10 mM HEPES buffer and pH maintained at 7.4.

2a.2.5. TFA/HFIP treatment of Aβ (1–40)

Aβ (1–40) was disaggregated using trifluoroacetic acid/1,1,1,3,3,3-hexafluuor-2-propanol (TFA/HFIP) by an established method. 0.1 mg of Aβ (1–40) was added to a 2.5 mL eppendorf tube and dissolved in TFA to obtain a homogeneous solution free of aggregates. TFA was then evaporated using argon gas. Any left-over TFA was further removed by adding HFIP followed by evaporation using argon gas flow to obtain a film like material. This process was repeated twice. To the eppendorf tube, 2.5 mL of HEPES (10 mM, pH 7.4) was added followed by sonication and vortexing to obtain a final concentration of 1.6 X 10^{-4} M. Fibril formation was monitored using a ThT binding assay.

2a.2.6. Preparation of Aβ1–40 aggregates and ThT Binding Assay

For the preparation of amyloid peptide aggregates, after the TFA/HFIP treatment for amyloid peptide, the Aβ1–40 (5 μM) was initially incubated with ThT (20 μM) at 37 °C for 72 hours (pH 7.4 in HEPES) with steady agitation. Further, dose dependent aggregation of Aβ1–40 amyloid fibrils were monitored with different time incubations by monitoring ThT (20 μM) fluorescent enhancement peak at λem 484 nm (λex 440 nm).

2a.2.7. Preparation of PF-HQ

PF-HQ (10 μM) polymer was regularly injected into molecular biology grade water with vigorous stirring at room temperature, using a syringe. After the injection of PF-HQ, the solution was filtered by membrane filter with 0.2 μm pore size. Then the collected PF-HQ was used for other studies.

2a.2.8. PF-HQ sample preparation for experiments.

5 μM, 10 μM and 20 μM of PF-HQ NPs were maintained in 1 mL of 10 mM HEPES buffer solution (pH 7.4) at room temperature. The mixtures of this solution were used for all the experiments like UV-Visible and fluorescence titrations.

2a.2.9. Modulating experiment for Aβ1–40

The red shifted emission spectra at 520 nm from 509 nm for PF-HQ (5 μM, 10 μM and 20 μM) with Aβ1-40 (10 μM) were measured while exciting at 355 nm. Aβ1-40 (10 μM) were mixed with different molar ratio of PF-HQ (1:0.5, 1:1 and 1:2) in 1 mL of 10 mM HEPES buffer solution (pH 7.4). Then, fluorescence spectra were monitored for all the samples in different interval of incubation time from 0-25 days at 37 °C in water bath.

2a.2.10. Inhibition of Aβ1–40 fibrils formation monitored by ThT assay experiment

ThT emission changes at 484 nm were measured for inhibition of Aβ1–40 fibrils formation for the mixture of PF-HQ with Aβ1-40 monomer in presence of ThT while exciting at 440 nm. Aβ1-40 monomer (10 μM) was mixed with PF-HQ (5 μM) in 1 mL of 10 mM HEPES buffer solution (pH 7.4) in presence of Thioflavin T (20 μM). Then, fluorescence spectra were monitored in different interval of incubation time from 0-25 days at 37 °C in water bath.

2a.2.11. Sample preparation for AFM images

To monitor the morphology, pristine solutions of Aβ1-40 and PF-HQ and PF-HQ coincubated Aβ1-40 were dissolved in 10mM HEPES (pH 7.4) and diluted 10 times and 5 μL of the sample was mounted onto the freshly cleaned glass slide and dried at room temperature for overnight. The data were recorded on an Agilent, Model 5500 series AFM with non-contact tapping mode and analyzed with WSxM 5.0 Develop 8.0 software.

2a.2.12. Sample preparation for FT-IR spectra

FT-IR spectra of Aβ1-40 solutions incubated with or without modulators were recorded on a Perkin Elmer 100 series FT-IR Spectrophotometer. 10 μL of each sample was mounted onto the freshly cleaned glass slide and dried at room temperature for overnight and samples prepared as KBr pellets before recording.

2a.2.13. Sample preparation for DLS and Zeta Potential

Zeta potential and DLS of pristine Aβ1-40 and PF-HQ samples and PF-HQ coincubated Aβ1-40 were determined with a Malvern Zetasizer Nano-ZS. A suspension of above incubated solutions of different concentrations were dissolved in 10mM HEPES (pH 7.4) and transferred into 3 mL zeta potential cuvette (DTS1060, Malvern) and DLS cuvette (DTS1060, Malvern). The data were collected and analyzed with Zetasizer software (version 7.11, Malvern).

2a.2.14. Sample preparation for Circular Dichroism (CD) Spectroscopy

CD Spectra of pristine Aβ1-40 and PF-HQ samples and PF-HQ coincubated Aβ1-40 were determined in a JASCO J-815 Spectrometer (JASCO Co., Tokyo, Japan), using a quartz cuvette (1 mm path length). The concentration of Aβ1-40 solution for CD analysis was 10 μM and the

Aβ40 solutions incubated without or with modulators were prepared at 0.5, 1 and 2 equiv (equiv was defined as the molar ratio of modulators to Aβ1-40 (10 μM)). All the samples were incubated at 37 °C in 10 mM HEPES buffer solution with a continuous agitation speed of 100 rpm for different time intervals before analyses. Spectra were calibrated by subtracting the buffer or sample solution baseline.

2a.2.15. Aβ1-40 control studies

Thioflavin T (ThT) is generally utilized for the recognizable proof and measurement of amyloid fibrils and in addition for the investigation of fibrillization kinetics of Aβ utilizing fluorescence spectroscopy. The observed emission at ~484 nm is thought to be specifically

corresponding to the amount of amyloid fibrils present, and in this manner, the kinetics of fibril formation can be trailed by measuring the time-dependent increment in fluorescence. Then again, a decrease in the ThT fluorescence is frequently taken as a sign of restraint of the macromolecular amyloid self-assembly processes.

The AFM images show long unbranched mature fibrillar Aβ1-40 aggregates. For control, Aβ1-40 was incubated to aggregate and the final fibril formation was confirmed using CD and FT-IR studies. CD spectrum of preformed Aβ1-40 fibrils show a positive peak around 196 nm and a negative peak around 202 nm confirming the β-sheet conformation of Aβ1-40. However, in presence of the polymer (PF-HQ), CD spectrum shows a negative peak around 193 nm and a positive peak around 199 nm indicating the conformational conversion of Aβ1-40. Analogously, the FT-IR spectrum of preformed Aβ1-40 fibrils shows a major band at 1631 cm-1 which indicates the parallel β-sheet conformation of Aβ1-40 aggregates. The parallel β-sheet conformation of Aβ1-40 changed in presence of the inhibitory modulator (PF-HQ) and a new peak emerges at around 1651 cm^{-1} due to the formation of polymer-protein co-aggregates.

2a.2.16. Fluorescence Measurements

5 μM PF-HQ emits at 504 nm in HEPES buffer (pH 7.4) on exciting at 355 nm while 10 μM PF-HQ and 20 μM PF-HQ emit at 510 nm in HEPES buffer (pH 7.4) on exciting at 355 nm. After 0-6 days of incubation at 37 °C, a marked decrease in fluorescence intensity was observed along with a red shift of 6-13 nm in all the control spectrum of PF-HQ. On further incubation from 7-16 days, a new peak appears at 438 nm with continuous increment in its intensity. When 10 μM Aβ1-40 was added to 5 μM PF-HQ, emission appeared exactly at 504 nm along with a slight decrease in intensity compared to the spectrum seen for 5 μM PF-HQ only. This decrease in intensity may attribute to the formation of disordered co-aggregate of Aβ1-40 and PF-HQ. After 24 hours of incubation, a slight increase in fluorescence intensity compared to the initial intensity along with a red shift of 12 nm (new peak at 516 nm) was observed. After 11 days of incubation, a new peak at 438 nm predominates and a small hump at 518 nm was seen. Upon separate addition of 10 μM of Aβ1-40 to 10 μM PF-HQ and 20 μM PF-HQ solutions, a blue shift of 6 nm was observed in both cases. Again initial peak arises at 504 nm like in case of 1:0.5 molar ratio of Aβ1-40 to PF-HQ. After 24 hours of incubation, peak shifts at 514 nm with a slight increase in fluorescence intensity compared to the initial intensity. After 1-11 days of incubation, fluorescence spectrum of 1:1 and 1:2 molar ratio of Aβ1-40 to PF-HQ resemble the spectrum seen for 10 μM PF-HQ and 20 μM PF-HQ except an increase in intensity was observed in case of coincubated solutions. In case of 1 equiv of PF-

HQ incubated Aβ1-40, a new peak arises at 440 nm along with a hump at 518 nm after 11 days of incubation while in case of 2 equiv of PF-HQ incubated Aβ1-40, peak appears at 438 nm predominates after 20 days of incubation. Higher concentration of polymer may lead to dominant attractive hydrophobic interaction among itself rather than the polymer-protein interaction.

2a.2.17. MTT Assay

Cell culture: U-87 MG cells is a glioblastoma, astrocytoma cell line derived from human malignant gliomas. U-87 MG cells were cultured in complete growth media, Dulbecco's Modified Eagle Medium (DMEM, HiMedia) with 10% fetal bovine serum (Gibco) and antibiotics (Anti-Anti, Gibco) at 37 °C in 5% CO_2 incubator. Cell line used in this study were gifted by National centre for cell science (NCCS), Pune.

U-87 MG cells were seeded into 96-well plates at an initial seeding density of 10,000 cells/well in 100 µl medium. The cells were cultured for 24 h at 37 °C in 5% CO_2. Then, cells of each well were treated with PF-HQ in a concentration range 0-20 µM in 100 µl serum free media. After incubation for 48 h, the 3-(4, 5-dimethylthiazol-2yl)-2, 5-diphenyltetrazolium bromide (MTT) solution (10 µl, 5 mg/mL in PBS) was added to each well. Plate is further incubated for 3 h at 37 °C in 5% CO_2, wrapped in aluminum foil. After incubation, MTT-containing medium was replaced by 100 µl Dimethyl Sulfoxide (DMSO) to solubilize MTT-formazan crystals. After incubation for 5 min at 37 °C, absorbance was measured at 570 nm and reference reading at 690 nm was recorded in ELISA microplate reader (Infinite 200 PRO, TECAN). Each of the samples was repeated with 7 replicates. The results were normalized by setting the cell viability of U-87 MG cells in tetrahydrofluran (THF) control to be 100%.

2a.3. Results

2a.3.1. Design and synthesis of polyfluorene homopolymer

PF-HQ homopolymer, possesses a fluorescent polyfluorene core appended with 8-hydroxyquinoline side chain moieties, intended to inhibit Aβ1-40 aggregation. A recent report shows that 8-hydroxyquinolines (HQ) hinder Aβ aggregation by targeting neurotoxic oligomeric intermediates.[54] In addition, polyfluorenes having a conjugated backbone, are known for their high thermal and oxidative stability, easy surface modification, amplified sensitivity and facile substitution at C-9 position and have been widely utilized in biological applications. Hence, a template comprising polyfluorene core attached with hydroxyquinoline

side-chains was proposed to hinder protein aggregation into toxic forms and instead create a polymer-protein nano co-aggregates by templating with Aβ via targeting hydrophobic residues of Aβ (LVFFA) which otherwise would have be considered responsible for fibrillization (Scheme 2a.1). Further, this unique 'amyloid like' PF-HQ template, which are micrometer in dimensions, display improved inhibitory impact towards Aβ fibrillation due to the availability of multiple binding sites and amyloid like surface that diminishes amyloid cytotoxicity. To prepare PF-HQ (Scheme 2a.2), fluorene was doubly alkylated by 1,6-dibromohexane,[57] followed by oxidative polymerization of the monomer in nitrobenzene. Appended bromines were substituted by 8-hydroxyquinolines in a post modification technique in DMF in presence of potassium carbonate. The desired polymer PF-HQ was obtained via precipitation from methanol and the structure confirmed via 1H and 13C NMR spectra in chloroform-d (Figure A2a.1-A2a.3).

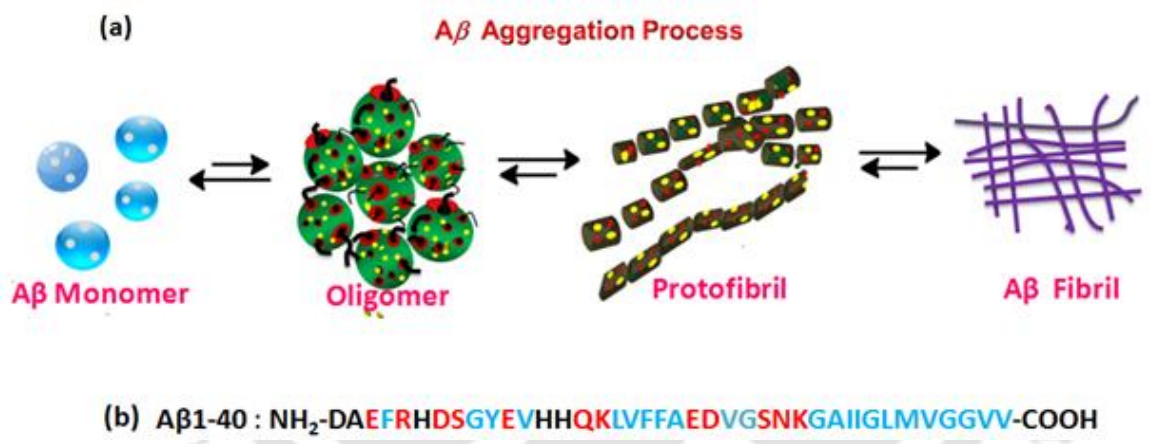

Scheme 2a.1. (a) Cartoon depiction of Aβ aggregation. (b) Amino acid sequences of Aβ1-40 in which hydrophobic residues are in cyan, hydrophilic residues are in red.

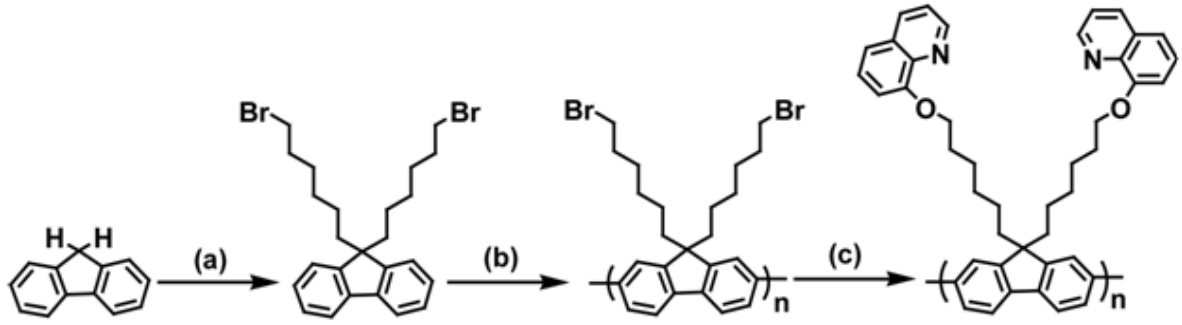

Scheme 2a.2. Synthetic outline of PF-HQ. (a) 1,6 Dibromohexane, 50% aq. NaOH, TBAI, (b) $FeCl_3$, Nitrobenzene, (c) 8-Hydroxyquinoline, K_2CO_3, DMF.

2a.3.2. Thioflavin T (ThT) fluorescence study

To investigate the modulation effect of PF-HQ on Aβ1-40 aggregation, the ThT fluorescence response in the presence as well as in the absence of different molar ratios of CP to Aβ1-40 were monitored. ThT assays were performed on 10μM Aβ1-40 in HEPES buffer (pH 7.4) (For Aβ1-40 and CSF controls, see Figure 2a.1a and A2a.4). 5 μM PF-HQ, 10 μM PF-HQ and 20 μM PF-HQ were separately incubated with 10 μM Aβ1-40 and 20 μM ThT in HEPES buffer (10 mM, pH 7.4) at 37 °C. ThT fluorescence was measured for all three mixtures (Figure 2a.1b) over a period of 25 days. For clarity, ThT fluorescence intensity obtained at 484 nm are plotted against the number of days. A similar set of Aβ1-40 (10μM) and ThT (20 μM) was incubated in HEPES buffer (pH 7.4) in absence of PF-HQ for control studies. The ThT fluorescence increases on Aβ1-40 fibrillation and reaches a plateau which indicates the presence of constant β-sheet content.[58] On the other hand, a decrease in the ThT fluorescence is often considered as an indication of inhibition or modulation of the macromolecular amyloid self-assembly process.[59]

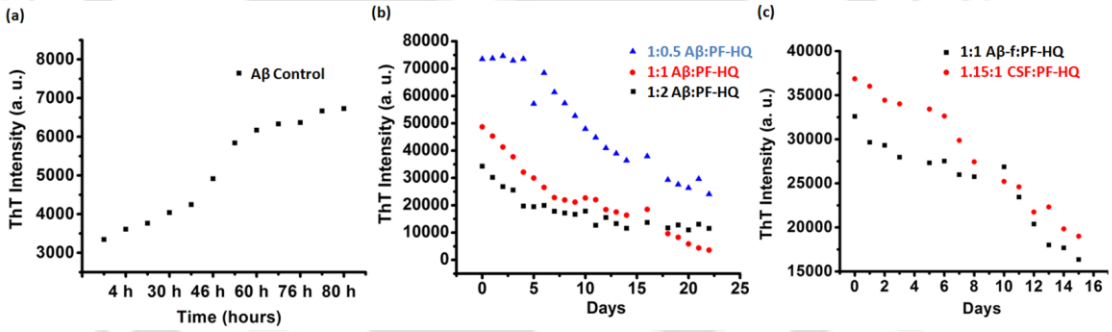

Figure 2a.1. (a) Control Aβ1-40 fibrillation kinetics (black squares) in absence of modulator was shown in 10 mM HEPES buffer (pH 7.4) at 37 °C. (b) ThT fluorescence assays to monitor Aβ 1-40 (10 μM) fibrillation kinetics in presence of 5 μM PF-HQ (blue triangles), 10μM PF-HQ (red circles), 20 μM PF-HQ (black squares). (c) ThT assay in presence of 10 μM PF-HQ in preformed Aβ1-40 fibril (Aβ-f, black squares, 10 μM) and in CSF (red circles, 11.5 μM). Samples were incubated in 10 mM HEPES buffer (pH 7.4).

Herein, for the experiments with 20 μM PF-HQ (i.e.,1:2 molar ratio of Aβ1-40 to PF-HQ), a lag phase of over a period of 5 days was observed, then a declining phase for next 10 days till a flat terrain is reached at the end after 15 days. However, in the other two mixtures, both in case of 10 μM PF-HQ and 5 μM PF-HQ (i.e., 1:1 and 1:0.5 molar ratio of Aβ1-40 to PF-HQ), ThT fluorescence decreases initially up to 5 days. ThT fluorescence response decreases continuously in 10 μM PF-HQ (i.e., 1:1 molar ratio of Aβ1-40 to PF-HQ) while achieving a level after 15 days in case of 5 μM PF-HQ (i.e., 1:0.5 molar ratio of Aβ1-40 to PF-HQ). Declining

ThT fluorescence intensity confirms that PF-HQ interacts with Aβ1-40 and alters its aggregation to final fibril formation and indicates excellent inhibitory effects towards Aβ1-40 aggregation. In order to study the effect of CP on amyloid intermediate, 10 μM CP was incubated with preformed Aβ1-40 fibrils containing oligomeric and prefibrillar aggregates (Aβ-f, 10 μM) under the fibril forming condition and the fibrillation monitored using ThT assay (Figure 2a.1c, black dots). An expected decay in ThT intensity was observed, confirming no further fibril formation. Thus, PF-HQ performs dual job of Aβ aggregation inhibition and β-sheet breaking as well. Further, ThT assay in chosen human cerebrospinal fluid (CSF) sample containing fibrillar Aβ (11.5 μM) was carried out in presence of 10 μM PF-HQ (Figure 2a.1c, red dots). As seen in the case of preformed Aβ fibrils, similar ThT optical responses were observed in these experiments also. Decreasing fluorescence response confirmed modulation of amyloid aggregates in real CSF samples, a known biomarker for AD. The intermolecular interaction between PF-HQ and Aβ1-40 is further supported by morphological studies and zeta potential measurements. The above results exhibit that PF-HQ represses the early structural transformation to toxic oligomeric and prefibrillar intermediates followed by redirecting the Aβ aggregation to form disordered aggregates. To our knowledge, there are no studies that report the inhibitory modulation on the redirected growth of toxic oligomeric and prefibrillar intermediates and to the final fibril formation by a CP template to exceptionally well defined structures thereby altering the original growth mechanism of amyloid peptides. This type of uncharacteristic supramolecular structure involving non-covalent interactions provides significant insights into the formation of distinct hybrid forms involving polyfluorene template based gradual reorganization of the toxic oligomeric and prefibrillar intermediates into large nanorods with typical dimensions of 200-250 nm and 5 nm in height.

2a.3.3. Morphological Studies

A few microscopy routines, for example, electron microscopy (EM) and atomic force microscopy (AFM) have been set up to portray the structural and morphological changes of non-crystalline protein fibrils.[60–62] Unlike electron microscopy, AFM provides 3D information without requiring metal staining protocols and inert environments. Hence, AFM was used to examine morphological changes accompanying Aβ1-40 aggregation in presence of different loadings of PF-HQ under ambient experiment conditions (in HEPES buffer, pH 7.4).

To visualize the inhibitory modulation and progressive evolution of nanoscale changes in the morphology, tapping mode AFM was utilized to investigate the time course for the growth of Aβ1-40 in presence of inhibitory modulator PF-HQ. To examine the inhibitory effects, Aβ1-40

(10 μM) was incubated with three different concentrations of PF-HQ (5 μM, 10 μM, 20 μM) along with Aβ1-40 (10 μM) and PF-HQ controls and their morphological changes were studied using AFM. The images showed no fibril formation in the presence of PF-HQ, indicating excellent inhibitory effects towards Aβ1-40 fibrillation. For AFM studies, the incubated samples were directly taken and diluted 10 times and then 5 μL of the sample was mounted onto a freshly cleaned glass slide and dried at ambient conditions overnight.

AFM image of 5 μM PF-HQ control showed (Figure 2a.2) disordered amyloid like protofibrillar aggregates of ~300 nm and ~10 nm in height and fibrillar surface (~200 nm and ~5 nm in height) motif after 7 days of incubation. When 5 μM PF-HQ was co-incubated with 10 μM Aβ1-40, polymer-protein co-aggregates were found to form network like structure (~300 nm and ~12 nm in height) after 7 days (Figure 2a.2b) of incubation. After further 11 days of aging (Figure 2a.2c), the same aggregates transform into rod like structures of diameter ~250 nm and ~5 nm in height (Table A2a.1).

Surprisingly, AFM images of 10 μM PF-HQ control showed extended amyloid like fibrillar surface with ~150 nm diameter and ~7 nm height along with protofibrillar aggregates of diameter ~150 nm and ~5 nm height (Figure 2a.2d). When 10 μM PF-HQ was co-incubated with 10 μM Aβ1-40, discrete protofibrillar aggregates (Figure 2a.2e) of diameter ~250 nm and ~7 nm in height were formed after 7 days incubation. Analogously, after 11 days incubation, these aggregates changed to rod like structures (Figure 2a.2f) along with large globular aggregates of diameter ~400 nm and ~20 nm in height (Table A2a.2).

However, 20 μM PF-HQ control showed well-ordered protofibrillar surface pattern (Figure 2a.2g) of diameter ~200 nm and ~5 nm in height. When 20 μM PF-HQ was co-incubated with 10 μM Aβ1-40, completely different aggregates (Figure 2a.2h) were formed after 7 days incubation, unlike previous co-aggregates. These aggregates were also transformed into nanorod aggregates (Figure 2i) alongside a few sparse, larger aggregates of diameter ~600 nm and ~20 nm in height (Table A2a.3) after 11 days of incubation.

The processes of peptide self-aggregation and fibrillation of Aβ1-40 follows a nucleation-dependent polymerization pathway, forming oligomeric and prefibrillar aggregates and ultimately leading to the evolution fibrillar nanostructures.

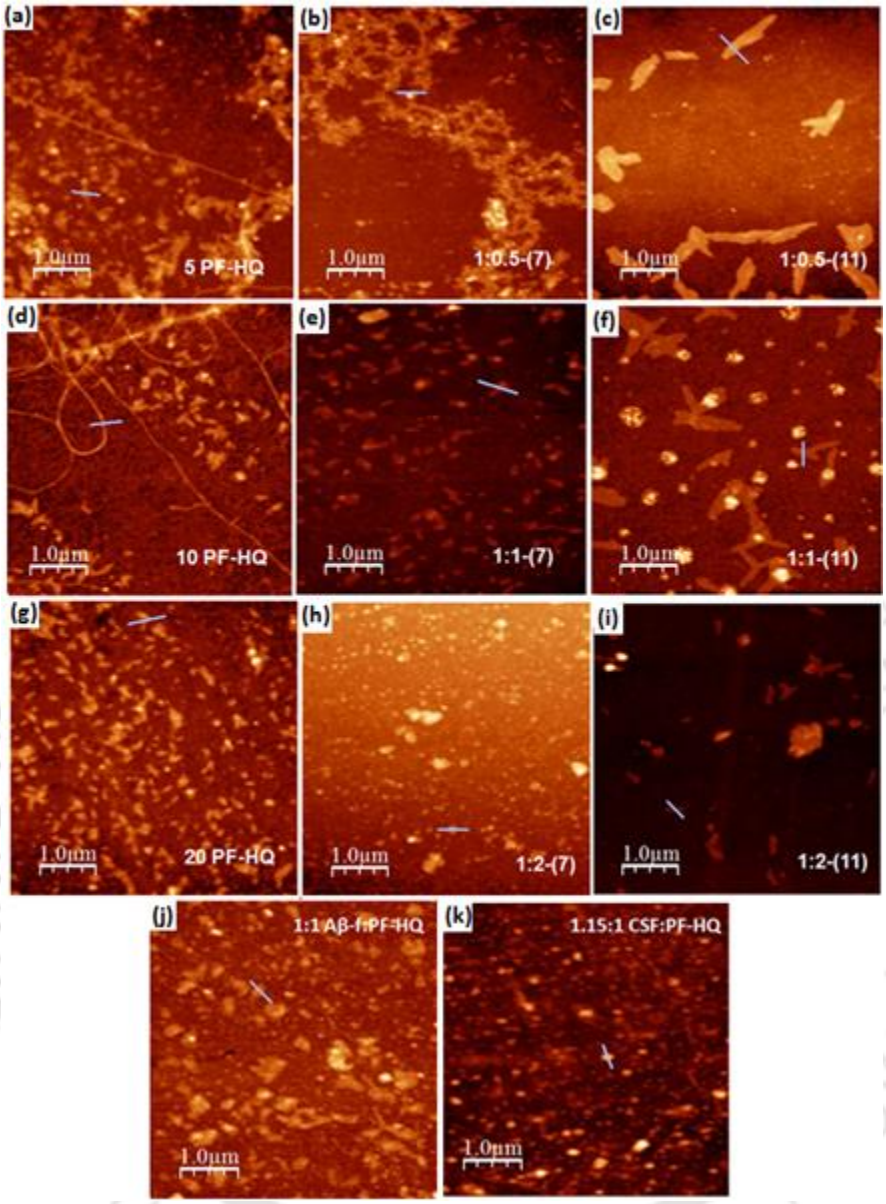

Figure 2a.2. AFM images of PF-HQ only and PF-HQ co-incubated Aβ1-40. Samples were incubated in 10 mM HEPES buffer (pH 7.4) at 37 °C. Image size is 5 X 5 μM2. (a) 5 μM PF-HQ. Aβ1-40 (10 μM) co-incubated with 5 μM PF-HQ (b) after 7 days, (c) after 11 days. (d) 10 μM PF-HQ. Aβ1-40 (10 μM) co-incubated with 10 μM PF-HQ (e) after 7 days, (f) after 11 days. (g) 20 μM PF-HQ. AFM image of Aβ1-40 (10 μM) co-incubated with 20 μM PF-HQ (h) after 7 days, (i) after 11 days. (j) Preformed Aβ1-40 fibril (10 μM) co-incubated with 10 μM PF-HQ after 11 days, (k) CSF (Aβ1-40: 11.5 μM) co-incubated with 10 μM PF-HQ after 11 days.

To check the effects of polymer on more neurotoxic intermediates10-14, preformed Aβ1-40 fibril containing premature fibrillar and oligomeric aggregates (Figure A2a.5 (a) and (b) and A2a.6) were incubated with 10 μM PF-HQ under fibril forming conditions. In presence of PF-HQ, no fibril (Figure 2a.2j) was formed and similar co-aggregates of diameter ~250 nm and

height ~7 nm were formed after 11 days of incubation. Similarly, CSF sample containing aggregated fibrillar amyloid were chosen (Figure A2a.6 (c)) and co-incubated with 10 μM PF-HQ to check its modulating effects on real samples. After 11 days of aging, polymer-protein co-aggregates of diameter ~ 150 nm and ~ 16 nm in height (Figure 2a.2k) were found to form. From AFM images it was envisioned that PF-HQ provides amyloid like surface motif to interact with Aβ1-40 and redirects the formation of polymer-protein co-aggregates, indicative of inhibiting the Aβ1-40 fibrillation. AFM studies revealed that due to identical surface theme, protein gets adsorbed to the CP PF-HQ surface and hydrophobic polymer core and the appended hydroxyquinolines are available for protein interactions and thus able to alter protein aggregation to non-toxic polymer-protein co-aggregates.

2a.3.4. Circular Dichroism and FT-IR

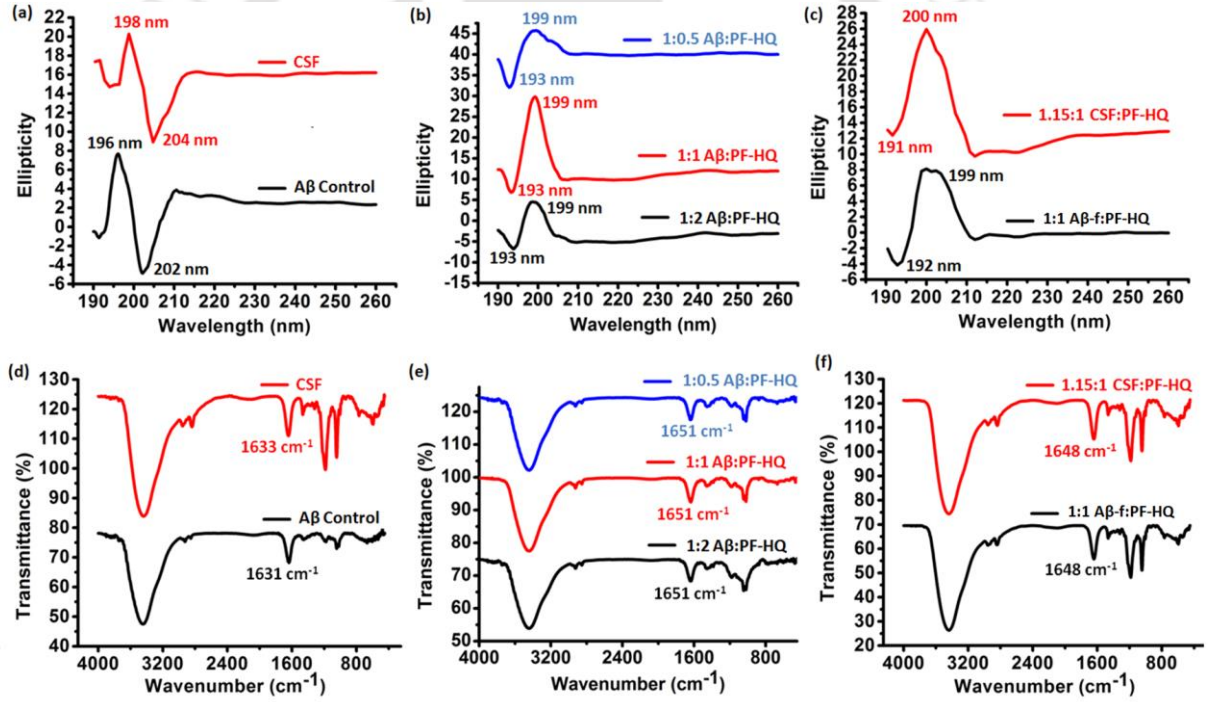

Figure 2a.3. (a) CD spectra and (d) FT-IR spectra of preformed Aβ1-40 fibrils (black line) and in real CSF (red line). (b) and (c) CD spectra, (e) and (f) FT-IR spectra of Aβ1-40 co-incubated with PF-HQ. Equiv. was defined as molar ratio of Aβ1-40 to PF-HQ. (b) and (e) Blue line denotes 0.5 equiv of PF-HQ, red line denotes 1 equiv. of PF-HQ and black line denotes 2 equiv. of PF-HQ co-incubated Aβ1-40. (c) and (f) Black line denotes 1 equiv. of PF-HQ (10 μM) co-incubated with preformed Aβ1-40 fibril (Aβ-f, 10 μM) and red line denotes 10 μM PF-HQ co-incubated with CSF (Aβ: 11.5 μM).

To further explore the impacts of PF-HQ on the early transition of Aβ1-40 aggregation, CD measurements were performed to get an insight into the secondary structures of polypeptides

and monitor the structural conversion over a span of time.[63,64] For control, Aβ1-40 was incubated to aggregate and the final fibril formation was confirmed using CD and FT-IR studies. CD spectrum of preformed Aβ1-40 fibrils show a positive peak at ~196 nm and a negative peak at ~202 nm (Figure 2a.3a, black line) confirming the β-sheet conformation of Aβ1-40.[69] Similarly, Aβ1-40 fibrils present in real CSF sample showed a positive peak at ~198 nm and a negative peak at ~204 nm (Figure 2a.3a, red line). Further, CD measurements were performed after 25 days incubation of Aβ1-40 (10μM) in the presence of different loadings of PF-HQ (i.e., 1:0.5, 1:1 and 1:2 molar ratios of Aβ1-40 to PF-HQ) in 10 mM HEPES buffer (pH 7.4). The CD studies showed a similar display after incubation of Aβ1-40 with 0.5 equiv, 1 equiv and 2 equiv of PF-HQ (Figure 2a.3b). A new curve was formed with a negative peak emerging at ~193 nm along with a positive peak at ~199 nm in the CD spectrum confirming no β-sheet formation. However, in the presence of the polymer (PF-HQ), CD spectrum showed a negative peak at ~193 nm and a positive peak at ~199 nm suggesting that the structural changes (random) of Aβ1-40 are mediated by PF-HQ and no peaks corresponding to the β-sheet formation appear in the CD spectrum. These results suggest that PF-HQ efficiently interacts with Aβ1-40 and inhibits its conformational changes from α-helix to ultimate β-sheet structure.

In order to understand the interaction with the peptide and the role of CP that inhibits fibril formation, 10 μM PF-HQ was co-incubated separately with preformed Aβ1-40 fibril (Aβ-f, 10 μM) containing oligomeric and premature fibrillar aggregates as well as with CSF containing preformed fibrillar amyloid aggregates (11.5 μM) and the conformational change occurring for Aβ1-40 secondary structure were investigated via CD spectroscopy after 11 days of aging. Results confirm that in the presence of CP under fibril forming conditions, a negative peak at ~192 nm along with a positive peak at ~199 nm in Aβ1-40 incubated sample and a negative peak at ~191 nm along with a positive peak at ~200 nm in CSF incubated sample, confirming no β-sheet structure (Figure 2a.3c). These outcomes confirm that PF-HQ not only inhibits β-sheet formation but also breaks the β-sheets to a random coil via interacting with more neurotoxic oligomeric and premature fibrillar amyloid intermediates.

Further, to corroborate the multiple results obtained from ThT fluorescence, AFM as well as CD studies, the co-aggregates of PF-HQ and Aβ1–40 were examined by using FT-IR spectroscopy. Preformed Aβ1–40 fibrils showed a major band at 1630±3 cm^{-1} (Figure 2a.3d) indicating the parallel β-sheet conformation of Aβ1–40 aggregates.[65] Even in real CSF sample containing fibrillar amyloid aggregate a band at 1633 cm^{-1} was observed. Further, a major band at ~1651 cm^{-1} (Figure 2a.3e, blue, red and black) were observed in all three PF-HQ co-

incubated Aβ1-40, which clearly suggested the inhibition of Aβ1-40 self-aggregation to final fibrillar parallel β-sheet conformation via intermolecular interaction of PF-HQ and Aβ1-40. Samples taken from ThT assays also showed similar results. PF-HQ control alone had a distinct broad band around 1600 cm-1 due to aromatic stretching. In case of preformed Aβ1-40 fibril and in real CSF sample, a band at ~1648 cm^{-1} (Figure 2a.3f) was observed which is attributed to random coil formation.[46,70] confirming that PF-HQ has the ability to inhibit Aβ1–40 self-aggregation and is in agreement with results obtained with other characterization techniques.

2a.3.5. DLS and Zeta Potential Measurements

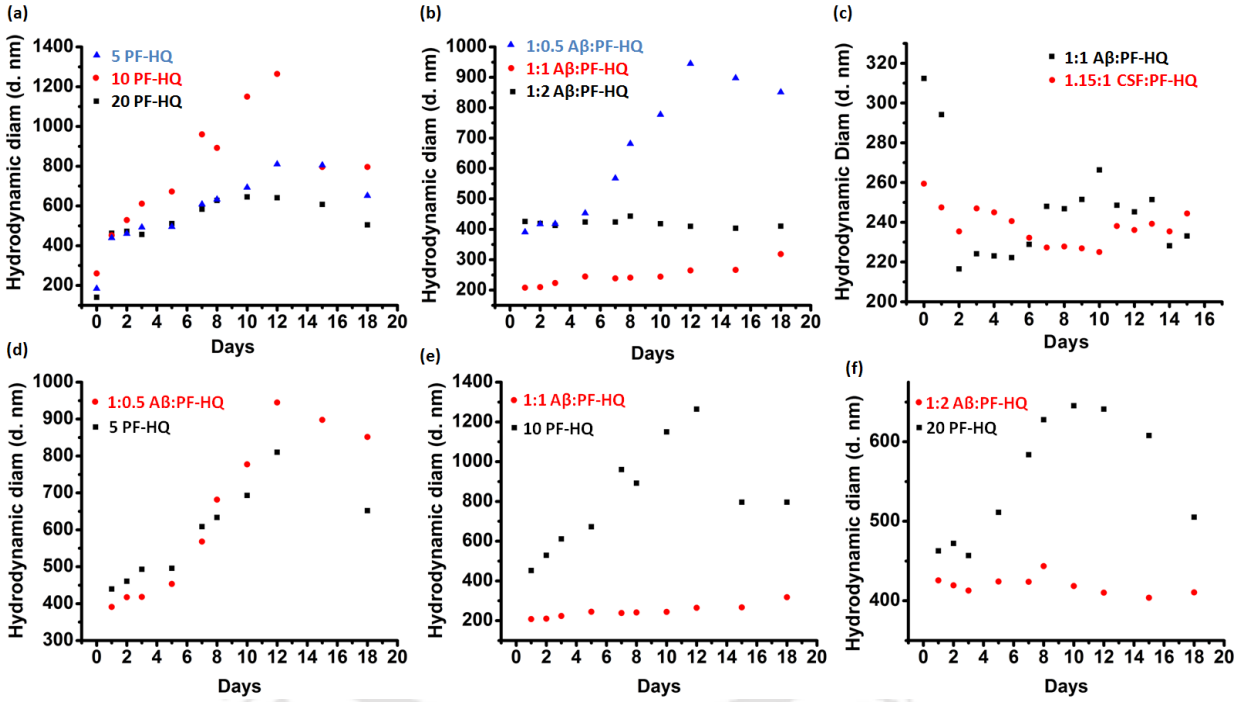

Figure 2a.4. (a) Hydrodynamic diameters of PF-HQ only over time. 5 PF-HQ (blue triangles), 10 PF-HQ (red circles) and 20 PF-HQ (black squares) was denoted to designate 5 μM, 10 μM and 20 μM Pristine, PF-HQ. (b) Hydrodynamic diameters of PF-HQ co-incubated Aβ1-40 over time. Blue triangles denote 0.5 equiv of PF-HQ, red circles denote 1 equiv of PF-HQ and black squares denote 2 equiv of PF-HQ co-incubated Aβ1-40. (c) Red circles denotes 10 μM PF-HQ co-incubated with CSF containing aggregated Aβ (11.5 μM) and black squares denotes 10 μM PF-HQ co-incubated with preformed Aβ1-40 fibril (Aβ-f, 10 μM). Differences in hydrodynamic diameters of co-aggregates and polymer (PF-HQ) self aggregates were shown in (d) 5 PF-HQ (black squares) and 1:0.5 Aβ:PF-HQ (red circles), (e) 10 PF-HQ (black squares) and 1:1 Aβ:PF-HQ (red circles) and (f) 20 PF-HQ (black squares) and 1:2 Aβ:PF-HQ (red circles).

The DLS helped to ascertain the comparison in size distribution of PF-HQ both in the presence and absence of Aβ1-40. Similar to previous reports, in these DLS measurements all particles in scattering volume are approximated by spheres to avoid prejudice in autocorrelation fitting caused by a priori assumptions about particle shape.[66] From the DLS results, compared to the hydrodynamic diameter of PF-HQ controls alone, the diameter of PF-HQ incubated with Aβ1-40 decreases much faster over aging (over a period of 20 days). Differences in hydrodynamic diameters of polymer-protein co-aggregates and polymer (PF-HQ) self-aggregates were clearly visible in DLS profiles (Figure 2a.4). When pristine PF-HQ controls were incubated in 10 mM HEPES buffer (pH 7.4) at 37 °C, a steady increase in hydrodynamic diameter (Figure 2a.4a) of CP upto 12 days of incubation was observed before reaching a level. Due to the formation of disordered structure in case of 5 μM PF-HQ, it showed larger hydrodynamic diameter in DLS compared to 10 μM PF-HQ and 20 μM PF-HQ. In case of 1:1 and 1:2 molar ratios of Aβ1-40 to PF-HQ (Figure 2a.4b), no significant change in hydrodynamic diameter was observed even after 18 days of incubation. Even in case of co-incubated preformed Aβ1-40 fibril, the hydrodynamic diameter decreased confirming the formation of co-aggregates (Figure 2a.4c, black dots). Surprisingly, in case of real CSF sample containing aggregated Aβ (11.5 μM) co-incubated with 10 μM PF-HQ, similar decrease in hydrodynamic diameter (220-260 nm) appeared (Figure 4c, red dots). In case of low loadings of polymer negligible changes in hydrodynamic diameter were observed (Figure 2a.4d) while significant changes occurred in case of co-incubated Aβ40 with PF-HQ of 1 equiv (Figure 2a.4e) and 2 equiv (Figure 2a.4f). These results demonstrate that, PF-HQ forms co-aggregate with Aβ1-40 and thus inhibits Aβ1-40 self-aggregation.

To probe the interaction between Aβ1-40 and PF-HQ, the zeta potentials of co-aggregates (Aβ1-40 co-incubated with three different concentrations of PF-HQ (0.5, 1 and 2 equiv)) and controls (Pristine PF-HQ and Aβ1-40 alone) (Figure 2a.5) were measured. Aβ40 itself (10 μM) shows a negative charged surface (-13.4± 1.08 mV) and the controls of pristine PF-HQ also show negatively charged surfaces (-14.3 ± 0.6 mV for 5 μM PF-HQ, -14.9 ± 0.6 mV for 10 μM PF-HQ and -23.6 ± 1.2 mV for 20 μM PF-HQ) in 10 mM HEPES buffer (pH 7.4). When Aβ40 was co-incubated with PF-HQ (2 equiv and 1 equiv), the co-aggregates showed negatively charged surfaces that are higher than pristine PF-HQ (-31 ± 0.65 mV in case of 1:2 molar ratio of Aβ1-40 to PF-HQ, -17.4 ± 1.9 mV in case of 1:1 molar ratio of Aβ1-40 to PF-HQ). The zeta potential of 0.5 equiv of PF-HQ incubated Aβ1-40 also showed a negative charged surface but slightly lesser than 5μM pristine PF-HQ (-13.3 ± 0.49 mV in case of 1:0.5 molar ratio of Aβ1-40 to PF-HQ). Similarly in case of preformed Aβ1-40 fibril (-15.5±0.6 mV) and in real CSF

sample (-17.4±0.6), the co-aggregates showed negatively charged surfaces that are higher than 10 μM pristine PF-HQ (-14.9 ± 0.6 mV). The results of zeta potential indicate that the co-aggregates are formed from peptide bound by PF-HQ via attractive intermolecular hydrophobic interaction instead of that from pure peptide and disturb the hydrophobic core to form final fibrillar network.

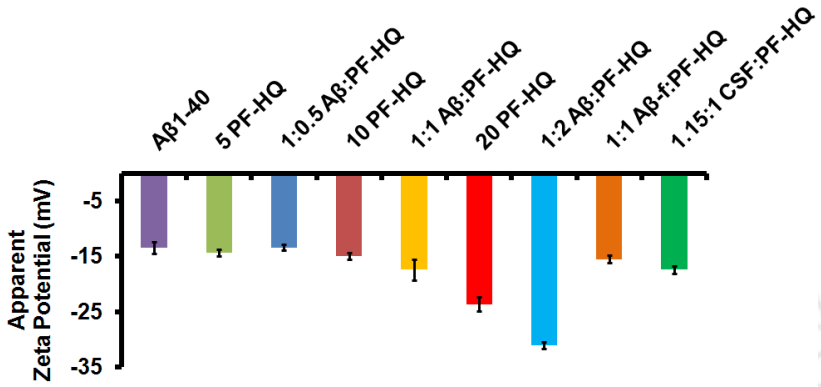

Figure 2a.5. Zeta potential of Aβ1-40 alone, Pristine PF-HQ and PF-HQ co-incubated Aβ1-40 in 10 mM HEPES buffer (pH 7.4). Error bars correspond to standard deviations of three measurements. 5 PF-HQ, 10 PF-HQ and 20 PF-HQ represent 5 μM, 10 μM and 20 μM Pristine PF-HQ.

2a.3.6. Fluorescence Measurements

To further evaluate if PF-HQ can be used as an optical probe for Aβ1-40 aggregation, we carefully observed fluorescence spectrum of Pristine PF-HQ and PF-HQ co-incubated Aβ1-40 solutions over a period of time (Figure 2a.6a-2a.6c). All the measurements were performed in 10 mM HEPES buffer (pH 7.4).

When 10 μM Aβ1-40 was added separately to different concentration of PF-HQ and the solutions were excited at 355 nm, fluorescence emission was observed at 504 nm. An increase in the fluorescence intensity was observed in case of 1 equiv and 2 equiv of PF-HQ incubated Aβ1-40 solutions compared to the spectrum of Pristine PF-HQ (Figure 2a.6b and 2a.6c) due to the formation of well-ordered polymer-protein structures while in case of 0.5 equiv of PF-HQ incubated Aβ1-40, fluorescence intensity decreased compared to the control (5 μM Pristine PF-HQ) (Figure 2a.6a). After 24 hours of incubation at 37 °C, a red shift of 8-12 nm was observed along with a slight increase in intensity in the fluorescence spectrum of all three co-incubated solutions while a marked decrease in intensity along with 6-8 nm red shifts occurs in all the control sample spectrum of pristine PF-HQ. Further incubation from 1-6 days

led to the decrease in fluorescence intensity in all the co-incubated and control samples. Finally, after 7-20 days of incubation, a new peak at 438-440 nm arises and predominates over the initial peak at 517-518 nm. Unfortunately, these results demonstrate no optical changes on forming co-aggregates of PF-HQ and Aβ1-40 except an increase in fluorescence intensity at 440 nm compared to PF-HQ controls. The fluorescence enhancement may be attributed to the accelerated formation of co-aggregates of PF-HQ and Aβ1-40 instead of PF-HQ and Aβ1-40 self-aggregation via attractive hydrophobic polymer-protein interaction.

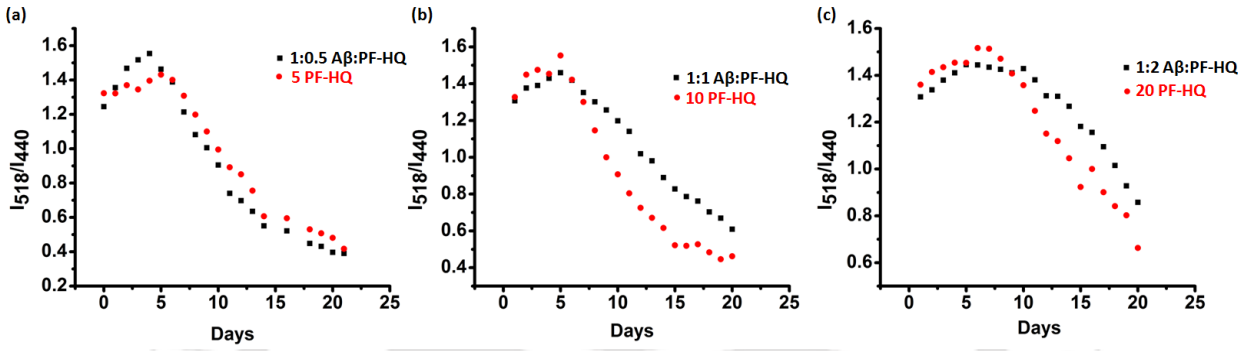

Figure 2a.6. Fluorescence profile (I_{518}/I_{440} vs Days) of pristine PF-HQ and PF-HQ co-incubated Aβ1-40. Samples were incubated in 10 mM HEPES (pH 7.4) at 37 °C. (a) 5 μM pristine PF-HQ (red circles) and co incubated Aβ1-40 (black squares) (b) 10 μM pristine PF-HQ (red circles) and co incubated Aβ1-40 (black squares), (c) 20 μM pristine PF-HQ (red circles) and co incubated Aβ1-40 (black squares).

To understand the role of PF-HQ on Aβ1-40 self-aggregation, 10 μM PF-HQ was incubated with preformed Aβ1-40 fibril containing oligomeric and prefibrillar aggregates and the optical changes were monitored (Figure 2a.7a). Unlike monomeric incubation [Excitation wavelength: 355 nm. Intensity vs Wavelength profiles were shown in supporting information (Figure A2a.7). Combined fluorescence profile (I518/I440 vs Days) of 6a, 6b and 6c were shown in supporting information (Figure A2a.8)], initial decrease in fluorescence intensity occurs much rapidly and no hump at 504 or 518 nm were observed. The peak at 440 nm appears after 6 days of incubation that became predominant after further incubation. This phenomenon can be attributed to the presence of oligomeric and premature fibrillar aggregates which interact with PF-HQ much faster, ultimately leading to the formation of polymer-protein co-aggregates. Due to faster polymer-protein interaction polymeric identity at 504 nm diminishes after 48 hours of incubation. After formation of well-ordered co-aggregates the peak at 440 nm became more prominent. Similar fluorescence response was observed in case of real CSF co-incubated sample (Figure 2a.7b). Due to the presence of fibrillar amyloid aggregates in CSF, PF-HQ responded similarly as in case of preformed Aβ1-

40 fibril. No hump was observed at 504 nm along with a predominant peak at 440 nm appearing concurrently. The fluorescence results further confirm that PF-HQ interact with toxic amyloid intermediate and ultimately convert it into unique nano co-aggregated structures.

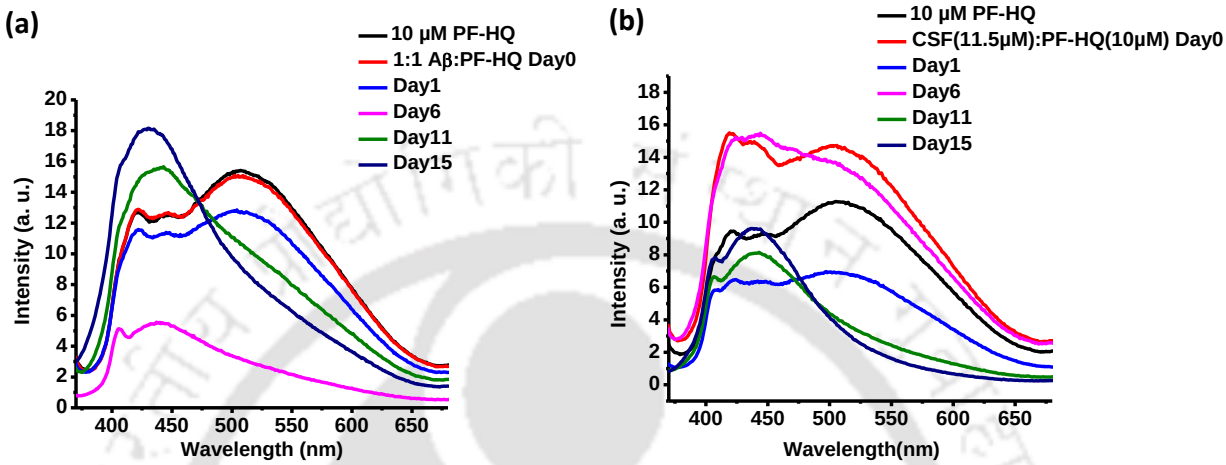

Figure 2a.7. Fluorescence profile of (a) 10 μM Pristine PF-HQ and PF-HQ co-incubated preformed Aβ1-40 fibril (Aβ-f, 10 μM) containing oligomeric and premature fibrillar aggregates. (b) 10 μM Pristine PF-HQ and co incubated CSF (Aβ: 11.5 μM). Samples were incubated in 10 mM HEPES buffer (pH 7.4) at 37 °C. Excitation wavelength: 355 nm.

2a.3.7. MTT Assay

To check intrinsic toxicity of pristine PF-HQ (Figure A2a.9), MTT (3-(4, 5-dimethylthiazol-2yl)-2, 5-diphenyltetrazolium bromide) assay on U-87 MG cells were performed. Cell viability assays indicate that even at higher concentration of PF-HQ (20 μM) less than 20% cell death occurred. Further, to look at the impact of PF-HQ on the lethality of Aβ1-40 aggregates toward cells, Aβ1-40 was initially incubated in serum free media without PF-HQ to permit prefibrillar aggregates to frame followed by co-incubating Aβ1-40 with three different concentrations of PF-HQ (0.5, 1 and 2 equivalent) in same serum free media to check the detoxification impacts. The presence of preformed Aβ1-40 fibrils cell viability reduced to ~60%, suggesting that these aggregates were toxic to U-87 MG cells, however, in presence of 1 equivalent of PF-HQ cell viability increased to ~85%. Similarly, polymer-protein co-aggregates showed more than 80% cell viability (Figure 2a.8) towards U-87 MG cells. Data confirms that PF-HQ modulates Aβ1-40 aggregation with a distinctive ability to attenuate cytotoxicity caused by Aβ aggregation.

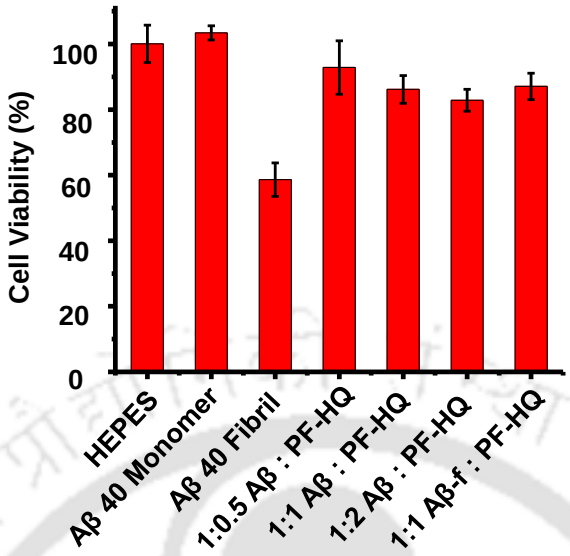

Figure 2a.8. Toxicity of polymer-protein co-aggregates. Both preformed Aβ1-40 fibrils and monomeric Aβ1-40 were taken as control. Error bar corresponds to standard deviations of eight sets of experiments.

2a.4. Discussion

These studies prove that PF-HQ has the ability to inhibit self-aggregation process of Aβ1-40 via sequestering mechanism and that the perturbation depends on surface properties of CP. PF-HQ itself forms amyloid like fibrillar and protofibrillar self-aggregates (Scheme 2a.3.a) and thus provides similar surface motif to interact with Aβ1-40 via hydrophobic interaction and finally inhibits protein aggregation. Being a polymeric material, PF-HQ also has the advantage of "multivalent effect" to interact with the target protein. Indeed, formation of polymer-protein co-aggregates steer the blocking of central hydrophobic protein core which is responsible for fibril formation. Lower CP concentration leads to the formation of disordered co-aggregates initially as in the case of lower concentration of CP enough surface areas are unavailable unlike in case of higher concentration of CP. However, at higher concentration of PF-HQ, a dominant hydrophobic attraction among CP itself exacerbate amyloid cytotoxicity as it is less available to form polymer-protein co-aggregates. 10 μM PF-HQ provides extensive amyloid like fibrillar templating surface to interact with hydrophobic core of Aβ1-40 and promotes the formation of polymer-protein co-aggregates. A low loading of PF-HQ concentration redirects the aggregation process to a disordered co-aggregate which finally transforms into well ordered nano co-aggregates on aging (Scheme 2a.3.b). Low intrinsic toxicity of PF-HQ even at higher concentration, it's negatively charged surface,

amyloid-like surface motif and abundant binding sites make this CP template a unique platform with excellent inhibitory modulation ability of Aβ1-40 aggregation and may likely find application as a potential therapeutic material for amyloid related diseases. These studies indicate that PF-HQ has the ability to trap the intermediate highly toxic oligomeric and premature fibrillar amyloid aggregates and finally transforming them into non-toxic co-aggregates. This CP shows a dual effect of inhibiting Aβ1-40 self-aggregation and as well as β-sheet breaking by first providing sufficient amyloid like surface so that the protein gets adsorbed and then the appended hydroxyquinolines binding sites available in abundant along with the hydrophobic polymeric core to trap the toxic intermediates, leading to the formation of nontoxic co-aggregates.

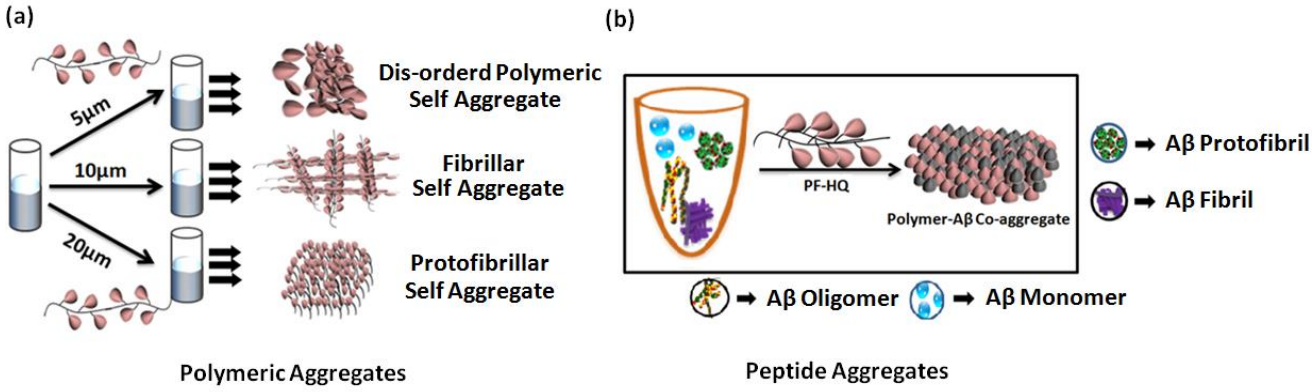

Scheme 2a.3. Cartoon depiction of (a) Polymer self aggregates and (b) Aβ1-40 aggregates and polymer-protein co-aggregates.

2a.5. Conclusion

PF-HQ successfully leads to an inhibitory effect on Aβ1-40 self-aggregation as well as attenuates its cytotoxicity and can be looked on as one of the most important future therapeutic surrogate. These findings suggest that the concentration of PF-HQ is important in modifying its own surface properties and eventually play a key role in the overall modulation of Aβ1-40 aggregation. Similar surface template engineered from polymeric nanoparticles show a significant modulation on amyloid fibrillogenesis in both commercial Aβ1-40 solution as well as in complex biological fluids. Thioflavin T (ThT) fluorescence, atomic force microscopy (AFM), circular dichroism (CD), Fourier transform infrared (FT-IR) studies confirm that PF-HQ inhibits Aβ fibrillization and modulates fibrillar aggregates as well into polymer-protein co-aggregates. Besides, MTT studies demonstrate that Aβ aggregates intervened by PF-HQ improves Aβ cytotoxicity towards U-87 MG cells. The hydrophobic

fluorene core with a suitable functionality over its side chain provides amyloid-like particle surfaces and abundant binding sites for protein interactions. Thus, PF-HQ plays a significant role in modulating highly neurotoxic oligomeric, prefibrillar amyloid intermediates and transforming them into non-toxic co-aggregates. Finally, and perhaps most importantly, polyflourene template offer a novel and powerful route to modify its surface properties for targeting amyloid and to define the intermolecular forces that hinders protein aggregation, thus, open a new window to fight against this devastating disease.

References

(1) Hamley, I. W. *Chem. Rev.* **2012**, *112*, 5147-5192.

(2) Holtzman, D. M.; Morris, J. C.; Goate, A. M. *Sci. Transl. Med.* **2011**, *3*, 77sr1.

(3) Brettschneider, J.; Tredici, K. Del, Lee, V. M.-Y.; Trojanowski, J. Q. *Nat. Rev. Neurosci.* **2015**, *16*, 109–120.

(4) Prince, M.; Bryce, R.; Albanese, E.; Wimo, A.; Ribeiro, W.; Ferri, C. P. *Alzheimers Dement.* **2013**, *9*, 63–75.e2.

(5) Caughey, B.; Lansbury, P. T. *Annu. Rev. Neurosci.* **2003**, *26*, 267–298.

(6) Nelson, R.; Sawaya, M. R.; Balbirnie, M.; Madsen, A. Ø.; Riekel, C.; Grothe, R.; Eisenberg, D. *Nature* **2005**, *435*, 773–778.

(7) Gazit, E. *Chem. Soc. Rev.* **2007**, *36*, 1263–1269.

(8) Carulla, N.; Zhou, M.; Giralt, E.; Robinson, C. V.; Dobson, C. M. *Acc. Chem. Res.* **2010**, *43*, 1072–1079.

(9) Selkoe, D. J. *Nature* **2003**, *426*, 900–904.

(10) Ferreira, S. T.; Vieira, M. N. N.; De Felice, F. G. *IUBMB Life* **2007**, *59*, 332–345.

(11) Bucciantini, M.; Calloni, G.; Chiti, F.; Formigli, L.; Nosi, D.; Dobson, C. M.; Stefani, M. *J. Biol. Chem.* **2004**, *279*, 31374–31382.

(12) Stefani, M.; Dobson, C. M. *J. Mol. Med.* **2003**, *81*, 678–699.

(13) Sommer, B. *Curr. Opin. Pharmacol.* **2002**, *2*, 87–92.

(14) Baglioni, S.; Casamenti, F.; Bucciantini, M.; Luheshi, L. M.; Taddei, N.; Chiti, F.; Dobson, C. M.; Stefani, M. *J. Neurosci.* **2006**, *26*, 8160–8167.

(15) Verdile, G.; Fuller, S.; Atwood, C. S.; Laws, S. M.; Gandy, S. E.; Martins, R. N. *Pharmacol. Res.* **2004**, *50*, 397–409.

(16) Wang, C.; Yang, A.; Li, X.; Li, D.; Zhang, M.; Du, H.; Li, C.; Guo, Y.; Mao, X.; Dong, M.; Besenbacher, F.; Yang, Y.; Wang, C. *Nanoscale* **2012**, *4*, 1895–1909.

(17) Re, F.; Airoldi, C.; Zona, C.; Masserini, M.; La Ferla, B.; Quattrocchi, N.; Nicotra, F. *Curr. Med. Chem.* **2010**, *17*, 2990–3006.

(18) Nie, Q.; Du, X.; Geng, M. *Acta Pharmacol. Sin.* **2011**, *32*, 545–551.

(19) McKoy, A. F.; Chen, J.; Schupbach, T.; Hecht, M. H. *J. Biol. Chem.* **2012**, *287*, 38992–39000.

(20) López, L. C.; Dos-Reis, S.; Espargaró, A.; Carrodeguas, J. A.; Maddelein, M.-L.; Ventura, S.; Sancho, J. *J. Med. Chem.* **2012**, *55*, 9521–9530.

(21) Bose, M.; Gestwicki, J. E.; Devasthali, V.; Crabtree, G. R.; Graef, I. A. *Biochem. Soc. Trans.* **2005**, *33*, 543–547.

(22) Zhu, F.; Wu, F., Ma, Y.; Liu, G.; Li, Z.; Sun, Y.; Pei, Z. *BMC Neurosci.* **2011**, DOI: 10.1186/1471-2202-12-125.

(23) Bieschke, J.; Herbst, M.; Wiglenda, T.; Friedrich, R. P.; Boeddrich, A.; Schiele, F.; Kleckers, D.; Lopez del Amo, J. M.; Grüning, B. A.; Wang, Q.; Schmidt, M. R.; Lurz, R.; Anwyl, R.; Schnoegl, S.; Fändrich, M.; Frank, R. F.; Reif, B.; Günther, S.; Walsh, D. M.; Wanker, E. E. *Nat. Chem. Biol.* **2011**, *8*, 93–101.

(24) Black, R. S.; Sperling, R. A.; Safirstein, B.; Motter, R. N.; Pallay, A.; Nichols, A.; Grundman, M. *Alzheimer Dis. Assoc. Disord.* **2013**, *24*, 198–203.

(25) Takahashi, T.; Mihara, H. *Acc. Chem. Res.* **2008**, *41*, 1309–1318.

(26) Zaman, M.; Ahmad, E.; Qadeer, A.; Rabbani, G.; Khan, R. H. *Int. J. Nanomedicine* **2014**, *9*, 899–912.

(27) Di Domizio, J.; Zhang, R.; Stagg, L. J.; Gagea, M.; Zhuo, M.; Ladbury, J. E.; Cao, W. *J. Biol. Chem.* **2012**, *287*, 736–747.

(28) Liu, R.; Su, R.; Liang, M.; Huang, R.; Wang, M.; Qi, W.; He, Z. *Curr. Med. Chem.* **2012**, *19*, 4157–4174.

(29) Feng, S.; Song, X.-H.; Zeng, C.-M. *FEBS Lett.* **2012**, *586*, 3951–3955.

(30) Shaw, C. P.; Middleton, D. A.; Volk, M.; Lévy, R. *ACS Nano* **2012**, *6*, 1416–1426.

(31) Wu, W. H.; Sun, X.; Yu, Y. P.; Hu, J.; Zhao, L.; Liu, Q.; Zhao, Y. F.; Li, Y. M. TiO2 *Biochem. Biophys. Res. Commun.* **2008**, *373*, 315–318.

(32) Linse, S.; Cabaleiro-Lago, C.; Xue, W.-F., Lynch, I., Lindman, S., Thulin, E., Radford, S. E., Dawson, K. A. *Proc. Natl. Acad. Sci. U. S. A.* **2007**, *104*, 8691–8696.

(33) Cabaleiro-Lago, C.; Lynch, I.; Dawson, K. A.; Linse, S. *Langmuir* **2010**, *6*, 3453–3461.

(34) Cabaleiro-Lago, C.; Szczepankiewicz, O.; Linse, S. *Langmuir* **2012**, *28*, 1852–1857.

(35) Cabaleiro-Lago, C.; Quinlan-Pluck, F.; Lynch, I.; Lindman, S.; Minogue, A. M.; Thulin, E.; Walsh, D. M.; Dawson, K. A.; Linse S. *J. Am. Chem. Soc.* **2008**, *130*, 15437–15443.

(36) Skaat, H.; Chen, R.; Grinberg, I.; Margel, S. *Biomacromolecules* **2012**, *13*, 2662–2670.

(37) Mahmoudi, M.; Akhavan, O.; Ghavami, M.; Rezaee, F.; Ghiasi, S. M. *Nanoscale* **2012**, *4*, 7322–7325.

(38) Dugan, L. L.; Turetsky, D. M.; Du, C.; Lobner, D.; Wheeler, M.; Almli, C. R.; Shen, C. K.; Luh, T. Y.; Choi, D. W.; Lin, T. S. *Proc. Natl. Acad. Sci. U. S. A.* **1997**, *94*, 9434–9439.

(39) Boridy, S.; Takahashi, H.; Akiyoshi, K.; Maysinger, D. *Biomaterials* **2009**, *30*, 5583–5591.

(40) Nilsson, K. P. R.; Aslund, A.; Berg, I.; Nyström, S.; Konradsson, P.; Herland, A.; Inganäs, O.; Stabo-Eeg, F.; Lindgren, M.; Westermark, G. T.; Lannfelt, L.; Nilsson, L. N. G.; Hammarström, P. *ACS Chem. Biol.* **2007**, *2*, 553–560.

(41) Nilsson, K. P. R.; Hammarström, P.; Ahlgren, F.; Herland, A.; Schnell, E. A.; Lindgren, M.; Westermark, G. T.; Inganäs, O. *ChemBioChem* **2006**, *7*, 1096–1104.

(42) Nilsson, K. P. R.; Lindgren, M.; Hammarström, P. *Methods Mol. Biol.* **2012**, *849*, 425–434.

(43) Nilsson, K. P. R.; Rydberg, J.; Baltzer, L.; Inganäs, O. *Proc. Natl. Acad. Sci. U. S. A.* **2003**, *100*, 10170–10174.

(44) Sigurdson, C. J.; Nilsson, K. P. R.; Hornemann, S.; Manco, G.; Polymenidou, M.; Schwarz, P.; Leclerc, M.; Hammarström, P.; Wüthrich, K.; Aguzzi, A. *Nat. Methods* **2007**, *4*, 1023–1030.

(45) Herland, A.; Björk, P.; Hania, P. R.; Scheblykin, I. G.; Inganäs, O. *Small* **2007**, *3*, 318–325.

(46) Muthuraj, B.; Hussain, S.; Iyer, P. K. *Polym. Chem.* **2013**, *4*, 5096–5107.

(47) Dwivedi, A. K.; Iyer, P. K. *Macromol. Biosci.* **2014**, *14*, 508–514.

(48) Ghosh, D.; Dutta, P.; Chakraborty, C.; Singh, P. K.; Anoop, A.; Jha, N. N.; Jacob, R. S.; Mondal, M.; Mankar, S.; Das, S.; Malik, S.; Maji, S. K. *Langmuir* **2014**, *30*, 3775–3786.

(49) Cacciatore, I.; Fornasari, E.; Baldassarre, L.; Cornacchia, C.; Fulle, S.; Di Filippo, E. S.; Pietrangelo, T.; Pinnen, F. *Pharmaceuticals* **2013**, *6*, 54–69.

(50) Fernández-Bachiller, M. I.; Pérez, C.; González-Muñoz, G. C.; Conde, S.; López, M. G.; Villarroya, M.; García, A. G.; Rodríguez-Franco, M. I. *J. Med. Chem.* **2010**, *53*, 4927–4937.

(51) Moosmann, B.; Behl, C. *Proc. Natl. Acad. Sci. U. S. A.* **1999**, *96*, 8867–8872.

(52) Zatta, P.; Drago, D.; Bolognin, S.; Sensi, S. L. *Trends Pharmacol. Sci.* **2009**, *30*, 346–355.

(53) Kenche, V. B.; Zawisza, I.; Masters, C. L.; Bal, W.; Barnham, K. J.; Drew, S. C. *Inorg. Chem.* **2013**, *52*, 4303–4318.

(54) Ryan, T. M.; Roberts, B. R.; Mccoll, G.; Hare, X. D. J.; Doble, P. A.; Li, Q.; Lind, M.; Roberts, A. M.; Mertens, X. H. D. T.; Kirby, N.; Pham, C. L. L.; Hinds, M. G.; Adlard, P. A.; Barnham, K. J.; Curtain, C. C.; Masters, C. L. *J. Neurosci.* **2015**, *35*, 2871–2884.

(55) Dwivedi, A. K.; Iyer, P. K. *J. Mater. Chem. B* **2013**, *1*, 4005–4010.

(56) Dwivedi, A. K.; Prasad, K. M.; Trivedi, V.; Iyer, P. K. *ACS Appl. Mater. Interfaces* **2012**, *4*, 6371–6377.

(57) Gopikrishna, P.; Das, D.; Iyer, P. K. *J. Mater. Chem. C* **2015**, *3*, 9318–9326.

(58) Hussain, S.; De, S.; Iyer, P. K. *ACS Appl. Mater. Interfaces* **2013**, *5*, 2234–2240.

(59) Hussain, S.; Malik, A. H.; Iyer, P. K. *ACS Appl. Mater. Interfaces* **2015**, *7*, 3189–3198.

(60) Hussain, S.; Malik, A. H.; Afroz, M. A.; Iyer, P. K. *Chem. Commun.* **2015**, *51*, 7207–7210.

(61) Ma, W.; Iyer, P. K.; Gong, X.; Liu, B.; Moses, D.; Bazan, G. C.; Heeger, A. J. *Adv. Mater.* **2005**, *17*, 274–277.

(62) Malik, A. H.; Hussain, S.; Tanwar, A. S.; Layek, S.; Trivedi, V.; Iyer, P. K. *Analyst* **2015**, *140*, 4388–4392.

(63) Dwivedi, A. K.; Saikia, G.; Iyer, P. K. *J. Mater. Chem.* **2011**, *21*, 2502–2507.

(64) Saikia, G.; Iyer, P. K. *Macromolecules* **2011**, *44*, 3753–3758.

(65) Sun, H.; Yin, B.; Ma, H.; Yuan, H.; Fu, B.; Liu, L. *ACS Appl. Mater. Interfaces* **2015**, *7*, 25390–25395.

(66) Donabedian, P. L.; Pham, T. K.; Whitten, D. G.; Chi, E. Y. *ACS Chem. Neurosci.* **2015**, *6*, 1526–1535.

(67) Zhu, C.; Liu, L.; Yang, Q.; Lv, F.; Wang, S. *Chem. Rev.* **2012**, *112*, 4687–4735.

(68) Margalith, I.; Suter, C.; Ballmer, B.; Schwarz, P.; Tiberi, C.; Sonati, T.; Falsig, J.; Nyström, S.; Hammarström, P.; Aslund, A.; Nilsson, K. P. R.; Yam, A.; Whitters, E.; Hornemann, S.; Aguzzi, A. *J. Biol. Chem.* **2012**, *287*, 18872–18887.

(69) Zhu, L.; Song, Y.; Cheng, P-N.; Moore, J. S. *J. Am. Chem. Soc.* **2015**, *137*, 8062–8068.

(70) Shivu, B.; Seshadri, S.; Li, J.; Oberg, K. A.; Uversky, V. N.; Fink, A. L. *Biochemistry* **2013**, *52*, 5176–5183.

Appendix

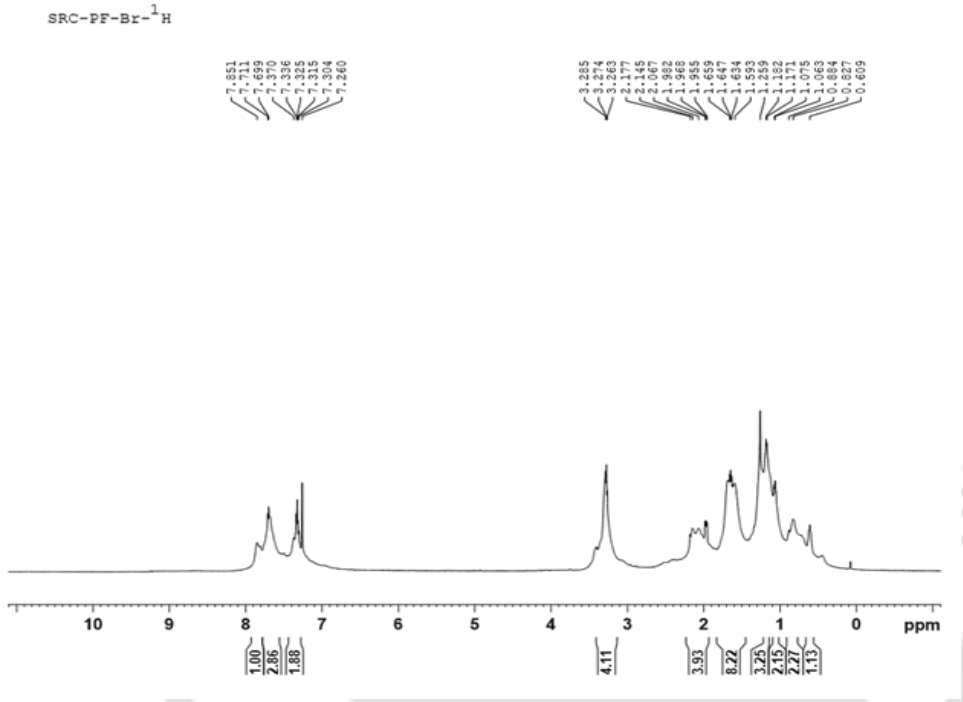

Figure A2a.1. ^{1}H NMR of PF-Br.

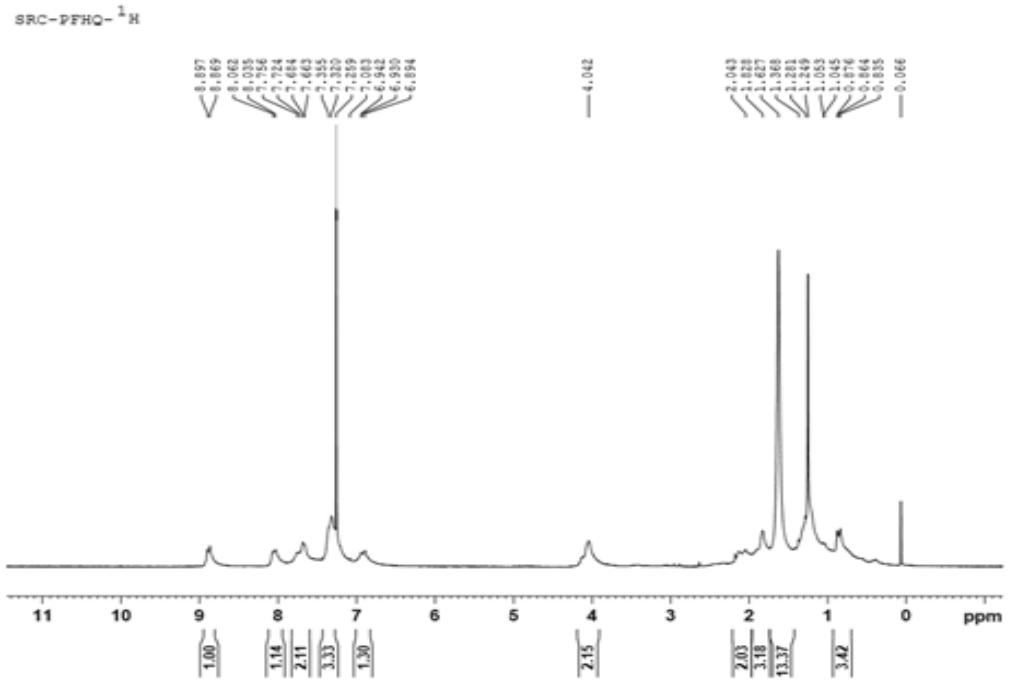

Figure A2a.2. ^{1}H NMR of PF-HQ.

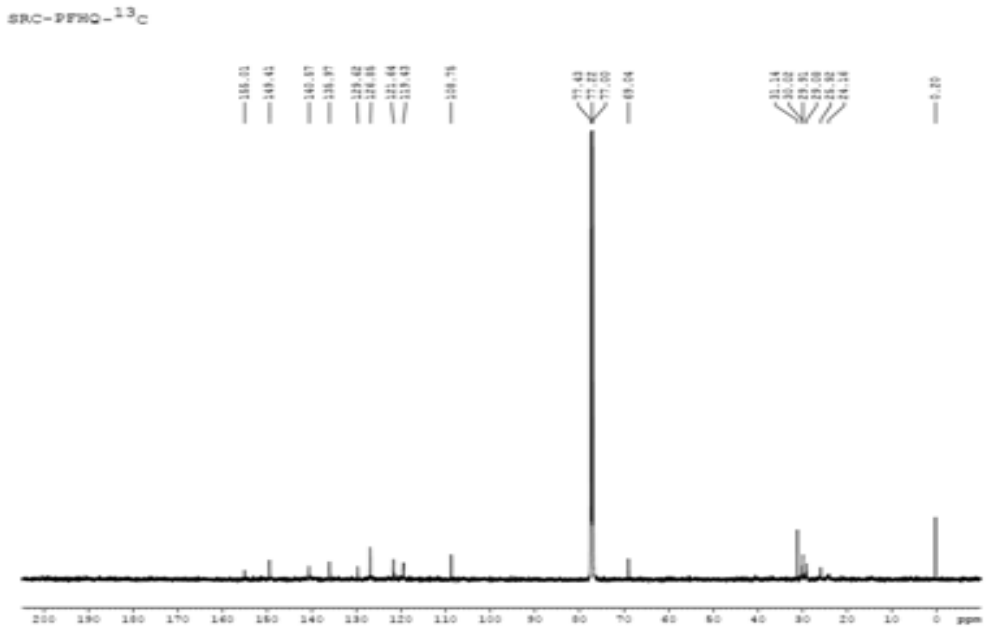

Figure A2a.3. ^{13}C NMR of PF-HQ.

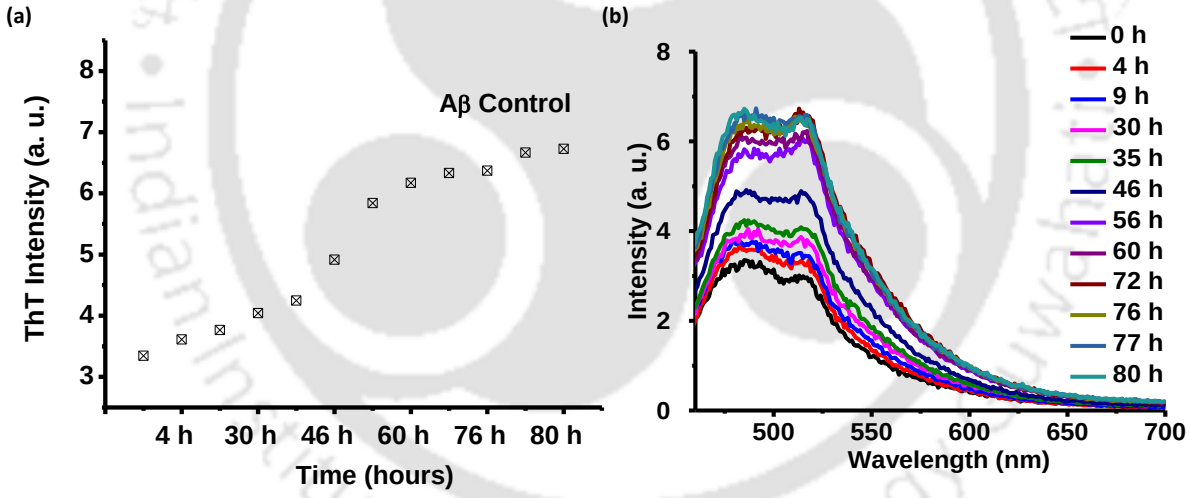

Figure A2a.4. ThT fluorescence assays to monitor Aβ 1-40 (10 μM) control fibrillation kinetics in absence of modulator (PF-HQ). Sample was incubated in 10 mM HEPES buffer (pH 7.4) at 37 °C.

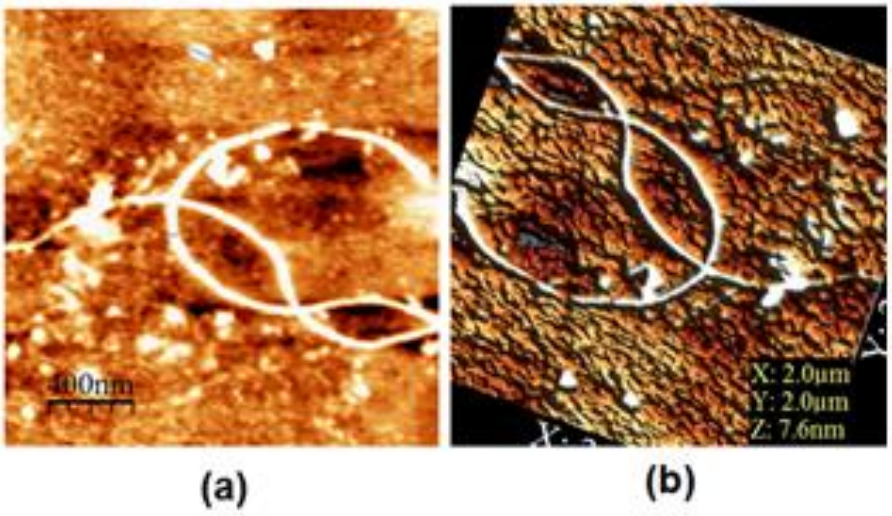

Figure A2a.5. AFM images of Aβ1-40 fibrils. (a) 2D image of long mature Aβ1-40 fibril, (b) 3D image of Aβ1-40 fibril. Image size is 2 X 2 μM². Samples were incubated in 10 mM HEPES buffer (pH 7.4) at 37 °C.

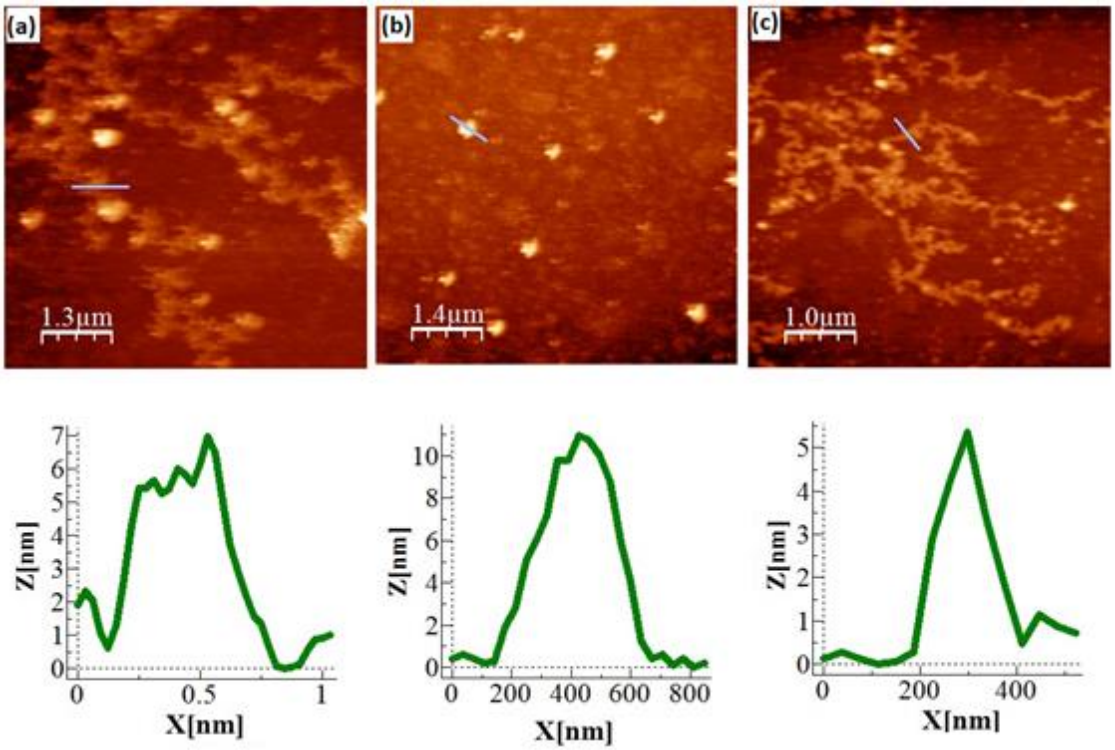

Figure A2a.6. AFM images of Aβ1-40 fibrils. (a) 2D image of pre-mature Aβ1-40 fibril, (b) 2D image of Aβ1-40 oligomers. (c) 2D image of Aβ1-40 fibrils in CSF. Image size is 5 X 5 μM². Samples were incubated in 10 mM HEPES buffer (pH 7.4) at 37 °C.

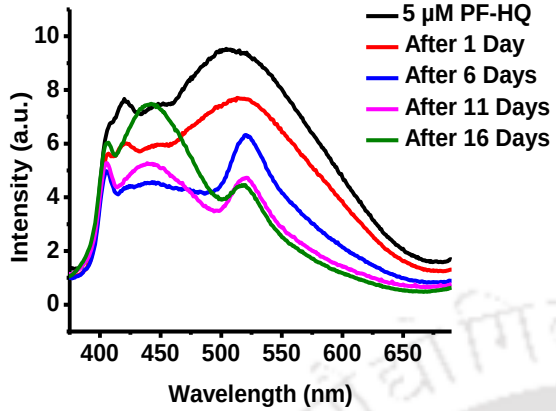

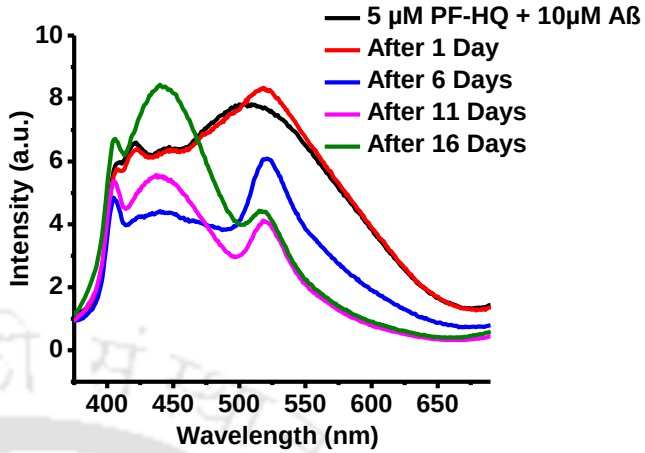

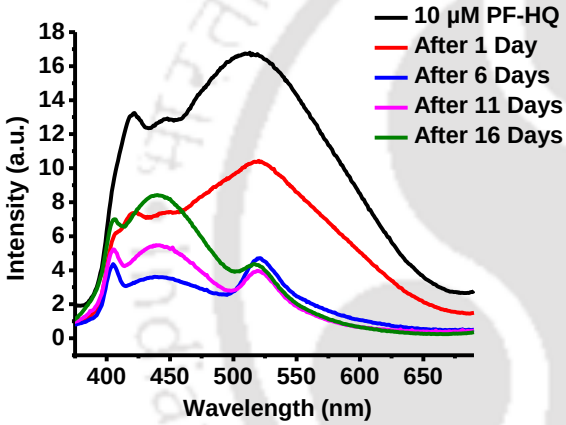

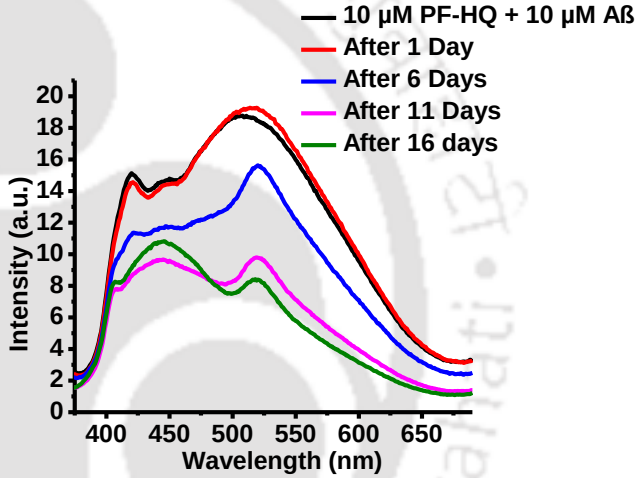

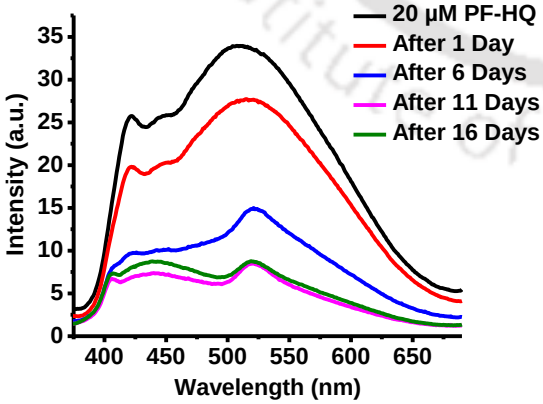

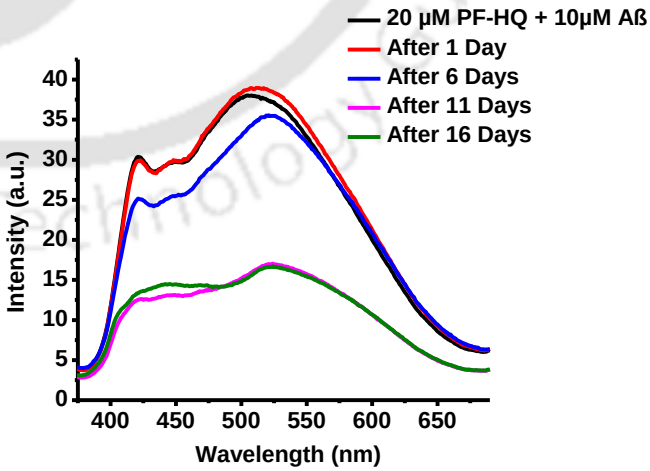

Figure A2a.7. Fluorescence profile (Intensity vs Wavelength) of PF-HQ alone and PF-HQ co-incubated Aβ1-40 over a period of 16 days. Samples were incubated in 10 mM HEPES buffer (pH 7.4) at 37 °C. Excitation wavelength: 355 nm.

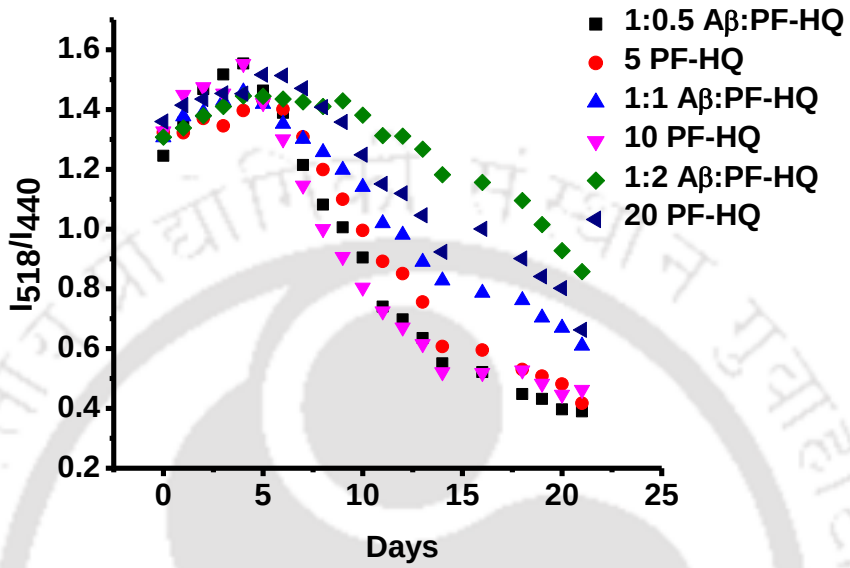

Figure A2a.8. Fluorescence profile (I518/I440 vs Days) of PF-HQ alone and PF-HQ co-incubated Aβ1-40. Samples were incubated in 10 mM HEPES buffer (pH 7.4) at 37 °C. Excitation wavelength: 355 nm.

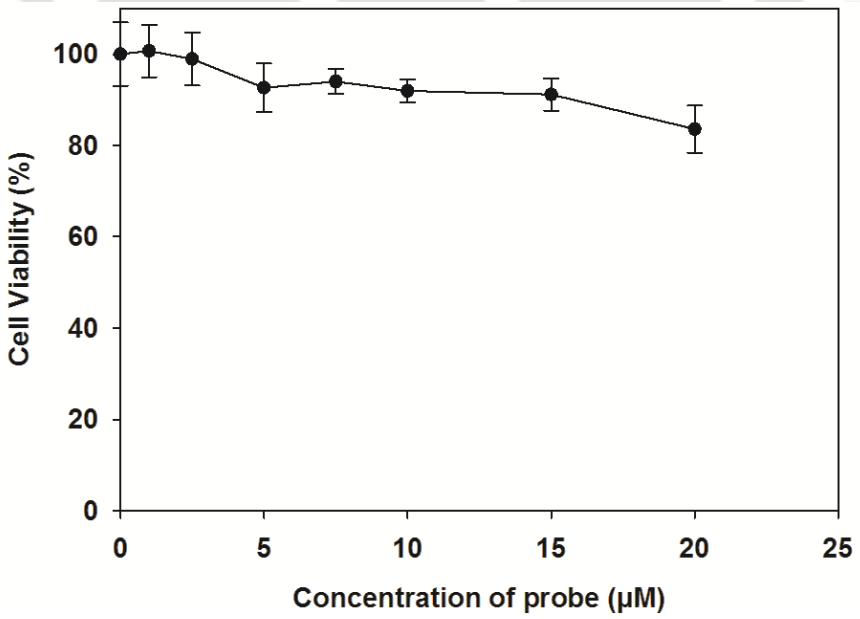

Figure A2a.9. Toxicity of PF-HQ alone towards U-87 MG cells. The cell viability of U-87 MG cells in THF is taken to be 100%. Error bar corresponds to standard deviations of seven sets of experiments.

Aggregates	Time	Description	Dimensions
5 μM PF-HQ (Figure 2a)	After 7 days of incubation	Disordered Protofibrillar and fibrillar amyloid like aggregates	~200 nm and ~5 nm in height (fibril) ~300 nm and ~10 nm in height (Protofibril)
5 μM PF-HQ+10 μM Aβ1-40 (1 : 0.5 Aβ : PF-HQ) (Figure 2b)	After 7 days of incubation	Network like structure	~300 nm and ~12 nm in height
5 μM PF-HQ+10 μM Aβ1-40 (1 : 0.5 Aβ : PF-HQ) (Figure 2c)	After 11 days of incubation	Nanorod co-aggregates	~250 nm and ~5 nm in height

Table A2a.1. Summary of morphological events, 5 μM polymer (PF-HQ) and 0.5:1 polymer-protein aggregates over aging.

Aggregates	Time	Description	Dimensions
10 μM PF-HQ (Figure 2d)	After 7 days of incubation	extended fibrillar and Protofibrillar aggregates	~150 nm and ~7 nm in height (fibrils)
10 μM PF-HQ+10 μM Aβ1-40 (1 : 1 Aβ : PF-HQ) (Figure 2e)	After 7 days of incubation	Protofibrillar co-aggregates	~250 nm and ~7 nm in height
10 μM PF-HQ+10 μM Aβ1-40 (1 : 1 Aβ : PF-HQ) (Figure 2f)	After 11 days of incubation	Nanorod and large globular co-aggregates	~200 nm and ~5 nm in height (Nanorod) ~400nm and ~20 nm in height (globular aggregates)

Table A2a.2. Summary of morphological events, 10 μM polymer (PF-HQ) and 1:1 polymer-protein aggregates over aging.

Aggregates	Time	Description	Dimensions
20 μM PF-HQ (Figure 2g)	After 7 days of incubation	Well-ordered Protofibrillar aggregates	~200 nm and ~5 nm in height
20 μM PF-HQ+10 μM Aβ1-40 (1 : 2 Aβ : PF-HQ) (Figure 2h)	After 7 days of incubation	Spherical co-aggregates	~200 nm and ~12 nm in height
20 μM PF-HQ+10 μM Aβ1-40 (1 : 2 Aβ : PF-HQ) (Figure 2i)	After 11 days of incubation	Nanorod and large co-aggregates	~200 nm and ~5 nm in height (nanorod) ~600 nm and ~20 nm in height (large aggregates)

Table A2a.3. Summary of morphological events, 20 μM polymer (PF-HQ) and 2:1 polymer-protein aggregates over aging.

Chapter 2b

Multifunctional (3-in-1) Cancer Theranostics Applications of Hydroxyquinoline Appended Polyfluorene Nanoparticles

Chowdhury, S. R.; Mukherjee, S.; Das, S.; Patra, C. R.; Iyer, P. K. Multifunctional (3-in-1) cancer theranostics applications of hydroxyquinoline appended polyfluorene nanoparticles. *Chem. Sci.* **2017**, *8*, 7566-7575.

Abstract

The accumulation of fluorescent hydroxyquinoline affixed polyfluorene (PF-HQ) nanoparticles and their utility for multi-color bio-imaging and drug delivery for cancer treatment is reported. The formation of nanoparticles (PF-HQ) containing hydrophobic pockets via three-dimensional growth of polymeric backbone in higher water fraction (THF: H2O = 1:9) was observed. The nanoparticles showed incredible dual state optical and fluorescence properties, which were further explored in multi-color cell imaging in both cancer and normal cells. The cell viability assay in various normal cells confirmed the biocompatible nature of PF-HQ, which was further supported by *ex vivo* (Chick Chorioallantoic Membrane assay) model. This encouraged us to fabricate PF-HQ based new drug delivery systems (DDS: PF-HQ-DOX) upon conjugation with FDA approved anticancer drug doxorubicin (DOX) by filling the hydrophobic pockets of the polymer nanoparticles. The enhanced anticancer activity of DDS (PF-HQ-DOX) compared with free DOX was observed in mouse melanoma cancer cells (B16F10) and subcutaneous mouse (C57BL6/J) melanoma tumor model upon administration of PF-HQ-DOX. *Ex vivo* biodistribution studies using fluorescence quantification method demonstrated the enhanced accumulation of DOX in tumor tissues in the PF-HQ-DOX treated group compared to free drug signifying the drug delivery efficacy of the delivery system by passive targeting manner. Based on the above biological data (*in vitro* and in the pre-clinical model), this robust and versatile fluorescent hydroxyquinoline annexed polyfluorene nanoparticles (PF-HQ) could be effectively utilized for multifunctional biomedical applications (biocompatible, bio-imaging and drug delivery vehicle).

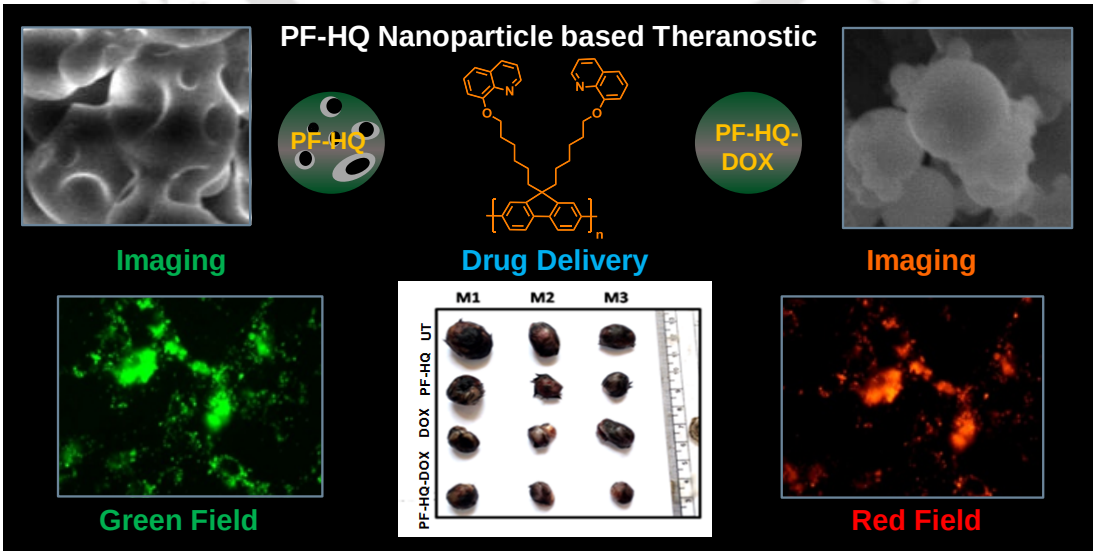

2b.1. Introduction

Dual state emitting (both solid and solution) organic luminogens are of greater practical applicability compared to aggregation caused quenching (ACQ) and aggregation induced emission (AIE) luminogens.[1] To date, most studies have inferred AIE molecules to overcome ACQ problems,[2-5] but both this phenomenon can be taken as an advantage and direct supramolecular networking toward biological applications. Common organic luminophores containing aromatic rings are generally considered to be rarely AIE active, owing to lack of aromatic rotors, since the restriction of intramolecular rotation plays an important role in the conversion of energy into photons and facilitates radiative decay. Fluorene is the most common organic luminophore and in past few decades structurally diverse derivatives have been developed and explored for a variety of antimicrobial and sensing applications. Moreover, polyfluorene based luminophores are used for organic lasing and light emitting devices[6-8] because of their thermal and chemical stability, color tunability, and high fluorescence efficiency.[9-12] Concentration, temperature and time dependent aggregation of polyfluorenes have been investigated in detail. Further, both the crystalline phases and the mesomorphic phases are distinguished by UV-Vis, photoluminescence (PL), grazing incidence X-ray diffraction, Raman spectra and microscopic analysis.[13-15] Numerous polyfluorene derivatives have been utilized as light up the sensory probe, detection, and quantification of biomolecules in the last two decades due to their high fluorescence brightness, good photostability and signal amplifying properties.[16,17] Polyfluorene can also be directed to form nanoparticles via reprecipitation method without adding any additive like hydrophobes or surfactants and these nano-scale materials are known to be used as biosensor, devices and staining agents.[18,19] Non-planarization of the conjugated backbone which was once taken as a huge disadvantage by the scientific community has now triggered towards controlled self-aggregation by choosing proper rotor over the side chain of the aromatic backbone. Unlike polyelectrolytes, they do not contain charges over the side chain and thus promise to work more selectively toward analytes since electrostatic interaction no longer plays any role. In the present study, self-aggregation behavior was taken as an advantage and synthetically guided the 3-dimensional polymerization towards the formation of nano objects in the water.

This chapter details aggregation behavior of polyfluorene homopolymer anchored with hydroxyquinoline appended on hydrophobic alkyl chain substituted at 9, 9’ of fluorene backbone. Hydroxyquinolines guide the main chain aggregation in water and are shown to form nanoparticles (PF-HQ). These ordered self-assemblies present a novel class of

luminescent compounds. Although known as a classical ACQ molecule, they behave uniquely with a marked increase in fluorescence intensity observed with increasing concentration accompanied by a red shift in the spectrum. Surprisingly, they do not follow classical AIE rules either. Hence, these materials show poor quantum yield in an aqueous medium. However, PF-HQ is utilized for the live cell imaging (*in vitro*) in various cell lines, due to its biocompatibility (*in vitro* and *ex vivo*) and excellent fluorescence property. PF-HQ also shows mild dose dependent cytotoxicity toward cancer cells, observed by cell viability assay. Further, a drug delivery system (DDS: PF-HQ-DOX) was designed using PF-HQ as a delivery vehicle and doxorubicin (DOX) as an anti-cancer drug. Administration of PF-HQ-DOX shows improved anti-cancer efficacy compare to free DOX in B16F10 cancer cells and subcutaneous mouse melanoma tumor models (*in vivo*) in a passive targeting manner through enhanced permeability and retention (EPR) effect. These robust fluorescent polymer nanoparticles (PF-HQ) could be beneficial for various bio-medical applications for cancer theranostics.

2b.2. Experimental Section

2b.2.1. Materials

Doxorubicin (DOX), Dulbecco's modified Eagle medium (DMEM), phosphate buffer saline (PBS), kanamycin, streptomycin, penicillin, ribonuclease (RNase), fetal bovine serum (FBS), HBSS buffer (Hank's balanced salt solution, MTT (3-(4,5-dimethylthiazol-2-yl)-2,5-diphenyltetrazolium bromide) and propidium iodide (PI) were procured from Sigma Aldrich Chemicals, USA and used without any purification. For Chick Chorioallantoic Membrane assay (CAM) assay, fertilized Chicken eggs were brought from Directorate of Poultry Research, Rajendra Nagar, Hyderabad.

Cell lines: COS-1: Cercopithecus aethiops monkey kidney fibroblast cell lines, NIH-3T3: mouse fibroblast cell lines, B16F10: mouse melanoma cell lines and A549: human lung cancer cell lines were bought from ATCC, USA.

Animals: Female C57BL6/J mice (8-9 weeks old and each weighing ~18-20 gm) were purchased from National Institute of Nutrition (NIN), Hyderabad. All mouse experiments were performed after approval by the animal ethical committee of CSIR IICT, Hyderabad (IAEC Approval No. IICT/19/2016).

Antibodies: Ki-67 antibody (primary antibody, host: rabbit, cat. number # PA5-19462) was purchased from Thermoscientific, USA. Phycoerythrin tagged goat anti-rabbit IgG (Cat. Number # SC-3739) was purchased from Santa Cruz Biotechnology, Inc. USA.

Stock Solution preparation: A stock solution of 2.7 μg/μL of PF-HQ was prepared in (H2O-THF at a volume ratio of 9:1) and used for all biological studies.

2b.2.2. Cell culture experiments

All cancer (A549 and B16F10) and normal (COS-1 and NIH-3T3) cell lines were cultured in DMEM complete media supplemented with FBS (10%), antibiotics (0.005% penicillin-streptomycin-kanamycin) and 5% L-glutamine, at 37oC in a humidified CO2 incubator. Samples were sterilized by UV irradiation for 10-15 minutes before any treatment.

2b.2.3. Cell imaging study using fluorescence microscopy

All normal and cancer cell lines (NIH-3T3, COS-1 and B16F10) were seeded in 24 well plates (2×104 cells/well) and cultured for 24 h in humidified cell incubator. Further, all the cell lines were incubated with PF-HQ (50 - 100 μg/mL) for 14 hours. All the treated cell lines were washed extensively with PBS and finally, the fluorescence images were captured by fluorescence microscope (Nikon Eclipse TE2000-E). The fluorescence emission in the green field (λem = 525 nm) was collected after excitation at λex = 420-495 nm and red emission (λem = 605 nm) was collected after excitation at λex = 510-560 nm with a 20X microscope objective. Similarly, the blue fluorescence emission (λem = 485 nm) was collected after excitation at λex = 380 nm at 20 X magnification.[20]

2b.2.4. *In vitro* cell viability assay using MTT reagent

All normal and cancer cell lines (NIH-3T3, COS-1, A549 and B16F10) (1×104 cells/well) were seeded in 96 well plates and cultured for 24 h. Cell viability assay of all normal and cancer cell lines was carried out using MTT reagents after 24 h incubation with PF-HQ at different doses (27-540 μg/mL) according to the published procedure.[21] Importantly, all the treated cell lines were washed extensively with PBS to remove any surface attached nanoparticles. Later, the washed cell lines were incubated with 100 μL of MTT solutions (0.5 mg/mL in PBS) and incubated for 4 h under dark conditions. Further, the MTT solution was replaced by freshly prepared DMSO: MeOH (1:1) to solubilize the formazan dye and the absorbance of each well was recorded at λ = 575 nm. The cell viability results were calculated as percent cell viability

using following equation: % cell viability = {[A570 (treated cells) - background] / [A570 (untreated cells) - background]} ×100.[21]

2b.2.5. Chick Chorioallantoic Membrane (CAM) Assay

The CAM assay is a typical assay for the analysis of *ex vivo* biocompatibility of any nanomaterials or drugs in chicken egg embryo. Fertilized chicken eggs were incubated (~60% humidity and 37 °C) for 4 days before the experimental study. During the experiment, a small window was created very carefully in the top of the egg shell. Sterile filter paper discs were soaked in 100 µg of PF-HQ solutions and were placed on egg yolks for about 4 h. Finally, bright field images of untreated and PF-HQ treated eggs were captured at a different time (0 h & 4 h) of treatment by a stereomicroscope (Leica).[22]

2b.2.6. Conjugation of doxorubicin with PF-HQ (PF-HQ-DOX)

In order to prepare the nanoconjugates (PF-HQ-DOX), DOX (100 µg of 1 mg/mL) was added in 1 mL of PF-HQ (1 mg/mL) in an Eppendorf under vortex condition for 45-60 minutes. The orange-brownish intense PF-HQ-DOX nanoconjugate solution was ultra-centrifuged (14,000 rpm at 14°C for 30 mins) using centrifugation (Labogene, Scanspeeo 1730R). The PF-HQ-DOX nanoconjugate pellet was collected (50 µL) and utilized for all the physicochemical characterizations, biological studies (*in vitro* and *in vivo*). The supernatant of PF-HQ-DOX nanoconjugate was used to determine the % attachment of DOX in PF-HQ-DOX pellets using spectrofluorimetry technique after making a standard curve. Similarly, PF-HQ was also centrifuged (14,000 rpm at 14°C for 30 minutes) and the pellet was used for all biological experiments in order to compare with PF-HQ-DOX.

2b.2.7. *In vitro* drug delivery of PF-HQ-DOX (MTT assay)

To determine the cancer cell killing ability of PF-HQ-DOX, murine melanoma cancer cell lines (B16F10) were incubated with (i) PF-HQ (5.25-42 µg/mL), (ii) DOX (0.625-5 µM) and (iii) PF-HQ-DOX (DOX concentration: 0.625-5 µM, PF-HQ dose: 5.25-42 µg/mL) for 24 hours. All the untreated and treated cell lines were washed extensively with PBS to remove surface attached nanoparticles/nanoconjugates. Finally, the cell viability of untreated and treated cell lines was determined using MTT assay according to our previously published protocols.[20]

2b.2.8. Cell cycle assay

B16F10 cancer cell lines (4 × 105 cells/well) were cultured in 6 well dishes in DMEM medium for 24 h. In order to check cellular DNA content of B16F10 cancer cells, B16F10 cancer cell lines were incubated with (i) PF-HQ (21 μg/mL), (ii) DOX (2.5 μM) and (iii) PF-HQ-DOX (concentration of DOX=2.5 μM and concentration of PF-HQ= 21 μg/mL) for 24 h. Untreated B16F10 cells were kept as control. After 24 h of treatment, all the treated or untreated cell lines were extensively washed with DPBS, trypsinized and cell cycle analysis was carried out using PI-RNase staining by a flow cytometer (FACS Canto II, Becton Dickinson, San Jose, CA, U.S.) according to our already published protocols.[23]

2b.2.9. Analysis of apoptosis by flow cytometry

B16F10 cancer cell lines (3 × 105 cells/well) were cultured in a 6-well dish in DMEM complete media for 24 h. To check the extent of apoptosis, B16F10 cancer cell lines were incubated with (i) PF-HQ (21 μg/mL), (ii) DOX (2.5 μM) and (iii) PF-HQ-DOX (concentration of DOX=2.5 μM and concentration of PF-HQ=21 μg/mL) for 24 h. Untreated B16F10 cells were kept as control. Finally, the treated and untreated cell lines were trypsinized and stained using FITC Annexin V Apoptosis Detection Kit (BD Biosciences) using FACScan flow cytometer, as per manufacturer's protocol.[20]

2b.2.10. Animal Experiment: *In vivo* tumor regression studies in murine melanoma model

Initially, *in vivo* melanoma tumor model was developed in female C57BL6/J mouse using a subcutaneous injection of B16F10 cells (~2.5×105 cells in 100 μL of sterile HBSS buffer) into the lower left abdomen of each mouse. When tumor volume reached ~50-75 mm3 (post 16-17 days of cancer cell implantation), the tumor bearing mice were erratically categorized into four distinct groups (n = 3) such as Gr-I: untreated control group, Gr-II: mice treated with PF-HQ (34 mg/kg/b.w.), Gr-III: mice treated with free DOX (2.5 mg/kg/b.w.) and Gr-IV: mice treated with PF-HQ-DOX (where, the dose of DOX and PF-HQ were 2.5 mg/kg/b.w. and 34 mg/kg/b.w., respectively). All the treatments were injected intraperitoneally (IP) on alternate days over a period of 10 days (total 5 doses for each group). The tumor volume was measured by using the formula ($0.5 \times ab^2$), where 'a' symbolizes the greatest dimension and 'b' corresponds to the shortest dimension of the tumors, measured by digital vernier caliper. Also, the volume, weight and optical images of the untreated and treated tumors were taken after the sacrifice of respective mice by CO_2 euthanasia upon completion of the animal

experiment. All the mice were regularly observed for weight loss/gain, allergy, mortality or morbidity during the tumor regression experiment.

2b.3. Results

In order to prepare PF-HQ, fluorene was first doubly alkylated by 1,6-dibromohexane utilizing known protocol,[24] taken after polymerization of this alkyl-brominated fluorene in nitrobenzene by means of oxidative polymerization procedure. Finally, the alkyl added bromines were substituted by 8-hydroxyquinolines in a post alteration system in DMF with potassium carbonate.[25] The coveted polymer PF-HQ was acquired through precipitation from methanol and the structure was affirmed by means of ^{1}H and ^{13}C NMR spectra in chloroform-d (Shown in Chapter 2a).

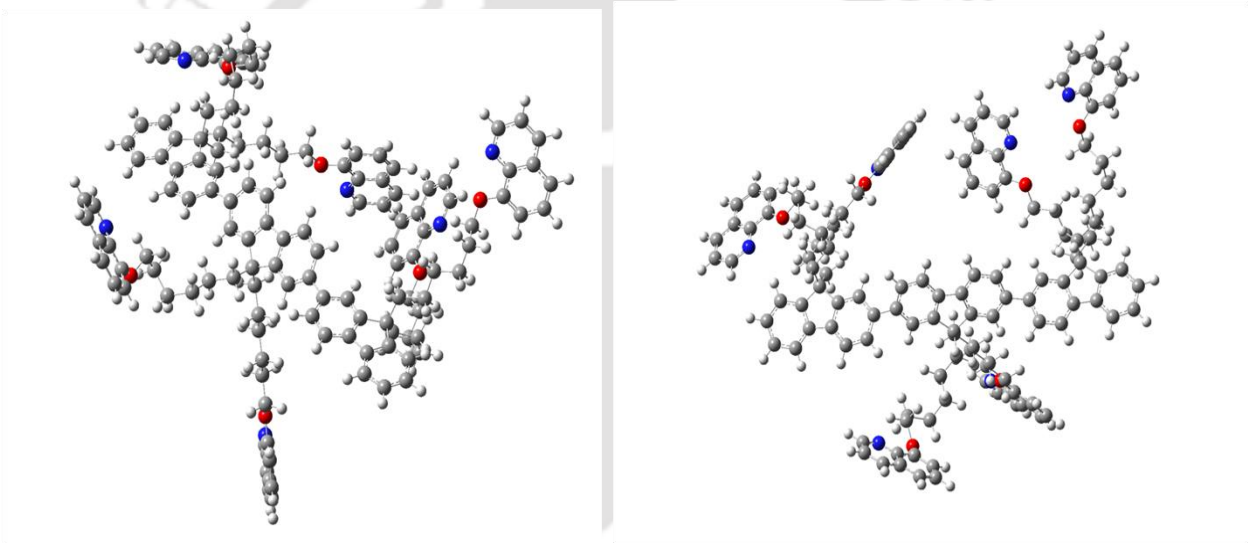

Scheme 2b.1: PF-HQ and the three-dimensional growth of fluorene backbone in water.

Herein, the aggregation behavior of this organic fluorophore, PF-HQ based on poly (9,9'–Bis–(6–bromohexyl)–fluorene) has been delineated in an aqueous environment. PF-HQ (excitation 362 nm) emits in the blue region (410-418 nm) in all common organic solvents (Fig. 2b.1.a). Although polyfluorenes behave as a common ACQ molecule, their emission abruptly changes in the aqueous environment. A new peak at 523 nm was observed unlike in the case of organic solvents. This unusual orange emission (huge 151 nm of stokes shift) was attributed to either intermolecular self-assembly behaviour or due to the J-type aggregation as evident from the UV-Visible spectrum of the polymer (Fig. 2b.1.b) and is known as dual state emission behaviour or aggregation caused red shifted emission, examples are which are very rare. Furthermore, this self-aggregation of PF-HQ was also confirmed by quantum yield

(Φ) calculation (Table A2b.1). Yet, in THF solvent the isolated polymers quantum yield was found to be 79.6% (at 412 nm). Moreover, no significant emission band appeared (at 523 nm) in THF, whereas, in the case of H2O medium (at 523 nm), the aggregated polymer quantum yield was calculated to be only 1.18%. The intensity of the emission peak at 412 nm decreases (Fig. A.2b.1a) with increasing concentration of polymer following ACQ rules but the peak at 523 nm increases with increasing concentration (Fig. A2b.1b-A2b.1d). This new peak at 523 nm is further red shifted in presence of buffer (PBS, HBSS) confirming aggregation among polymer chains (Fig. 2b.1.c-d). To confirm whether this aggregation is based on the planarity of the conjugated backbone, the trimer of PF-HQ polymer was used as a model to obtain energy optimized structures by DFT using B3LYP functional and 3-21G basis set in Gaussian 03 program (Scheme 2b.1).[26]

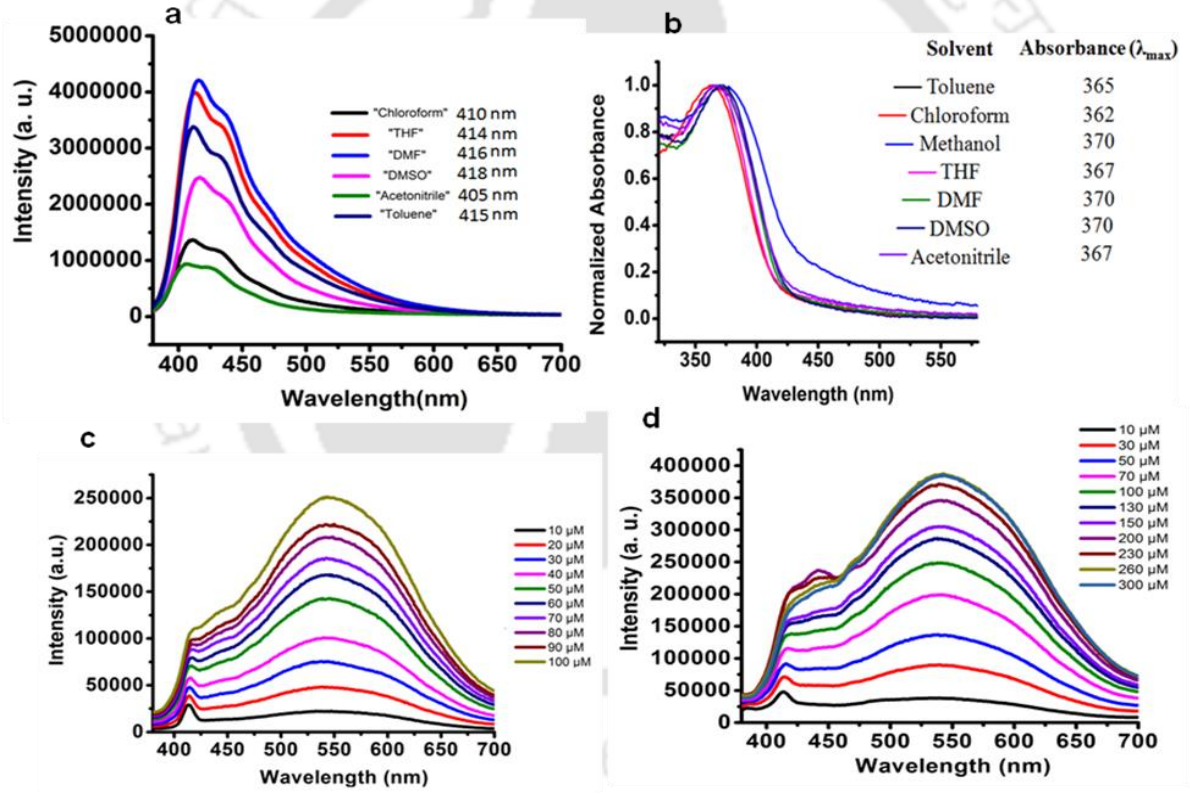

Figure 2b.1.a-d (a) Emission spectra of PF-HQ (20 μM) in common organic solvents. (b) UV-vis absorption of PF-HQ (20 μM) in different solvents (10 μM) emission spectra of PF-HQ in (c) PBS buffer (10 μM-100 μM, pH 7.4) and (d) HBSS buffer (10 μM-300 μM, pH 7.4).

Further to confirm aggregation, the lifetime of this dual-state emitting PF-HQ (10 μM) was measured in both THF (412 nm) and in aqueous media (520 nm) using pulse excitation at 375 nm. In THF solution, PF-HQ showed a biexponential decay with a lifetime [T1 = 0.622 ns

(91.9%) and T2 = 1.568 ns (8.8%)] whereas in water, a tri-exponential decay was observed having species with higher lifetime [T1 = 0.265 ns (13.52%), T2 = 1.1 ns (37.27%) and T3 = 3.638 (49.20%)] (Fig. A2b.2). Further to check the optical stability in an aqueous environment, the emission intensity of PF-HQ (30 μM) was observed for 24 h and the spectrum was recorded using fluorescence spectrophotometer using excitation wavelength at 362 nm at an interval of 2 h. To check the effect of pH, fluorescence spectra of PF-HQ (30 μM) was recorded at varying pH, from pH=2 to pH=13 to observe nearly linear stability over this wide pH range (Fig. A2b.3). PF-HQ showed significant optical stability, however, aggregation among polymer chains leads to maximum quenching of only 39% (Fig. A2b.4). Highly fluorescent well known organic luminophore (polyfluorene) shows excellent fluorescence stability due to aggregation even in an aqueous environment. Being totally hydrophobic, it can be made more selective toward analyte and the optical response due to 3D aggregation among polymer chains could be used for biological applications. The stable optical response of PF-HQ encouraged us to check its applicability toward cell imaging, biocompatibility and whether a theranostic contribution can be made utilizing this unique conjugated polymer system.

2b.3.1. Cell imaging of PF-HQ using fluorescence property

From the fluorescence spectroscopic data, it was confirmed that PF-HQ (already in THF: H2O = 1:9) showed bright red fluorescence property. However, the fluorescence emission peak was broad when PF-HQ was mixed with PBS or HBSS in buffer (Fig. 2b.1.c-d). Hence, PF-HQ had the ability to display multi-fluorescence properties. This multi-color imaging ability of PF-HQ was primarily confirmed by fluorescence microscopy. PF-HQ showed intense bright green and red fluorescence when coated on a glass plate (Fig. A2b.8†). To monitor the cellular bio-imaging property of PF-HQ, different normal (NIH-3T3, COS-1) and cancer (B16F10) cell lines were treated with PF-HQ (50-100 μg/mL) for 12-14 h. The fluorescence images were recorded after extensive washing with PBS under fluorescence microscopy. PF-HQ exhibited intense green (λex = 420–495 nm and λem= 525 nm) and red (λex = 510–560 nm and λem = 605 nm) fluorescence inside different normal and cancer cell lines (Fig. 2b.2.a-b, Fig. A2b.5). Interestingly, PF-HQ exhibited slight blue fluorescence (λem = 485 nm at λex = 380 nm) exclusively from B16F10 melanoma cancer cells, but not in normal cells (NIH-3T3 and COS-1). (Fig. 2b.2.a-b, Fig. A2b.9†).

2b.3.2. Cell viability (MTT) and Chick Chorioallantoic Membrane (CAM) assay

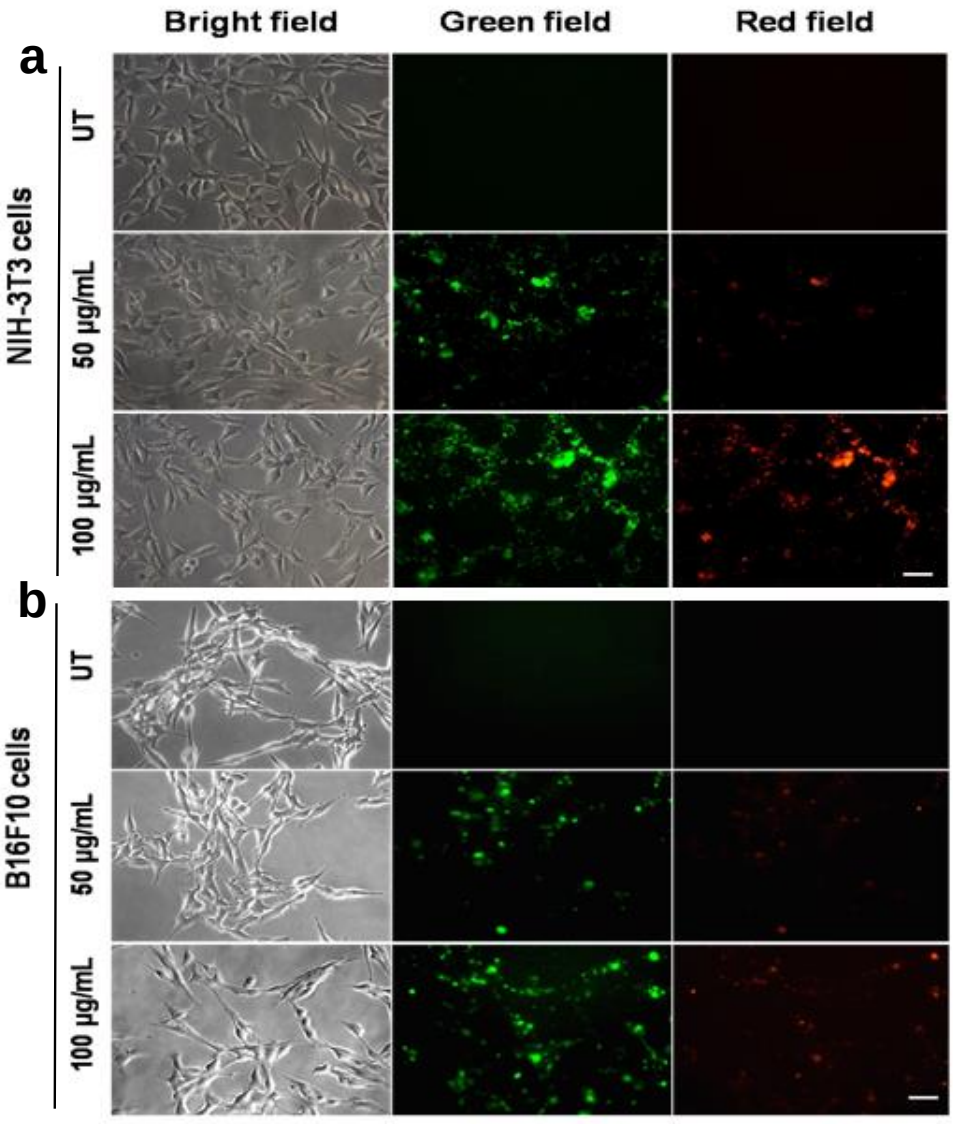

Figure 2b.2.a-b: Fluorescence images of normal (a: NIH-3T3) and cancer (b: B16F10) cells incubated with PF-HQ (50 and 100 µg/mL) for 14 h were taken using fluorescence microscopy at 20X magnification. Scale bar: 50 microns.

Cell viability assay, a critical assay for the determination of cytotoxicity was performed for various normal (NIH-3T3 & COS-1) and cancer cell lines (A549 & B16F10) after incubation of cells with PF-HQ (in THF:H2O = 10:90 solvent system) in a dose dependent manner (27-540 µg/mL) for 24 h (Fig. 2b.3.a-d). The results confirmed that PF-HQ did not exhibit any inhibition of normal cell (NIH-3T3 & COS-1) proliferation after 24 h incubation up to concentration 540 µg/mL, indicating the biocompatibility of the nanomaterials. However, PF-HQ showed slight dose dependent cytotoxicity (~10-30%) in different cancer cell lines (A549 & B16F10) indicating insignificant cancer cell killing ability of PF-HQ.

Chick chorioallantoic membrane (CAM) assay or egg yolk assay is a standard test to evaluate the *ex vivo* toxicity of nanomaterials or drugs. Additionally, to determine the *ex vivo* biocompatibility of PF-HQ, fertilized chicken eggs were incubated with PF-HQ (100 µg) for 4 h (Fig. 2b.3.f-f'). Untreated fertilized chicken eggs were kept as control (Fig. 2b.3.e-e'). CAM assay results demonstrated that PF-HQ (100 µg) did not show any inhibition of blood vessel formation of fertilized chicken egg till 4 h like an untreated egg (Fig. 2b.3.e-i). Several angiogenic parameters such as blood vessel length, size, and junction were quantified using Angioquant software and results showed no change in any of the three parameters (Fig. 2b.3.g-i). This indicates biocompatibility of PF-HQ at high doses (100 µg) in chicken egg model. The results obtained from cell viability and CAM assay together support the biocompatibility of PF-HQ, which could be helpful for several biomedical applications including drug delivery.

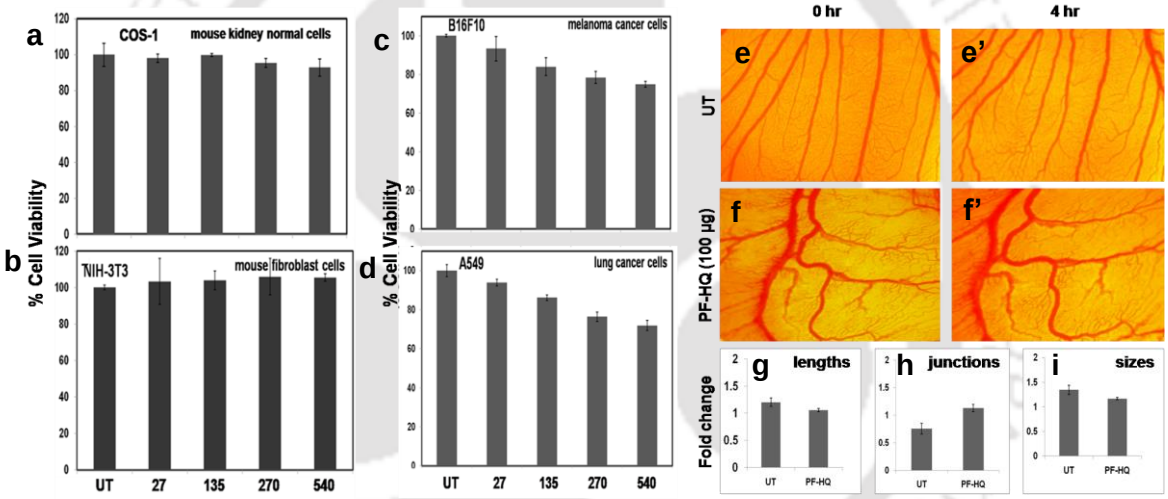

Figure 2b.3.a-i: (a-d) Cell viability assay of PF-HQ in different normal and cancer cells in a dose dependent manner for 24 h of treatment. The numerical value represents the dose of treatment in µg/mL, (e-f') *In vivo* CAM assay of embryos incubated with PF–HQ (100 µg) from 0 to 4 h. (g-i) Several angiogenic parameters such as blood vessel length, size, and junction were quantified and presented as histogram using the Angioquant software.

2b.3.3. Drug conjugation, % attachment, DLS, zeta potential and probable bonding

Biocompatible nature of PF-HQ encouraged us to design and develop a drug delivery system (DDS: PF-HQ-DOX) using PF-HQ as a delivery vehicle and DOX as an anti-cancer drug. Since PF-HQ showed anti-cancer properties, it has been hypothesized that PF-HQ-DOX could exhibit enhanced anti-cancer effects compared to pristine DOX when combined in synergy

with each other. A smart fabrication technique was developed to fill the hydrophobic pockets (Fig. 2b.4) of the polymer nanoparticles using doxorubicin conjugation to make the surface more hydrophilic that could be used as an anticancer agent as well as drug delivery system. The size, shape, and morphology of both PF-HQ and PF-HQ-DOX were monitored by FE-SEM. PF-HQ showed a fine spherical structure with the presence of spherical pores inside it (Fig. 2b.4.a-b). On the other hand, PF-HQ-DOX did not show pore like structure upon conjugation suggesting the filling of pores by drug molecules (Fig. 2b.4.c-d).

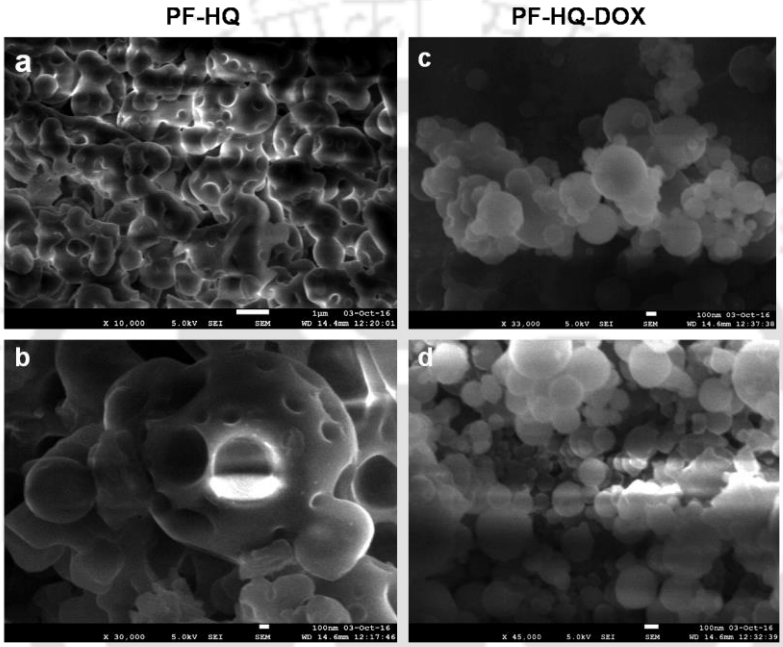

Figure 2b.4.a-d: (a-b) FE-SEM images of PF-HQ (in THF:H2O=1:9). (c-d) FE-SEM images of PF-HQ-DOX.

DLS results further demonstrated that the hydrodynamic diameter of PF-HQ-DOX (~223 nm) was greater than the hydrodynamic diameter of PF-HQ (~197 nm) (Fig. A2b.6) indicating possible inclusion/attachment of DOX with PF-HQ. Discrepancies in sizes in FE-SEM images and DLS particle size are common and are attributed to the drying and localization effects when the polymer chains tend to aggregate, giving rise to a bigger size in scanning microscope compared to DLS measurements. Further, the negative zeta potential (ξ) of PF-HQ-DOX (-25.1 ± 6.4 mV) decreased than the ξ of PF-HQ (-25.4 ± 5.6 mV) after DOX attachment. The decrease in the negative zeta potential further supported the possible attachment of positively charged DOX (+2.7 ± 0.8 mV) with negatively charged PF-HQ by weak electrostatic attraction.[27] Furthermore, to check the possible nature of bonding between PF-HQ and DOX, FTIR analysis was carried out (Fig. A2b.7). The IR peak at 1614 cm^{-1} (assigned as –NH stretching from a secondary amine of PF-HQ) was shifted to 1598 cm-1 upon conjugation with

DOX (Fig. A2b.8). This indicated the possible hydrogen bonding between DOX (–OH and –NH2) with the free lone pair of the secondary amine of PF-HQ (Fig. A2b.12†).[28] Hence, DLS and FTIR studies revealed that the bonding between DOX and PF-HQ was through weak electrostatic and hydrogen bonding interaction. Additionally, the attachment of DOX (in PF-HQ-DOX pellet) with PF-HQ was calculated by using the standard curve of DOX by fluorescence spectrometer. It was determined that around ~60% of DOX was attached to the PF-HQ nanoparticles in its conjugate form (Fig. A2b.9 and A2b.10).

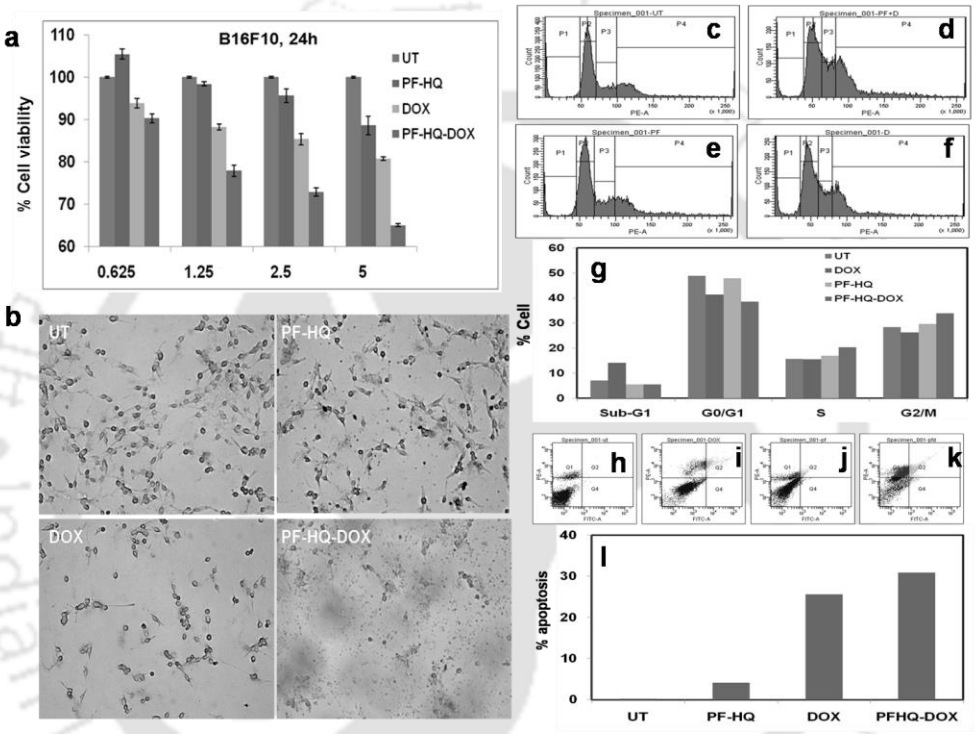

Figure 2b.5.a-l: (a) *In vitro* cell viability assay of B16F10 cancer cells incubated with PF-HQ, DOX and PF-HQ-DOX in a dose dependent manner for 24 h of treatment, the numerical value in abscissa represents the concentration (μM) of DOX treatment. (b) representative bright field images of B16F10 cells incubated with PF-HQ, DOX (2.5 μM) and PF-HQ-DOX (2.5 μM w.r.t DOX) for 24 h were taken using inverted microscope at 10X magnification, scale bar= 50 microns (c-g) Total DNA content was analyzed using PI/RNase by FACS in B16F10 cells treated with (c) untreated cells were kept as control, cells treated with (d) free DOX (2.5 μM), (e) PF-HQ or (f) PF-HQ-DOX (2.5 μM w.r.t DOX) for 24 hours;. (g) quantification of cell cycle analysis; (h-l) analysis of apoptosis by flow cytometry using Annexin V-FITC assay in B16F10 cells treated with (i) DOX (2.5 μM), (j) PF-HQ, (k) PF-HQ-DOX (2.5 μM w.r.t DOX), (h) untreated control cells were kept as control; (l) quantification data of apoptosis.

2b.3.4. *In vitro* cytotoxicity of PF-HQ-DOX (MTT assay)

In order to test the *in vitro* cytotoxicity nature of the nanoconjugates (PF-HQ-DOX), melanoma cancer (B16F10) cell lines were incubated with (i) PF-HQ, (ii) DOX and (iii) PF-

HQ-DOX in a dose dependent manner (where, concentration of DOX = 0.625, 1.25, 2.5 & 5 μM and concentration of PF-HQ = 5.25, 10.5, 21, 42 μg/mL, respectively) for 24 h (Fig. 2b.5.a). Cell viability results displayed the improved inhibition of cancer cell proliferation after incubation with PF-HQ-DOX compared to free DOX in a dose dependent manner. This was further supported by the bright field images of B16F10 cell lines treated with (i) PF-HQ (21 μg/mL), (ii) DOX (2.5 μM) and (iii) PF-HQ-DOX (2.5 μM w.r.t. DOX, 21 μg/mL of PF-HQ) (Fig. 2b.5.b). The DDS exhibited around 10-15 % more melanoma cancer cell killing compared to free DOX under similar experimental conditions. This enhanced inhibition of aggressive murine melanoma cancer cell proliferation of PF-HQ-DOX encouraged us to perform further mechanistic studies along with tumor regression studies (*in vivo*) in C57BL6/J mouse melanoma tumor model.

2b.3.5. Cell cycle analysis and analysis of apoptosis using FACS

According to published reports, enhanced cytotoxicity of PF-HQ-DOX in cancer cell lines can cause arrest in any of the four cell cycle phase, namely sub-G1, G0/G1, S, and G2/M.[29] Consequently, the DNA content of untreated B16F10 cell lines and cells incubated with (i) PF-HQ, (ii) DOX and (iii) PF-HQ-DOX was quantitatively estimated using FACS by PI-RNase staining (Fig. 2b.5.c-g). The FACS result showed the higher cell population (~7 %) in sub-G1 phase of B16F10 cells incubated with free DOX (2.5 μM) compared to untreated cells that indicate programmed cell death (Fig. 2b.5.c-g).[30] Concurrently, the cell population increased significantly (~5.5 %) in the G2/M phase in B16F10 cell lines incubated with PF-HQ-DOX (2.5 μM) compared to the untreated B16F10 cells and cells incubated with naked DOX (2.5 μM) indicating G2/M arrest (Fig. 2b.5.c-g).[31] Further, cellular arrest in G2/M upon treatment with PF-HQ-DOX could trigger programmed cell death or apoptosis.[32] The cellular arrest caused by nanoconjugates (PF-HQ) might impact the apoptosis process attributable to the cytotoxic character of the DDS.[33] Further, to test the degree of apoptosis, the apoptosis assay was performed by FITC Annexin-V staining in B16F10 cells treated with (i) PF-HQ, (ii) DOX and (iii) PF-HQ-DOX for 24 h. The apoptosis results displayed that B16F10 cells incubated with PF-HQ-DOX showed ~31% apoptosis in the late apoptotic phase. The extent of apoptosis in B16F10 cancer cells incubated with PF-HQ-DOX was reasonably higher than that of pristine DOX (~25.6%) and PF-HQ (4.1%) (Fig. 2b.5.h-l). However, the untreated control cells did not show any apoptosis (~0.2 %). Altogether, the FACS and apoptosis results demonstrated the potential applicability of the DDS for the treatment of melanoma cancer.

2b.3.6. Effect of PF-HQ-DOX in tumor regression, biodistribution, and bio-imaging studies

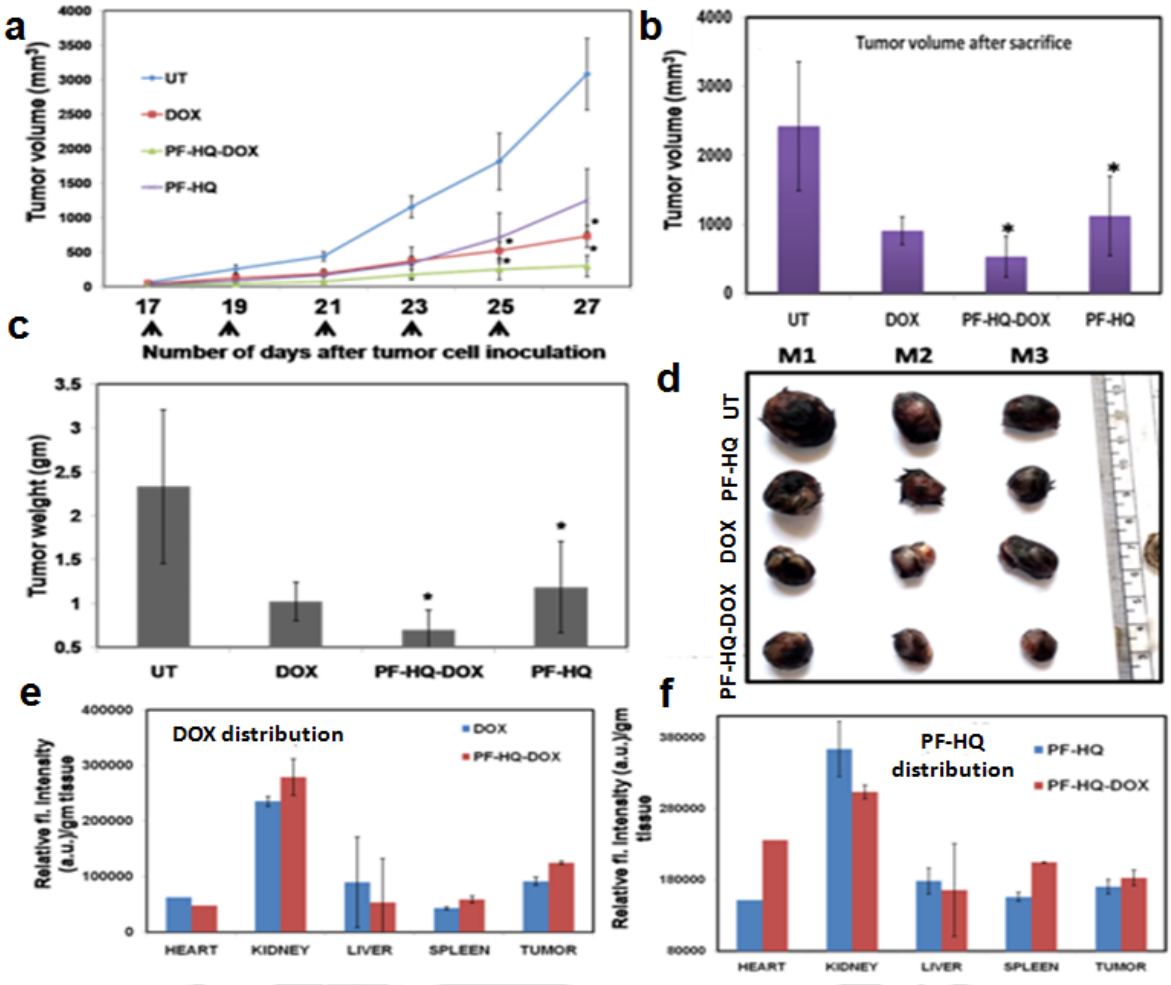

Figure 2b.6.a-f: (a-f) *In vivo* allograft mice (C57BL6/J) melanoma tumor regression model. (a) Tumor volume data after subcutaneous inoculation of B16F10 cancer cells into C57BL6/J mice followed by alternate intraperitoneal treatment of either PF-HQ (34 mg/kg/b.w.), DOX (2.5 mg/kg/b.w.) and PF-HQ-DOX (where, the dose of DOX and PF-HQ were 2.5 mg/kg/b.w. and 34 mg/kg/b.w.; respectively) for total period of 10 days (n=3) [* represents $p<0.05$]. (b) Tumor volume and (c) tumor weight data of each group after the sacrifice of all mice; (d) optical images of the tumors of untreated and other treated groups. (e-f) bio-distribution study of (e) DOX and (f) PF-HQ (represented as relative fluorescence intensity per gm of tissues) in different organs and tumor using spectrofluorimeter.

Malignant melanoma is the sixth most recurrent cancer in the U.S., with estimated deaths of ~48,000 worldwide every year.[34,35] Poor prognosis and advanced rate of malignancy increase the rate of mortality.[34,35] B16F10 is an aggressive melanoma cancer cell line of mouse origin and has the potential of rapid tumor growth, metastasis, evasion, and malignancy. Our *in vitro*

cell viability data showed significant inhibition of melanoma cancer cell proliferation using PF-HQ-DOX that encouraged us to perform the tumor regression studies (*in vivo*) in subcutaneous mouse murine melanoma model (C57BL6/J).

Highly aggressive melanoma cancer cells were injected into the flank region of each mice and tumor was developed within 15-16 days of cell implantation. The tumor bearing mice were treated intraperitoneally (IP) on alternative day with (i) PF-HQ (34 mg/kg/b.w.), (ii) DOX (2.5 mg/kg/b.w.) and (iii) PF-HQ-DOX (Dox=2.5 mg/kg/b.w. and PF-HQ=34 mg/kg/b.w.) intraperitoneally (IP). Untreated tumor bearing mice were kept as a control group (n=3). The tumor regression results revealed that PF-HQ-DOX showed a significant reduction in melanoma tumor compared to pristine DOX and PF-HQ, as confirmed by tumor volume and tumor weight data (before sacrifice and after the sacrifice of the mice) (Fig. 2b.6.a-c). The optical images of the tumors isolated after the sacrifice of each group further proved that PF-HQ-DOX has maximum tumor regression ability compared to other experimental groups (Fig. 2b.6.d). Interestingly, unlike *in vitro* data, PF-HQ itself showed significant tumor regression ability probably due to high dose (34 mg/kg/b.w.). Additionally, the bio-distribution of DOX in mice treated with DOX and PF-HQ-DOX was determined by spectrofluorimetry (Fig. 2b.6.e). Biodistribution of DOX demonstrated the maximum accumulation of DOX in kidney and tumor tissue as quantified by the red fluorescence intensity of DOX using spectrofluorimetry. Moreover, the quantity of DOX that got through the tumor site was higher in PF-HQ-DOX treated mice compared to the free DOX treated mice. This indicates the possible passive targeting ability of PF-HQ-DOX due to EPR effect.[36] Thus, tumor specific uptake of DOX could help to accomplish the improved therapeutic target using PF-HQ as a delivery vehicle. Notably, cardiotoxicity of DOX is well reported.[37] Hence, the lower amount of DOX reaching the mice heart in the treatment group of PF-HQ-DOX would be very vital to avoid or reduce the unwanted cardio toxicity. Interestingly, PF-HQ exhibited intense bright green fluorescence inside live cells (*in vitro*), observed by fluorescence microscopy (Fig. 2b.2.a-b). Hence, *ex vivo* uptake studies were performed in PF-HQ and PF-HQ-DOX in the respective treatment groups by spectrofluorimetry studies using their green fluorescence in tumors and other organs (Fig. 2b.6.f). The quantification data showed the distribution of PF-HQ and PF-HQ-DOX in tumor and other organs (majorly observed in kidney). Thus, green fluorescence property of PF-HQ could be utilized to check the bio-distribution of the drug conjugates in *ex vivo* conditions.

2b.3.7. Immunohistochemistry and TUNEL assay

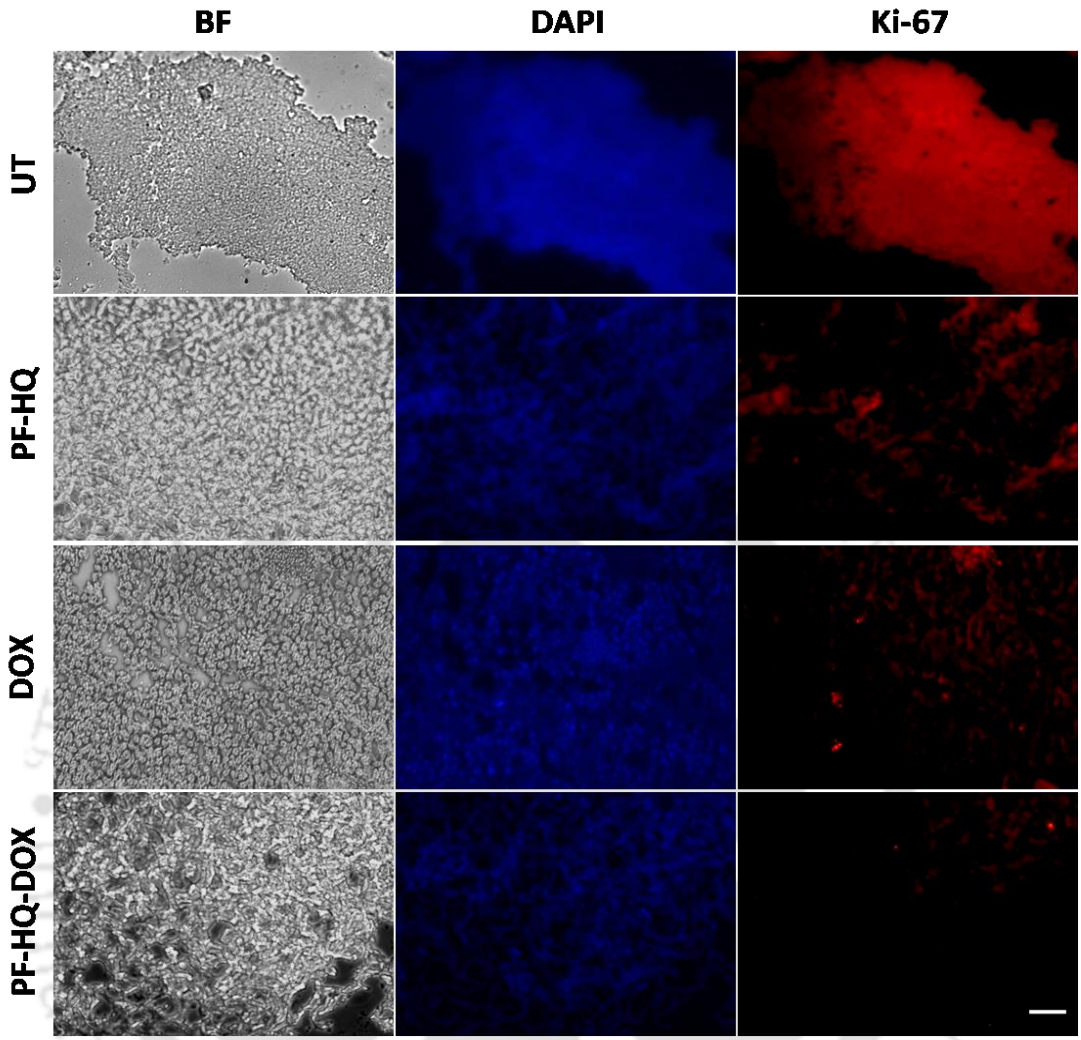

Figure 2b.7: Immunohistochemistry (Ki-67) analysis of untreated tumor tissue and tumor bearing mice treated with PF-HQ, DOX, and PF-HQ-DOX. All the H&E images were taken at 20X magnification. Scale bar: 50 microns.

Numerous studies demonstrated the role of cancer proliferation marker like Ki-67 in the impediment of tumor growth. Ki-67 is a nuclear protein which is subsequently linked with ribosomal RNA transcription process.[38] Figure 2b.7 demonstrated the immunohistochemistry images of untreated and treated (DOX, PF-HQ, and PF-HQ-DOX) mice tumor sections stained for Ki-67 markers. Mice tumor sections of PF-HQ-DOX treated group showed less red fluorescence intensity in comparison to untreated and other treated groups that indicated a decrease in the Ki-67 expression (Fig. 2b.7). This inevitably supported the improved tumor regression of PF-HQ-DOX compared to free DOX. Additionally, it is well-known that Ki-67 silencing inhibits the tumor growth and further instigates apoptosis in tumor regions. In order to check the extent of apoptosis in tumor lesions, the TUNEL assay was performed.[39]

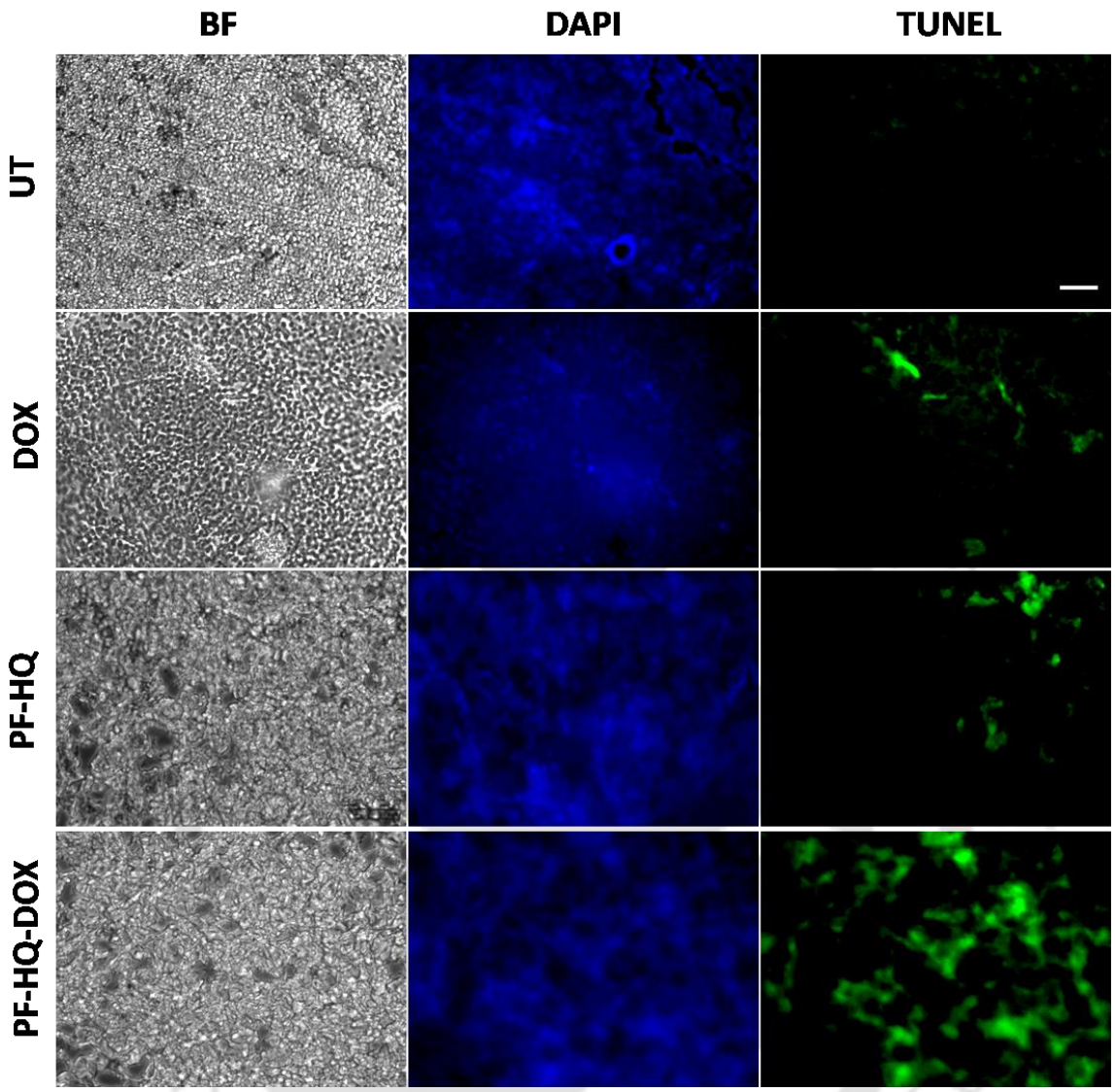

Figure 2b.8: TUNEL assay of untreated and treated (free DOX, PF-HQ, and PF-HQ-DOX) tumor tissue. The first column represented bright field; the second column represented the DAPI staining (visible by blue fluorescence) and the third column represented the apoptotic cells in tumor tissues (visible by green fluorescence). Images were captured at 20 X magnification. Scale bar: 50 microns.

Figure 2b.8 showed the TUNEL images of untreated and treated (DOX, PF-HQ, and PF-HQ-DOX) tumor lesions. Green fluorescence (due to FITC) indicated the apoptotic tumor cells while the blue fluorescence (due to DAPI staining) indicated the cell nucleus. From TUNEL assay images, it was evident that PF-HQ-DOX treated tumor tissue sections displayed a higher degree of apoptosis (higher green fluorescence) compared to untreated control and treated groups. Considering the Ki-67 and TUNEL assay results it was concluded that PF-HQ-DOX

demonstrated improved tumor regression property compared to naked DOX and PF-HQ in mouse melanoma tumor model.

2b.4. Discussion

Delivery of an anti-cancer drug to the target tumor site poses a pivotal challenge as the free anti-cancer drugs lack target specificity, demonstrate poor bio-availability, fast excretion, inevitable side effects and drug resistance. Additionally, the development of single Theranostics systems (therapeutic as well as diagnostics) is increasingly becoming a challenging task to overcome complexity, high cost, and to acquire multifunctional approach. Metal nanoparticles based nanotheranostics agent often have serious challenges regarding bio-degradability, toxicity, and clearance from the body.[40,41] On the other hand, polymer based nanoparticles mostly overcome these challenges and can successfully deliver anti-cancer drugs to the target disease site without any side effects.[42,43] In recent past, ACQ and AIE based nanoparticles have gained immense attention as multifunctional nanotheranostics agent due to interesting fluorescence property, biocompatibility, high drug loading ability, cancer selective toxicity and biodegradability.[20,44,45] Due to these several exciting properties, these nanoparticles may open a new area in the development of novel multifunctional nanotheranostics agent. In the present study, fluorescent hydroxyquinoline appended polyfluorene nanoparticles were shown to demonstrate various multifunctional (3-in-1 applications) cancer theranostics applications (biocompatible, bio-imaging and drug delivery vehicle). However, pristine PF-HQ demonstrated insignificant cancer cell killing ability. Notably, the nontoxicity of the THF: H2O solvent system (1:9) in cancer and normal cell lines (B16F10 and CHO) was reported previously.[20] Hence, cancer cell killing ability of PF-HQ solely depended on the anticancer effect of PF-HQ itself. Moreover, the biocompatible PF-HQ was utilized to prepare nano-drug delivery systems (PF-HQ-DOX) with high loading efficacy due to pore like structures. PF-HQ-DOX was further utilized for successful delivery of drug to melanoma cancer cells (*in vitro*) and in mouse melanoma tumor models (*in vivo*) with high efficiency and improved anticancer effects. A smart fabrication technique was developed to fill the hydrophobic pockets with high drug loading efficacy (Fig. 2b.4.a-d) of the conjugate polymer nanoparticles using DOX to make the surface more hydrophilic. PF-HQ was successfully explored as an anticancer agent as well as drug delivery system. Moreover, the intense green and red fluorescence property of PF-HQ was used for the cell, tissue and organ bio-imaging purposes. The fluorescence quenching and red-shift of the emission upon aggregation are well known in polyfluorene as due to the presence of a small concentration of

fluorenone defects[46] during synthesis but this small presence did not interfere with imaging and/or drug delivery. Polyfluorene nanoparticle (PF-HQ) showed no peak at 1722 cm^{-1} unlike fluorenone in FT-IR spectra (Fig. A2b.11). Further, organic polymer based PF-HQ and PF-HQ-DOX could be biodegradable and excreted to the renal or hepatobiliary route. Our results altogether show the multifunctional applications of PF-HQ and PF-HQ-DOX in cancer theranostics. Nevertheless, several other critical issues need to be addressed before applying this nano-drug delivery system in clinical models. These include (i) active targeting of nano-drug delivery systems in tumor sites, (ii) long term toxicity and immunogenicity studies, (iii) biodegradability, metabolic fate, and unchallenging excretion, (iv) proper dosage regimen selection and (v) detailed pharmacokinetics and pharmacodynamics (PK/PD) studies.

2b.5. Conclusions

In conclusion, PF-HQ displayed dual state emission properties with unusually high >150nm red shift in an aqueous medium which facilitated bio-imaging inside live cells to acquire bright green and red fluorescence. More importantly, PF-HQ showed high biocompatibility in normal cell lines (*in vitro*) and in CAM assay (*ex vivo*). PF-HQ was further utilized to design and fabricate a drug delivery system (PF-HQ-DOX) that successfully inhibited the cancer cell proliferation and tumor growth in mice melanoma tumor model. Mechanistic studies demonstrated inhibition of Ki-67 and subsequent apoptosis in PF-HQ-DOX treated the tumor. Altogether, the *in vitro* and *in vivo* studies revealed that fluorescent hydroxyquinoline appended polyfluorene nanoparticles (PF-HQ) is highly probable candidates for various bio-medical applications.

References

(1) Chen, G.; Li, W.; Zhou, T.; Peng, Q.; Zhai, D.; Li, H.; Yuan, W. Z.; Zhang, Y.; Tang, B. Z. *Adv. Mater.* **2015**, *27*, 4496–4501.

(2) Wakamiya, A.; Mori, K.; Yamaguchi, S. *Angew. Chem. Int. Ed.* **2007**, *46*, 4273–4276.

(3) Zhao, C-H.; Wakamiya, A.; Inukai, Y.; Yamaguchi, S. *J. Am. Chem. Soc.* **2006**, *128*, 15934–15935.

(4) Xie, Z.; Yang, B.; Li, F.; Cheng, G.; Liu, L.; Yang, G.; Xu, H.; Ye, L.; Hanif, M.; Liu, S.; Ma, D.; Ma, Y. *J. Am. Chem. Soc.* **2005**, *127*, 14152–14153.

(5) Kaiser, T. E.; Wang, H.; Stepanenko, V.; Würthner, F. *Angew. Chem. Int. Ed.* **2007**, *46*, 5541–5544.

(6) Gopikrishna, P.; Das, D.; Iyer, P. K. *J. Mater. Chem. C* **2015**, *3*, 9318–9326.

(7) Ma, W.; Iyer, P. K.; Gong, X.; Liu, B.; Moses, D.; Bazan, G. C.; Heeger, A. J. *Adv. Mater.* **2005**, *17*, 274–277.

(8) Malik, A. H.; Hussain, S.; Tanwar, A. S.; Layek, S.; Trivedi, V.; Iyer, P. K. *Analyst* **2015**, *140*, 4388–4392.

(9) Becker, S.; Ego, C.; Grimsdale, A. C.; List, E. J. W.; Marsitzky, D.; Pogantsch, A.; Setayesh, S.; Leising, G.; Müllen, K. *Synth. Met.* **2001**, *125*, 73–80.

(10) Hung, M.-C.; Liao, J.-L.; Chen, S.-A.; Chen, S.-H.; Su, A-C. *J. Am. Chem. Soc.* **2005**, *127*, 14576–14577.

(11) Morgado, J.; Alcacer, L.; Charas, A. *Appl. Phys Lett.* **2007**, *90*, 201110–1.

(12) Lu, H.-H.; Liu, C.-Y.; Chang, C.-H.; Chen, S.-A. *Adv. Mater.* **2007**, *19*, 2574–2579.

(13) Lakhwani, G.; Meskers, S. C. J. *Macromolecules,* **2009**, *42*, 4220–4223.

(14) Bright, D. W.; Dias, F. B.; Galbrecht, F.; Scherf, U.; Monkman, A. P. *Adv. Funct. Mater.* 2009, 19, 67–73.

(15) Liu, B.; Lin, J.; Liu, F.; Yu, M.; Zhang, X.; Xia, R.; Yang, T.; Fang, Y.; Xie, L.; Huang, W. *ACS Appl. Mater. Interfaces 8*, 21648–21655.

(16) Dwivedi, A. K.; Saikia, G.; Iyer, P. K. *J. Mater. Chem.* **2011**, *21*, 2502–2507.

(17) Hussain, S.; Malik, A. H.; Afroz, M. A.; Iyer, P. K. *Chem. Commun.* **2015**, *51*, 7207–7210.

(18) Tuncel, D.; Demir, H. V. *Nanoscale* **2010**, *2*, 484–494.

(19) Feng, L.; Zhu, C.; Yuan, H.; Liu, L.; Lv, F.; Wang, S. *Chem. Soc. Rev.* **2013**, *42*, 6620-6633.

(20) Muthuraj, B.; Mukherjee, S.; Patra, C. R.; Iyer, P. K. *ACS Appl Mater. Interfaces* **2016**, *8*, 32220–32229.

(21) Mukherjee, S.; Rao, B. R.; Sreedhar, B.; Paik, P.; Patra, C. R. *Chem. Commun.* **2015**, *51*, 7325–7328.

(22) Mukherjee, S.; Sriram, P.; Barui, A. K.; Nethi, S. K.; Veeriah, V.; Chatterjee, S.; Suresh, K. I.; Patra, C. R. *Adv Healthc Mater*. **2015**, *4*, 1722–1732.

(23) Mukherjee, S.; Dasari, M.; Priyamvada, S.; Kotcherlakota, R.; Bollu, V. S.; Patra, C. R. *J. Mater. Chem. B* **2015**, *3*, 3820–3830.

(24) Saikia, G.; Iyer, P. K. *J. Org. Chem*. **2010**, *75*, 2714-2717.

(25) Chowdhury, S. R.; Agarwal, M.; Meher, N.; Muthuraj, B.; Iyer, P. K. *ACS Appl. Mater. Interfaces* **2016**, *8*, 13309-13319.

(26) Chidthong, R.; Hannongbua, S. *J. Comput. Chem*. **2010**, *31*, 1450.

(27) Mukherjee, S.; Sau, S.; Madhuri, D.; Bollu, V. S.; Madhusudana, K.; Sreedhar, B.; Banerjee, R.; Patra, C. R. *J. Biomed. Nanotechnol.* **2016**, *12*, 165-181.

(28) Song, Y. J.; Jang, K. H.; Kim, S. B. *Biochemistry* **2009**, *44*, 1133–1138.

(29) Alabsi, A. M.; Ali, R., Ali, A. M.; Al-Dubai, S. A.; Harun, H.; Abu Kasim, N. H.; Alsalahi, A. J. *Cancer Prev*. **2012**, *13*, 5131–5136.

(30) Beach, J. A.; Nary, L. J.; Hirakawa, Y.; Holland, E.; Hovanessian, R.; Medh, R. D. *J. Mol. Signal*. **2011**, *6*, 1–13.

(31) Siu, W. Y.; Yam, C. H.; Poon, R. Y. C. *FEBS Lett*. **1999**, *461*, 299–305.

(32) Satapathy, S. R.; Mohapatra, P.; Preet, R.; Das, D.; Sarkar, B.; Choudhuri, T.; Wyatt, M. D.; Kundu, C. N. *Nanomedicine* **2013**, *8*, 1307–1322.

(33) Ferreira, C. G.; Tolis, C.; Span, S. W.; Peters, G. J.; Lopik, T. V.; Kummer, A. J.; Pinedo, H. M.; Giaccone, G. *Clin. Cancer Res*. **2000**, *6*, 203–212.

(34) Skin cancer mortality statistics, Cancer Research UK, 2016, http://www.cancerresearchuk.org/health-professional/cancer-statistics/statistics-by-cancer-type/skin-cancer/mortality.

(35) American Cancer Society. Cancer Facts & Figures, 2016 Atlanta: American Cancer Society.

(36) Kobayashi, H.; Watanabe, R.; Choyke, P. L. *Theranostics* **2013**, *4*, 81-89.

(37) Volkova, M.; Russell, R. *Curr Cardiol Rev*. **2011**, *7*, 214–220.

(38) Curran, M. A.; Montalvo, W.; Yagita, H.; Allison, J. P. *Proc Natl Acad Sci. U.S.A.* **2010**, *107*, 4275–80.

(39) Sau, S.; Agarwalla, P.; Mukherjee, S.; Bag, I.; Sreedhar, B.; Bhadra, M. P.; Patra, C. R.; Banerjee, R. *Nanoscale* **2014**, *6*, 6745–6754.

(40) Braakhuis, H. M.; Gosens, I.; Krystek, P.; Boere, J. A.; Cassee, F.; Fokkens, P. H.; Post, J. A.; van Loveren, H.; Park, M. V. *Part Fibre Toxicol.* **2014**, *11*, 49.

(41) Schrand, A. M.; Rahman, M. F.; Hussain, S. M.; Schlager, J. J.; Smith, J. D. A.; Syed, A. F. *Wiley Interdiscip. Rev. Nanomed. Nanobiotechnol.* **2010**, *2*, 544-568.

(42) Masood, F. *Mater. Sci. Eng. C. Mater. Biol. Appl.* **2016**, *60*, 569-578.

(43) Kumari, A.; Yadav, S. K.; Yadav, S. C. *Colloids Surf B Biointerfaces* **2010**, *75*, 1-18.

(44) Wan, Q.; Zeng, G.; He, Z.; Mao, L.; Liu, M.; Huang, H.; Deng, F.; Zhang, X.; Wei, Y. *J Mater. Chem. B* **2016**, *4*, 5692-5699.

(45) Wang, K.; Fan, X.; Zhao, L.; Zhang, X.; Zhang, X.; Li, Z.; Yuan, Q.; Zhang, Q.; Huang, Z.; Xie, W.; Zhang, Y. *Small* **2016**, *12*, 6568-6575.

(46) Gong, X.; Iyer, P. K.; Moses, D.; Bazan, G. C.; Heeger, A. J.; Xiao, S. S. *Adv. Funct. Mater.* **2003**, *13*, 325-330.

Appendix

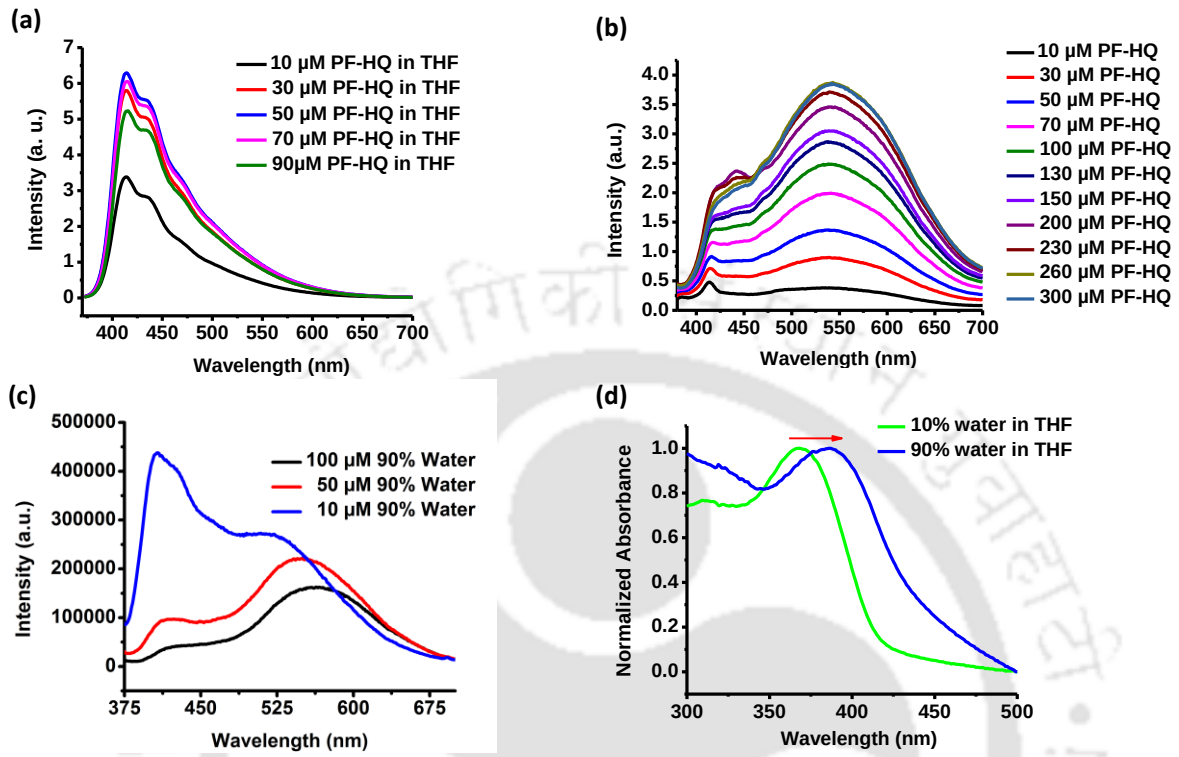

Figure A2b.1. Fluorescence profile of (a) PF-HQ (10 μM-90 μM) in THF showing decrease in emission intensity with increasing concentration (b) PF-HQ (10 μM-300 μM) in PBS buffer (pH 7.4) showing increase in emission intensity with increasing concentration (c) PF-HQ (10 μM-100 μM) in 90% water in THF and normalized absorbance of (d) 10 μM PF-HQ in 10 % water and in 90 % water showing significant red shift in the UV-vis spectra.

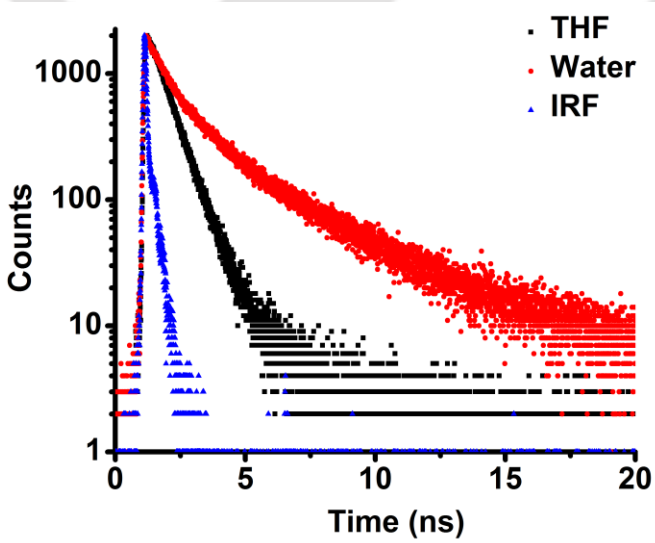

Figure A2b.2. Time resolved fluorescence decay profile of PF-HQ in THF (black) and in water (red).

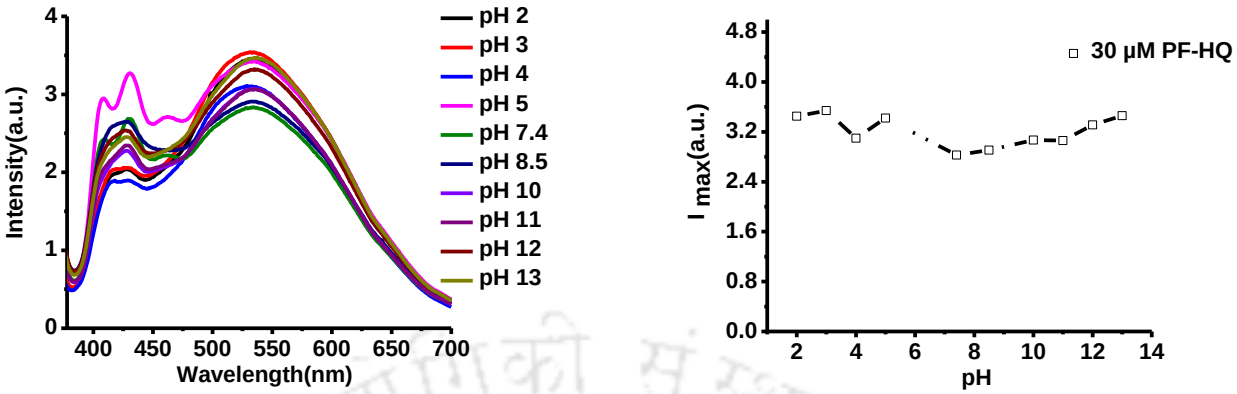

Figure A2b.3. Effect of pH was monitored for PF-HQ using fluorescence spectroscopy.

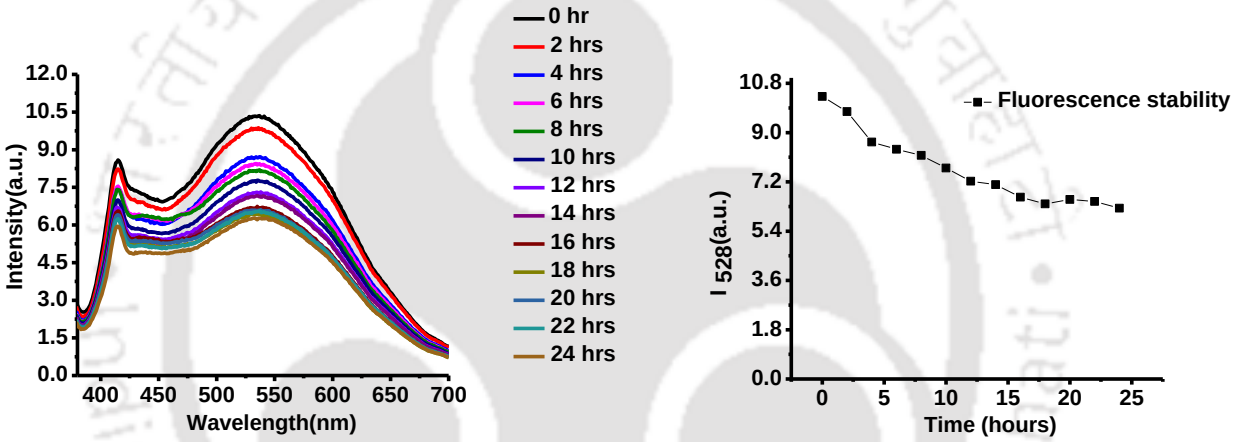

Figure A2b.4. Stability of optical response was monitored for PF-HQ at 523 nm using fluorescence spectroscopy.

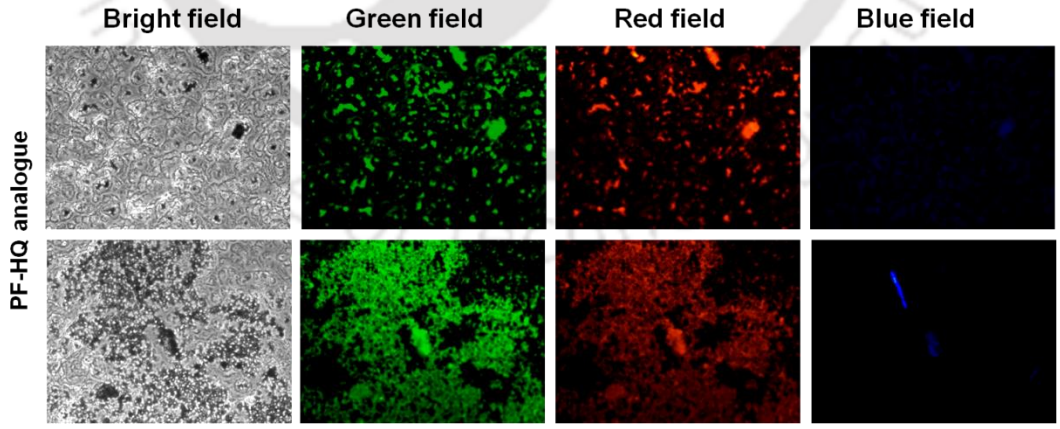

Figure A2b.5. Fluorescence imaging of only PF-HQ without cells.

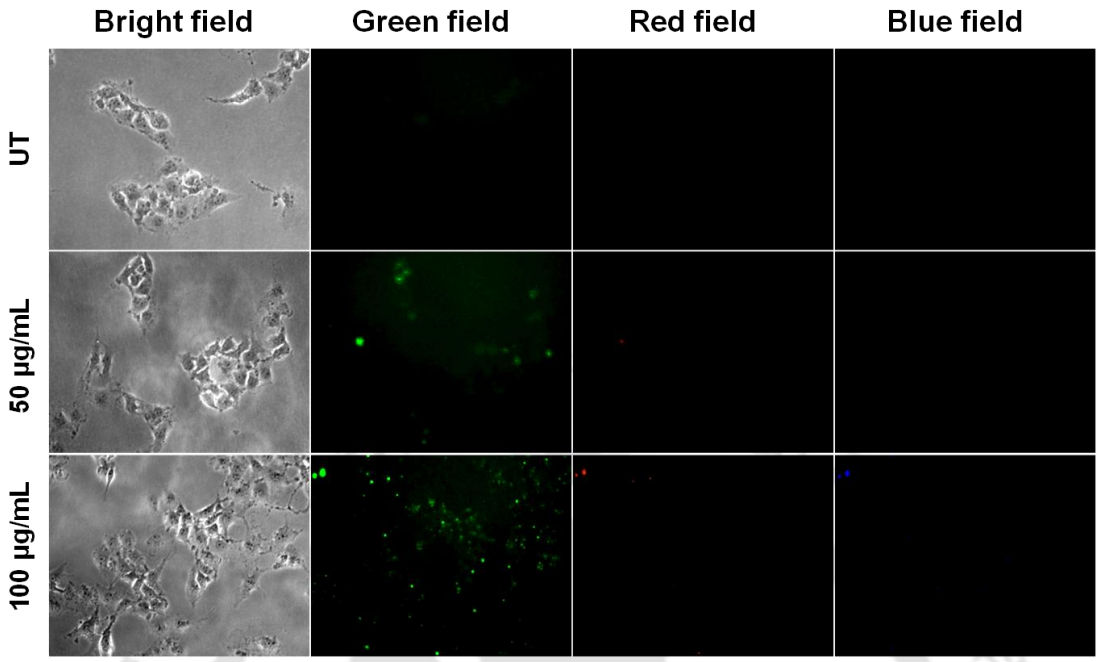

Figure A2b.6. Cell imaging of COS-1 cells after incubation with PF-HQ (50 and 100 µg/mL) for 14 h using fluorescence microscopy at 20X.

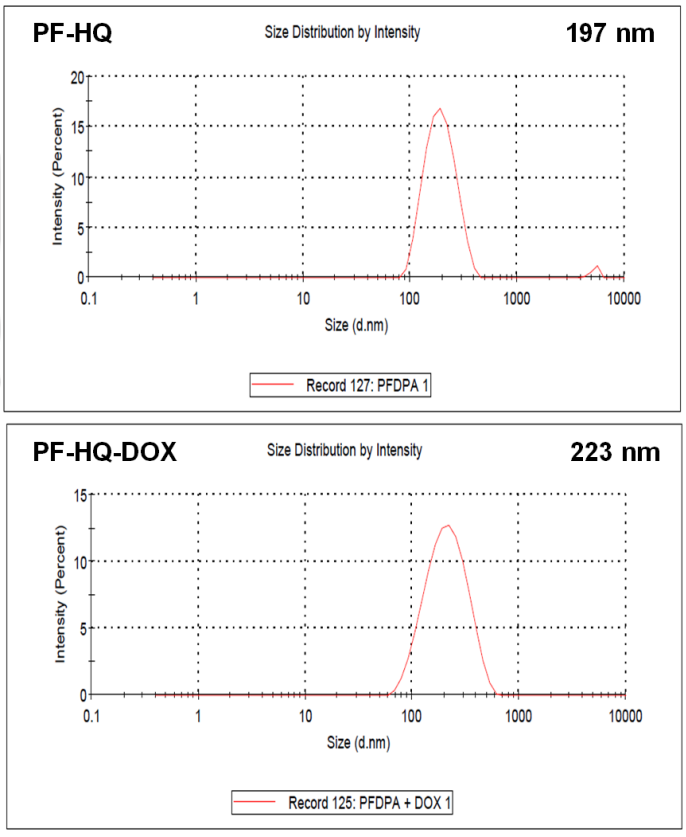

Figure A2b.7. Hydrodynamic diameter of PF-HQ and PF-HQ-DOX.

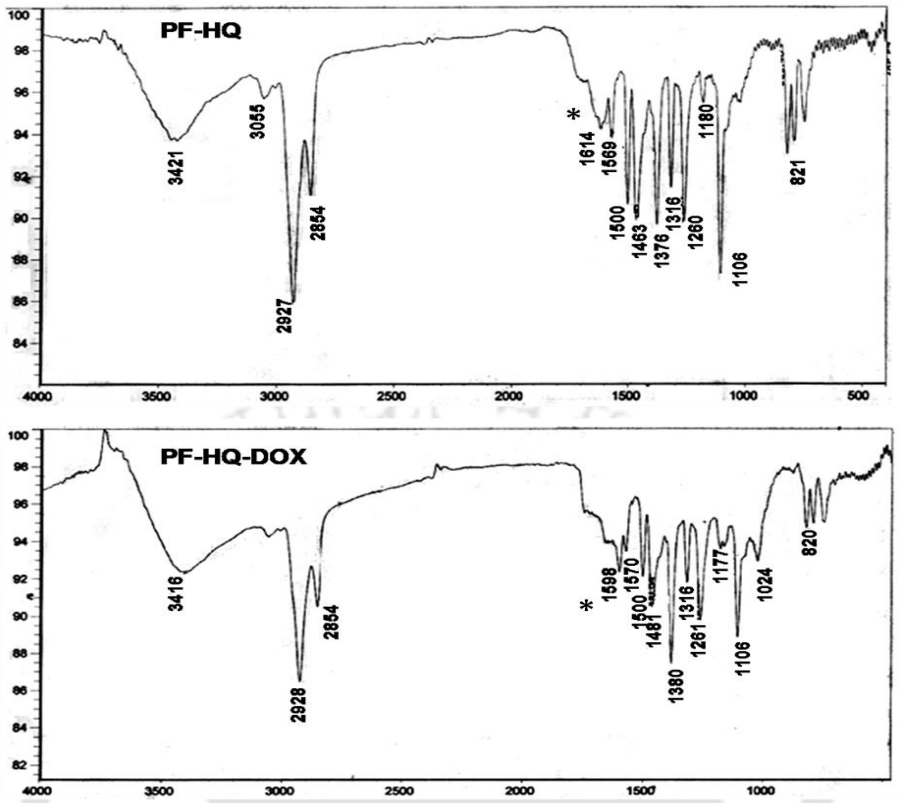

Figure A2b.8. FTIR data of PF-HQ and PF-HQ-DOX confirms the attachment of DOX in PF-HQ.

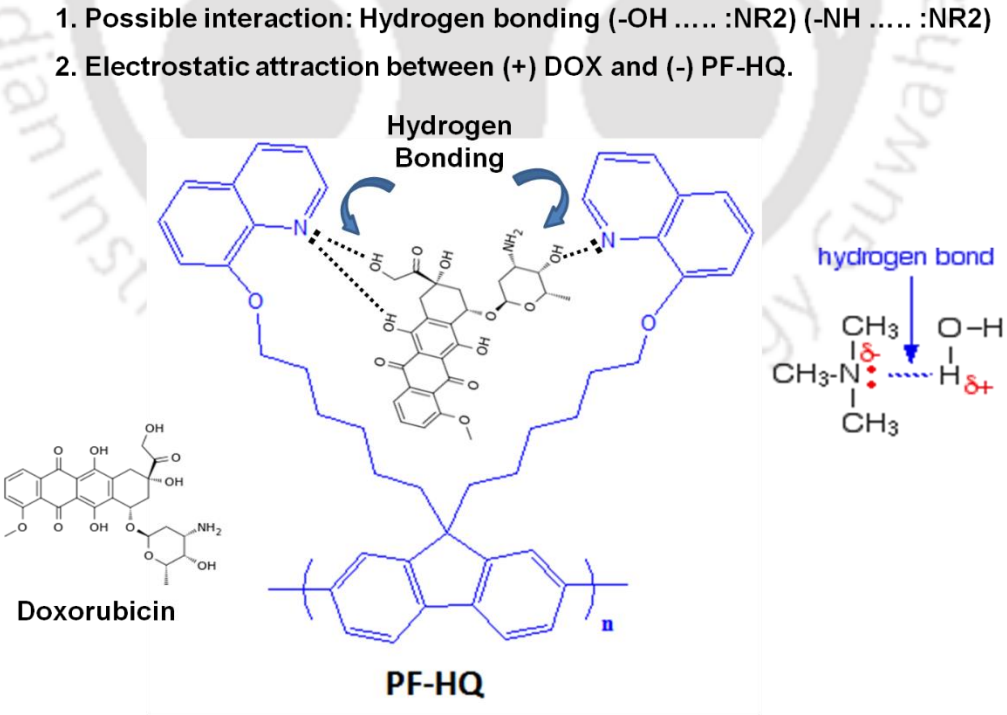

Figure A2b.9. Probable bonding between PF-HQ and DOX.

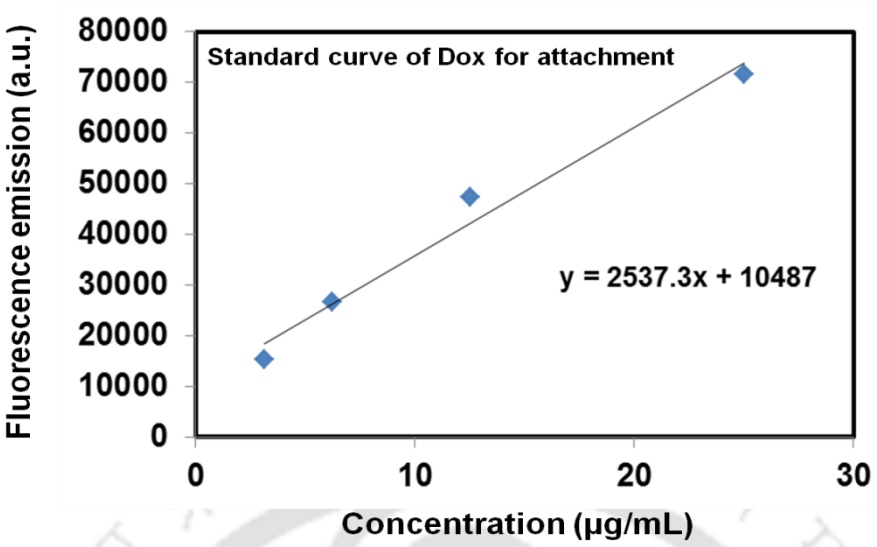

Figure A2b.10. Standard curve of DOX using spectrofluorimetry.

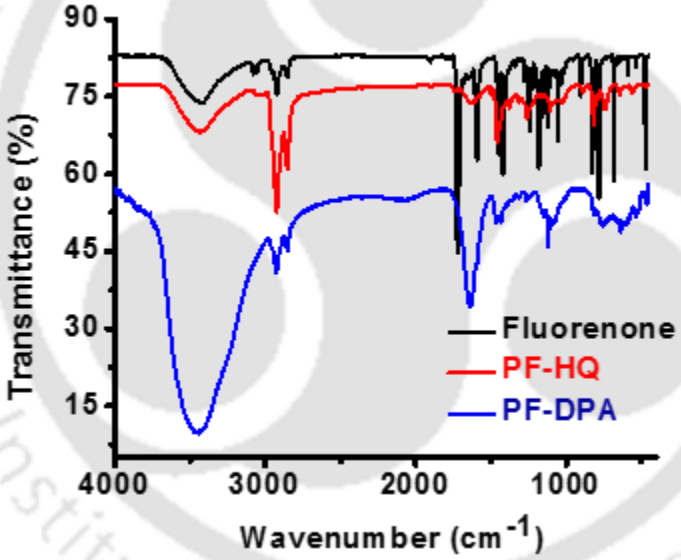

Figure A2b.11. FT-IR spectra of Fluorenone (black), PF-HQ (red) and PF-DPA (blue). PF-HQ is presented in the present study. PF-DPA was explored in Chapter 3. No peak was found in the case of polymers at 1722 cm^{-1}.

FT-IR, SEM and DLS measurement

For the identification of functional groups present in the nanomaterial (PF-HQ) and to know its interaction after conjugation with DOX, FT-IR analysis was carried out. The brownish colored pellet of PF-HQ and brownish-orange pellet of PF-HQ-DOX were lyophilized to make them dry powder. They were pelletized separately in IR grade KBr. The spectra were scanned

over a range of 4000–500 cm–1 and recorded in the diffuse reflectance mode at a resolution of 4 cm-1in Thermo Nicolet Nexus 670 spectrometer.

FE-SEM was carried out to observe the size, shape, and morphology of PF-HQ and PF-HQ-DOX (JEOL 7601L). DLS was employed to measure the size and surface charge of PF-HQ and PF-HQ-DOX nanomaterials. The hydrodynamic radii and surface charge (zeta potential) of both the nanomaterials were measured using a Zetasizer Ver. 6.20, Malvern Instruments Ltd. by mixing homogeneously 10 µL of each corresponding pellet in 1 mL Milli-Q water. The measurements were taken after placing the solutions separately in a quartz cuvette.

Solvent	$\lambda_{abs.}$ Max (nm)	ε [$M^{-1}cm^{-1}$]	$\lambda_{em.}$ Max (nm)	Φ
Water	372	18297.4	523	0.011826
DMF	372	10120.7	415	0.682689
DMSO	371	4753.6	415	0.581993
THF	370	28904.5	412	0.796193
MeOH	376	25052.2	404	0.147163
CH_3CN	376	19999.8	406	0.167516
DCM	367	6818.6	412	0.560916

Table A2b.1. Absorbance (λabs.), the absorption coefficient (ε), fluorescence maxima (λem.) and quantum yield (Φ) of PF-HQ in different solvents.

Standard curve preparation of DOX

Initially, a set of various concentration of DOX standard solution was prepared by mixing the different amount of DOX (3.125-25 µg/mL) in 1 mL of PF-HQ supernatant (obtained after centrifugation of PF-HQ). The fluorescence emission intensities at 600 nm of each set of standard solution were recorded upon excitation at 480 nm. Finally, a standard curve of DOX was made by plotting the fluorescence emission intensities of each solution against the respective concentration of DOX.

Biodistribution studies

To determine the bio-distribution of PF-HQ and doxorubicin in tumors and other vital organs in the treated C57BL6 mice, we collected all the required organs and tumors from the sacrificed C57BL6/J mice (from group II-IV) after completion of dosing regimens. All organ and tumor samples were then washed with DPBS, weighed and held overnight at 4oC in acidified isopropanol (75 mM HCl, 10% water, 90% isopropanol) solutions followed by gentle

vortexing. Finally, these samples were centrifuged at 13,000 rpm. for 15 min at 4oC, and the supernatant was collected and placed into a 96-well plate (100 µL per well in triplicate). The PF-HQ and doxorubicin bio-distribution in tumor and organ tissues were quantified using a spectrofluorimeter (FLx800 Fluorescence Microplate Reader-Bio-Tek, USA) upon λex at 480 nm and λem at 580 nm (for DOX) and λex at 350 nm and λem at 530 nm (for PF-HQ). The results were corrected for the auto- fluorescence values obtained from untreated mouse tissues. The data are expressed as relative fluorescence units per gm tissue.

Immunofluorescence studies

Prior to immunostaining, the tumor tissue samples were fixed in ~ 4% PFA overnight and then washed with PBS for 2-3 times. 10 µm thicknesses of respective tissues were prepared by a Cryostat (Leica CM1950) and mounted on microscopic slides. The tumor tissue slides were dipped into isopropanol for 3-5 minutes followed by xylene for 3 minutes each and 10 mM citrate buffer (pH= 6.0) was used for antigen retrieval by heating sections in sub-boiling condition for 10 minutes. After cooling the slides, sections were washed locally by Milli-Q water three times at room temperature. 3% BSA solution in 1xTBST was used as blocking solution for 1 hour at room temperature. Later, sections were washed locally for three times with 1x TBST for five minutes each. Then the sections were incubated with primary antibody (Ki-67 Primary (PA5-19462, Thermoscientific; 1:100) at 4°C overnight without disturbing the slides. The secondary antibody (goat anti-rabbit IgG-PE, sc-3739, Santa Cruz; 1:100) was added after the sections were washed with 1x TBST and incubated for half an hour at room temperature. After washing the sections with 1x TBST, each section was mounted with fluorescence mounting medium (DAPI) and sealed with a coverslip using nail-polish. The images were captured using fluorescence microscope (Nikon Eclipse: TE 2000-E, Japan) at 20 X magnification.

Tunel assay

To check the tissue apoptosis caused by PF-HQ-DOX, the fixed (4% formalin) tumor tissues were subjected to Tunel assay using an APO-DIRECT™ kit (BD Pharmingen, Cat. No. # 6536KK) according to the manufacturer's protocol. DAPI was used to tag the nucleus of the tumor cells. Images were acquired using a fluorescence microscope (Nikon Eclipse TE2000-E). The green fluorescence emission (λem = 525 nm) was collected after excitation at λex = 420-495 nm at 40X magnification. Similarly, the blue fluorescence emission (λem = 485 nm) was collected after excitation at λex = 380 nm at 40X magnification.

Chapter 3

Polymer-Polymer Scaffold Tweaks Early Amyloid Aggregates and Crosses Blood Brain Barrier Efficiently

Chowdhury, S. R.; Mondal, S.; Balaji, S. N.; Trivedi, V.; Iyer, P. K. Remarkably Efficient Blood-Brain Barrier Crossing Polyfluorene-Chitosan Nanoparticle Selectively Tweaks Amyloid Oligomer in CSF and Aβ1-40. (Manuscript Submitted)

Abstract

Amyloid oligomers are considered as the prime suspects in Alzheimer's dementia. In order for new materials to address diagnostic or therapeutic potential they must cross the blood-brain barrier (BBB) efficiently and target the toxic aggregates among other heterogenic amyloid aggregates which may be present in equilibrium. Successful modulation of early aggregates can provide a new approach toward presenile dementia. In this study, polyfluorene nanoparticles have been prepared using chitosan as an additive which enables it to cross BBB efficiently and employed as a highly efficient amyloid oligomer modulator. The polymer conjugate, Polyfluorene-Chitosan (PC) shows no toxicity in MTT assay and precludes self-aggregation of Aβ1-40 and human cerebrospinal fluid (CSF) oligomers to final fibril formation. This modulation strategy is supported by Thioflavin T (ThT) assay, atomic force microscope (AFM) images, circular dichroism (CD), and Fourier transforms infrared (FTIR) studies. Polymer-protein interface exhibits the presence of co-aggregates and responded with a stable optical response. The straightforward synthesis in desired size and shapes and photophysical properties, biocompatibility, non-toxicity and most prominently BBB permeability make this polymer conjugate very unique and highly attractive for modulation of amyloid oligomers selectively as well as for developing next generation nano-theranostic materials toward pre-senile dementia.

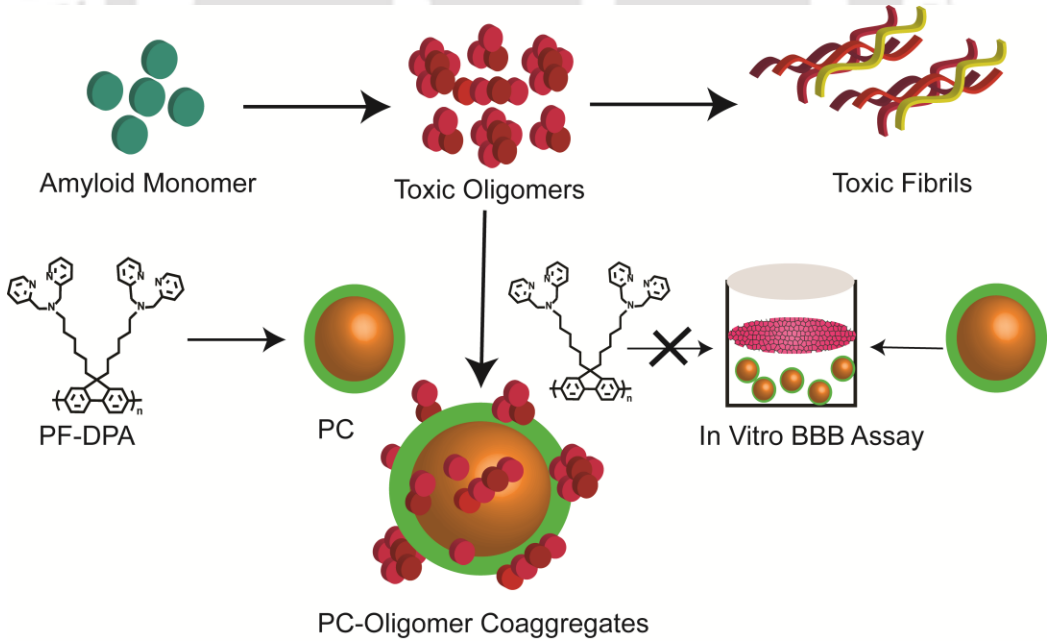

3.1. Introduction

Inhibition and modulation of amyloid aggregation using small molecule and as well as the polymeric template have always been a preferred choice of the amyloid community to disturb protein aggregation. Recent vaccination with Aducanumab significantly lowered the amyloid burden in patients and work like a homing device.[1] But the search for structures in order to trap intermediates of nucleation-dependent peptide polymerization still remains tricky and challenging. Monomeric Aβ formed inside brain after immediate cleavage by β and γ secretase may have some physiological role.[2-5] Thus de novo protein aggregation may not be necessary but a refinement of structures are in need in terms of oligomeric and protofilament structures formed due to Aβ aggregation.[6-18] Development of precursor biomarkers and as well as therapies targeting these neurotoxic diverse structural protein aggregates may shed light on presenile dementia leading to a halt in disease progression in terms of improving memory and slowing down cognitive decline. As observed in previous chapter, a similar surface weapon is needed to fight against these heterogenic structures of this endogenous peptide.[19] Designing efficient drugs for targeting these early aggregates across the blood brain barrier (BBB) makes the scenario even more complex due to small interaction surface area of the higher order heterogenic aggregates and crossing the barrier efficiently. The BBB is embraced of endothelial cells "glued" together to form junctions and a large portion of brain homeostasis is regulated by influx and efflux at the BBB through these junctions. This barrier has likewise the capacities to avert passage of and effectively expel undesirable molecules from the brain and it manages the inundation of essential supplements, signaling molecules and immune cells into the brain.[20-22] Molecular recognition in order to tackle this dual adventure is in scarce. This report details a polymer-polymer platform (PC) using a polyfluorene derivative (PFDPA) and chitosan which can easily cross endothelial monolayer (shown as a BBB mimic) unlike its precursor polyfluorene and as well as modulates amyloid aggregates. Polymerization of amyloid oligomers to final fibrils in real CSF samples and as well as in commercial Aβ1–40 were examined both in presence and absence of modulators after different time intervals by monitoring Thioflavin T (ThT) fluorescent response. Secondary structure information of Aβ proteins both in presence and absence of modulators were gathered using CD and FT-IR studies. Morphological updates in presence modulator were collected using AFM images. This polymeric conjugate also showed a distinct optical response in presence of Aβ1-40 oligomers due to preferred surface motif and further hydrophobic interaction with the hydrophobic core of the peptide resulted in inhibition to final fibril formation.

3.2. Experimental Section

3.2.1. Materials

Chitosan, Di-(2-picolyl)amine, 1,6-Dibromohexane, Fluorene, Ferric chloride, potassium carbonate, PBS, HFIP, TFA, DMEM, FBS and other chemicals were purchased from Merck, Sigma Aldrich Chemicals, Ranbaxy (India) and were used without further purification. Human Amyloid- β (1-40) was purchased from G L Biochem Ltd., Shanghai, China. Cerebrospinal fluid (CSF), human samples were collected from Guwahati Neurological Research Center and Hospital, Six Mile, Guwahati, India.

3.2.2. Synthesis of PF-DPA and PC

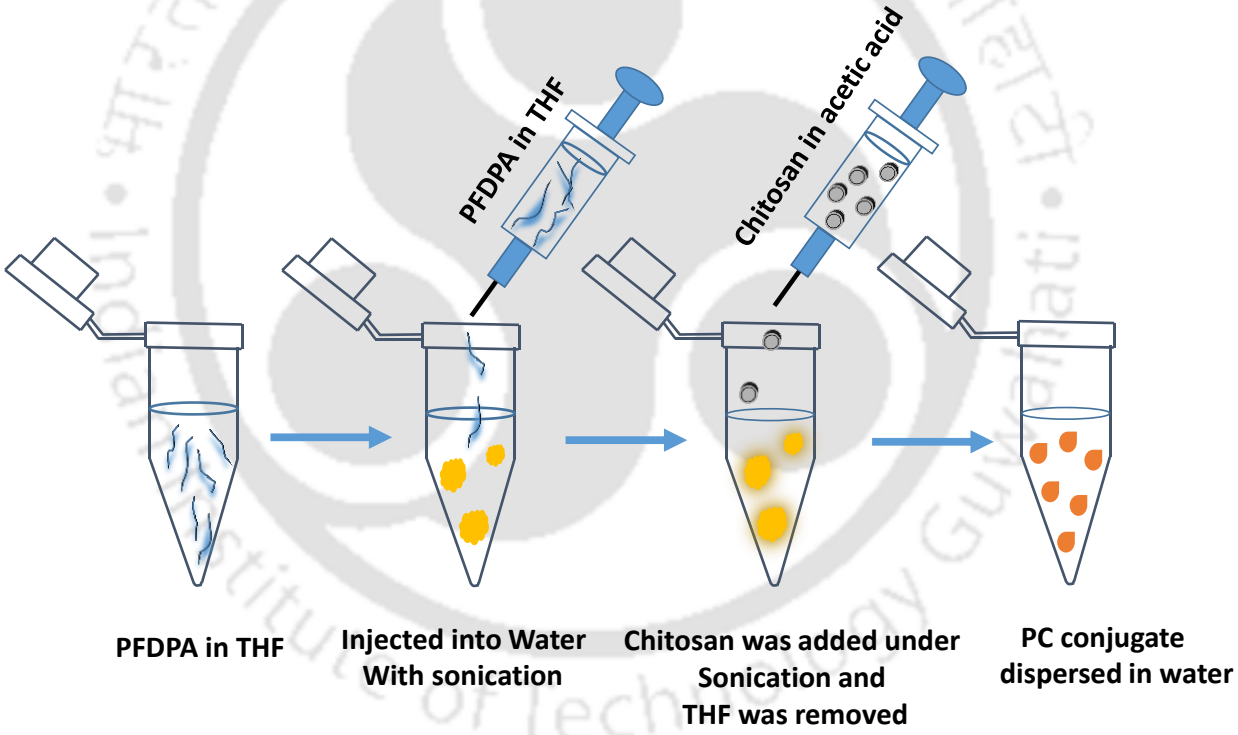

Scheme 3.1. Schematic preparation of PC from PFDPA and chitosan.

Fluorene was first alkylated using 1, 6-dibromohexane in 50% aqueous sodium hydroxide and the crude was purified using Column Chromatography to get the desired doubly alkylated product as a yellow viscous liquid. Then the purified double alkylated monomer was polymerized via oxidative polymerization using ferric chloride as a catalyst and nitrobenzene as a solvent under argon atmosphere. The resulting polymer was precipitated in methanol and

dried under vacuum and finally to prepare PF-DPA, appended bromines were substituted by di-(2-picolyl) amine in DMF in presence of K_2CO_3. The desired polymer PFDPA was purified via precipitation from methanol and the attachment was confirmed via ^1H and ^{13}C NMR spectra in chloroform-d (Scheme S1).[23] In order to prepare the nanoconjugates (PFDPA-Chitosan, PC), Chitosan (100 µg of 1 mg/mL) was added in 1 mL of PFDPA (1 mg/mL) in an Eppendorf under vortex condition for 30 minutes. The orange-brownish intense PC nanoconjugate solution was ultra-centrifuged (14,000 rpm at 4 °C for 30 minutes) using centrifugation. The PC nanoconjugate pellet was collected (50 µL) and utilized for all the studies. Similarly, PFDPA was also centrifuged (14,000 rpm at 4 °C for 30 minutes) and the pellet was used for all experiments in order to compare with PC (Scheme 3.1).

3.2.3. Instrumentation

Atomic force microscope (AFM) images were taken using Bruker, Innova with non-contact tapping mode using a large scanner. Malvern Zetasizer Nano series Nano-ZS90 instrument was used to measure DLS. CD measurements were done in a JASCO J-1500-150 Spectrometer (JASCO Co. Tokyo, Japan), using a quartz cuvette (1 mm path length). NMR spectra of PFBr, PFDPA and precursor monomers were taken in a Bruker AscendTM 600 MHz spectrometer using CDCl3 as a solvent. Thioflavin T fluorescence measurements were done in a Tecan microplate reader using Corning 96 Flat Bottom black, clear bottom Polystyrene Cat. No.: 3631 plate reader. For fluorescence spectra in 1 ml solution, a 10 mm x 10 mm quartz cuvette was used and emission was collected at 90 ° relatives to the excitation beam using Fluoromax-4 Spectrofluorometer-Horiba Scientific.

3.2.4. In-vitro Cell Viability and Blood-Brain Barrier Assay

To check the intrinsic toxicity of all the precursor polymers (PFBr, PFDPA) along with the final conjugate (PC), in vitro toxicity was studied by both hemolysis assay and the MTT cell survival assay with RBCs and Ea hy926.1 respectively as described in our previous report.[23] Endothelial cells (EA hy926.1) were harvested as usual in complete growth media, Dulbecco's Modified Eagle Medium (DMEM, HiMedia) with 10% fetal bovine serum (Gibco) and antibiotics (Anti-Anti, Gibco) at 37 °C in 5% CO_2 incubator and 25,000 cells were seeded per well in a 96-well plate. Twelve hours later, cells were treated with different concentrations of PFBr, PFDPA, and PCs (0–100 µg/ml) for 12 h and the cell survival was determined by standard MTT assay.

Prior to cell viability, in-vitro blood-brain barrier assay (BBB) was performed by making an endothelial monolayer barrier. Briefly, endothelial cells were seeded in a special cell culture plate (60 mm) which poses 3-micron pore for crossing. Endothelial cells were grown densely till completely seal the pores. This plate was maintained in a 100 mm sterile plate with an adequate amount of media. PFBr, PFDPA and PCs solutions (50 μg/ml) were prepared in complete media and gently added in three different 60 mm dishes (upper chamber) and the media was collected from the 100 mm dish (lower chamber) after every 1-hour interval till 6 hrs. Further, the permeability was checked by measuring fluorescence of all the test compounds. Leakage was corrected by using Evans blue as a control and to calculate the actual permeability of the precursor polymers and conjugates.

3.2.5. Preparation of stock solution

1 mM PFDPA and PFBr stock solutions were prepared in 10 mL THF. This stock solution was diluted to the desired concentration for further incubation during modulation and imaging studies. PC conjugates were prepared at a concentration 20 mg/ml in 10 mM deionized water and finally, 1 mg/ml was diluted in phosphate buffer saline (PBS) for modulation studies. All the experiments like UV-Visible, FT-IR and fluorescence titrations were performed in 10 mM PBS buffer and pH maintained at 7.4. PFDPA (10 μM) polymer was regularly injected into deionized water with vigorous stirring at room temperature, using a syringe. After the injection of PFDPA, the solution was filtered by membrane filter with 0.2 μm pore size. Then the collected PFDPA was used for other studies. Chitosan was dissolved in 2% acetic acid solution and the conjugates were freshly prepared in deionized water.

3.2.6. Oligomerization of Aβ (1–40)

TFA/HFIP was used to disaggregate Aβ (1–40) initially following our previous protocol[24] to obtain a final concentration of 0.2 mM. Then it was kept at 37 °C for 24 hours in dark conditions for oligomerization and confirmed by taking AFM images using Bruker, Innova instrument. Further fibril formation and modulation were examined using a Thioflavin T (ThT) fluorescence assay in a Tecan microplate reader.

3.2.7. Preparation of Aβ1–40 aggregates and ThT Binding Assay

Aβ1–40 and CSF were used as a source of amyloid oligomers. Aggregation of Aβ1–40 (20 μM) was examined by incubating with ThT (40 μM) at 37 °C for 24 hours (pH 7.4 in 10 mM PBS) without stirring for the preparation of oligomeric amyloid peptide aggregates. Further,

aggregation of Aβ1–40 amyloid fibrils were monitored both in presence and absence of modulators with different time incubations by monitoring ThT (20 μM) fluorescent enhancement peak at λem 482 nm (λex 440 nm) using a microplate reader. Similarly to confirm the presence of Aβ aggregates in human CSF sample, first ThT fluorescence was measured in the saline buffer and corrected with Aβ1-40 reading as a control. AFM images validated the presence of CSF oligomers which similarly formed mature fibrils on further incubation in saline buffer.

3.2.8. Modulating Experiment for Aβ1–40 Aggregates

The modulating ability of polymeric conjugate (PC) was examined by the changes in the fluorescence spectra in presence of Aβ1–40 in commercial and in real CSF samples and as well as studying CD spectra to investigate the changes in secondary structure. The samples were prepared in the final volume of 1 mL in 10 mM PBS (pH 7.4) buffer and incubated at 37 °C with Aβ1-40 and CSF separately. Fluorescence spectra were recorded at a different time interval in order to correlate protein aggregation and the optical signal of the polymeric conjugate. First, when Aβ1–40 oligomers were incubated with PC (1 mg/ml) solution was excited at polymeric conjugate excitation at 429 nm, we observed initial emission peak at 630 nm. However, changes after further incubation (0–84h) at 37 °C (pH 7.4) were observed carefully. Finally, a similar study was repeated with the preformed Aβ fibril and as well as real CSF sample. All of the measurements were recorded in a fluorescence spectrophotometer (Horiba, Fluoromax 4) at 293 K and 2 nm × 2 nm excitation and emission slit widths.

3.3. Results

Alzheimer's disease is pathologically linked to Aβ aggregation which has no physiological roles. Our previous efforts in finding structural varieties in modulating either these robust amyloid structures or inhibiting the aggregation process of this endogenous peptide made us believe that the development of polymeric nanoparticle may lead to future theranostic precursors.[24,25] PFDPA was found to be a perfect modulator for amyloid beta (Aβ1-40) due to its hydrophobic nature but failed to pass through the blood-brain barrier (endothelial monolayer). To solve this issue, water-dispersible nanoparticles were made using chitosan and PFDPA as discussed in section 2.2 (Figure 3.1). In vitro toxicity and blood-brain barrier permeability of this polymeric conjugate (PC) was further checked prior to its use for modulation of Aβ and discussed in details.

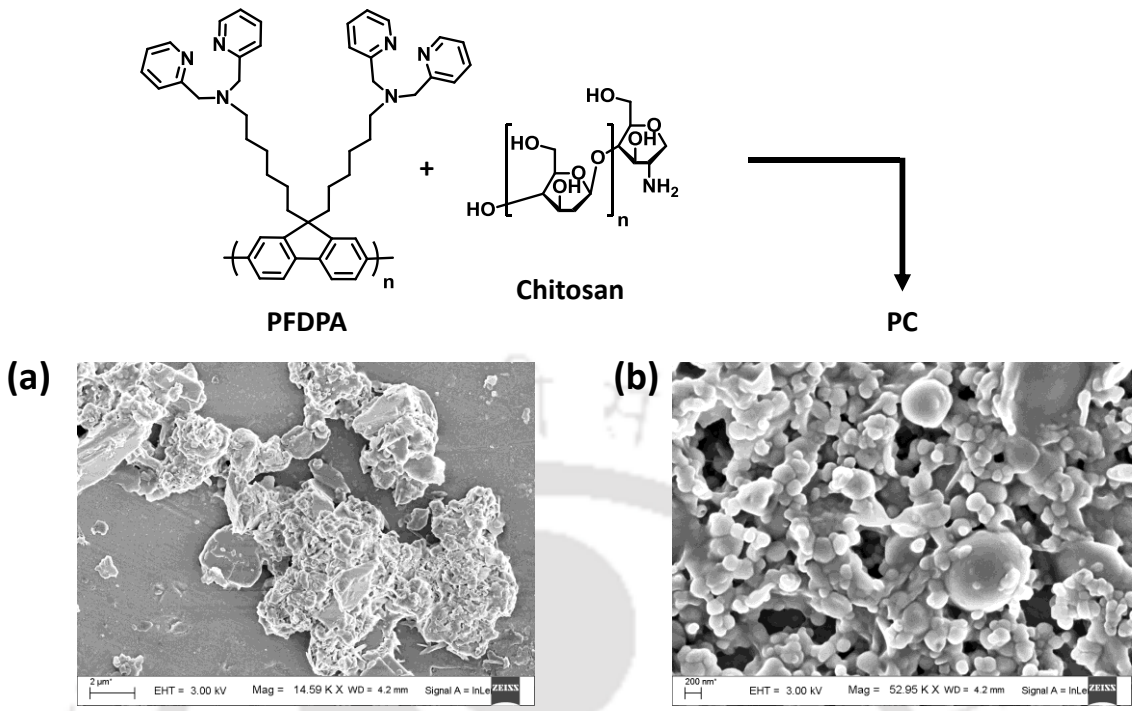

Figure 3.1. FESEM image of (a) PFDPA (scale bar is 2 µm) and (b) PC (scale bar is 200 nm).

3.3.1. In vitro Toxicity and BBB Permeability

Prior to the in vitro BBB assay, both the polymeric conjugate (PC) and their precursor's (PFBr and PFDPA) toxicity was studied by MTT cell survival assay with RBCs and Ea hy926.1 respectively (Figure 3.2). Two different conjugates namely PC2 and PC3 were made using both low molecular weight and high molecular weight poly (D-glucosamine) along with PFDPA to assess toxicity and permeability of the conjugates.

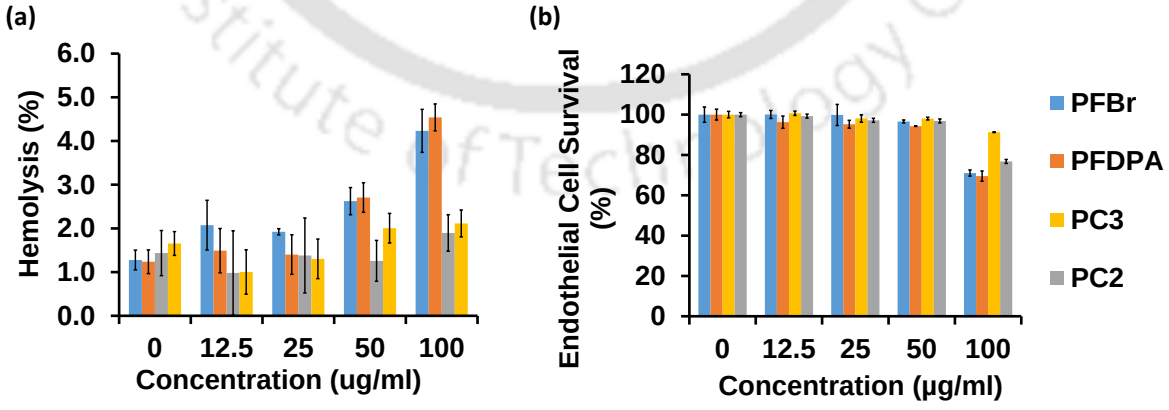

Figure 3.2. Cytotoxicity of PC2, PC3, PFBr, and PFDPA (0-100µg/ml) in (a) human red blood cells and (b) endothelial cells (EA.hy926). Error bars correspond to standard deviations of six sets of experiments.

In hemolysis assay, PFDPA and PFBr were shown mild toxicity (~ 4 - 5 %) to the RBC around at 100 µg/ml of concentration (Figure 3.2a). The lower concentration was not toxic to the RBCs whereas both the PC2 and PC3 showed lesser than 2 % toxicity at maximum concentration (100 µg/ml) (Figure 3.2a). In MTT cell survival assay, polymer compounds of PC2 were shown less than 10 % toxicity whereas other were shown 10 to 30 % toxicity at the maximum concentration (Figure 3.2b). But at 50 µg/ml and lower concentration, they have not shown significant toxicity to the endothelial cells. Based on the toxicity assay results 50 µg/ml concentration was used to test the in vitro BBB permeability assay (Figure 3.3).

The permeability efficiency of the test compounds was assessed as mentioned in the methodology section 2.4. The endothelial monolayer permeability assay resulted as follows 46.9 ± 0.1 %, 18.1 ± 3.8 % and 0.2 ± 0.7 % movement across the barrier correspondingly to PC2, PC3, and PFBr at the first hour (Figure 3.3b, d, and f). It was troublesome to calculate the PFDPA concentration by the fluorescence method as it was sparingly soluble in culture media and gave erroneous results. Permeability efficiency of PC2, PC3 and PFBr were tabulated in the below table. Cellular integrity in presence of polymer conjugates was checked and remained intact throughout the experiment (Figure 3.3a, c, and e). From the BBB secretion studies, it has been confirmed that polymeric conjugate (PC) was able to pass through the monolayer much easier compared to polyfluorene precursors i.e. PFBr and PFDPA. Conjugate made up of low molecular weight chitosan, PC2 was able to cross BBB efficiently than PC3 and further utilized as a modulator (denoted as PC) present study.

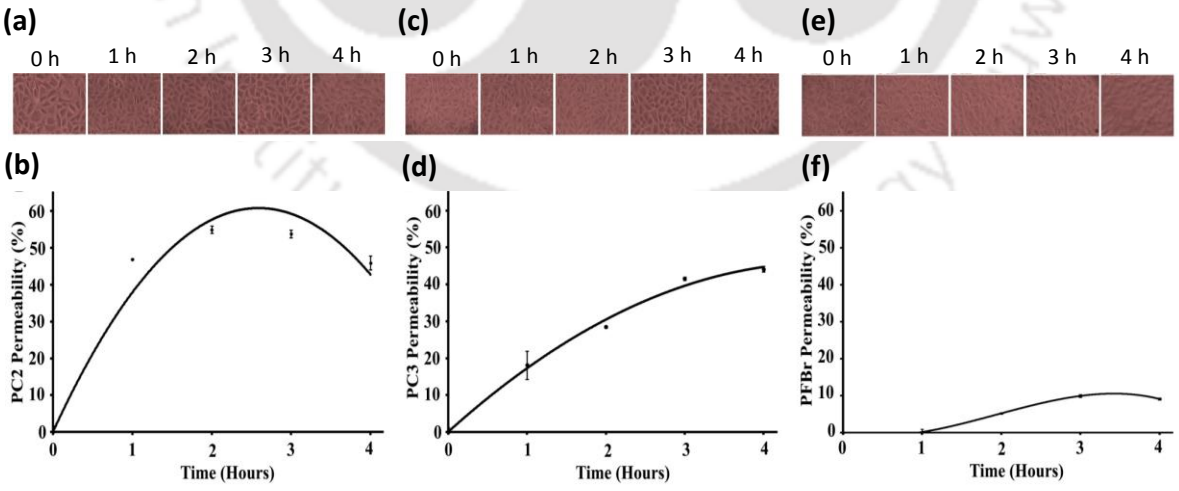

Figure 3.3. BBB assay of PC2, PC3, and PFBr (50 µg/ml). Optical images showing cellular integrity in presence of (a) PC2, (c) PC3, and (e) PFBr during the experiment. Movement of (b) PC2, (d) PC3, and (f) PFBr through endothelial monolayer from 0-4 hours. Evans Blue was taken as a control. Error bar corresponds to the standard deviation of five sets of experiments.

3.3.2. Modulatory studies using Thioflavin T assay

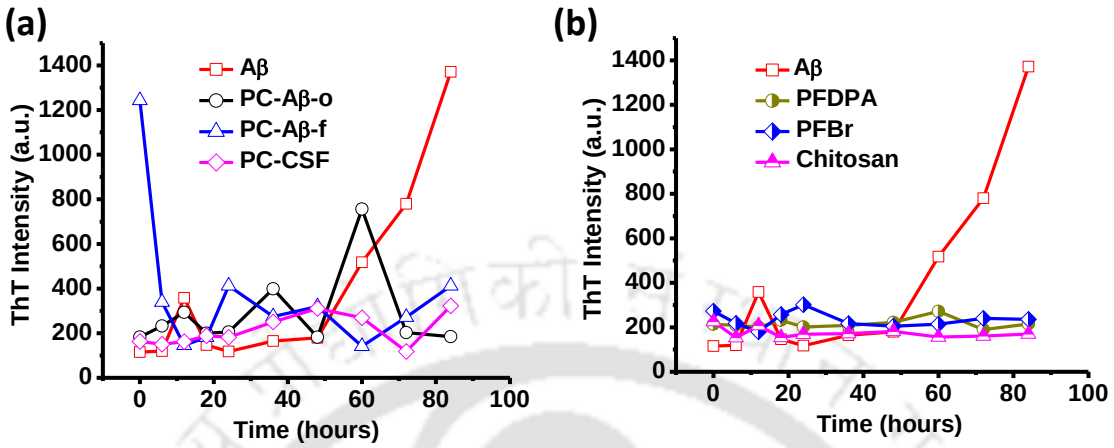

Figure 3.4. Thioflavin T assay of only Aβ1-40 (20 μM, squares) and (a) PC (1 μg/mL) with coincubated Aβ oligomers (circles), Aβ fibrils (triangles), and CSF oligomers (15 μM, diamonds); (b) PFDPA (1 μg/mL, half-filled circles), PFBr (1 μg/mL, half-filled diamonds), and Chitosan (low molecular weight, 1 μg/ml, half-filled triangles) coincubated with Aβ1-40 (20 μM) in 5 mM PBS (pH 7.4).

Thioflavin T assay (ThT) was prepared to examine the modulatory properties of the polymeric conjugate (PC) both in presence of commercial Aβ1-40 and as well as human CSF sample. Further the effects of other precursors used in making the polymeric conjugate have been checked on amyloid fibrillation (Figure 3.4). First, 100 μM Aβ1-40 was incubated with 10 μg/ml PC in 10 mM PBS at 37 °C and used as a stock solution. To check the effects on amyloid fibrillation samples were collected from the above stock solution at different time intervals starting from 0-84 hours and diluted in 5 mM PBS. 40 μM ThT was added to each well of the microplate reader before recording ThT emission at 482 nm using microplate reader. 100 μM Aβ1-40 was treated with TFA and HFIP to disaggregate as discussed in section 2.6 before incubating at 37 °C and used as a control. ThT assay of Aβ1-40 control showed a lag phase up to 50 hours (Figure 3.4a, and b, squares) before an increment in ThT fluorescence intensity due to the formation of the fibrillar network. This increase in intensity was not observed in presence of PC (1 μg/ml, Figure 3.4a, circles) and the same was observed in the case of CSF sample (15 μM, Figure 3.4a, diamonds). The decrease in ThT fluorescence intensity suggested that amyloid fibril formation was inhibited in presence of the polymeric conjugate, PC and it was also able to disturb amyloid aggregation even in real CSF sample. Further, PC was incubated with preformed Aβ1-40 fibrils to check the effects on already formed fibrillar networks. An initial high fluorescence intensity at t0 was decreased sharply and reached a plateau after 20 hours of incubation (Figure 3.4a, triangles). To figure out the effects of other

precursors which were used to prepare PC, 100 μM Aβ1-40 was incubated separately with 10 μg/ml PFDPA, PFBr, and chitosan (low molecular weight) separately in 10 mM PBS at 37 °C. PFDPA and PFBr stock solutions were prepared initially in THF. Then it was vigorously added into the water with continuous shaking and the final pellet was collected after centrifugation. These pellets were used further as inhibitors and incubated with Aβ. Chitosan was dissolved in dilute acetic acid solution and diluted from this acidic solution to a final solution of 10 μg/ml in 10 mM PBS at pH 7.4. ThT fluorescence maintained almost a straight line profile in presence of all the polymers unlike control (Figure 3.4b) suggesting a successful inhibition of amyloid aggregation. ThT profile also showed that in presence of PC amyloid aggregation was nearly similar as in the case of control till the growth phase is reached. ThT intensity started decreasing after 60 hours and followed a different path unlike control (Figure 4A, squares, and circles). This divulged that unlike other precursors, PC was able to disturb the more neurotoxic amyloid oligomers or other aggregation intermediates which exist in the growth phase and directed the amyloid aggregation in a different pathway.

3.3.3. Changes in Secondary Structure

To investigate the changes in the peptide secondary structure in presence of PC, CD spectrum of only Aβ1-40, CSF (controls) and as well as coincubated with polymeric conjugate were recorded at different time intervals. All the samples were incubated at 37 °C in 10 mM PBS and diluted in 1 mM PBS before recording CD spectra. The spectra of only Aβ showed negative minimum (around 200 nm) upon 24 hours of incubation confirming the formation of ordered β-sheet aggregation from the initial random coil. Small positive maxima at 191-193 nm and a negative minimum were observed in the control (Figure 3.5a, black line) Aβ1-40 solution. Aβ1-40 oligomers showed no such negative peak in presence of PC. After 84 hours of incubation, the negative hump was reversed and a new positive maximum (around 196 nm) was observed (Figure 3.5a, red line). This observation confirmed that PC successfully modulated Aβ oligomers and directed toward a different aggregation pathway as no increase in β-sheet conformation was found, unlike controls. Even in the case of pre-fibrillar Aβ1-40 (20 μM) coincubated with PC (1 μg/ml), a small positive hump at 205 nm along with a negative peak at 194 nm appeared (Figure 3.5a, blue line). Ordered β-sheet aggregation of Aβ1-40 required for final fibril formation was proved to be disturbed in presence of polymer conjugate PC and followed a different pathway. Interestingly, in the case of real human CSF (15 μM) coincubated with PC (1μg/ml) showed a broad negative minimum from 210-230 nm and a positive maximum at 191-194 nm. Unlike in the case of commercial Aβ1-40 oligomers where PC was

able to enhance the total fraction of β-turn and random coil formation, α-helicity was restored in the case of real CSF sample (Figure 3.5a, pink line). Individual time-dependent CD spectra of Aβ1-40 oligomer, pre-fibrillar aggregates and CSF were given in supporting information (Figure A3.1).

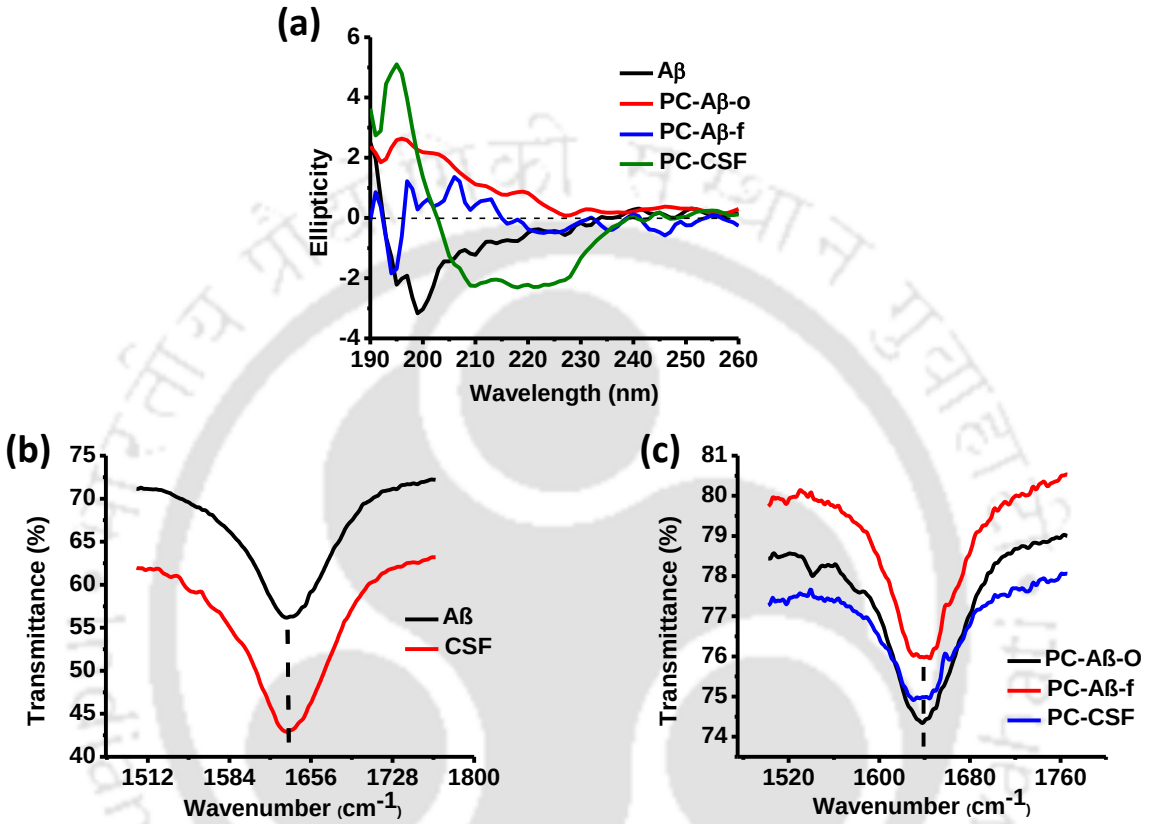

Figure 3.5. CD and FT-IR spectra for Aβ1-40 (20 μM) both in presence and absence of PC (1μg/ml). (a) CD spectra of only Aβ1-40 (20 μM, black line), PC+Aβ oligomers (red line), PC+Aβ fibrils (blue line), and PC+CSF (green line) in 1 mM PBS at pH 7.4. FT-IR spectra for (b) Aβ1-40 (black) and CSF fibrils (red), (c) PC+Aβ oligomers (black), PC+Aβ fibrils (red), and PC+CSF (blue).

Further, to confirm the peptide secondary β-sheet formation FT-IR spectra of both controls and coincubated with polymeric conjugate (Figure 3.5b and c) were taken. In the case of controls, Aβ1-40 and CSF showed a peak at 1633 cm^{-1} which indicated the presence of β-sheet conformation (Figure 3.5b).[26,27] As seen from CD studies, the ordered peptide aggregation was disturbed in presence of PC, showed FT-IR amide band at 1640 cm-1 after 84 hours of incubation (Figure 3.5c). Most likely β-rich oligomers were trapped in presence of polymeric conjugate PC and due to the increased fraction of turn as observed in CD spectra, amide β-band in FT-IR spectra in presence of polymer conjugate. Further these changes (modulation) were visualized using AFM images.

3.3.4. Morphological Changes

Changes in amyloid aggregation in presence of PC and other polymer precursors were visualized using AFM. Aβ1-40 and CSF oligomers showed similar AFM profile (Figure 6A-C). Aβ oligomers (Figure 3.6a) were 150 nm in diameter and 25 nm in height whereas CSF oligomers (Figure 6C) were approximately 300 nm in diameter with a similar height profile as that of commercial Aβ1-40 oligomers (Figure A3.2). Preformed Aβ1-40 oligomers were incubated with PC at 37 °C and after 84 hours larger aggregates (Figure 3.6b) of diameter 0.6 µm and 50-60 nm in height (Figure A3.2) were found to form. PC was able to block the oligomers to come close to each other and thus directed peptide aggregation in a different pathway inhibiting the final fibril formation unlike controls (Figure A3.3). Mature fibrils of Aβ1-40 and CSF showed a diameter of 150 nm and average height was 6-9 nm.

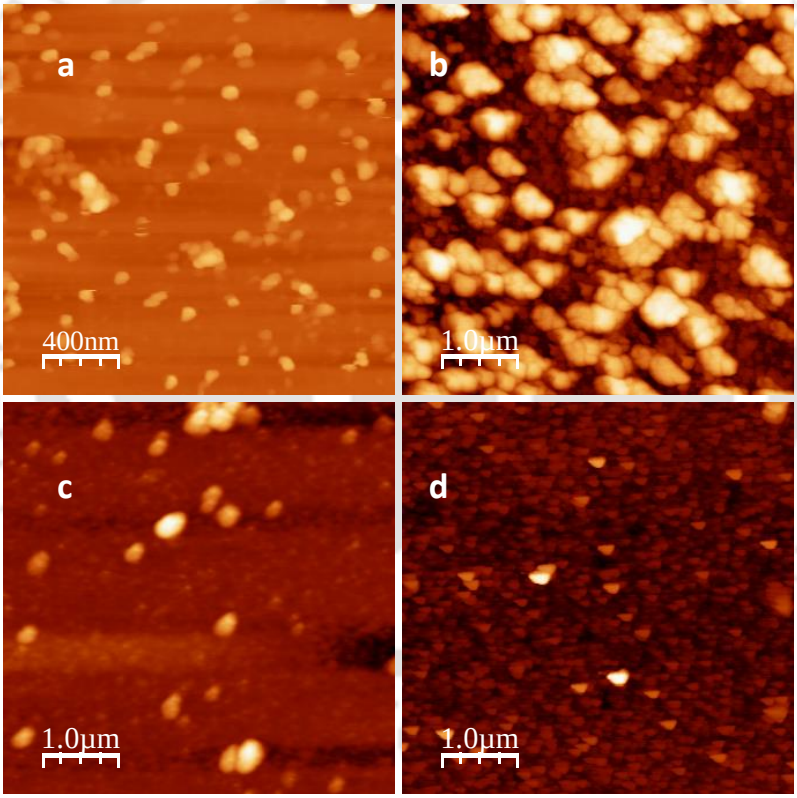

Figure 3.6. AFM images of (a) Aβ1-40 oligomers, (b) PC+Aβ1-40 oligomers, (c) CSF oligomers, and (d) PC+CSF oligomers. Images of coincubated samples were taken after 84 h of incubation at 37 °C in 10 mM PBS (pH 7.4) and Aβ1-40, CSF, and PC concentrations were 20 µM, 15 µM, and 1 µg/ml. Scale bar for figure A was 400 nm and for figure B, C, and D is 1 µm.

Further to investigate the structural contribution of polymer conjugate precursors on amyloid aggregation, Aβ1-40 oligomers were incubated separately with PFBr, PFDPA, and chitosan

(1µg/ml) and the changes in amyloid aggregation were captured after 84 hours of incubation at 37 °C (Figure A3.4). In the case of polyfluorene derivatives coincubated with Aβ1-40 oligomers resulted in larger aggregates of 0.6-0.8 µm in diameter and 70 nm in height. Peptide oligomers were trapped and no fibrillation has occurred. But in presence of Chitosan coincubated with peptide oligomers, the sparse population of Aβ1-40 oligomers were visible along with chitosan co-aggregates showing particles of two different diameters and height profiles. Aβ1-40 oligomers showed a diameter of 100-150 nm and 20 nm in height as observed in controls and co-aggregates were found to have a larger diameter of 300 nm and 70 nm in height. Morphological observations suggested that a synergistic effect resulted in successful inhibition of amyloid fibrillation of toxic oligomers in Aβ1-40 and as well as in CSF in presence of PC. A similar surface motif of PC helped to adsorb the peptide oligomers to the polymeric surface and these hydrophobic nanoparticles dispersed in water would able to modulate amyloid oligomers in Aβ1-40 and CSF to form mature fibrils.

3.3.5. Optical Correlation

Interestingly PC was able to optically distinguish oligomers, unlike PFDPA. PFDPA orange emission in buffer was blue shifted to 434 nm in presence of Aβ1-40 aggregates (both monomers and pre-fibrillar aggregates) due to the formation of larger polyfluorene aggregates (as visible in AFM images, Figure A3.4a and A3.4b). But the polymeric conjugate PC showed distinct optical features in presence of oligomers. In order to figure out the polymer-protein interaction, we have incubated Aβ1-40 (20 µM) and CSF (15 µM) oligomers in presence of PC (2mg/ml) and recorded the optical spectrum of the co-incubated samples. PC coincubated with Aβ1-40 oligomers showed initial fluorescence emission at 570 nm (Figure 3.7A). Further incubation resulted in an increase in fluorescence intensity with a blue shift of approximately 140 nm (Figure 7A, 429 nm) after 24 hours of incubation. Finally a stable peak at 442 nm along with a small hump at 543 nm appeared after 84 hours of incubation (Figure A3.5a). Thus due to the similar surface, peptide oligomers were adsorbed onto PC surface and the hydrophobic polymeric conjugate was able to interact with peptide oligomers. Finally a stable polymeric aggregate was formed in presence of peptide oligomers. The similar outcome was also appeared in presence of CSF oligomers (Figure 3.7B). Initial peak at 570 nm was blue shifted at 436 nm after immediate addition of CSF oligomers to the polymeric solution. The response found in CSF was weaker compared to commercial Aβ1-40 due to lesser concentration of Aβ in CSF and presence of preformed oligomers (immediate response was better compared to Aβ1-40 co-incubated sample). Finally, in CSF co-incubated with polymeric

solution resulted a stable peak at 442 nm and a small hump at 547 nm after 84 hours of incubation as it was observed in case of Aβ1-40 co-incubated sample (Figure A3.5b). To rule out the contribution of polymeric aggregation we have incubated pristine polymer solution in 10 mM PBS buffer at 37 °C. No blue shift was observed in absence of the peptide supporting the polymer-protein interaction. From these optical changes, we confirmed the selectivity of PC on Aβ1-40 oligomers over other precursor's viz., PFBr, PFDPA, and chitosan. We have also performed a selectivity studies and recorded the fluorescence spectra of PC co-incubated with neurotoxic brain metals and other amino acids upto 100 μM. A decrease in the initial polymeric peak at 570 nm was observed but in no case blue shift was found as observed in presence of oligomers (Figure A3.6). Mutual aggregation resulted in a stable optical response due to the probable interaction of polymer conjugates and early amyloid aggregates and formation of distinct polymeric aggregates which was highlighted in the optical profile as a hypsochromic shift.

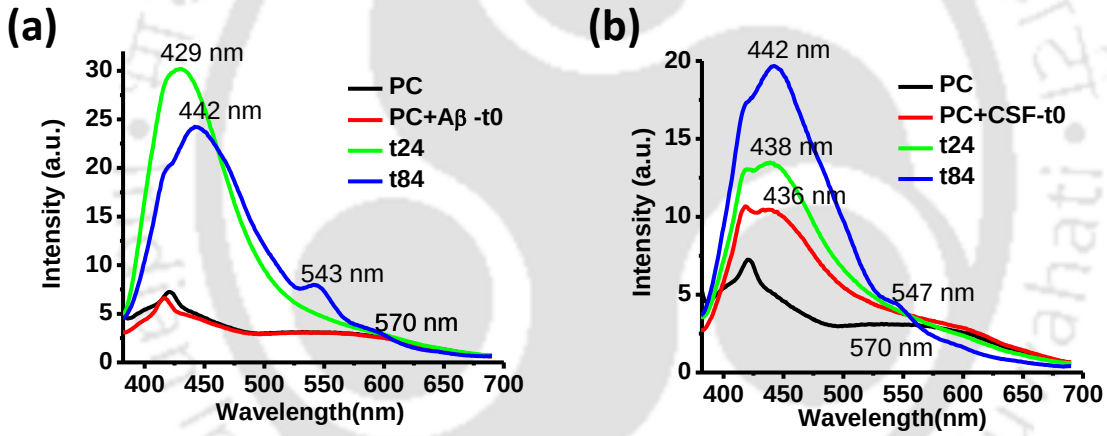

Figure 3.7. Optical response of PC (2 mg/ml) in presence of Aβ1-40 and CSF oligomers. Time-dependent (0-84 hours) fluorescence emission of (A) 2 mg/ml PC in presence of 20 μM Aβ1-40 and (B) 2 mg/ml PC in presence of CSF (15 μM). Samples were incubated in 10 mM PBS buffer (pH 7.4) at 37 °C and excited at 364 nm.

3.4. Discussion

Crossing the blood brain barrier is one of the largest hurdle needs to be overcome to deliver potential therapeutic or diagnostic agents to the brain. In the human brain, there is approximately 100 billion capillaries and a BBB surface area of 20 m^2, as compared to 0.021 m^2 for the blood-cerebral spinal fluid barrier and most of the entry is thereby controlled by this barrier.[19,20] In order to prescribe a successful modulator, one must address the two most important factors viz., targeting robust and heterogenic amyloid aggregates and ability to

cross BBB. Our findings over the last decade made us believe that polyfluorene nanoparticles are the promising candidate in modulating amyloid aggregates.[24,29] In the present study, these hydrophobic conjugate polymer nanoparticles were modified with chitosan and utilized as a modulator in amyloid aggregation. The primary main thrust for the development of nanoparticles is the hydrophobic effect as polymer chains have a tendency to abstain from water and therefore fold into round shapes.[30] Additionally, these polymer nanoparticles did not interact with free metals and other amino acids.[23,25] As seen in ThT assay (Figure 3.4) and fluorescence spectra (Figure 3.7), these nanoparticles can be directed to target selectively Aβ oligomers. Further, this modulation is supported by the stable optical response of PC in presence of Aβ1-40 aggregates (Figure 3.7b). Morphological studies indicated the changes in amyloid aggregation and CD spectra showed no parallel β-sheet formation in the peptide secondary structures (Figure 3.5a). Weak amide stretching shifted to 1640 cm^{-1} from 1633 cm^{-1} in presence of PC suggested the coexistence of both polymer and protein oligomers but directed amyloid aggregation into a non-fibrillar pathway as evident from AFM images. In oligomers the hydrophobic core is placed deep inside and therefore, they are more robust to modulate. Similar structural Motif (Figure 3.1) helped them to adsorb into the polymer surface and thus the proximity to other oligomers is prohibited (Figure 3.6b) and thus modulated final fibril formation. Nevertheless, several other issues remain to be checked which includes the essential function of BBB through influx and efflux in presence of PC and how the brain plasticity changes after in vivo experiments but these are time-consuming and presently beyond our scope.

3.5. Conclusion

In summary, this new polymer conjugate (polyfluorene-chitosan, PC) was able to optically sense oligomers as well as modulate the toxic amyloid aggregates in Aβ1-40 and in CSF. ThT assay showed a response in the growth phase targeting the pre-fibrillar aggregates which were further validated by fluorescence emission of the polymer conjugate in presence of in vitro Aβ1-40 and CSF oligomers. Precursor polyfluorene derivatives were also shown to inhibit amyloid aggregation as well indicating a synergistic effect played an important role in modulating amyloid oligomers. CD spectra showed no parallel β-sheet formation which is considered as the pathological progression of amyloid aggregation and results in fibril formation, and has been modulated by the polymer conjugate. PC was also able to cross BBB efficiently irrespective of the molecular weight of the additive without disintegrating the endothelial monolayer, unlike polyfluorene precursors. Hydrophobic conjugate nanoparticles

can be made efficient amyloid modulators which can not only cross BBB efficiently but also can target selectively the early neurotoxic amyloid oligomers and modulate these robust aggregates into a non-pathological pathway. We believe that our findings may open a new hope of making therapeutic nanomaterials that can be used to predict and fight against Alzheimer's and pre-senile dementia.

References

(1) Sevigny, J.; Chiao, P.; Bussière, T.; Weinreb, P. H.; Williams, L.; Maier, M.; Dunstan, R.; Salloway, S.; Chen, T.; Ling, Y.; O'Gorman, J.; Qian, F.; Arastu, M.; Li, M.; Chollate, S.; Brennan, M. S.; Quintero-Monzon, O.; Scannevin, R. H.; Arnold, H. M.; Engber, T.; Rhodes, K.; Ferrero, J.; Hang, Y.; Mikulskis, A.; Grimm, J.; Hock, C.; Nitsch, R. M.; Sandrock, A. *Nature* **2016**, *537*, 50–56.

(2) Pearson, H. A.; Peers, C. *J. Physiol.* **2006**, *575*, 5–10.

(3) Morley, J. E.; Farr, S. A.; Banks, W. A.; Johnson, S. N.; Yamada, K. A.; Xu, L. *J. Alzheimers Dis.* **2010**, *19*, 441-9.

(4) Bishop, G. M.; Robinson, S. R. *Drugs Aging*. **2004**, *21*, 621-30.

(5) Cárdenas-Aguayo, M. del C.; Silva-Lucero, M. del C.; Cortes-Ortiz, M.; Jiménez-Ramos, B.; Gómez-Virgilio, L.; Ramírez-Rodríguez, G.; Vera- Arroyo, E.; Fiorentino-Pérez, R.; García, U.; Luna-Muñoz, J.; Meraz-Ríos, M. A. Physiological Role of Amyloid Beta in Neural Cells: The Cellular Trophic Activity, 2014, Neurochemistry, Dr. Thomas Heinbockel (Ed.), InTech, DOI: 10.5772/57398.

(6) Haass, C.; Selkoe, D. J. *Nat. Rev. Mol. Cell Biol.* **2007**, *8*, 101-112.

(7) Sakono, M.; Zako, T. *FEBS J.* **2010**, *277*, 1348-58.

(8) Benilova, I.; Karran, E.; De Strooper, B. *Nat. Neurosci.* **2012**, *15*, 349–357.

(9) Hefti, F.; Goure, W. F.; Jerecic, J.; Iverson, K. S.; Walicke, P. A.; Krafft. G. A. *Trends Pharmacol. Sci.* **2013**, *34*, 261–266.

(10) Tanokashira, D.; Mamada, N.; Yamamoto, F.; Kaori Taniguchi, K.; Tamaoka, A.; Lakshmana, M. K.; Araki, W. *Mol. Brain* **2017**, 10:4.

(11) Stine, W. B.; Jungbauer, L.; Yu, C.; Ladu, M. J. *Methods Mol. Biol.* **2011**, *670*, 13–32.

(12) Viola, K. L.; Klein, W. L. *Acta Neuropathol.* **2015**, *129*, 183–206.

(13) Izzo, N. J.; Staniszewski, A.; To, L.; Fa, M.; Teich, A. F.; Saeed, F.; Wostein, H.; Walko III, T.; Vaswani, A.; Wardius, M.; Syed, Z.; Ravenscroft, J.; Mozzoni, K.; Silky, C.; Rehak, C.; Yurko, R.; Finn, P.; Look, G.; Rishton, G.; Safferstein, H.; Miller, M.; Johanson, C.; Stopa, E.; Windisch, M.; Hutter-Paier, B.; Shamloo, M.; Arancio, O.; LeVine III, H.; Catalano. S. M. *PLoS One*. **2014**, *9*, e111898.

(14) Senguptaa, U.; Nilsona, A. N.; Kayed, R. *EBioMedicine* **2016**, *6*, 42–49.

(15) Sandberg, A.; Luheshi, L. M.; Söllvander, S.; Pereira de Barros, T.; Macao, B.; Knowles, T. P.; Biverstål, H.; Lendel, C.; Ekholm-Petterson, F.; Dubnovitsky, A.; Lannfelt, L.; Dobson, C. M.; Härd, T. *Proc. Natl. Acad. Sci. U. S. A.* **2010**, *107*, 15595-600.

(16) Smith, L. M.; Strittmatter, S. M. *Cold Spring Harb. Perspect. Med.* **2017**, *7*, a024075.

(17) Wang, Z. X.; Tan, L.; Liu, J.; Yu, J. T. *Mol. Neurobiol.* **2016**, *53*, 1905-1924.

(18) Folch, J.; Petrov, D.; Ettcheto, M.; Abad, S.; Sánchez-López, E.; García, M. L.; Olloquequi, J.; Beas-Zarate, C.; Auladell, C.; Camins, A. *Neural Plast*. **2016**, 2016:8501693.

(19) Chen, Y.; Liu, L. *Adv. Drug Deliv. Rev.* **2012**, *64*, 640-665.

(20) Pardridge, W. M. *Mol. Interv.* **2003**, *3*, 90-105.

(21) Abbott, N. J.; Patabendige, A. A.; Dolman, D. E.; Yusof, S. R.; Begley, D. J. *Neurobiol. Dis.* **2010**, *37*, 13-25.

(22) Robinson, M.; Lee, B. Y.; Leonenko, Z. *AIMS Mol. Sci.* **2015**, *2*, 332-358.

(23) Muthuraj, B.; Mukherjee, S.; Patra, C. R.; Iyer, P. K. *ACS Appl. Mater. Interfaces* **2016**, *8*, 32220–32229.

(24) Chowdhury, S. R.; Agarwal, M.; Meher, N.; Muthuraj, B.; Iyer, P. K. *ACS Appl. Mater. Interfaces* 2016, 8, 13309–13319.

(25) Muthuraj, B. Design and Synthesis of fluorescent probes for applications in sensors and modulating amyloid β fibrils. Ph. D. Thesis, IIT Guwahati, India, **2015**; Chapter 3b, pp 106-130.

(26) Zandomeneghi, G.; Krebs, M. R. H.; McCammon, M. G.; Fändrich, M. *Protein Sci.* **2004**, *13*, 3314–3321.

(27) Sarroukh, R.; Goormaghtigh, E.; Ruysschaert, J.-M.; Raussens, V. *Biochim. Biophys. Acta* **2013**, *1828*, 2328–2338.

(28) Biancalana, M.; Koide, S. *Biochim. Biophys. Acta* **2010**, *1804*, 1405-12.

(29) Dwivedi, A. K.; Iyer, P. K. *Macromol. Biosci.* **2014**, *14*, 508–514.

(30) Tuncel, D.; Demir, H. V. *Nanoscale* **2010**, *2*, 484–494.

Appendix

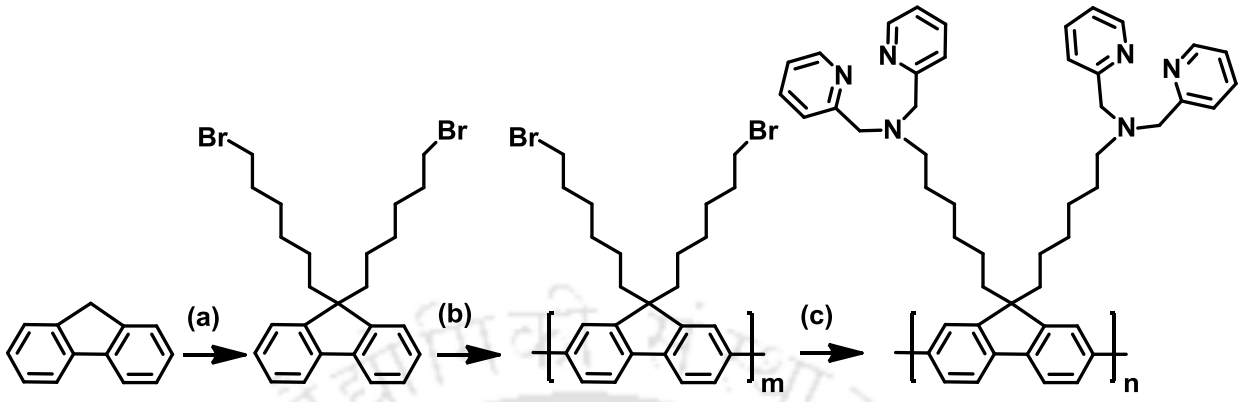

Scheme A3.1. (a) 1,6 dibromohexane, 50% aq. NaOH, TBAI (b) FeCl3, Nitrobenzene, Inert Atmosphere, room temperature (c) Di-(2-picolyl)amine, DMF, K2CO3, 100 °C. Synthetic outline of PFDPA.

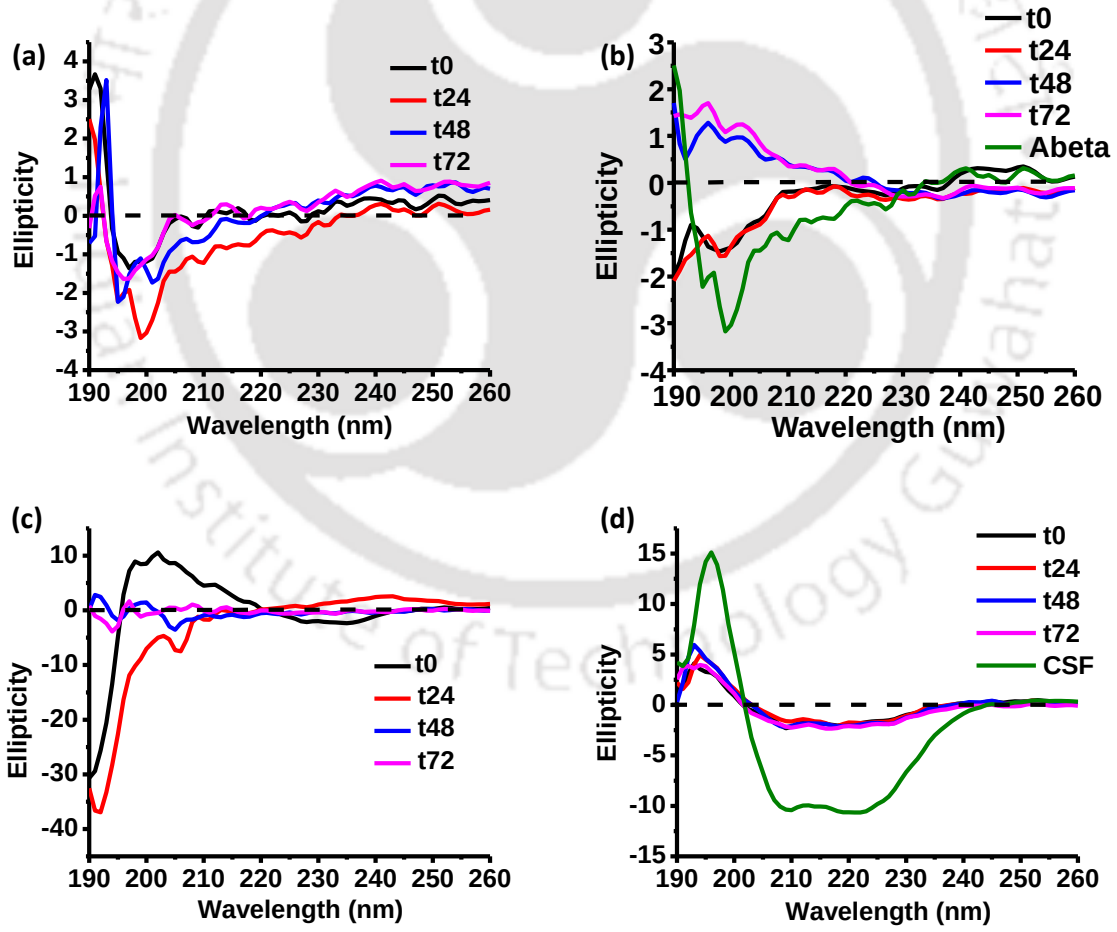

Figure A3.1. CD spectra for (a) 20 μM Aβ1-40, PC (1 mg/mL) coincubated with (b) Aβ1-40 oligomers, (c) preformed Aβ1-40 fibrils and (d) CSF (15 μM) in 1 mM PBS up to 0-72 hours.

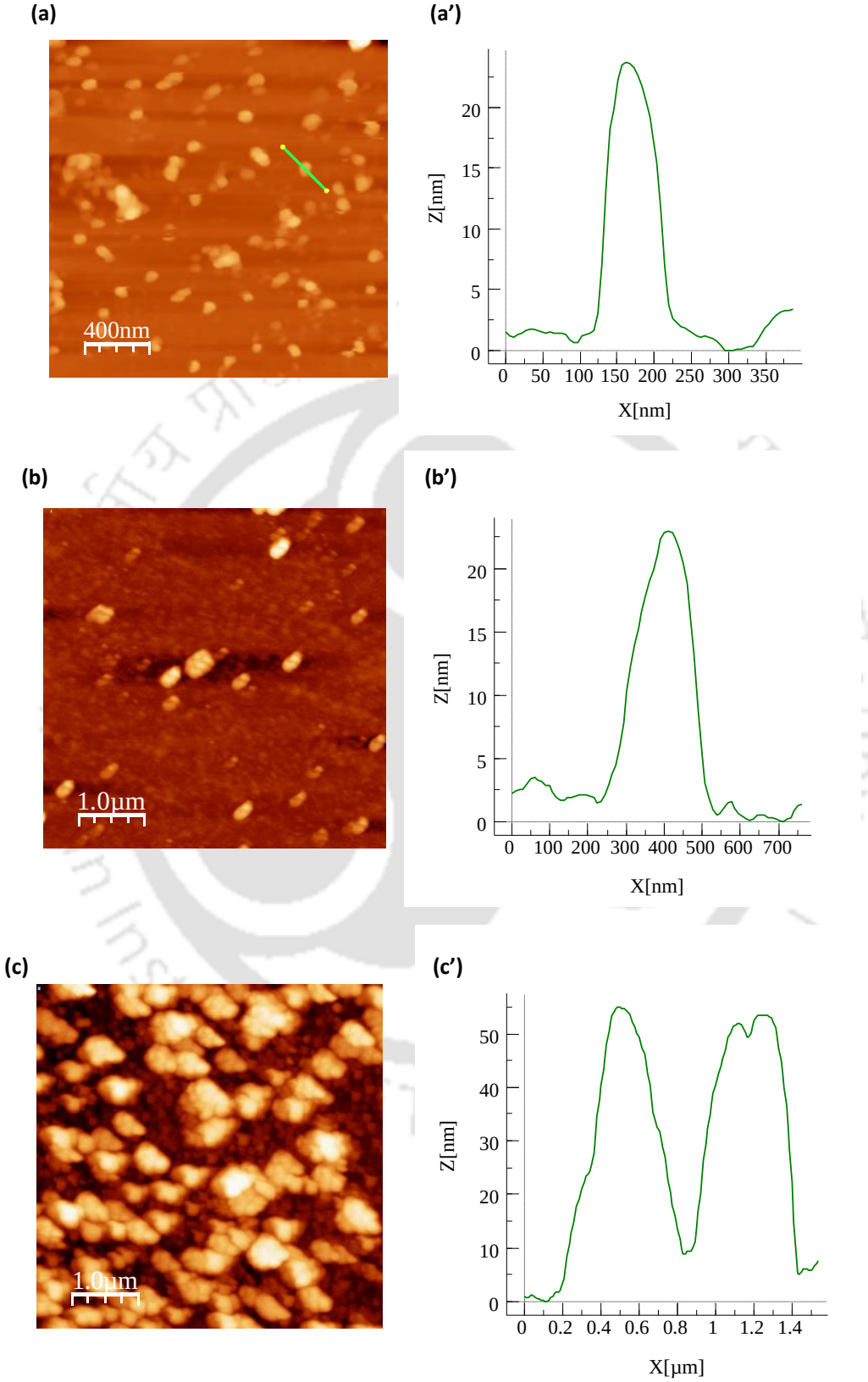

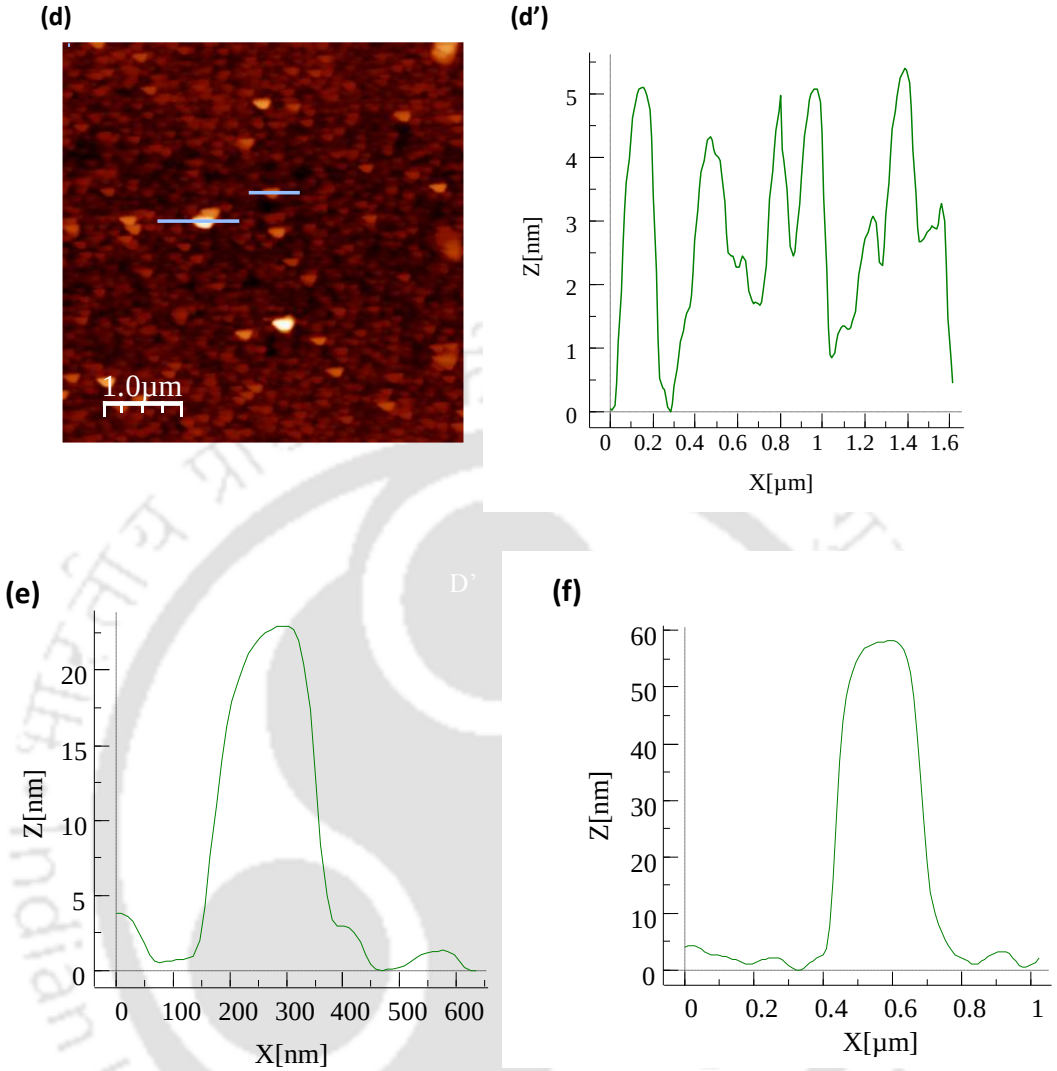

Figure A3.2. AFM images and height profile of (a, and a') Aβ1-40 oligomer, (b, and b') CSF oligomer, (c, and c') Aβ1-40 oligomer + PC, and (d, d', e, and f) CSF+PC. Samples were incubated at 37 °C in 10 mM PBS and images were taken after 84 hours of incubation.

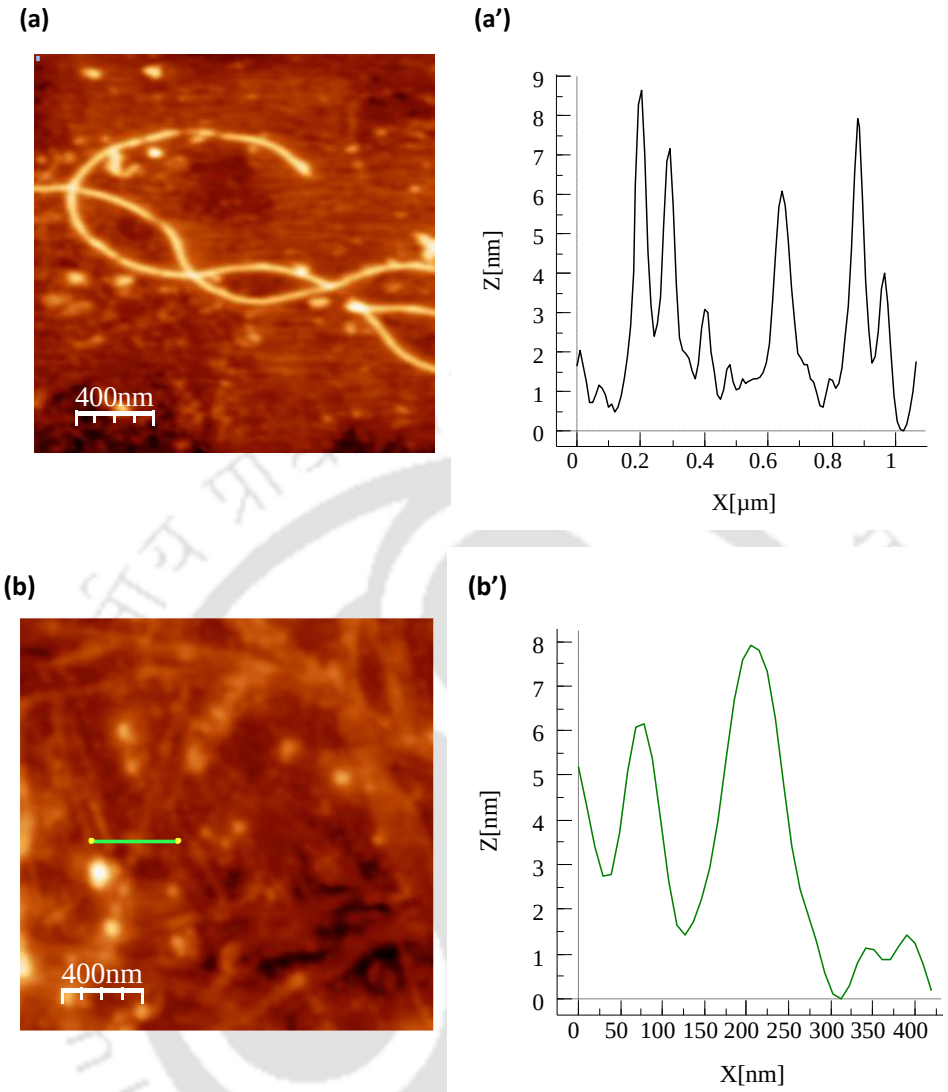

Figure A3.3. AFM images of (a, and a') Aβ1-40 fibrils and (b, and b') CSF fibrils.

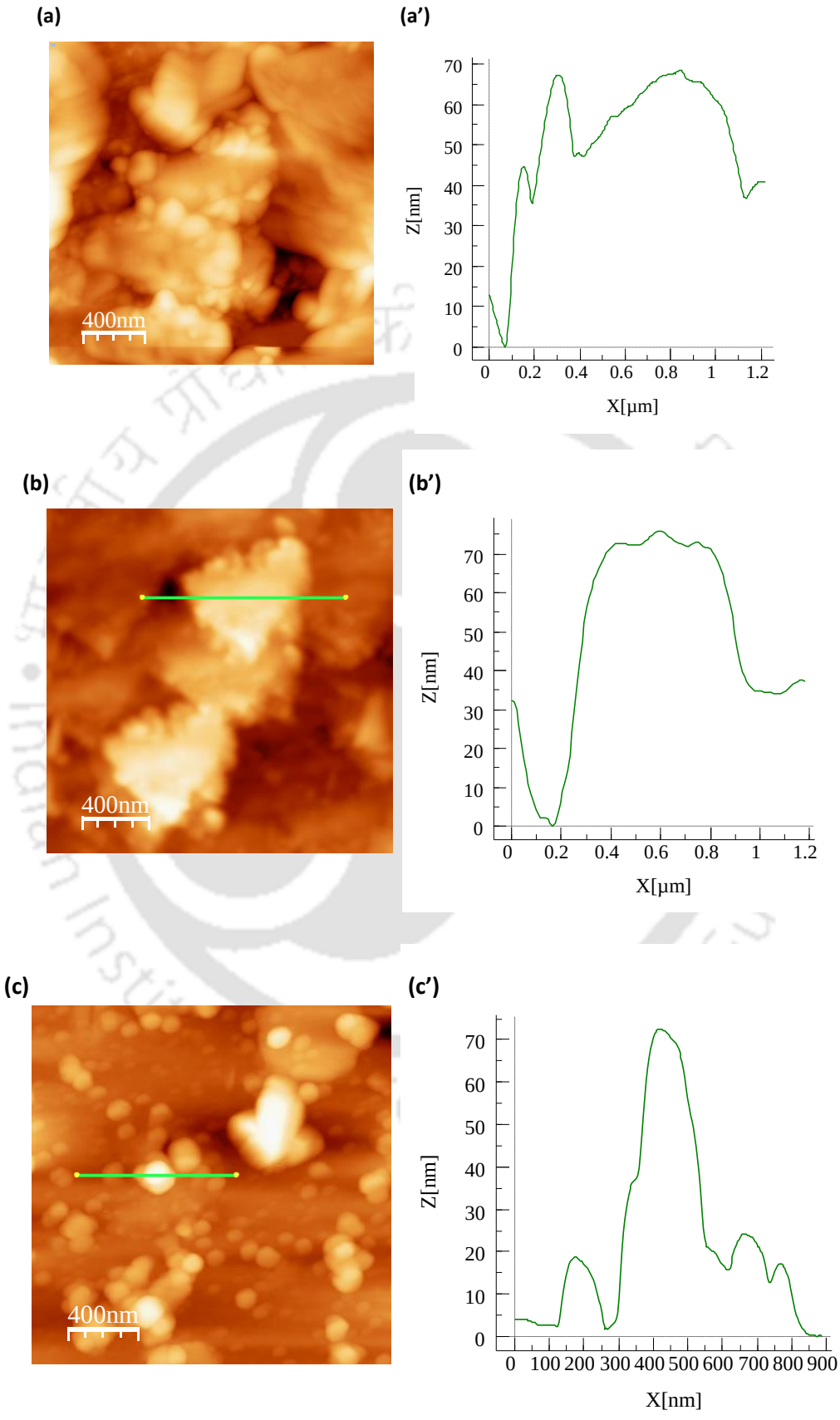

Figure A3.4. AFM images of (a, and a') Aβ1-40 oligomers + PFBr (b, and b') Aβ1-40 oligomers + PFDPA, and (c, and c') Aβ1-40 oligomers + chitosan. Samples were incubated at 37 °C in 10 mM PBS and images were taken after 84 hours of incubation.

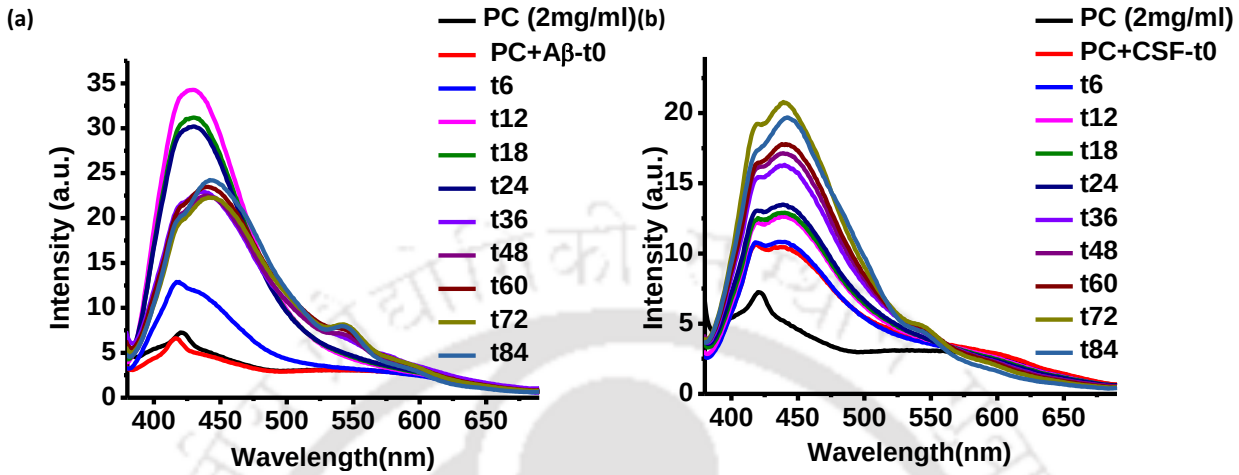

Figure A3.5. Optical response of PC (2 mg/ml) in presence of Aβ1-40 and CSF oligomers. Time-dependent (0-84 hours) fluorescence emission of (A) 2 mg/ml PC in presence of 20 μM Aβ1-40 and (B) 2 mg/ml PC in presence of CSF (15 μM). Samples were incubated in 10 mM PBS buffer (pH 7.4) at 37 °C and excited at 364 nm.

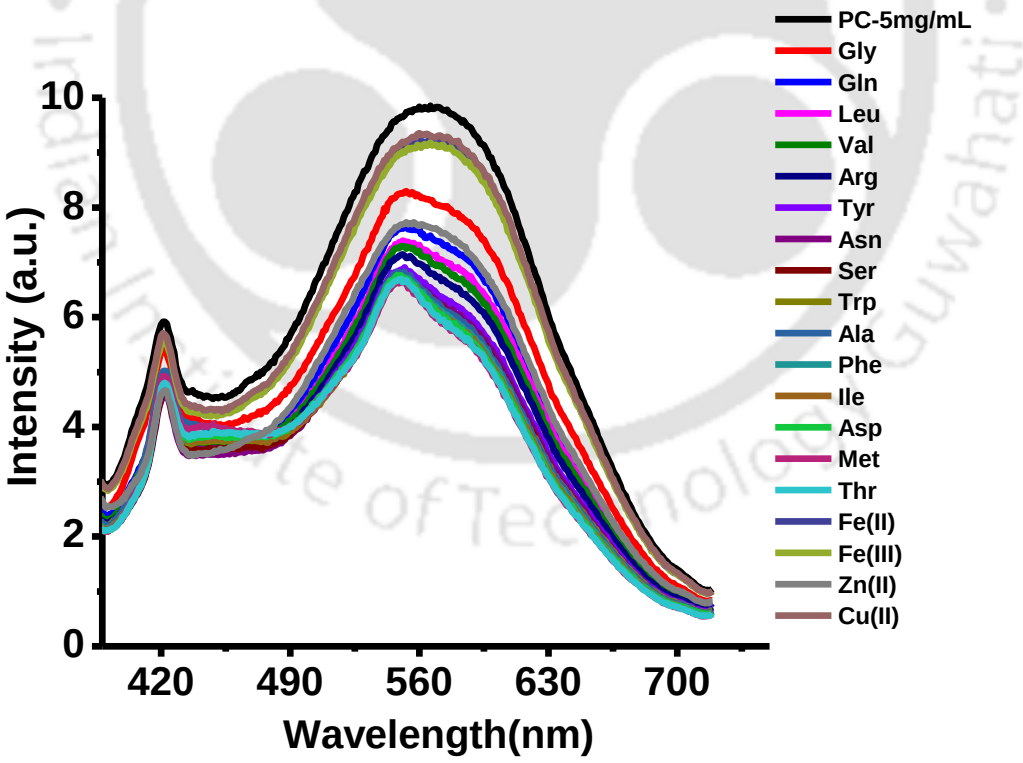

Figure A3.6. Optical response of PC (5 mg/ml) in presence of amino acids and neurotoxic metals. Emission spectra were measured in 10 mM PBS buffer (pH 7.4) at 37 °C and the solutions were excited at 364 nm.

Chapter 4

Modulating Early Stage Amyloid Aggregates by Dipeptide Linked Perylenebisimides: Structure Activity Relationship, Inhibition of fibril formation in Human CSF and Aβ1-40

Chowdhury, S. R.; Balaji, S. N.; Mondal, S.; Meher, N.; Trivedi, V.; Iyer, P. K. Modulating Early Stage Amyloid Aggregates by Dipeptide Linked Perylenebisimides: Structure Activity Relationship, Inhibition of fibril formation in Human CSF and Aβ1-40. (Submitted).

Abstract

Amyloid aggregation is observed in many neurodegenerative diseases but the formation of final plaque seldom correlates to the disease severity. Early and intermediate structures such as soluble oligomers are considered as primary toxic species in protein misfolding diseases specifically linked to Aβ in Alzheimer's disease (AD). Two peptides linked perylenebisimide isomers (PAPAP and APPPA) were developed to study the structure-activity relationship with toxic Aβ oligomer in commercial Aβ as well as in human cerebrospinal fluid (CSF), diminish and inhibit them and prevent them to form toxic amyloid fibrils from an early stage. Self-aggregation of perylenebisimides enables to form nano/micro-objects that is used to interact with the hydrophobic regions of peptide and direct the peptide aggregation into an 'off-pathway' preventing mature fibril formation. Remarkably, one of the Ala-Phe dipeptides linked perylenebisimide isomer (APPPA) showed high selectivity toward Aβ oligomer and could also cross endothelial monolayer barrier (blood-brain barrier-BBB) efficiently than the other derivative (PAPAP). Kinetic ThT studies and AFM imaging provided strong proof of both the isomers being able to inhibit fibrillation of prefibrillar and oligomeric Aβ in both commercial Aβ1-40 peptide as well as in real human CSF sample. Further, a correlation has been built using pristine fluorescence of perylenebisimides, showing modulation and 'oligo-blocking'. The obtained data provides clear evidence that the mutual aggregation between the modulator and amyloid aggregate becomes predominant compared to their individual aggregation. These results reinforce the development of structural platform design to diminish toxic oligomers, inhibit them and prevent forming toxic amyloid fibrils at an early stage.

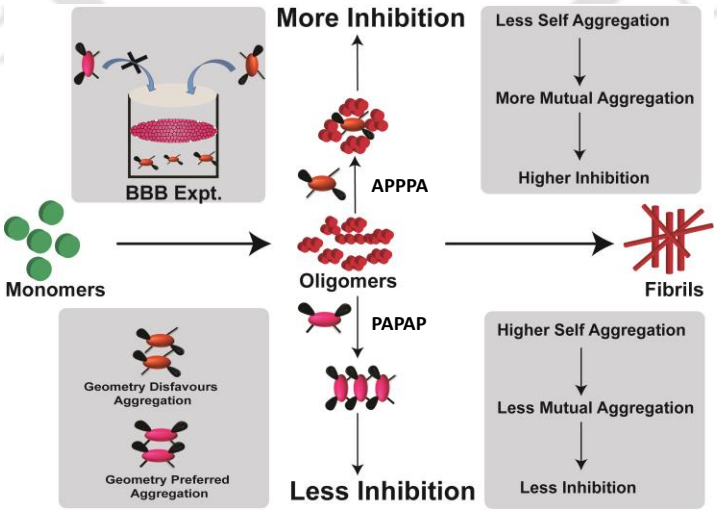

4.1. Introduction

Most common, cryptic neurodegenerative activity, viz., Alzheimer's disease (AD) emerge on a neuropathological background in the brain and are recognized post mortem by the presence of senile plaques. Specific biochemical hypotheses were developed in other neurodegeneration in contrast to AD research where identification of extracellular senile plaques and intracellular neurofibrillary tangles lead to disease genotype to decipher the process of synaptic dysfunction and pre-senile degeneration resulting in cognitive impairment. Numerous reports supporting “the toxic oligomers” have attracted the scientific community of AD in support of the fact that the soluble Aβ species may have a direct correlation with episodic declarative memory during the course of progression and ultimately killing neurons. A direct comparison of data of different results seems impossible but a common ground has been reached on the role of Aβ in disease pathogenesis and genetic risk factor of affecting APOE4 on Aβ oligomerization.[1,2] A general consensus on the fact that nontoxic monomeric Aβ converts to soluble Aβ oligomeric and metastable protofibrils with higher β-sheet content that finally transforms into fibrillar species in saline buffers in vitro is widely reported.[3] Such intermediate species are more emphatically correlated than amyloid plaques with disease symptoms when compared with brain tissues of patients having AD.[4,5] There is evidence that the penchant of oligomerization increases in case of no less than two clinical mutations in amyloid precursor protein (APP) itself amidst the Aβ peptide.[6,7] Both, preventing the accumulation and degradation or clearance of the aggregates remains the primary target as the struggle against this disease continues. Apart from its metabolic inert conditions, Aβ improves the survival of hippocampal neurons,[8,9] cooperates with extracellular matrix to stimulate neurite outgrowth[10] that may have a role in the normal function of the nervous system and brain plasticity. Therefore, Aβ should not be regarded merely as a toxic species as a whole, and inhibiting its production and dissolving the final plaques would not avoid either progression or severity. Numerous modulating attempts of targeting Aβ were considered as a viable quest with structural variations such as molecular chaperons,[11] small molecule inhibitors,[12] γ-secretase allosteric modulators,[13,14] etc. that have been designed over the past decade. Although several approaches to either inhibit or modulate Aβ are known, it remains extremely difficult to selectively pursue for soluble oligomers at an early stage.[15,16] Both computational and experimental research in general, has helped to understand nucleation as well as to develop numerous Aβ inhibitors and modulators over the past decade but none of them have been used for either pre-senile diagnosis or thera-peutics.[17-19] Herein, a new

structural strategy is devised to selectively target Aβ oligomers and an inhibitory modulation in support of the newly emerging consensus of 'toxic oligomers' and inhibit the process of further amyloid fibrillation at the primitive stage that is less understood. Two dipeptides linked perylenebisimides isomers (PAPAP and APPPA) were designed to trap the soluble amyloid transient aggregation intermediates. Initially, in vitro toxicity and blood brain barrier permeability (BBB) of both the dipeptide isomers PAPAP and APPPA were studied before checking their potential in the modulation of amyloid oligomers into final fibrillation under physiological conditions. Thioflavin T (ThT) assay, AFM images, and docking studies reveal the modulation activity of the isomers toward amyloid self-aggregation through hydrophobic interaction in commercial Aβ1-40 as well as in human CSF. The presence of amyloid aggregate intermediates lead to distinct optical responses with both isomers thus offering a correlation between optical spectra and protein secondary structures which were further confirmed using CD studies. Besides the structure-activity relationship, complementary self-aggregation and surface motif are primitive requirements for the development of next generation early inhibitors of therapeutic potential and trap the oligomers. This work substantiates that complementary aggregation achieved using dipeptide linked perylenebisimide derivatives has the unique potential to interact with the hydrophobic site of the peptide to interrupt self-aggregation even at an early stage and prevent final fibril formation.

4.2. Experimental Section

4.2.1. Materials

Dipeptides (Phe-Ala and Ala-Phe), Perylene-3,4,9,10-tetracarboxylic dianhydride (PTCDA), imidazole, phosphate buffer saline (PBS), hexafluoroisopropanol (HFIP), trifluoroacetic acid (TFA), fetal bovine serum (FBS), Dulbecco's modified Eagle medium (DMEM) and other chemicals were purchased from Merck. HPLC grade sol-vents and Milli-Q water were utilized in all the experiments. Aβ1-40, the human was bought from GL Biochem Ltd., Shanghai, China. Cerebrospinal fluid (HCSF) samples used in this study were collected from GNRC and hospital, Six Mile, Guwahati, India.

4.2.2. Synthetic procedures of PAPAP and APPPA

PTCDA (100 mg, 0.254 mmol), Phe-Ala/Ala-Phe (126 mg, 0.535mmol), Zinc acetate (1 mg, 0.005 mmol) and imidazole (1.5 g) were heated at 130 °C for 12 h with stirring. Then the reaction mixture was cooled to 90 °C before pouring into 2M HCl solution. Precipitates were

washed several times with water and dried under vacuum to obtain the red color solid (150 mg, 71% PAPAP; 139 mg, 65% APPPA).

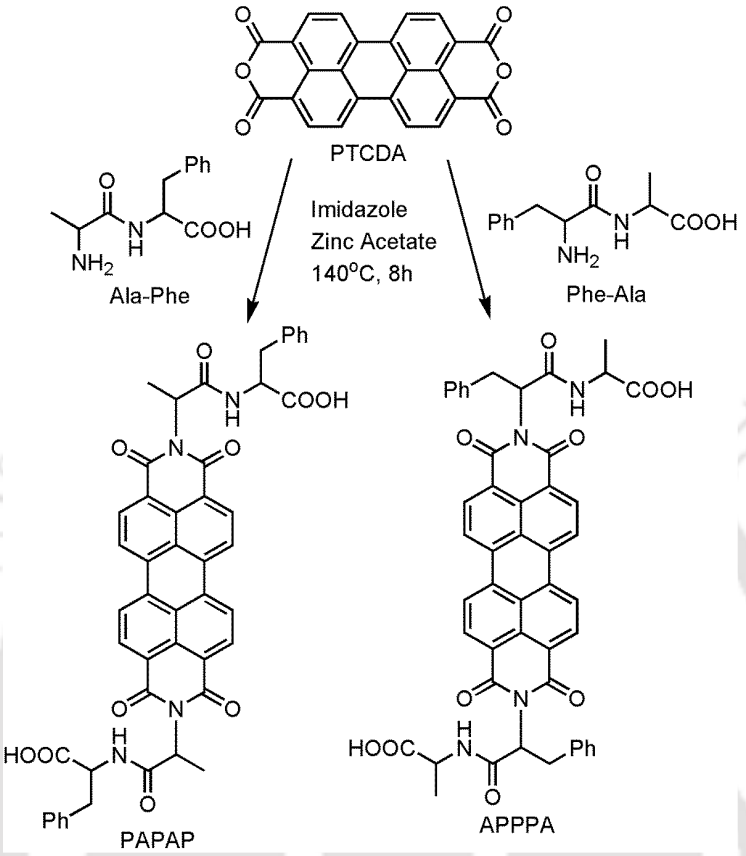

Scheme 4.1. Synthetic outline of PAPAP and APPPA.

4.2.3. Instrumentation

Fluoromax-4 Spectrofluorometer-Horiba Scientific was used to measure the fluorescence using a 10 x 10 mm quartz cuvette for solution spectra and emission was collected at 90° relative to the excitation beam. ThT assays were carried out on a Tecan microplate reader using Corning 96 Flat Bottom black, clear bottom Polystyrene plate reader. Deionized water was obtained from Milli–Q system (Millipore). Atomic force microscopy (AFM) was recorded on Bruker, Innova with non-contact tapping mode using a large scanner. DLS and Zeta Potentials were studied using Malvern Zetasizer Nano series Nano-ZS90 instrument. CD measurements were done on a JASCO J-1500-150 Spectrometer (JASCO Co. Tokyo, Japan), using a quartz cuvette (1 mm path length). NMR spectra of PAPAP and APPPA were recorded on a Bruker AscendTM 600 MHz spectrometer using DMSO-d^6 as a solvent.

4.2.4. In-vitro Cell Viability and Blood-Brain Barrier Assay

To check the intrinsic toxicity of all the precursor polymers (PFBr, PFDPA) along with the final conjugate (PC), in vitro toxicity was studied by both hemolysis assay and the MTT cell survival assay with RBCs and Ea hy926.1 respectively as described in our previous report.[23] Endothelial cells (EA hy926.1) were harvested as usual in complete growth media, Dulbecco's Modified Eagle Medium (DMEM, HiMedia) with 10% fetal bovine serum (Gibco) and antibiotics (Anti-Anti, Gibco) at 37 °C in 5% CO_2 incubator and 25,000 cells were seeded per well in a 96-well plate. Twelve hours later, cells were treated with different concentrations of PFBr, PFDPA, and PCs (0–100 μg/ml) for 12 h and the cell survival was determined by standard MTT assay.

Prior to cell viability, in-vitro blood-brain barrier assay (BBB) was performed by making an endothelial monolayer barrier. Briefly, endothelial cells were seeded in a special cell culture plate (60 mm) which poses 3-micron pore for crossing. Endothelial cells were grown densely till completely seal the pores. This plate was maintained in a 100 mm sterile plate with an adequate amount of media. PFBr, PFDPA and PCs solutions (50 μg/ml) were prepared in complete media and gently added in three different 60 mm dishes (upper chamber) and the media was collected from the 100 mm dish (lower chamber) after every 1-hour interval till 6 hrs. Further, the permeability was checked by measuring fluorescence of all the test compounds. Leakage was corrected by using Evans blue as a control and to calculate the actual permeability of the precursor polymers and conjugates.

4.2.5. Preparation of stock solution

1 mM PAPAP and APPPA stock solutions were prepared in 10 mL PBS. This stock solution was diluted to the desired concentration for further incubation during modulation and imaging studies. All the experiments like UV-Visible, FT-IR and fluorescence titrations were performed in 10 mM PBS buffer and pH maintained at 7.4.

4.2.6. Cell Viability Assay

Cell viability assay of PAPAP and APPPA was performed following a known protocol using two different cell lines (U-87 MG and EA hy926.1) and hemolysis assay.[20,21] U-87 MG cells were sowed into 96-well plates at an underlying sowing thickness of 10,000 cells/well in 100 μL medium. The cells were developed for 24 h at 37 °C in 5% CO2. Then the cells in each well were treated with PAPAP and APPPA separately in a concentration range 0-20 μM in 100 μL serum-free media. After incubation for 48 h, the Methylthiazolyldiphenyl-tetrazolium bromide (MTT) solution (10 μL, 5 mg/mL in PBS) was added to each well. The plate was

further incubated at 37 °C in 5% CO2 for 3 h. Then MTT-containing medium was charged by 100 μL DMSO to solubilize MTT-formazan crystals. Absorbance was measured at 570 nm after incubation for 5 min at 37 °C, and reference reading was recorded at 690 nm in ELISA micro-plate reader (Infinite 200 PRO, TECAN). The results were normalized by setting the cell viability of U-87 MG cells in phosphate buffer saline (PBS) control to be 100%. Cytotoxicity of APPPA and PAPAP were further evaluated by hemolysis assay as described previously.[21] Fresh blood was drawn from healthy volunteers in EDTA container and hematocrit was separated from plasma by brief centrifugation. Further, hematocrit was washed thrice with dextrose (1 mg/ml) containing PBS. After washing, hematocrit (5 % v/v) was treated with 0 to 100 μg/mL of APPPA or PAPAP individually and incubated at 37 °C for 6 h. After that hemoglobin was measured from the collected supernatant at 540 nm by using a microtitre plate reader (Spectromax M2e). Hemolysis percentage was determined with the 0.1 % (v/v) Triton x 100 lysed positive controls. Endothelial cells (EA hy926.1) were harvested from culture plate, and 25,000 cells were seeded per well. Cells were treated with different concentrations of APPPA and PAPAP (0–100 μg/mL) for 12 h and the cell survival was determined by standard MTT assay.

4.2.7. TFA/HFIP treatment of Aβ1-40

1 mg of Aβ1–40 was initially dissolved in trifluoroacetic acid (TFA) to obtain a homogeneous solution in a 1.5 mL micro centrifuge tube. The TFA was evaporated under argon flow later. A film like material was obtained after removing TFA. HFIP was added and similarly evaporated using argon gas flow. This process was repeated thrice. Finally, 1 mL PBS (10 mM, pH 7.4) was added to the micro centrifuge tube to obtain a final concentration of 1.358 X 10^{-4} M. Amyloid fibril formation was monitored using ThT binding assay in a Tecan microplate reader.

4.2.8. Preparation of Aβ1–40 aggregates and ThT Binding Assay

After the TFA/HFIP treatment for amyloid peptide, the Aβ1–40 (20 μM) was incubated with ThT (40 μM) at 37 °C for 72 h (pH 7.4 in 10 mM PBS) for the preparation of amyloid peptide aggregates. Further, aggregation of Aβ1–40 amyloid fibrils were monitored both in presence and absence of modulators at specified time incubations by monitoring ThT (20 μM) fluorescent enhancement peak at λem 482 nm (λex 440 nm) using a microplate reader.

4.2.9. Confirmation of Aβ1–40 aggregates in human cerebrospinal fluid (HCSF)

The presence of Aβ fibrils in HCSF was confirmed by adding 50 μL HCSF (1 μM) solution into ThT (40 μM) solution (10 mM PBS, pH 7.4). A similar fluorescence enhancement in ThT spectrum in presence of Aβ1-40 at 482 nm was observed upon binding with amyloid aggregates in HCSF. Further, aggregation of Aβ1–40 amyloid fibrils in HCSF was monitored both in the presence and absence of modulators with different time incubations by monitoring ThT (20 μM) fluorescence enhancement peak at λem 482 nm (λex 440 nm) using a microplate reader.

4.2.10. Modulating Experiment for Aβ1–40 Aggregates

The modulating ability of PAPAP and APPPA were examined by the changes in the fluorescence spectra in presence of Aβ1–40 in commercial and in real HCSF samples. The samples were prepared in PBS buffer (10 mM, pH 7.4) and incubated at 37 °C. When PAPAP and APPPA (5 μM) solutions were excited respectively at 495 nm and 497 nm, dual emission peaks at 547 nm along with a shoulder at 589 nm was observed in case of PAPAP and at 549 nm and the hump at 591 nm in case of APPPA. Further, upon addition of Aβ1–40 fibrils (20 μM) and HCSF Aβ fibrils (1 μM) into the PAPAP and APPPA solution (5 μM), the fluorescence changes observed instantly in PAPAP/APPPA + Aβ1–40 and PAPAP/APPPA + HCSF aggregate mixtures were minimum. However, after incubation (0–90 h) at 37 °C (pH 7.4), gradual fluorescence quenching occurred in the PAPAP/APPPA + Aβ1–40 and PAPAP/APPPA + HCSF solutions, respectively.

4.2.11. In vitro Blood Brain Barrier Assay

In vitro blood brain barrier assay (BBBA) was also performed using an endothelial monolayer. First, endothelial cells were seeded in a special cell culture plate (60 mm) which poses 3-micron pore for small molecule crossing. Endothelial cells were grown densely till they completely seal the pores. This plate was maintained in a 100 mm, sterile plate with an adequate amount of media. 50 μg/mL of APPPA or PAPAP were gently added to a 60 mm dish and the media collected from the 100 mm dish at 1 h interval from 0 to 6 h. Both APPPA and PAPAP level was measured by Fluorescence spectroscopy. Evans blue was used to check the leakage in the system as well as to correct the actual permeability of the test molecules.

4.3. Results

4.3.1. Design, Synthesis, and Characterization of PAPAP and APPPA as an amyloid modulator

The amino acid sequence Aβ16-23 (KLVFFAED) has a strong statistical preference for β-strand structure[22,23] and previous findings on perylenebisimides as in vitro amyloid modulator encouraged the selectivity studies using this aromatic core as well as to investigate the possible interactions with toxic Aβ1-40 oligomers. Amyloid plaques do not correlate with the severity of the cognitive decline or lead to plaque-only dementia whereas soluble oligomeric species and small protofilaments (having much smaller diameters than mature fibrils) are known to induce neuronal cell death and disturb neuro-transmission.[4,5,24-26] Herein, two dipeptides functionalized perylenebisimides (Scheme 4.1) have been designed as modulators for early stage Aβ aggregates to trigger the aggregation phenomenon once the oligomeric species are present. Two consecutive hydrophobic residues from Aβ16-23, phenyl alanine and alanine were chosen as tentacles on the aromatic core of perylene, resulting in two different perylenediimide fluorophores. Though their molecular weights are identical they differ in attachment site, thereby giving rise to distinct aggregation pattern in an aqueous environment. Till date, aggregation-caused quenching (ACQ) phenomenon in perylenebisimide diminished their optical response, yet they retain their ability to prevent amyloid oligomers to final fibrillation. In this work, both commercial Aβ1-40 and human cerebrospinal fluid (HCSF) were used as a source of in vitro amyloid in saline buffer (pH 7.4) and co-incubated in presence of both PAPAP and APPPA isomers to check their potential as Aβ modulators. These small molecule isomer-protein interactions have been validated using ThT fluorescence, AFM, CD and FT-IR studies. Dipeptides were attached to perylene core in good yields using a known synthetic procedure and the products (both PAPAP and APPPA) were purified after precipitating out in dilute acidic solution. Finally, the obtained red color solids were characterized by MALDI-TOF mass spectrometry and 1H NMR spectroscopy (Figure A4.1-A4.4).

4.3.2. Inhibitory effects of PAPAP and APPPA on Aβ1-40 peptide aggregates

The formation of Aβ fibrils and the prevention of protein self-aggregation was monitored by measuring ThT fluorescence enhancement.[27-30] Upon addition of Aβ1–40 (20 μM) monomer into ThT (40 μM), a gradual enhancement of the emission peak at 488 nm was observed over

0–72 h incubation time (λex – 440 nm) (Figure 4.1a, red line) as it self-associates into the β-rich fibril structures. The native unfolded state of Aβ slowly changes into a partially folded state causing the initial lag phase in ThT assay,[31,32] which then gradually follows a nucleation-growth mechanism to form protofibrils via seeding effect and finally these protofibrils are further self-assembled into long fibrillar aggregates that result into a flat terrain in ThT plot (Figure 4.1a).

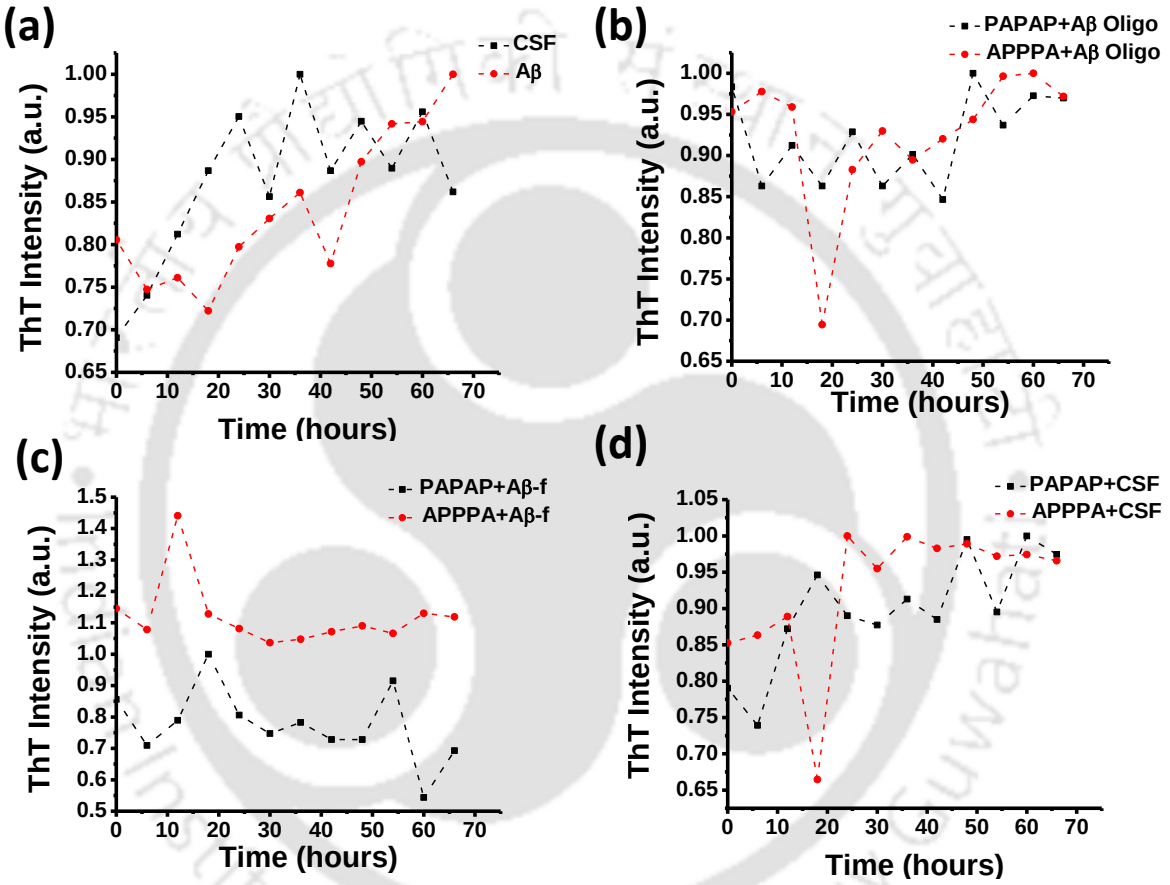

Figure 4.1. ThT Assay. (a) Fibrillation kinetics of HCSF (red circles, 1μM) and commercial Aβ1-40 (black squares, 20 μM) (b) Aβ (20 μM) oligomers in presence of 5 μM PAPAP (black squares) and APPPA (red circles) (c) Pre-fibrillar Aβ (Aβ-f, 20 μM) in presence of 5 μM PAPAP (black squares) and APPPA (red circles) (d) HCSF oligomers (1μM) in presence of 5 μM PAPAP (black squares) and APPPA (red circles). Samples were incubated at 37 °C in 10 mM PBS buffer at pH 7.4 and 40 μM ThT was added before recording fluorescence spectra.

The existence of the growth phase in ThT fluorescence profile of HCSF proved the presence of Aβ oligomers in HCSF and that particular HCSF sample containing Aβ oligomers was chosen for further studies (Figure 4.1a, black squares). On adding 50 μL (~1μM) of HCSF (in presence

of 40 μM ThT, pH 7.4 in 10 mM PBS) fluorescence intensity of ThT increased initially up to 24 h. It was further incubated till 72 h to obtain a plateau. Both enhancements indicated the presence of Aβ oligomers which was transformed to mature fibril (Figure 4.1a). 20 μM Aβ1-40 was incubated at 37 °C in PBS (pH 7.4) for 24 h in dark after pre-treatment to make in vitro amyloid oligomers. These oligomers were further incubated with 5 μM PAPAP and APPPA separately in 10 mM PBS buffer (pH 7.4) for 72 h. An instant decrease in ThT fluorescence intensity was observed (Figure 4.1b, red circles) when APPPA was present with Aβ oligomers unlike PAPAP, where ThT intensity follows a flat profile (Figure 4.1b, black squares). When preformed fibrils were incubated under the same conditions in presence of both the modulators separately, ThT intensity initially increased from 0-15 h in case of APPPA and 0-20 h in case of PAPAP and then started decreasing before becoming a plateau (Figure 4.1c). Surprisingly, even with HCSF sample (~1 μM) containing oligomeric amyloid aggregates an almost similar ThT intensity profile was seen in case of preformed Aβ1-40 oligomers (Figure 4.1d). A steep decrease in ThT fluorescence was observed within first 20 h of incubation with 5 μM APPPA (Figure 4.1d, red circles) containing HCSF oligomers. In presence of 5 μM PAPAP, ThT intensity increased initially before reaching a flat terrain (Figure 4.1d, black squares). Attachment of the dipeptides played an interesting role in their self-aggregation and accordingly toward interactions with amyloid. In the case of APPPA, phenyl group of phenyl alanine stays close to the aromatic core, unlike PAPAP. The ThT assay gave a hint of preference for amyloid oligomers in one of the small molecules (APPPA) and the perylene core provided sufficient hydrophobic interaction with the hydrophobic surface of the amyloid aggregates resulting in the inhibition and formation of the final fibrillar network. Structural differences between PAPAP and APPPA led to the distinctive differences in reactivity toward amyloid aggregate and the position of the phenyl ring of the attached phenyl alanine in both perylenebisimide derivatives likely played a pivotal role in modulating the amyloid aggregation.

4.3.3. Effect of PAPAP and APPPA on the secondary structure of Aβ1-40

To confirm the effects of modulators on the protein secondary structure, CD measurements of amyloid aggregates (both Aβ1-40 and HCSF) were performed both in the presence and absence of APPPA and PAPAP at specified time interval. For control, 20 μM Aβ1-40 was diluted in 1 mM PBS from the incubated 100 μM Aβ1-40 stock solution at 37 °C in 10 mM PBS (pH 7.4) and the conformational transition into ordered β sheet via aggregation was measured using CD measurements. Initially, a negative peak at around 192 nm was observed indicating

an initial random coil which slowly transformed into ordered β-sheet when incubated at 37 °C in PBS buffer (pH 7.4). A positive maximum at 193 nm and a broad negative minimum at 215 nm appeared after 24 h incubation which indicated the structural transition of Aβ1-40 (20 μM) from the initial random coil to β-sheet structure (Figure A4.5a), consistent with previous studies.[33] A similar response was also observed in the case of chosen HCSF sample (Figure A4.5b). When Aβ1-40 oligomers were incubated with the APPPA, negative minimum at 193 nm was blue shifted and a new positive maximum appeared at 195 nm (Figure 4.2a) after 24 h and ultimately disappeared after 60 h of incubation, confirming no ordered β-sheet formation. In the case of PAPAP, there was a hint of ordered β-sheet formation from Aβ1-40 oligomers after 24 h incubation i.e. a positive maximum at 193 nm along with a broad minimum of around 215 nm was observed which diminished after 60 h incubation (Figure 4.2b).

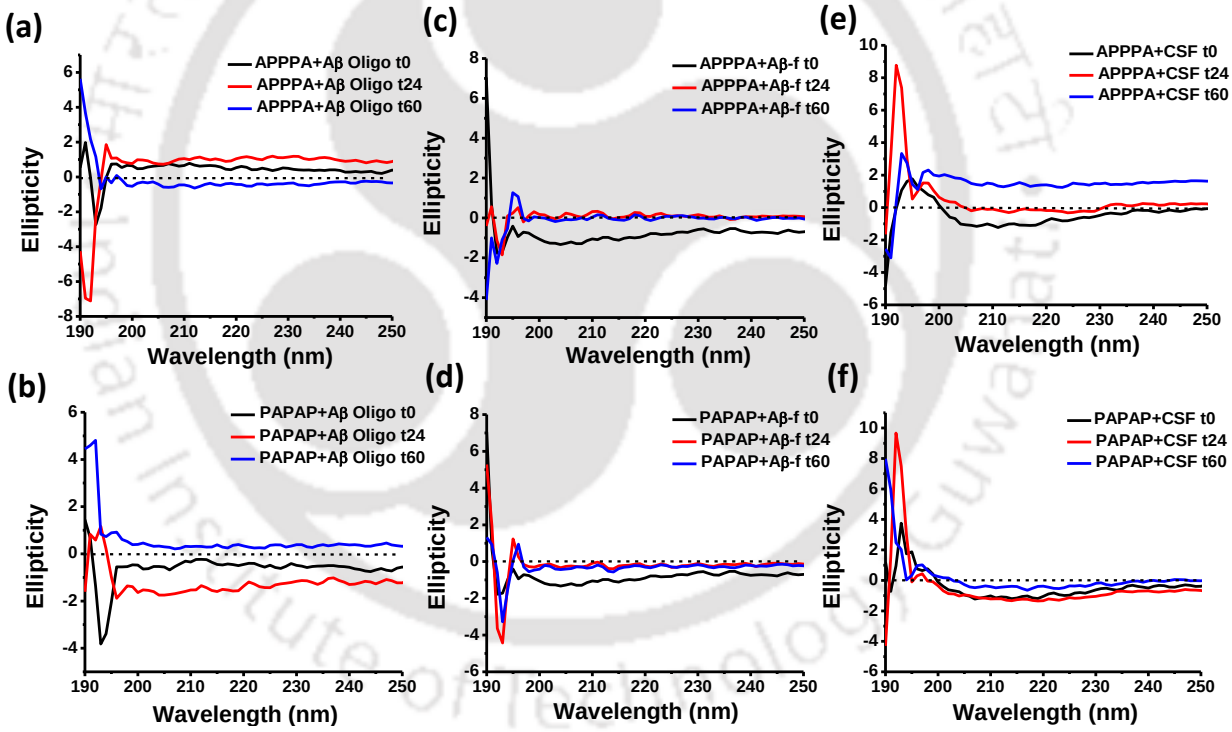

Figure 4.2. CD spectra of Aβ coincubated with PAPAP and APPPA (a) Aβ1-40 oligomers (20 μM) in presence of APPPA (5 μM) (b) Aβ1-40 oligomers (20 μM) in presence of PAPAP (5 μM) (c) Prefibrillar Aβ1-40 (20 μM) in presence of APPPA (5 μM) (d) Prefibrillar Aβ1-40 (20 μM) in presence of PAPAP (5 μM) (e) HCSF (1 μM) in presence of APPPA (5 μM) (f) HCSF (1 μM) in presence of APPPA (5 μM) after 0-60 h of incubation in 1 mM PBS (pH 7.4).

No significant ellipticity was observed except only a positive peak at 191 nm alongside a small hump at 195 nm. These results confirm the selectivity of APPPA for the amyloid oligomers

over PAPAP. When prefibrillar Aβ1-40 aggregates were incubated with APPPA, broad negative peak at 205-215 nm disappeared and only a negative peak at 193 nm showed up after 24 h incubation. After 60 h incubation, a positive peak at 194 nm appeared and the negative minimum shifted to 191 nm (Figure 4.2c). In presence of PAPAP, ordered β-sheet structure of prefibrillar Aβ1-40 changed after 24 h incubation. The negative minimum at 215 nm weakened and a positive hump at 194-196 nm appeared along with a negative minimum at 192-193 nm (Figure 4.2d). In HCSF, a sample containing Aβ oligomeric aggregates showed a similar negative hump at around 205-215 nm alongside a positive maximum at 194 nm in presence of APPPA initially and after 24 h incubation the negative minimum disappeared, a positive peak at 191 nm alongside a small hump at 197 nm was observed (Figure 4.2e). Further incubation (up to 60 h) led to a small positive peak at 192 nm indicating no further ordered peptide β-sheet formation. The ordered β-sheet aggregates persisted even after 24 h incubation, but after 60 h incubation, the negative hump diminished along with negligible ellipticity except for a small hump at 196 nm (Figure 4.2f) in presence of PAPAP. Hence, both APPPA and PAPAP were able to interrupt Aβ self-aggregation in both Aβ1-40 and HCSF samples, whereas, APPPA was found to be more reactive towards toxic oligomeric structures. Remarkably, both APPPA and PAPAP were shown to redirect the nucleation of the prefibrillar Aβ1-40 aggregates. To comprehend the structural features, FT-IR spectra of APPPA and PAPAP incubated with Aβ1-40 oligomers and prefibrillar aggregates were recorded to observe the amide band at 1633-1643 cm-1 (Figure A4.6) which are mainly ascribed to the native FT-IR β-band conformation.[34] These observations suggest that the already existing β rich oligomers (present in FT-IR spectra, Figure A4.6) are inhibited to aggregate in presence of PAPAP and APPPA (small molecular modulator, as shown in CD spectra). Precisely APPPA was able to interact with Aβ oligomers and early stage intermediates more rapidly compared to PAPAP, successfully inhibiting its conformational changes to final fibril formation and their mutual aggregation direct fibrillation into "off-pathway'.

4.3.4. Morphological changes in Aβ aggregates in presence of PAPAP and APPPA modulators

Morphological changes of Aβ aggregates have been studied using atomic force microscopy (AFM) (Figure A4.7) both in the presence and absence of PAPAP and APPPA as modulators. Freshly prepared native Aβ solution was incubated in dark for 24 h to obtain small oligomers as observed in the topography image (Figure A4.7a). The diameters of Aβ oligomers were observed to be ~60 nm and ~5 nm height (Figure A4.8a). After 72 h incubation, Aβ fibrils

were formed as seen in the topography image (Figure A4.7b) with ~100 nm diameter and ~2.5 nm height (Figure A4.8b) confirming that these early stage monomers and small oligomers continue to accumulate to form protofibrils and then into mature fibrils. HCSF sample containing oligomeric Aβ were also confirmed to be topography images of the real HCSF sample (Figure A4.7c) and showed a large number of oligomers of similar width ~60-70 nm and height 5-7 nm (Figure A4.8c). After 24 h incubation, similar fibrillar structure was found in HCSF sample (Figure A4.7d). The diameter of Aβ fibrils in HCSF was observed to be ~90-100 nm diameter and ~1.5-2 nm height (Figure A4.8d). Aβ1-40 (20 μM) and HCSF (1 μM) co-incubated with APPPA and PAPAP (5 μM each) at 37 °C showed no fibril formation (Figure 4.3) after 72 h. In presence of APPPA and Aβ1-40, oligomers were blocked to approach each other and resulted in an increase in their diameter from ~100-300 nm and 30-50 nm height (Figure A4.9a) due to the presence of both aggregates (shown using a black arrow in figure 4.3a).

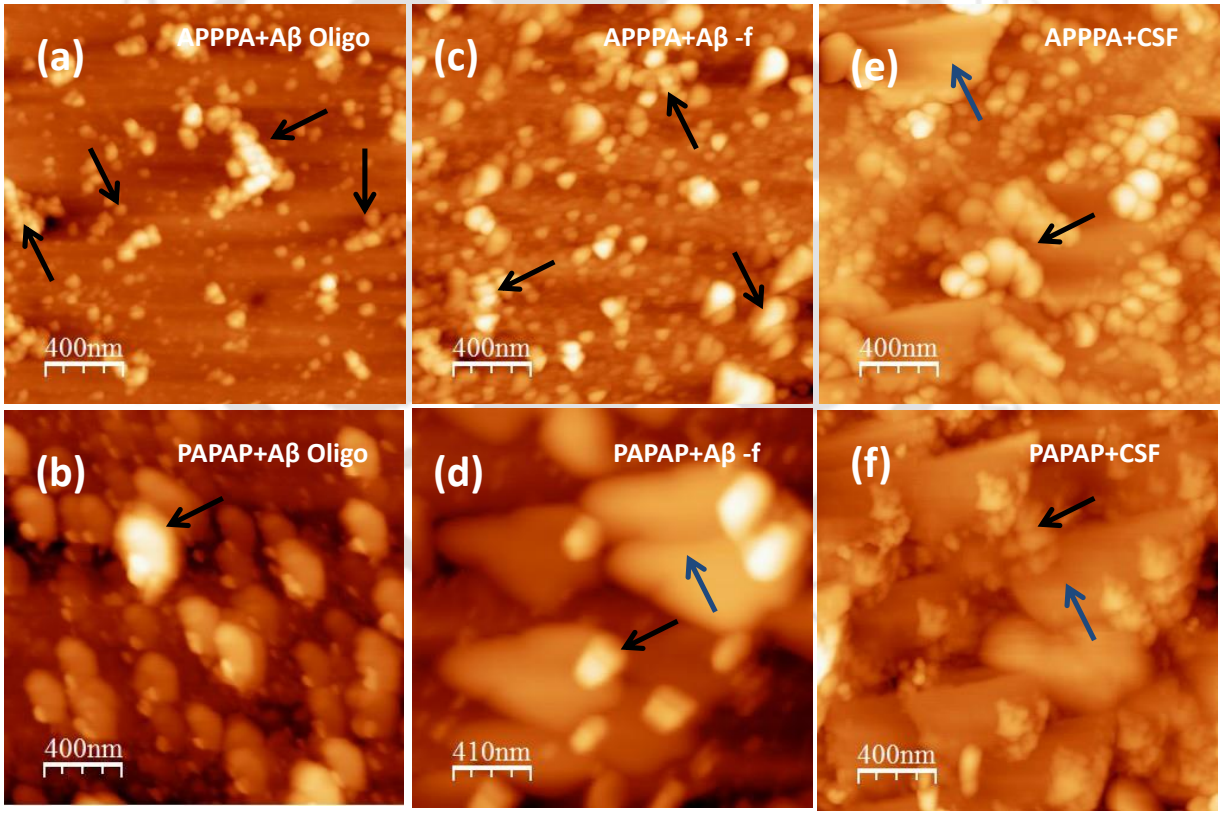

Figure 4.3. AFM images of PAPAP and APPPA co-incubated Aβ samples after 72 h of incubation at 37 °C. (a) Aβ oligomers in presence of APPPA (b) Aβ oligomers in presence of PAPAP (c) Prefibrillar Aβ in presence of APPPA (d) Prefibrillar Aβ in presence of APPPA (e) HCSF in presence of APPPA and (f) HCSF in presence of PAPAP. Large perylene aggregates were shown using the blue arrow and black arrow represented the presence of both Aβ and PAPAP/APPPA aggregates.

Whereas with the PAPAP molecule, self-aggregation was prevalent compared to APPPA and as a result, PAPAP co-incubated with Aβ1-40 showed aggregates having larger diameters of 0.2-0.4 μM (Figure 4.3b) with a height profile of 30-60 nm (Figure A4.9b). When prefibrillar Aβ1-40 aggregates were incubated with APPPA (5μM) for 72 h, these aggregates were found to have a diameter of ~200 nm (Figure 4.3c) with 20-40 nm height (Figure A4.9c). In presence of prefibrillar Aβ1-40 aggregates, PAPAP aggregated more through π stacking (Figure 4.3d) with a diameter ranging from 0.5-0.8 μM and 40-80 nm height (Figure A4.9d) unlike in the case of APPPA. In the case of HCSF oligomer co-incubated with APPPA, aggregates having diameter ~200-400 nm (Figure 4.3e) and 35-60 nm height (Figure A4.9e) were formed after 72 h incubation. In presence of PAPAP, the peptide aggregation in HCSF was similarly blocked and the aggregates were found to have larger diameter of ~0.2-0.6 μM (Figure 4.3f) and 25-35 nm height (Figure A4.9f). These morphological data suggested that both small molecule and peptide aggregation was complementary to each other and APPPA had an advantage of blocking the oligomers over PAPAP due to its similar surface motif as Aβ1-40 oligomers. Briefly, no prefibrillar structures were converted to fibrillar network in the presence of modulators except sparse population of larger self-aggregates (more in case of PAPAP compared to APPPA) of small molecules as APPPA stacking was less compared to PAPAP and the same was observed in their UV-Vis studies (Self-aggregation was shown using blue arrow in figure 4.3d, 4.3e, and 4.3f).

4.3.5. Correlation between peptide aggregation and optical response of PAPAP and APPPA

With the aim of evaluating protein aggregation using optical responses of these two chromophores, Aβ1-40 (20 μM) was co-incubated with PAPAP and APPPA (5 μM each). Fluorescence spectrum of the co-incubated samples were recorded at different incubation time (Figure 4.4). When APPPA co-incubated with Aβ1-40 (20 μM) and HCSF (1 μM) was excited at 497 nm, fluorescence enhancement of the emission peak at 552 nm with a prominent shoulder at 591 nm was observed after 24 h (Highest intensity was observed after 12 h co-incubation with peptide oligomers, Figure A4.10) incubation favoring the oligomer-APPPA interaction through available hydrogen bonding and non-covalent interaction (Figure 4.4a and 4.4e). APPPA fluorescence intensity (5 μM) decreased upon further incubation up to 66 h at 37 °C (pH 7.4) due to the likely formation of larger aggregates of both small molecule and peptide. But, in the presence of prefibrillar aggregates of Aβ1-40, APPPA fluorescence intensity gradually decreased (Figure 4.4c). PAPAP (5 μM) co-incubated with Aβ1-40

oligomers, pre fibrillar aggregates (20 μM) and HCSF (1 μM) did not show any significant optical response (emission peak at 550 nm and the hump at 590 nm remained unchanged in Figure 4.4b, 4.4d, and 4.4f) when excited at PAPAP excitation of 495 nm. To rule out the contribution of self-aggregation and environmental effects, fluorescence experiments were performed in the absence of peptides. APPPA showed a minor increase in intensity in organic solvents but optical responses of PAPAP remained static even after 5 days of incubation at 37 °C (Figure A4.11). However in aqueous environment quenching occurred due to favorable π-stacking. Changes in PAPAP were more compared to APPPA as it was less prone to self-aggregation. This was further evident from fluorescence spectra when concentration of the perylenebisimides was varied from 1-100 μM. In both the cases, highest intensity was observed at lower concentration (from 1-15 μM) before it started decreasing due to aggregation (Figure A4.12). Almost negligible changes were observed in presence of other amino acids and brain metals (Figure A4.12). These observations revealed that the presence of oligomers enhanced APPPA fluorescence, unlike prefibrillar aggregates. Change in the optical spectrum was visible only in case of APPPA unlike PAPAP co-incubated aggregates due to the more dominant self-aggregation in PAPAP.

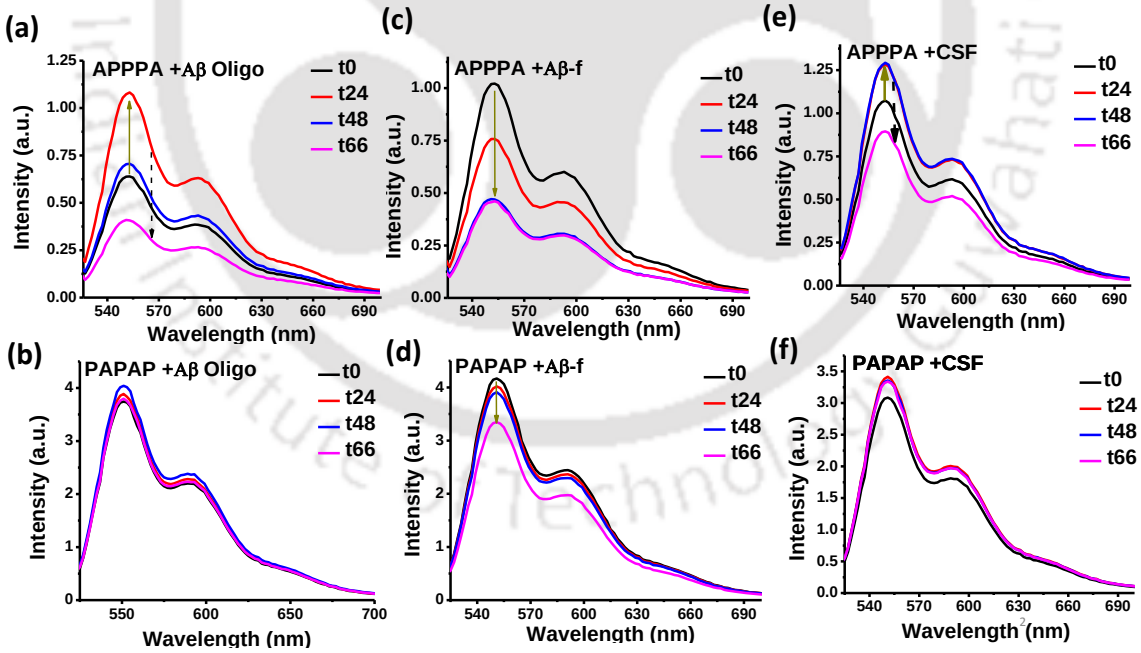

Figure 4.4. Emission spectra of PAPAP and APPPA co-incubated with Aβ (0-66 h). Fluorescence spectra of (a) 5 μM APPPA in presence of Aβ oligomers (20 μM) (b) 5 μM PAPAP in presence of Aβ oligomers (20 μM) (c) 5 μM APPPA in presence of prefibrillar Aβ (20 μM) (d) 5 μM PAPAP in presence of prefibrillar Aβ (20 μM) (e) 5 μM APPPA in presence of HCSF (1 μM) (f) 5 μM APPPA in presence of HCSF (1 μM). Samples were incubated at 37 °C in 10 mM PBS (pH 7.4). PAPAP λex = 495 nm and APPPA λex = 497 nm.

4.3.6. Cytotoxicity and Permeability

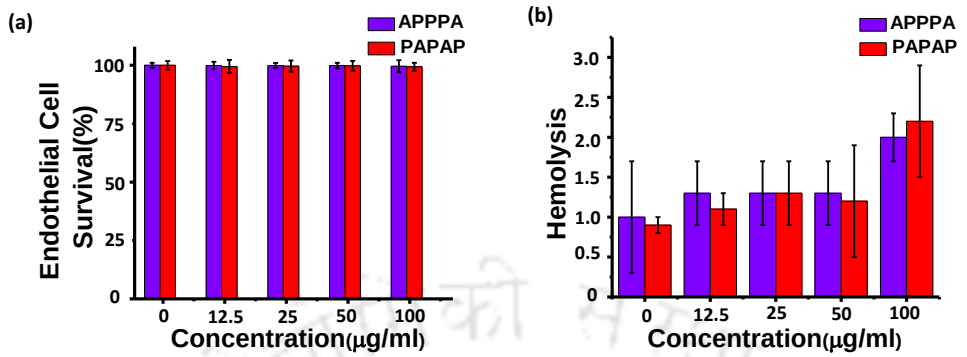

Figure 4.5. Cytotoxicity assay. Cytotoxicity of PAPAP and APPPA (0-100 μg/ml) toward (a) endothelial cells, EA.hy926 (b) human red blood cells.

Perylenebisimides are well known to form supramolecular assemblies via π-stacking unless bay positions are substituted. In this work we have explored few unfamiliar facts of perylene chemistry. First is their aqueous solubility parameter which was remarkably improved by attaching dipeptide tails and second, utilizing their inherent aggregation nature to disrupt the robust amyloid aggregates from early aggregate stage itself. More remarkably, their biocompatibility is enhanced significantly and are permeable to blood brain barrier (BBB), which is another unique feature observed for the first time with these molecules. To address the solubility issue UV-Vis studies have been carried out with varying concentration from 0-100 μg/mL and when optical density was plotted against concentration, a linear relationship was achieved in both cases (Figure A4.13). At pH 7.4 and at lower concentration (0-120 μM) both the isomers were highly soluble and did not precipitate out from solution. Cytotoxic effects of APPPA and PAPAP were evaluated by three different assays. As described in the experimental section, treatment of different concentration (0-100 μg/mL) of APPPA and PAPAP with human red blood cells for 6 h resulted in 2 % and 2.3 % hemolysis respectively at 100 μg/mL. But 50 μg/mL and other lower concentrations did not cause significant hemolysis as compared to the control. Further, the toxicity of APPPA and PAPAP were also tested on endothelial cells and U-87 MG human astrocyte cells by MTT assay as described in the experimental section. More than 80% cells (U-87 MG) were viable in presence of both the small molecules up to 0-20 μM (0-16 μg/mL) of concentration (Figure A4.14). During the test period of 12 h, till the maximum concentration (100 μg/mL) of test compounds, no toxicity was observed with the endothelial cells (Figure 4.15a). Although the test compounds did not show any toxicity to the endothelial cells, at maximum concentration (100 μg/mL), they showed mild toxicity to the RBCs. Cytotoxicity studies confirmed that both the test

compounds (small molecules) are very safe at below 50 µg/mL (60.32 µM, Figure 4.15b). By considering these observations, 50 µg/mL concentrations were chosen for in vitro BBB assay as described in the experimental sections.

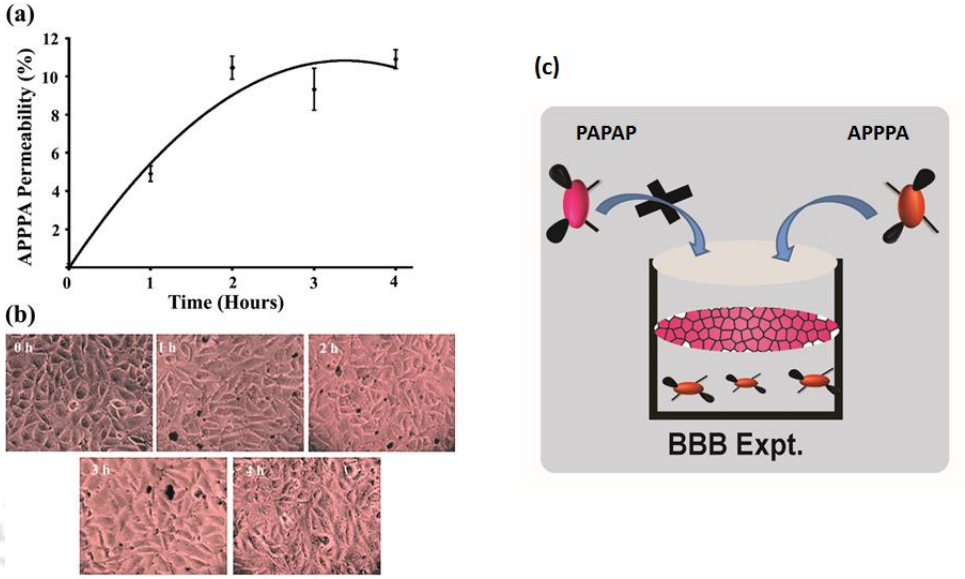

Figure 4.6. Dipeptide Linked Perylenebisimide APPPA has potential to cross the Blood-Brain barrier to target Aβ aggregates inside the brain. (a) Delivery of APPPA (50 µg/ml) across endothelial monolayer system as an ex-vivo blood-brain barrier model. (b) The integrity of endothelial monolayer during the course of treatment with APPPA (50µg/ml) from the beginning (0 h) to the end (4 h) of the experiment (c) Schematic presentation of Blood-brain barrier mimic made up of endothelial cells and secretion of PAPAP and APPPA. Initially, APPPA and PAPAP solutions were placed in the upper chamber and after every 1 h collected from the lower chamber and quantified using fluorescence spectroscopy. Evans blue was taken as a control.

To examine the BBB crossing ability of PAPAP and APPPA, a monolayer of human endothelial cells, EA.hy926, were used as an in vitro BBB model. PAPAP and APPPA (100 µM) solutions were prepared in complete media, and after every 1 h interval the media (~1 mL) was collected and quantified by fluorescence spectroscopy (excitation at 495 nm and 497 nm for PAPAP and APPPA respectively). Evans blue was used as a control to check the leakage in the system as well as to correct the actual permeability of APPPA and PAPAP. Cellular integrity was checked by carefully observing the morphology of the endothelial mono-layer during the experiment with an inverted microscope TS100 attached to the high-resolution camera. Both APPPA (Figure 4.6a and A4.16a, A4.16b) and PAPAP (Figure A4.16c, A4.16d) did not cause any damage to the cellular integrity and the morphology remains intact till 6 h (Figure A4.16-A4.18). But the permeability of APPPA through the endothelial monolayer was found to reach ~10.5 % (~ 6.3 µM, Figure 6) at 2 h, whereas PAPAP was permeable maximally only ~2 % (~

1.2 μM, Figure 6c, A4.15, and Table A4.1) at 1 h. These observations from in vitro endothelial monolayer permeability model directly indicated that APPPA can across BBB more efficiently than PAPAP likely due to their less aggregation tendency through π-stacking which is indirectly related to their structural properties. Although BBB is comprised of very dense endothelial cells, the aforementioned assay may not perfectly mimic the actual complexity of the neurodegeneration. Nevertheless, the prerequisite for any new molecule to be considered for these advanced in vivo studies is to possess properties of efficient BBB permeability. Further in vivo efficacy has to be tried in clinical systems considering the presence of transport and receptor proteins and is beyond the scope at present.

4.4. Discussion

It is widely mentioned that Aβ oligomers deliver potential accounts for the toxicity of the extracellular Aβ peptide and prompt the sensitive neurons to form intra-cellular tau aggregates. Based on the previous findings and to explore structurally efficient motifs that can detect and interact with amyloid oligomers, the perylenebisimide core was chosen as a preferred molecule with dipeptide (chosen from hydrophobic residues of Aβ1-40) tails. These π-conjugated chromophores are normally hydrophobic in nature and apparently, they are insoluble in aqueous media, yet in this work, the judicious selection of dipeptide tentacles made these two isomers soluble in water and their mutual aggregation guided the fibrillation into an 'off-pathway' which has not been observed previously with perylenebisimides thereby providing vital breakthrough in modulation of early stage amyloid peptides. As depicted in UV-vis spectra (Figure A4.5a) of both APPPA (1 μM in DMSO), all recorded spectra exhibited two main absorbance peaks at ~525-528 nm and ~488-491 nm corresponding to 0→0 and 0→1 transition in organic solvents. In water, they were slightly red-shifted to 504 nm and 538 nm and A0→0/A0→1 becomes 1.5 to 1, the ratio of the intensity of peak absorbance of the lowest two energy transitions clearly indicating their changes in aggregation behaviour. In the case of PAPAP, both 0→0 and 0→1 transition peaks were found to be almost at similar wavelength ~525-528 nm and ~489-491 nm in organic solvents (Figure A4.5b) and A0→0/A0→1 becomes 1.5 to 0.7 in presence of water at a particular concentration. Thus, change in position of attachment to the aromatic core led to distinct modes of aggregation as with normal Franck-Condon progression, this ratio should be around 1.6 whereas for aggregated species typical values are <0.7.[35-37] Both APPPA and PAPAP structures were optimized using DFT studies (using B3LYP function and 631G basis set) and their stable conformations were found to have a direct link with their aggregation behaviour. In APPPA,

phenyl alanine is attached to perylene core and the phenyl rings of the appended phenyl alanines are placed above and below the perylene core thus producing steric hindrance to avoid aggregation via π-stacking (Figure A4.19a). Unlike in the case of PAPAP, both phenyl rings hang on one side of the aromatic core since they are far apart from perylene core. Thus perylene core in PAPAP is better positioned for π-stacking and hence more prone to aggregation (Figure A4.19b). Interestingly, docking results revealed that in the presence of Aβ, phenyl rings of APPPA are hooked towards one side of the perylene core unlike their original structure and thus more approachable toward peptide hydrophobic core compared to PAPAP (Figure A4.20). Due to this hydrophobic encounter, APPPA formed spherical aggregates (very distinct and larger than peptide oligomers as shown in the morphological analysis) similar to peptide oligomers. Previous finding on surface motif modification helped us to decide that probes with similar ability were needed to target toxic amyloid intermediate since it is not always a particular species of definite size and shape rather a more nucleation-dependent dynamic fibrillogenesis process itself. A structural motif prone to aggregate in water behaves differently in the presence of these self-aggregating peptides and their aggregation becomes complementary to each other. As a result, oligomers and early stage structures were seen to be trapped in between perylene aggregates (Figure 4.3) and similar surface motif of APPPA that resulted in a higher selectivity toward peptide oligomers compared to PAPAP.

4.5. Conclusion

In conclusion, two dipeptide linked perylenebisimide isomers were synthesized via two distinct reactions and utilized them to study the early stage process of oligomer assembly into toxic amyloid which is less understood. In parallel, a unique approach to complementary aggregation was presented using these two perylenebisimide derivatives having dipeptide (phe-ala and ala-phe) tentacles with distinct atomic connectivity to modulate Aβ oligomers in Aβ1-40 as well as in HCSF sample containing Aβ oligomers. Different attachment in these two isomers leads to structural dissimilarities between them and consequently a different degree of self-aggregation in an aqueous environment results. This self-aggregation was disturbed in presence of peptide self-aggregation and becomes complementary to each other. Since phenyl alanine is not attached to the perylene core in case of PAPAP, it allows the benzene ring to hang on one side of the aromatic core that resulted in higher self-aggregation in water unlike its other sibling, APPPA. However, in the presence of Aβ, APPPA was shown to have phenyl rings directed towards the hydrophobic core along with the aromatic perylene moiety available for non-covalent interactions with the hydrophobic pocket of Aβ. In both the cases,

the aromatic core was found to be slightly twisted to prevent extreme self-aggregation among them and complementary aggregation stands tall to inhibit Aβ fibrillation. Through this work a new class of peptide-based motif to investigate the structure-activity relationship with early stage as well as intermediate peptide aggregates has been established. These dipeptide-based isomers minimized the toxic pathways of Aβ aggregation leading to protein misfolding from early stage structure assemblies and which still persists as one of the most difficult challenges and help in the development of improved inhibitors and biomarkers toward pre-senile therapeutics.

References

(1) De Strooper, B. *Physiol. Rev*. **2010**, *90*, 465–494.

(2) Castellano, J. M.; Kim, J.; Stewart, F. R.; Jiang, H.; DeMattos, R. B.; Patterson, B.W.; Fagan, A. M.; Morris, J. C.; Mawuenyega, K. G.; Cruchaga, C.; Goate, A. M.; Bales, K. R.; Paul, S. M.; Bateman, R. J.; Holtzman, D. M. *Sci. Transl. Med*. **2011**, *3*, 89ra57.

(3) Cerf, E.; Gustot, A.; Goormaghtigh, E.; Ruysschaert, J. M.; Raussens, V. *FASEB J*. **2011**, *25*, 1585–1595.

(4) McLean, C. A.; Cherny, R. A.; Fraser, F. W.; Fuller, S. J.; Smith, M. J.; Beyreuther, K.; Bush A. I.; Masters C. L. *Ann. Neurol*. **1999**, *46*, 860–866.

(5) Mc Donald, J. M.; Savva, G. M.; Brayne, C.; Welzel, A. T.; Forster, G.; Shankar, G. M.; Selkoe, D. J.; Ince, P. G.; Walsh, D. M. *Brain* **2010**, *133*, 1328–1341.

(6) Nilsberth, C.; Westlind-Danielsson, A.; Eckman, C. B.; Condron, M. M.; Axelman, K.; Forsell, C.; Stenh, C.; Luthman, J.; Teplow, D. B.; Younkin, S. G.; Näslund, J.; Lannfelt, L. *Nat. Neurosci*. **2001**, *4*, 887–893.

(7) Tomiyama, T.; Nagata, T.; Shimada, H.; Teraoka, R.; Fukushima, A.; Kanemitsu, H.; Takuma, H.; Kuwano, R.; Imagawa, M.; Ataka, S.; Wada, Y.; Yoshioka, E.; Nishizaki, T.; Watanabe, Y.; Mori, H. *Ann. Neurol*. **2008**, *63*, 377–387.

(8) Whitson, J. S.; Selkoe, D. J.; Cotman, C. W. *Science* **1989**, *243*, 1488–1490.

(9) Pearson, H. A.; Peers, C. *J. Physiol*. **2006**, *575*, 5–10.

(10) Koo, E. H.; Park, L.; Selkoe, D. J. *Proc. Natl. Acad. Sci. U.S.A*. **1993**, *90*, 4748–4752.

(11) Muchowski, P. J.; Wacker, J. L. *Nat. Rev. Neurosci*. **2005**, *6*, 11-22.

(12) Nie, Q.; Du, X.-G.; Geng, M.-Y. *Acta Pharmacologica Sinica* **2011**, *32*, 545–551.

(13) Kukar, T. L.; Ladd, T. B., Bann, M. A.; Fraering, P. C.; Narlawar, R.; Maharvi, G. M.; Healy, B.; Chapman, R.; Welze, A. T.; Price, R. W.; Moore, B.; Rangachari, V.; Cusack, B.; Eriksen, J.; Jansen-West, K.; Verbeeck, C.; Yager, D.; Eckman, C.; Ye, W.; Sagi, S.; Cottrell, B.

A.; Torpey, J.; Rosenberry, T. L.; Fauq, A.; Wolfe, M. S.; Schmidt, B.; Walsh, D. M.; Koo, E. H.; Golde, T. E. *Nature* **2008**, *453*, 925-929

(14) Sheltona, C. C.; Zhua, L.; Chau, D.; Yang, L.; Wang, R.; Djaballah, H.; Zheng, H.; Li, Y.-M. *Proc. Natl. Acad. Sci. U.S.A.* **2009**, *106*, 20228-20233.

(15) Chandra, B.; Halder, S.; Adler, J.; Korn, A.; Huster, D.; Maiti, S. *Chem. Phys. Lett.* **2017**, *675*, 51–55.

(16) Meli, G.; Visintin, M.; Cannistraci, I.; Cattaneo, A. *J. Mol. Biol.* **2009**, *387*, 584–606.

(17) Narayan, P.; Ganzinger, K. A.; McColl, J.; Weimann, L.; Meehan, S.; Qamar, S.; Carver, J. A.; Wilson, M. R.; George-Hyslop, P. St.; Dobson, C. M.; Klenerman, D. *J. Am. Chem. Soc.* **2013**, *135*, 1491–1498.

(18) Viola, K. L.; Klein, W. L. *Acta Neuropathol.* **2015**, *129*, 183–206.

(19) Nguyen, P.; Derreumaux, P. *Acc. Chem. Res.* **2014**, *47*, 603-611.

(20) Muthuraj, B.; Layek, S.; Balaji, S. N.; Trivedi, V.; Iyer, P. K. *ACS Chem. Neurosci.* **2015**, *6*, 1880–1891.

(21) Balaji, S. N.; Trivedi, V. *Indian J. Clin. Biochem.* **2012**, *27*, 178–185.

(22) Lührs, T.; Ritter, C.; Adrian, M.; Riek-Loher, D.; Bohrmann, B.; Döbeli, H.; Schubert, D.; Riek, R. *Proc. Natl. Acad. Sci. U.S.A.* **2005**, *102*, 17342–17347

(23) Petkova, A. T.; Ishii, Y.; Balbach, J. J.; Antzutkin, O. N.; Leapman, R. D.; Delaglio, F.; Tycko, R. *Proc. Natl. Acad. Sci. U.S.A.* **2002**, *99*, 16742–16747

(24) Benilova, I.; Karran, E.; De Strooper, B. *Nat. Neurosci.* **2012**, *15*, 349–357.

(25) Walsh, D. M.; Lomakin, A.; Benedek, G. B.; Condron, M. M.; Teplow, D. B. *J. Biol. Chem.* **1997**, *272*, 22364–22372.

(26) Harper, J. D.; Wong, S. S.; Lieber, C. M.; Lansbury, P. T. *Chem. Biol.* **1997**, *4*, 119–125,

(27) Biancalana, M.; Koide, S. *Biochim. Biophys. Acta* **2010**, *1804*, 1405-12

(28) Wu, C.; Wang, Z.; Lei, H.; Duan, Y.; Bowers, M. T.; Shea, J. E. *J. Mol. Biol.* **2008**, *384*, 718–729.

(29) Wu, C.; Wang, Z.; Lei, H.; Zhang, W.; Duan, Y. *J. Am. Chem. Soc.* **2007**, *129*, 1225–1232.

(30) Krebs, M. R.; Bromley, E. H.; Donald, A. M. *J. Struct. Biol.* **2005**, *149*, 30–37.

(31) Hard, T. J. *Phys. Chem. Lett.* **2014**, *5*, 607–614.

(32) Roychaudhury, R.; Yang, M.; Hoshi, M. M.; Teplow, D. B. *J. Biol. Chem.* **2009**, *284*, 4749–4753.

(33) Pellarin, R.; Caflisch, A. *J. Mol. Biol.* **2006**, *360*, 882–892.

(34) Shivu, B.; Seshadri, S.; Li, J.; Oberg, K. A.; Uversky, V. N.; Fink, A. L. *Biochemistry* **2013**, *52*, 5176–5183.

(35) Wang, W.; Han, J. J.; Wang, L.-Q.; Li, L.-S.; Shaw, W. J.; Li, A. D. Q. *Nano Lett.* **2003**, *3*, 455–458.

(36) Wang, W.; Wan, W.; Zhou, H.-H.; Niu, S.; Li, A. D. Q. *J. Am. Chem. Soc.* **2003**, *125*, 5248–5249.

(37) Fink, R. F.; Seibt, J.; Engel, V.; Renz, M.; Kaupp, M.; Lochbrunner, S.; Zhao, H.-M.; Pfister, J.; Würthner, F.; Engels, B. *J. Am. Chem. Soc.* **2008**, *130*, 12858–12859.

Appendix

Perylene-3, 4, 9, 10-tetracarboxylic dianhydride (100 mg, 0.254 mmol), Phe-Ala/Ala-Phe (126 mg, 0.535mmol), Zinc acetate (1 mg, 0.005 mmol) and imidazole (1.5 g) were heated at 140°C for 8 hours with continuous stirring. Then the mixture was allowed to cool to 90°C and then poured into 2 M HCl solution. Precipitates were washed several times with water and dried under vacuum to obtain the red colored solids (150 mg, 71% PAPAP; 139 mg, 65% APPPA).

1.1. PAPAP: Yield 150 mg, 71%, ^{1}H NMR (600MHz, DMSO-d6), δ (ppm): 11.7(s, COOH), 8.2(bp, PrH and NH), 7.05-7.28(m, ArH), 5.5(bp, CH), 4.4(bp, CH), 2.6-3.1(bp, CH2), 1.6(bp, CH3). bp: broad peak, PrH: Perylene H, ArH: Phenyl H. MALDI TOF: 851.949 ($M+Na^+$), 712.557

1.2. APPPA: Yield 150 mg, 71%, ^{1}H NMR (600MHz, DMSO-d6), δ (ppm): 8.8(s, NH), 8.4(s, PrH), 8.3(d, PrH), 7.05-7.1(m, ArH), 5.7(bp, CH), 4.4(d, CH), 3.5(bp, CH2), 1.2(m, CH3). bp: broad peak, PrH: Perylene H, ArH: Phenyl H. MALDI TOF: 852.069 ($M+1+Na^+$), 712.684.

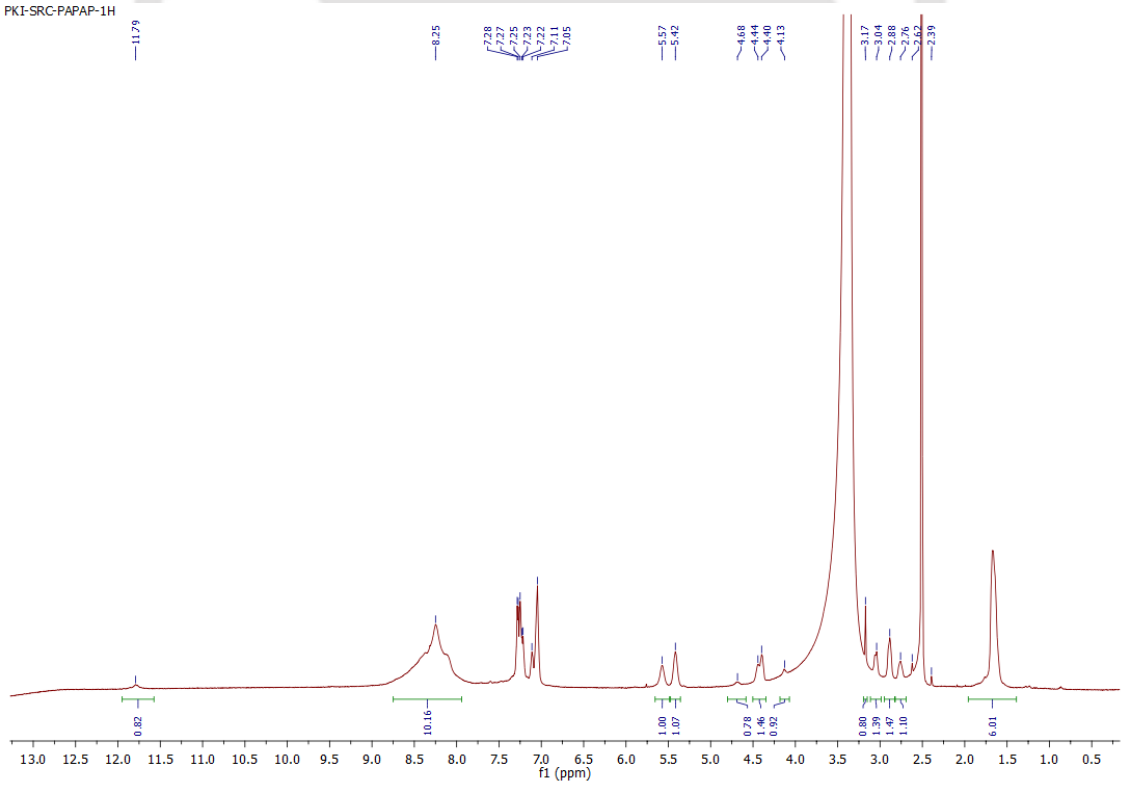

Figure A4.1. 1H NMR of PAPAP.

D:\User Data\U bora\RKR_OM_BT_2BR_(321)\PAPAP\0_J7\1\1SRef

Comment 1

Comment 2

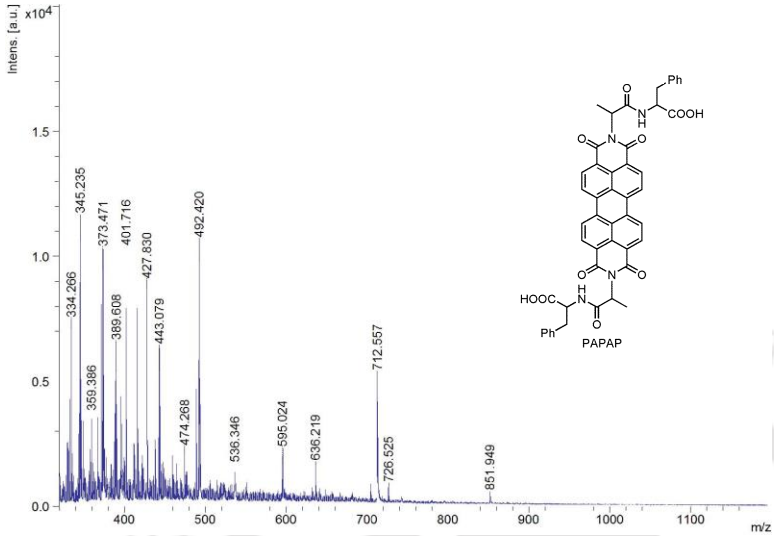

m/z	S/N	Quality Fac.	Res.	Intens.	Area
329.088	7	218	1749	2233	558
330.117	6	94.4	1749	2122	530
332.221	11	456	2151	3736	708
334.266	22	8830	2969	7081	1092
343.205	12	6310	1639	4051	1188
344.224	8	971	1860	2718	666
345.235	33	41978	1814	10629	2712
349.170	9	1389	922	2996	1581
358.357	6	1200	1713	2119	563
359.386	8	478	2072	2801	605
360.366	8	348	1969	2704	656
366.844	8	297	1392	2569	919
371.451	24	6414	1766	7637	2325
373.471	30	17018	1796	9467	2758
387.633	6	972	2553	2067	391
388.592	14	2784	2353	4288	962
389.608	17	4359	2225	5392	1320
395.109	10	627	1414	3212	1253
396.834	8	681	686	2487	2033
401.716	34	10613	2117	10094	2706
411.743	6	353	886	1997	1268
415.855	27	6577	3154	7703	1437
427.830	31	17431	2102	8664	2564
438.001	8	2371	3601	2297	376
442.056	8	751	2786	2218	457
443.079	20	18124	3339	5431	1043
444.096	8	1097	3646	2355	384
459.169	6	290	2462	1788	451
474.268	8	519	2244	2134	626
488.381	34	28170	3734	7490	1449
492.420	45	82507	1989	9768	3730
536.346	6	1083	645	1309	1394
595.024	11	1869	2186	1680	721
596.056	11	668	1984	1574	722
636.219	14	7759	4123	1651	385
704.474	9	2130	5588	770	135
712.557	75	7721	2060	5344	3393
726.525	10	3498	5580	800	155
851.949	13	4939	2619	572	318

Figure A4.2. MALDI-TOF of PAPAP.

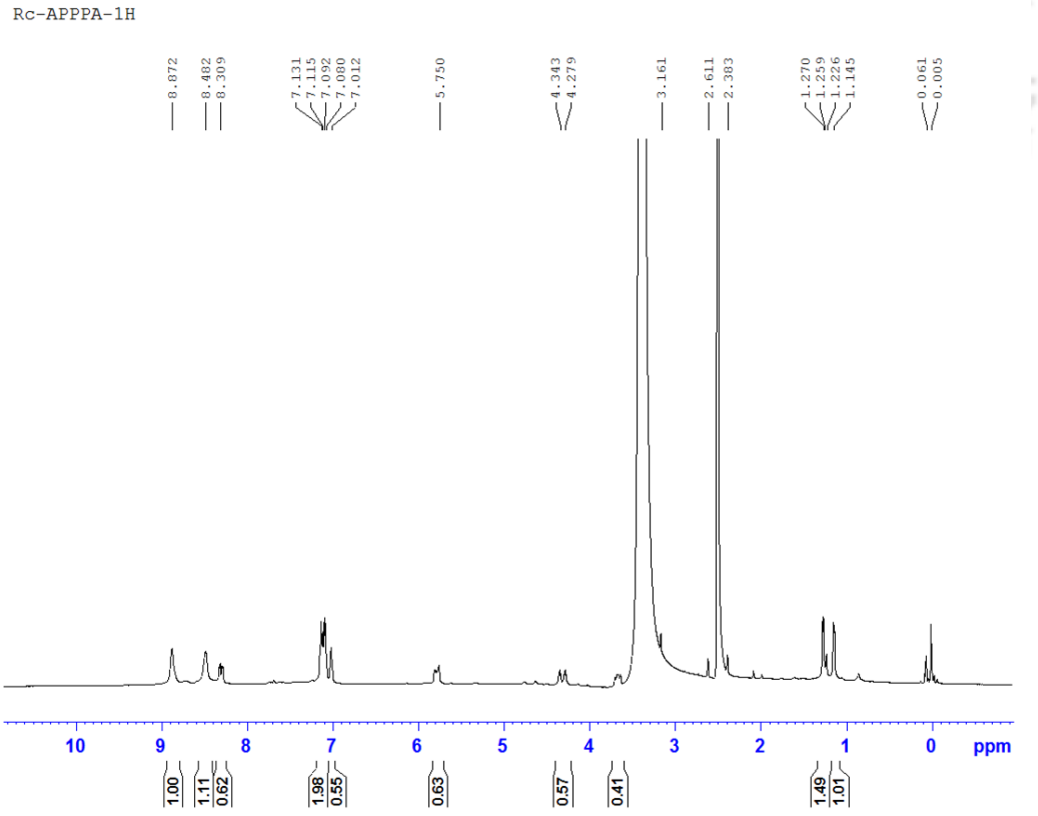

Figure A4.3. 1H NMR of APPPA.

D:\User Data\PKI\LRA_O\SRC-APPPA\SRC-APPPA\0_B20\1\1SRef

Comment 1

Comment 2

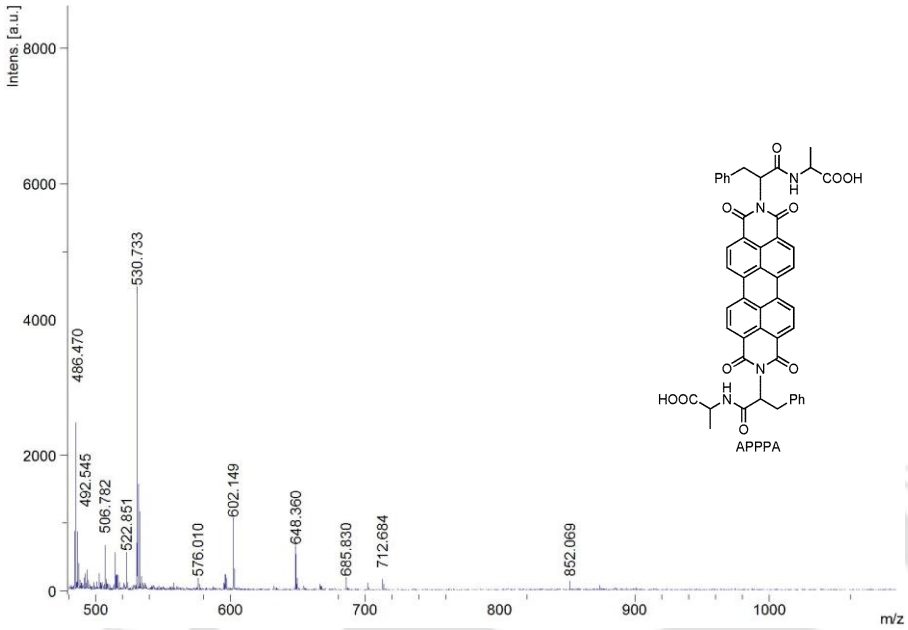

m/z	S/N	Quality Fac.	Res.	Intens.	Area
484.366	36	510	4073	815	150
485.427	119	9080	4720	2656	413
486.470	29	768	4920	651	106
492.545	34	759	4413	761	122
493.420	11	188	3329	247	56.6
499.553	7	51.6	3682	178	33.4
502.574	10	134	3729	227	42.4
506.782	36	2461	8057	787	72.5
514.663	24	674	5103	523	80.7
516.655	8	159	3723	192	39.3
522.851	25	2072	9518	537	45.2
530.733	210	59467	6133	4383	593
532.766	45	6237	6790	947	120
576.010	8	440	5427	163	27.3
596.183	12	313	6376	223	32.9
602.149	59	26443	7682	1050	137
648.360	39	9497	7470	619	92.9
685.830	12	1336	10669	174	18.2
701.849	8	901	13011	120	10.9
712.684	20	2427	9525	272	35.5
852.069	14	1373	11410	171	22.7

Figure A4.4. MALDI-TOF of APPPA.

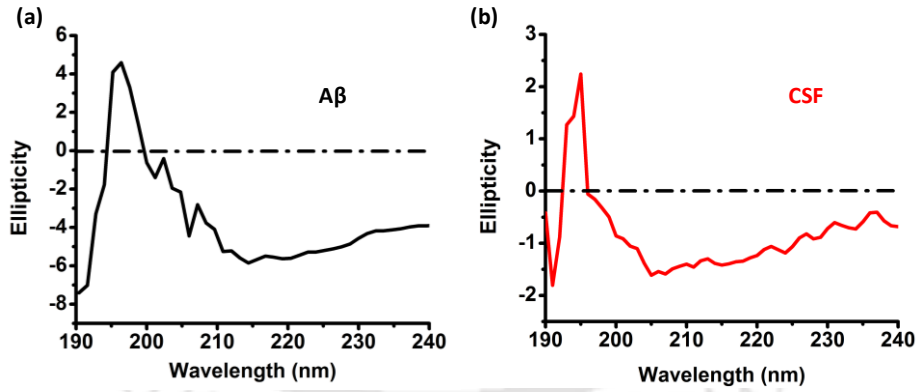

Figure A4.5. CD spectra of (a) Aβ1-40 (20μM) and (b) HCSF in 1 mM PBS buffer at pH 7.4.

20 μM Aβ1-40 was incubated at 37 °C in 10 mM PBS (pH 7.4) and the conformational transition to ordered β sheet via aggregation was measured using CD measurements in 1 mM PBS. A positive maximum at 193 nm and a broad negative minimum at 215 nm appeared after 24 hours of incubation which clearly indicates the structural transition of Aβ1-40 (20 μM) from the initial random coil to the β-sheet structure. A similar response was also observed in the case of chosen HCSF sample.

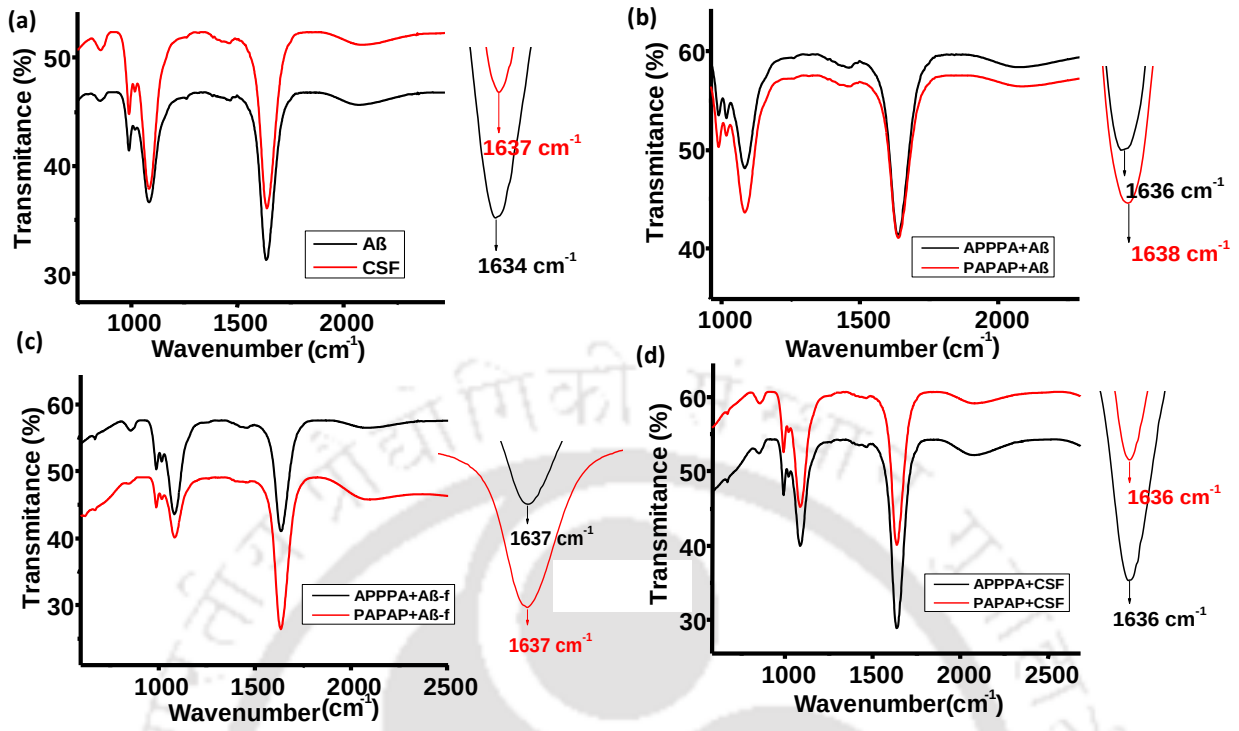

Figure A4.6. FT-IR spectra of (a) Aβ1-40 and HCSF (b) APPPA and PAPAP.

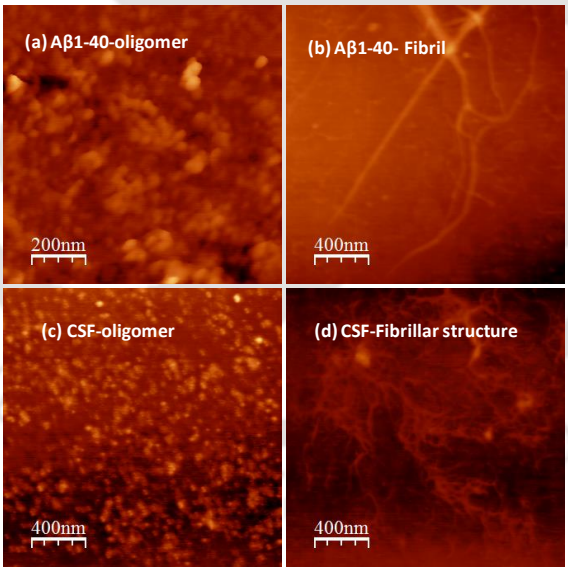

Figure A4.7. AFM images of oligomers and fibrillar network in (a) and (b) Aβ1-40 and (c) and (d) HCSF respectively.

The diameter of Aβ oligomers was observed to be ~60 nm and ~5 nm height (Figure A4.9a). After 72 hours of incubation, Aβ fibrils were found to form in the topography image (Figure S10) with ~100 nm diameter and ~2.5 nm height (Figure A4.9b) confirming that the

monomers and small oligomers continue to self-assemble to form protofibrils and then into fibrils. HCSF sample containing oligomeric Aβ is also confirmed as topography images of the real CSF sample (Figure A4.9c) showed a large number of oligomers of similar width ~60-70 nm and height 5-7 nm. After 24 hours of incubation similar fibrillar structure was found in CSF sample. The diameter of Aβ fibrils in CSF was observed to be ~90-100 nm diameter and ~1.5-2 nm height (Figure A4.9d).

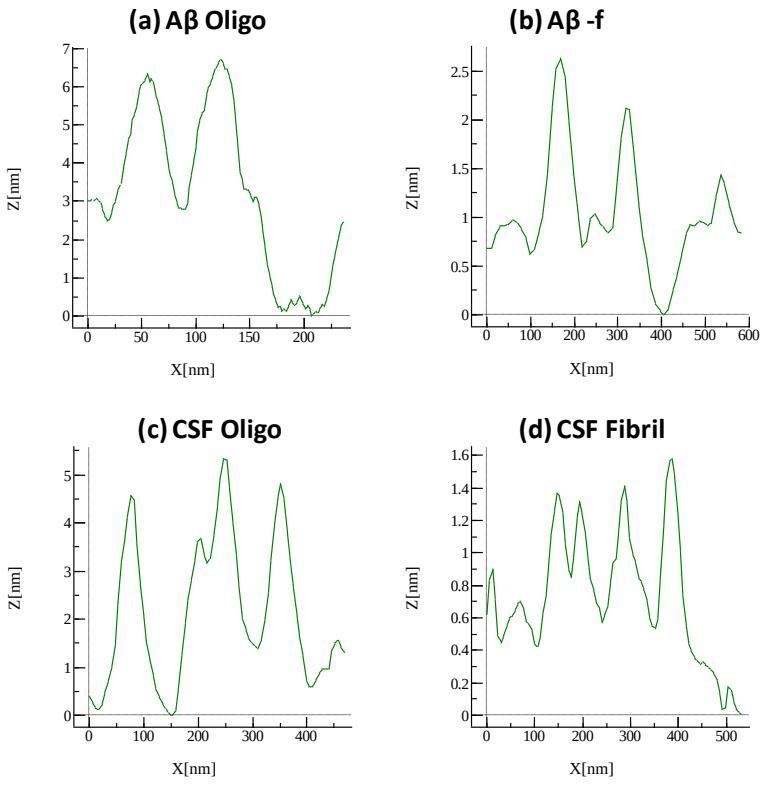

Figure A4.8. Height profiles of (a) Aβ oligomer, (b) Aβ fibrils, (c) CSF oligomers and (d) CSF fibrils.

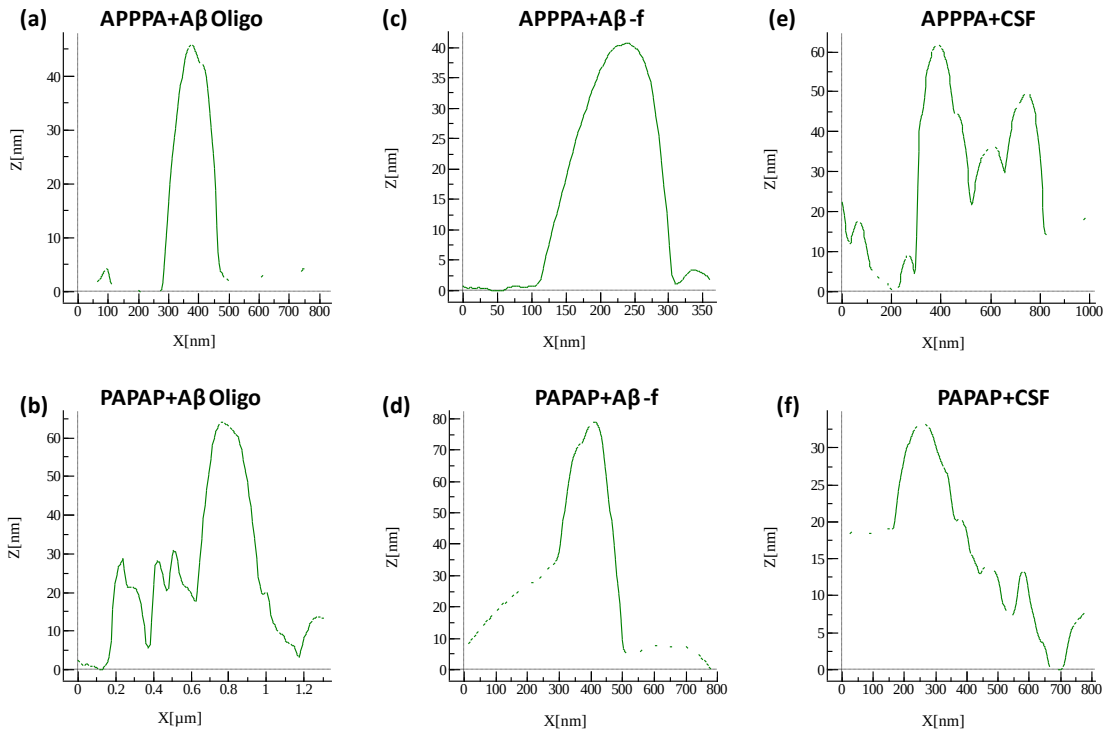

Figure A4.9. Height profiles of PAPAP and APPPA coincubated Aβ samples after 72 hours of incubation at 37oC. (a) Aβ oligomers in presence of APPPA (b) Aβ oligomers in presence of PAPAP (c) Prefibrillar Aβ in presence of APPPA (d) Prefibrillar Aβ in presence of APPPA (e) HCSF in presence of APPPA and (f) HCSF in presence of PAPAP.

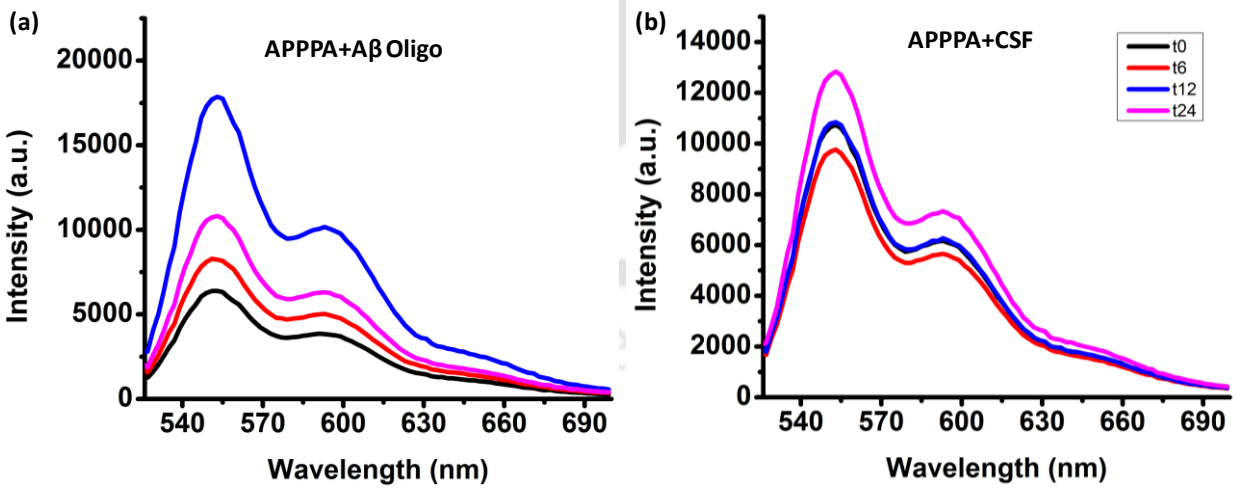

Figure A4.10. Emission spectra of APPPA (a) coincubated with Aβ oligomers and (b) HCSF (0-24 hours). Samples were incubated at 37oC and measurements were done in 10 mM PBS (pH 7.4). APPPA λexcitation = 497 nm.

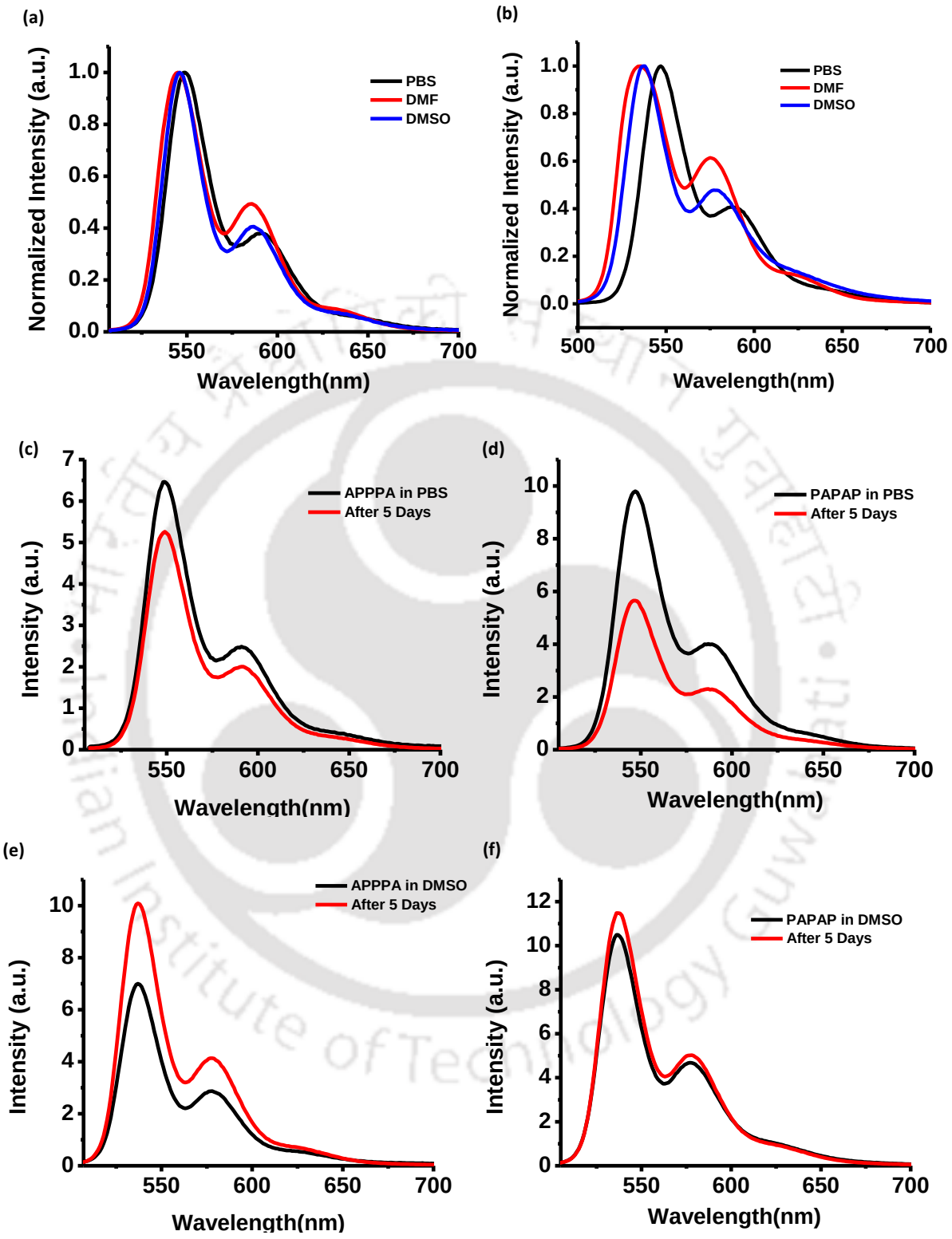

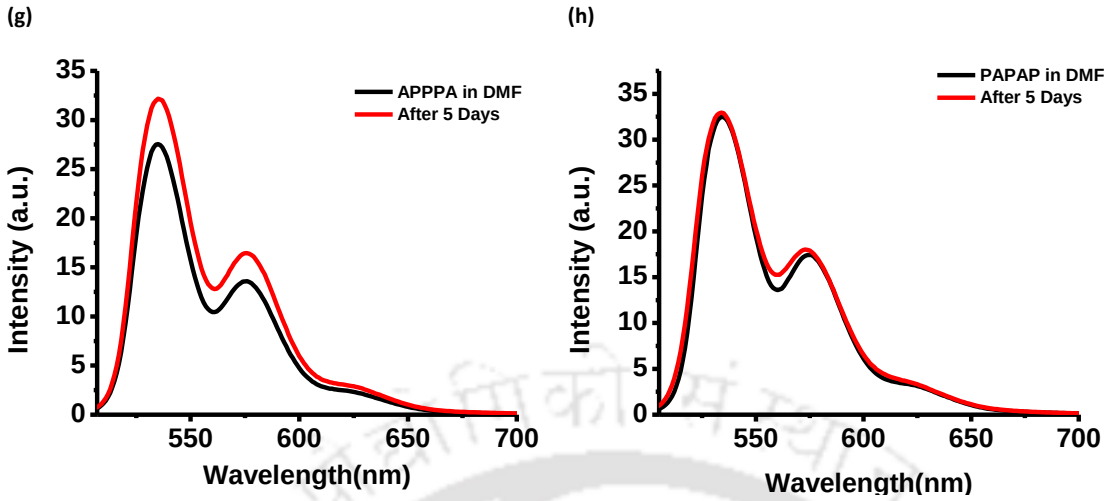

Figure A4.11. Emission spectra of (a)-(h) APPPA and PAPAP in organic and aqueous solvent and changes after 5 days of incubation at 37°C. Samples were incubated at 37°C and measurements were done in 10 mM PBS (pH 7.4), DMSO and DMF. APPPA λexcitation = 497 nm and PAPAP λexcitation = 495 nm.

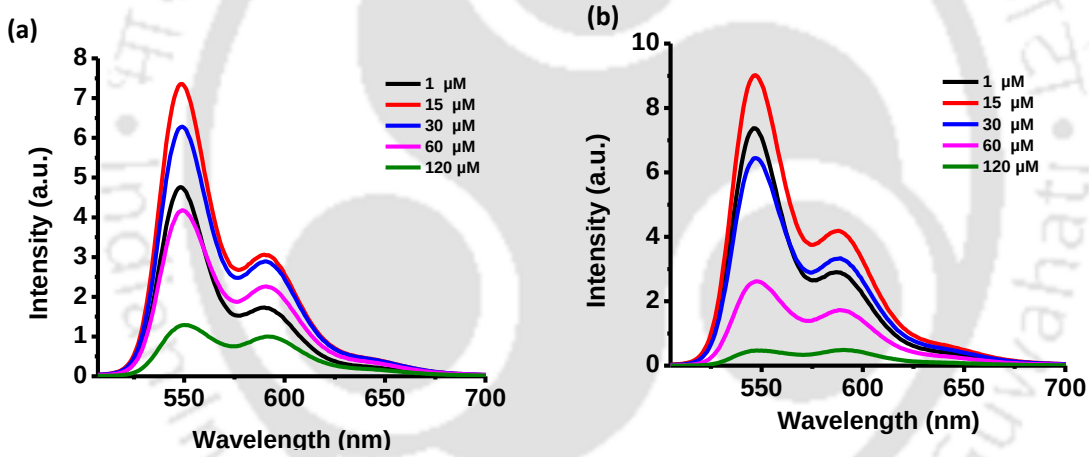

Figure A4.12. Emission spectra of (a) APPPA and (b) PAPAP with varying concentration from 1-120 μM (1-100 μg/ml).

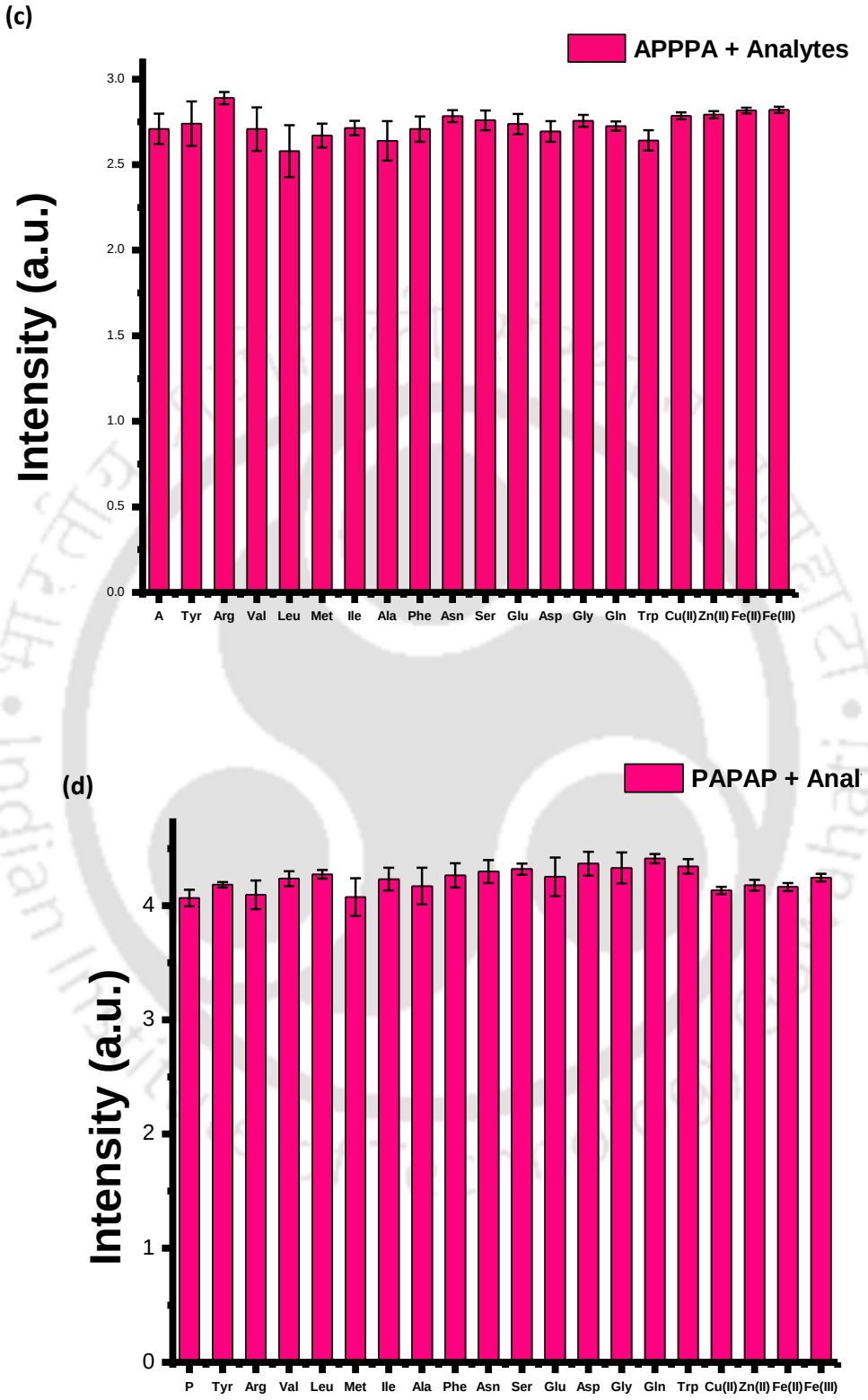

Figure A4.12. Emission spectra of APPPA and PAPAP in (c) and (d) represent the negligible change in APPPA and PAPAP emission (at λmax 547 and 549 nm) after adding 100 μM of respective analytes. Error bars correspond to

standard deviations of five records. Fluorescence measurements were done in 10 mM PBS (pH 7.4). APPPA λexcitation = 497 nm and PAPAP λexcitation = 495 nm.

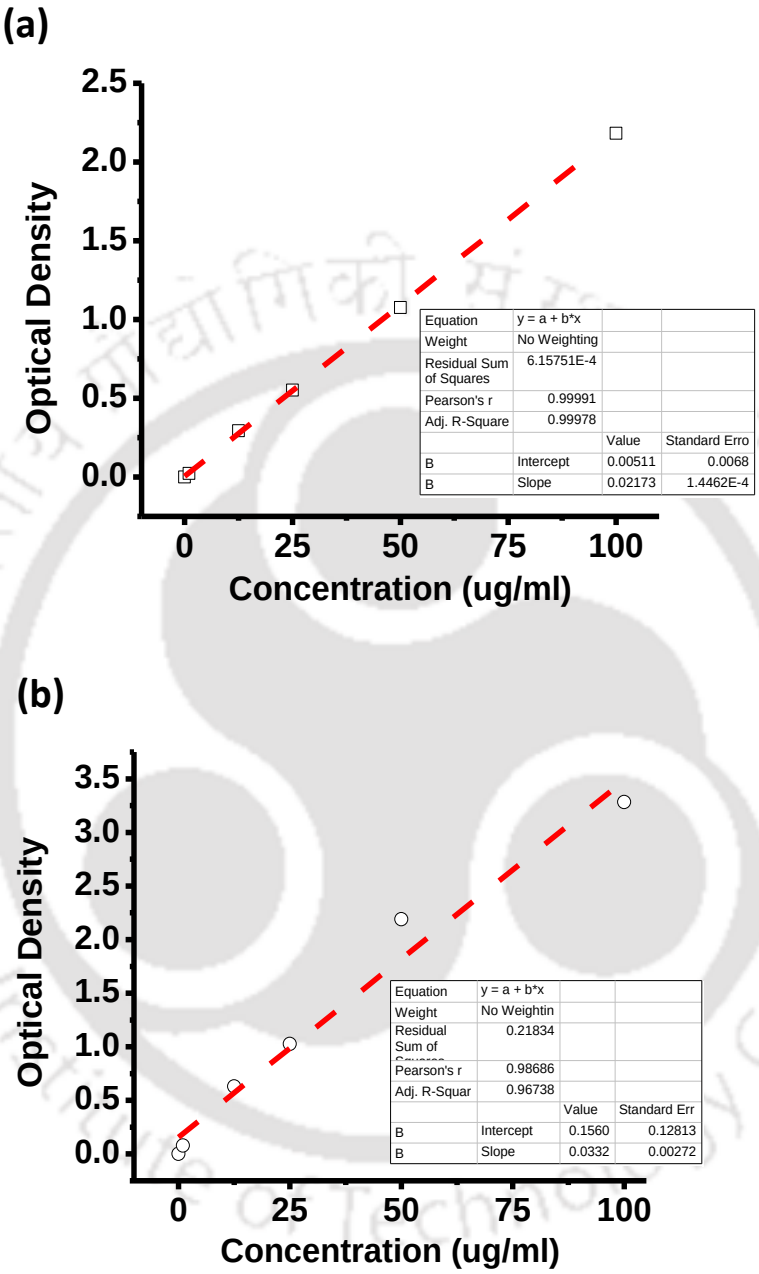

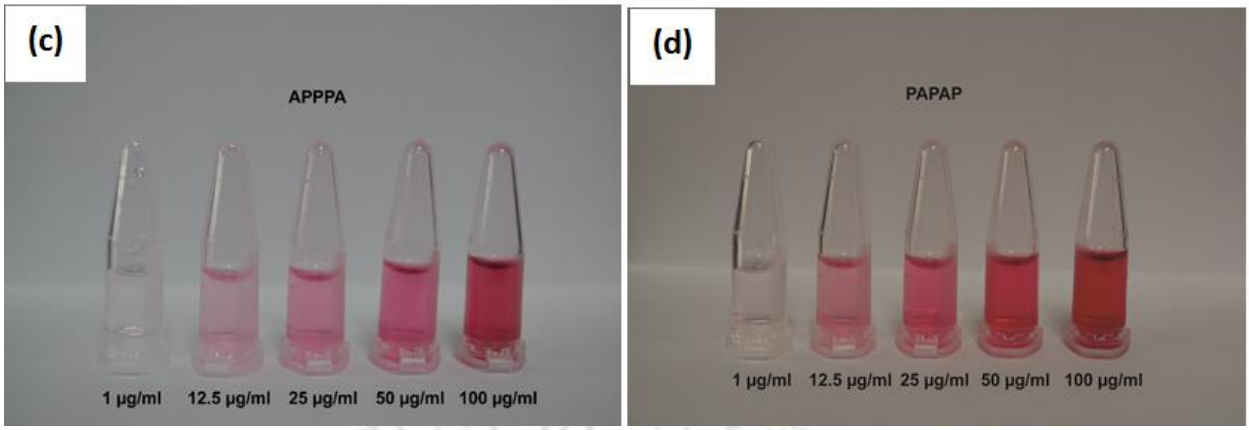

Figure A4.13. Optical density vs Concentration profile for (a) APPPA and (b) PAPAP in 10 mM PBS (pH 7.4), Solution of (c) APPPA and (d) PAPAP in 10 mM PBS with a varying concentration from 1µg/ml to100 µg/ml showing no precipitation.

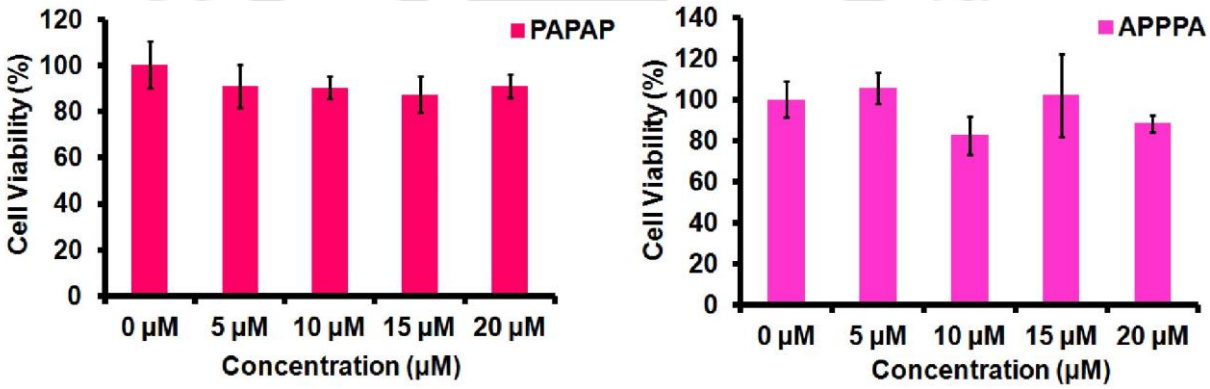

Figure A4.14. Cytotoxicity of PAPAP and APPPA (0-20 µM) toward U-87 MG cells.

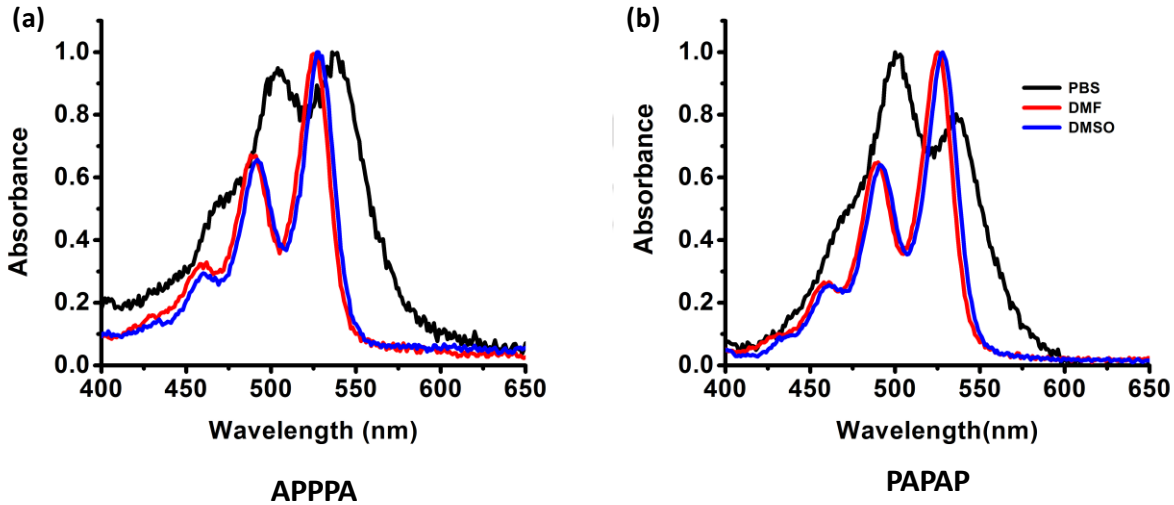

Figure A4.15. Normalized absorbance of (a) APPPA (5 μM) and (b) PAPAP (5 μM) in 10 mM PBS (pH7.4), DMF and DMSO.

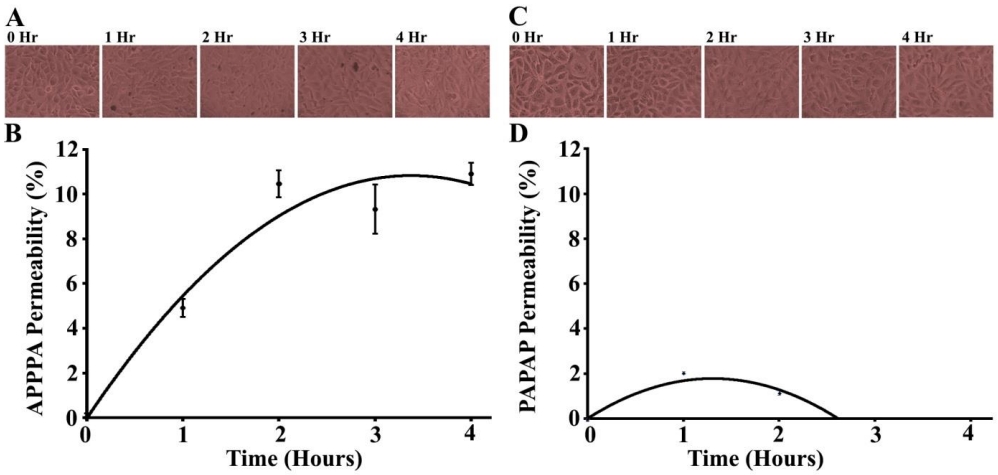

Figure A4.16. Morphology of the endothelial monolayer (cellular integrity) in presence of (A) APPPA and (C) PAPAP from 0-4 hours. Movement of (B) APPPA (50 μg/ml) and (D) PAPAP (50 μg/ml) across endothelial monolayer barrier. Initially, PAPAP and APPPA solutions were placed in the upper chamber and after every 1 hour collected from the lower chamber and quantified using fluorescence spectroscopy. Evans blue was taken as a control.

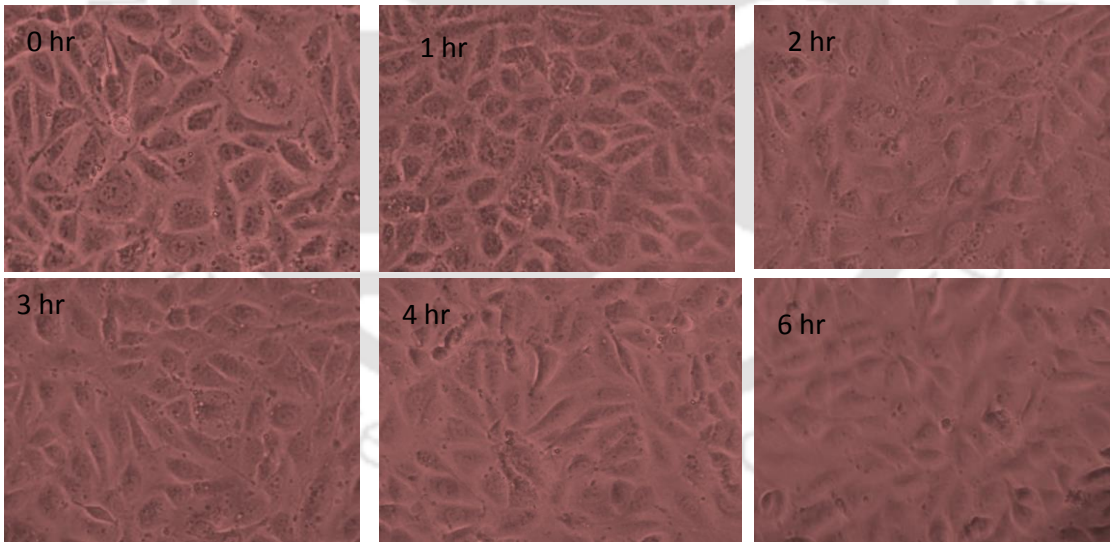

Figure A4.17. The morphology of the endothelial monolayer in presence of PAPAP from 0-6 hours. Images were taken using an inverted microscope TS100 attached to the high-resolution camera.

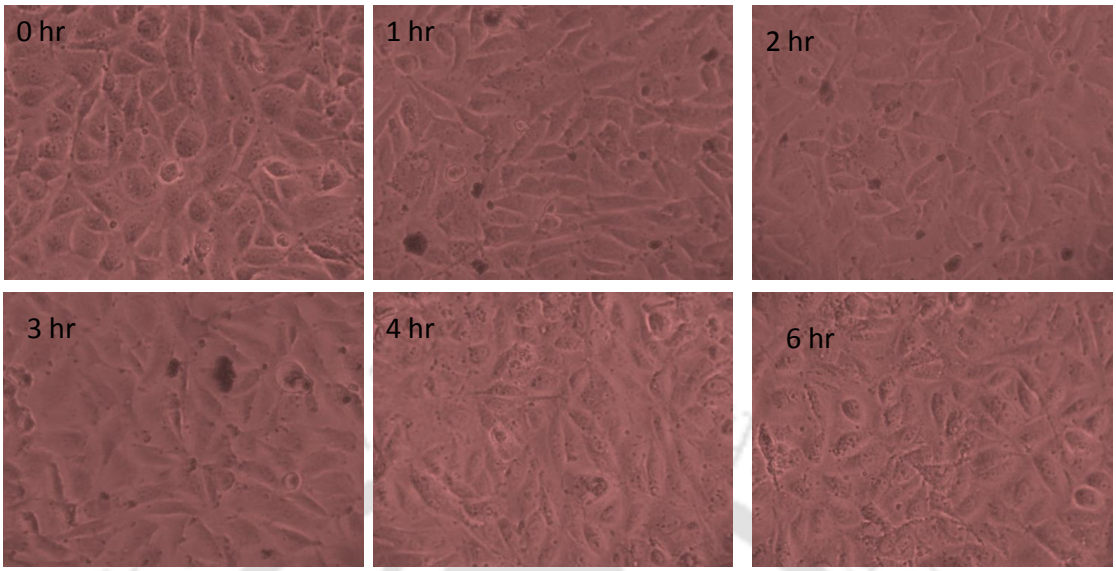

Figure A4.18. The morphology of the endothelial monolayer in presence of APPPA from 0-6 hours. Images were taken using an inverted microscope TS100 attached to the high-resolution camera.

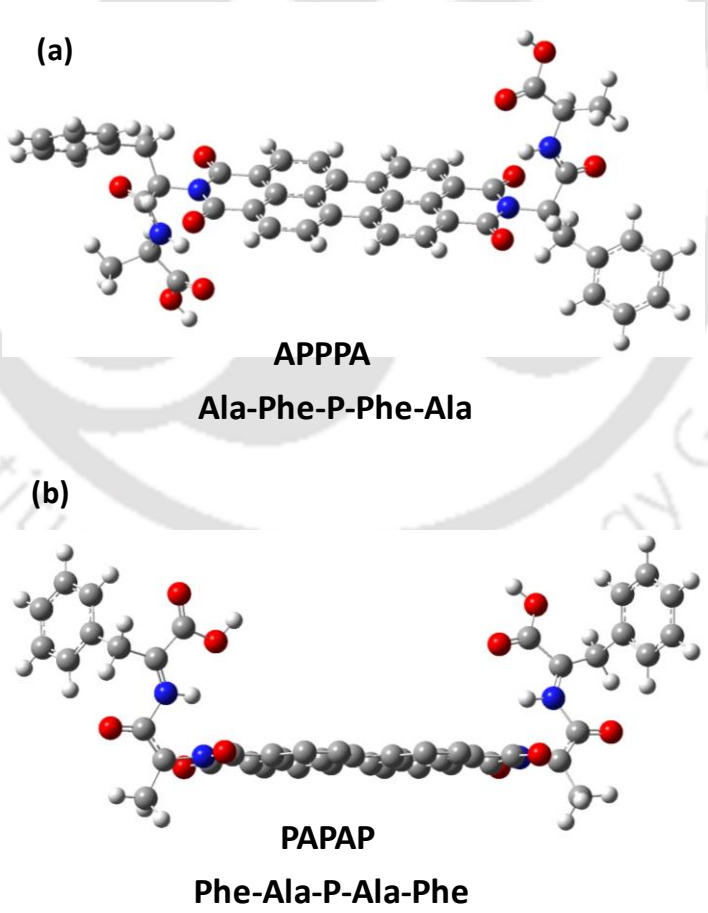

Figure A4.19. Optimized chemical structures of (a) APPPA and (b) PAPAP.

The docking studies of Aβ1-40 monomer in presence of PAPAP and APPPA were performed using AutoDock version 1.5.6 (http://autodock.scripps.edu/) on Windows 7. All the graphical analysis and image production was performed in PyMOL (https://www.pymol.org/) software. Docking was carried out using a Lamarckian genetic algorithm (LGA). For docking study, the protein was prepared by removing water molecules and then adding hydrogen and Gasteiger charges subsequently. Then non-polar hydrogen atoms were merged and atom types were fixed. Aβ (PDB code-2LFM) was covered by a grid box. Docking simulations were performed with total runs of 500. The PDB coordinates of PAPAP and APPPA were prepared using PRODRG. Docking results were examined based on the predicted free binding energy and best docking was selected on the basis of free energy rank and by visually inspecting molecule in PyMOL.

Further in silico binding investigation of PAPAP and APPPA with Aβ was performed through AutoDock version 1.5.6. The maximum binding energy of PAPAP and APPPA with Aβ1-40 monomer was obtained −9.1 and −8.9 kcal/mol respectively. Docking results revealed that most successful binding of both modulators showed a similar binding pattern with Aβ monomer (Figure A4.20). One part of the dipeptide tentacle and the aromatic core remained close to the N-terminal of the peptide and the remaining tail stayed close to residue 21-26. In both cases, perylene core was found to be slightly bent and the position of the phenyl ring of the attached phenyl alanine plays a vital role in inhibition of the self-aggregation. In the case of APPPA (Figure A4.20a), both the phenyl rings along with the perylene core are directed toward the hydrophobic residues (shown in magenta in figure A4.20a) unlike in the case of PAPAP (Figure A4.20b) where only one phenyl ring and the perylene π-moiety were available toward peptide hydrophobic core responsible for fibrillation. Since APPPA has the structural preference to reach the hydrophobic core of Aβ1-40, inhibition of peptide self-aggregation was much more prevalent than in the presence of PAPAP. H-bonding and other non-covalent interactions followed by their mutual aggregation between perylenebisimides and Aβ1-40 inhibit final fibril formation.

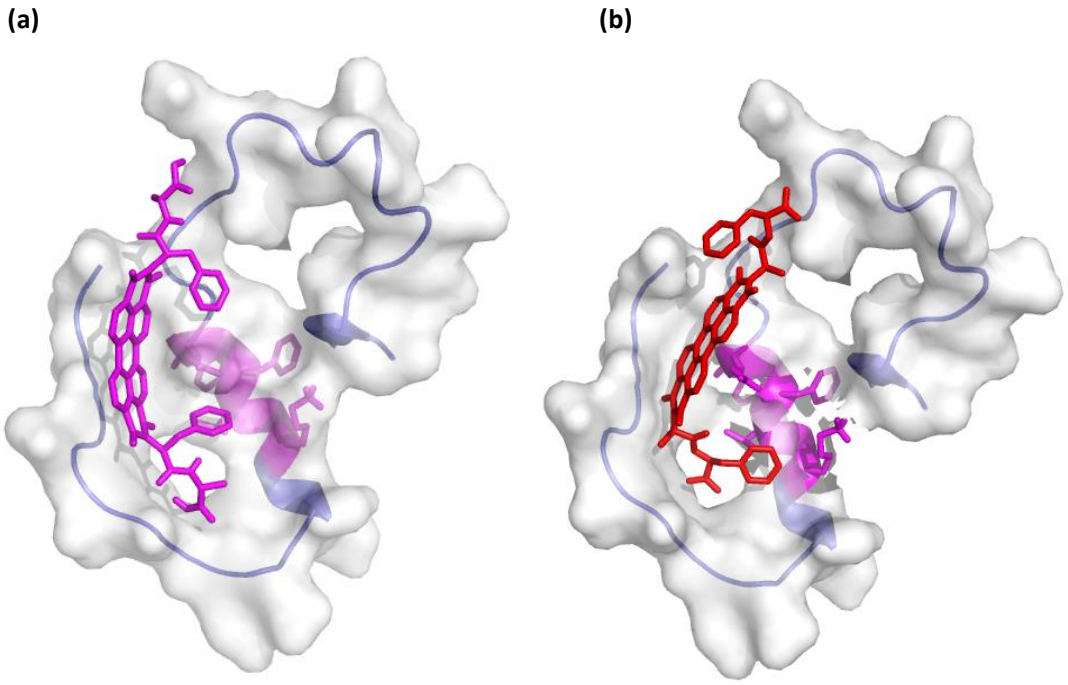

Figure A4.20. Molecular Snapshot for amyloid-β in the presence of (a) APPPA and (b) PAPAP.

Table A4.1. Permeability efficiency of APPPA and PAPAP across the endothelial monolayer is tabulated below.

Time (hours)	APPPA (%)	PAPAP (%)
0	0	0
1	4.9	2.0
2	10.5	1.1
3	9.3	-1.4
4	10.9	-5.7

Chapter 5

Inhibition of Insulin Amyloid using Synthetic Perylenebisimide Twins

Chowdhury, S. R.; Mondal, S.; Iyer, P. K. Blocking Oligomeric Insulin Amyloid Fibrillation via Perylenebisimides Containing Dipeptide Tentacles. (Manuscript submitted).

Abstract

Perylenebisimide interferes with amyloid fibrillation. Mutual aggregation happens in presence of these structural motifs and nucleation on the particle surface leads to inhibition of the fibrillization process. Oligomers are the primary toxic species that initiate pathogenic aggregation. In this study, the roles of perylenebisimide isomers (PAPAP and APPPA) were explored as modulators of insulin fibrillization. Early insulin aggregates are adsorbed into the modulator surface and result in an increase in lag phase. Fibrillation was monitored by Thioflavin T (ThT) fluorescence measurement in presence and absence of both the isomers, PAPAP and APPPA. Conformational modulation using far UV circular dichroism studies also highlighted their role as an aggregation inhibitor via reduction of α-helix into β-sheet along with increased random coil contents. Moreover, the inhibitory effects were more pronounced with the more aggregation prone derivative due to higher chances of a hydrophobic encounter between protein and the small molecule modulator.

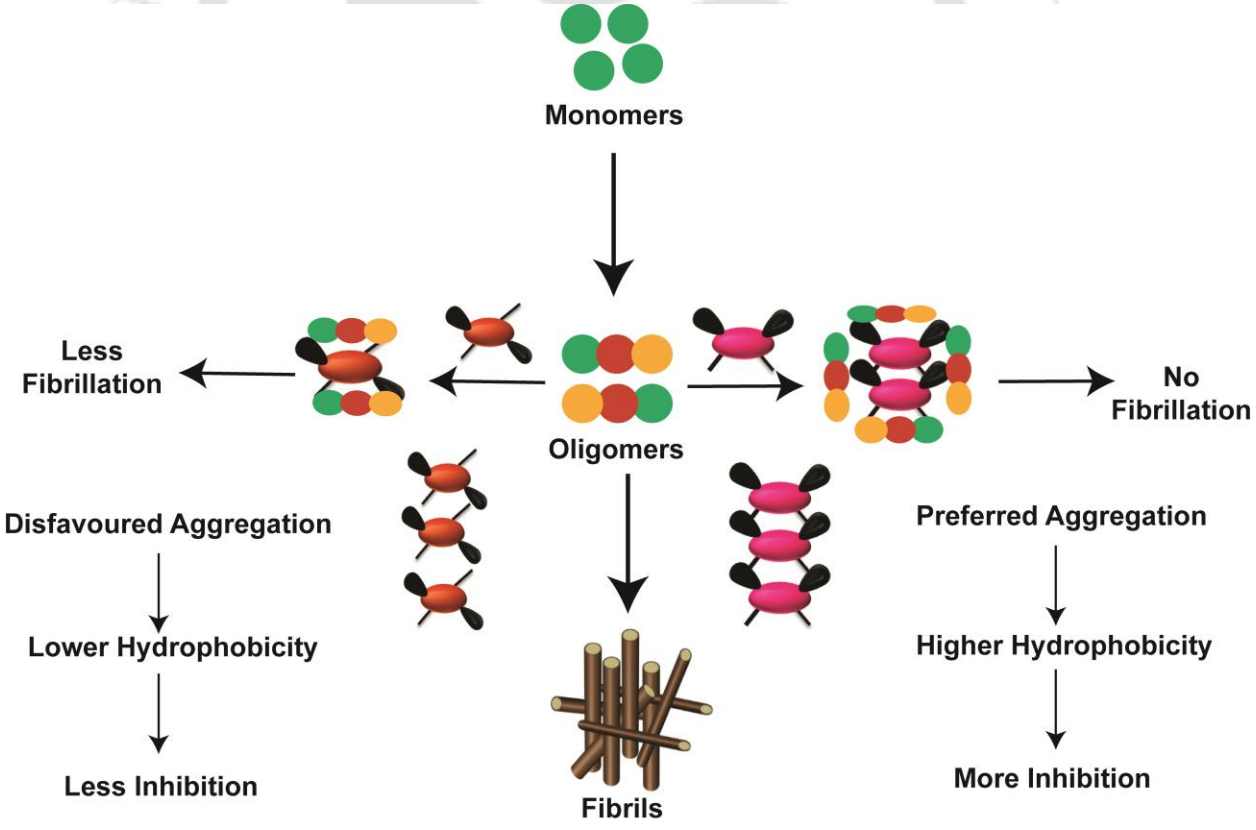

5.1. Introduction

Amyloid is an insoluble fibrillar form of the protein and play detrimental role in different aggregation based diseases viz. Alzheimer's disease, prion's disease, Parkinson's disease, and type 2 diabetes mellitus.[1-3] There are almost 27 different human protein which has been reported in systemic or localized amyloidosis and form toxic β-sheet rich oligomers through losing their native conformations under appropriate *in vitro* conditions.[4] These oligomeric intermediate structures subsequently form mature fibrils after assembling and lead the dysfunction into normal cellular physiology through either modulating membrane permeabilization or intracellular vesicular trafficking. Therefore, inhibition of the amyloid formation may offer a plausible therapeutic approach against these aggregation based disease.[5,6]

Insulin (~5.8 kDa) is a hypoglycemic peptide hormone that plays a crucial role in glucose metabolism and commonly used as an anti-diabetic drug. It is present in a hexameric form which is able to coordinate with two or four Zn (II) ions under physiological conditions. Monomeric insulin consists of two peptide chain-A and B of 21 and 30-residues long respectively. Both chains are connected through two inter disulfide linkage between A7-B7 and A20-B19 along with single intra chain disulfide linkage A6-A11.[7,8] Insulin fibrillation was reported at the site of insulin injection and clinical formulations. Insulin fibrillation kinetics illustrate a series of sequential three proceedings including nucleation, elongation and plateau phase where nucleation is the slowest phase during fibrillation. Electrostatic and hydrophobic interactions are considered as a determining force and signify the mechanistic involvement of noncovalent interactions during the insulin fibrillation. Disulfide linkage does not reshuffle and believed to cause a substantial topological constraint into the chain A.[9-11] It has been postulated that partial unfolding of native insulin trigger the fibrillation and form stable nuclei that subsequently intercede the β-sheet rich fibril formation during the elongation phase.[12,13] The effects of physicochemical factors viz. temperature, pH, ionic strength, nature of solvent, and surface chemistry on fibrillation kinetics have been reported.[13-16] Insulin fibrils has also been reported in different morphological isoforms such as protofibrils and spherulites with fascinating photophysical properties.[17-19] Various studies have investigated and demonstrated the cytotoxicity associated with the fibrils which formed under more closely resembling physiological conditions.[20-22] Numerous synthetic or natural compounds have been identified and explored to reduce or prevent the fibrillation process both *in vitro* and *in vivo*, for example, designed peptide conjugates,[23-25] antigen or epitope specific antibodies[26] and small

compounds consisting anti-aggregation property.[27-30] Amyloid pathogenicity mediated research has been the epicenter of extensive research since last two decades but still no efficient drug or effective approach able to complete eradication is available. Therefore, inhibition of the biogenesis of toxic aggregates/fibrils through synthetic compounds have emerged as potential therapeutic lines for the treatments of amyloid mediated pathogenesis.[31-33] This two dipeptide linked perylenebisimide twins (PAPAP and APPPA) modulate amyloid oligomers and one of them can cross blood brain barrier efficiently (shown in previous chapter). Even they can discriminate between prefibrillar and fibrillar aggregates under physiological conditions. These interesting findings inspire us to explore whether their aggregation will interfere the amyloidogenesis of insulin as well. In this chapter, the effect of both the isomers were discussed toward insulin fibrillation under physiological conditions. Interestingly, the isomer which is more prone to aggregation showed improved inhibition toward insulin compared to another derivative. This inhibition study was further validated by Thioflavin T (ThT), circular dichroism (CD), isothermal titration calorimetry (ITC), and atomic force microscope (AFM) studies.

5.2. Experimental Section

5.2.1. Materials

Insulin (recombinant human, expressed in yeast), Perylene-3,4,9,10-tetracarboxylic dianhydride (PTCDA), Thioflavin-T (ThT), Dipeptides (Phe-Ala and Ala-Phe), imidazole, and phosphate buffer saline (PBS) were purchased from Merck. Milli-Q water was used to prepare all stock solutions and buffers. Tris-HCl buffer was adjusted at pH 7.4 using pH tutor bench meter from Eutech Instruments with 1N HCl prior to modulation studies.

5.2.2. Synthetic procedures of PAPAP and APPPA

PAPAP and APPPA were synthesized using our previous protocol. 0.254 mmol (1 eqv) PTCDA, 0.535 mmol (2 eqv) Phe-Ala/Ala-Phe were heated at 130°C for 12 hours with stirring with imidazole (1.5 g), and 0.005 mmol (catalytic) Zinc acetate. Then the reaction mixture was poured into 2M HCl solution slowly to precipitate at 90°C. Finally, dark red colored precipitates were washed several times with water and dried under vacuum (139 mg, 65% APPPA; 150 mg, 71% PAPAP).[34]

5.2.3. *In Vitro* Insulin Fibrillation

Human insulin (HI) stock was prepared in 25 mM Tris-HCl (pH 7.4) containing 125 mM NaCl and 2 mM MgCl2. The final stock concentration was determined by measuring absorbance at 280 nm. Insulin fibrillation reaction was studied with 0.5 mg/ml of insulin concentration (~86 μM) at 37 °C at 60 rpm. Reaction mixtures were collected at different time intervals for further aggregation and modulatory studies.

5.2.4. Thioflavin-T (ThT) Fluorescence Kinetics

Thioflavin-T (ThT) (concentration was determined by absorbance at 412 nm using molar extinction coefficient 26,620 $M^{-1}cm^{-1}$) fluorescence was measured to investigate the kinetics associated with fibril formation of insulin as a function of time. ThT fluorescence was measured with incubated insulin solution at different time intervals was mixed with ThT solution in 1:2 ratio of protein and ThT dye consisting 10 μM and 20 μM final concentration of insulin and ThT. Fluorescence measurements were done on a Tecan infinite M1000 multi-mode microplate reader. The ThT fluorescence data were analyzed and fitted to the sigmoidal curve (excitation wavelength 450 nm and emission was collected at 482 nm).[13]

$$Y = y1 + m1x + {}^{yf + mfx}/_{1 + e - [\frac{x - x0}{\tau}]}$$

y denote the ThT fluorescence intensity, x is time and x0 is required time to achieve 50% of maximal fluorescence, therefore kapp represent the apparent rate constant of fibrillar growth given by 1/τ while time period in lag phase is derived by x0-2τ.

5.2.5. Circular Dichroism (CD) Spectroscopy

Jasco J-1500 spectrometer was used to record Circular dichroism (CD) spectra in 0.2 cm path length cuvette cell using a step size of 0.2 nm, the band width of 1 nm and a scan rate of 100 nm/min. 10 μM Insulin was taken in 5 mM Tris-HCl buffer at pH 7.4. Far-UV (190-250 nm) regions were recorded for the native and fibrillar insulin at room temperature both in presence and absence of the modulators. The spectra were recorded by averaging 5 scans and corrected by subtracting the Tris-HCl buffer spectra.

The percentage of α-helix can be obtained using following formula.

α- helix (%) = -MRE222-2340 / 30,300-2340 x 100

Where MRE222 is the experimentally reported MRE value at 222 nm, 2340 specify MRE of β-form and random coil structure at 222 nm while pure α-helix MRE value is 30,300 at same band.

$$MRE222 = \text{Intensity of CD (mdeg) at 222 nm} / 10\ nlC$$

Where n is the total number of amino acid residues present into the protein, l is the path length of the sample cell and C is the molar concentration of protein. Secondary structure components were analyzed using CONTIN and SELCON3 program available in Dichroweb server.

5.2.6. Isothermal Titration Calorimetry (ITC)

PAPAP and APPPA binding with monomeric insulin was examined by isothermal titration calorimetry using MicroCal iTC-200. Both protein, and inhibitor solutions were prepared in 20 mM Tris-HCl buffer (pH 8.4) to minimize the contribution of dilution heat. All solutions were degassed through Microcal THERMOVAC (Malvern) prior to use in ITC experiments. 50 μM native insulin was titrated with 0.5 mM of each inhibitors in the syringe. Characteristically, 25 successive injections of 1.5 μl each were injected into the sample cell containing protein at 37 ºC with a time interval of 90 sec between two successive injections. A constant stirring speed of 450 rpm was sustained to make sure proper mixing during the binding experiment.

The control experiment was also performed with same experimental conditions, where inhibitor titration was followed into the 20 mM Tris-HCl buffer, pH 8.4 and resulting heat change during control experiments were subtracted from the measured heat of respective sample titrations. ITC data were subsequently analyzed through one set of sites binding model in Origin 7 software. Gibbs free energy, ΔG, was derived from the equation $\Delta Gapp = \Delta H - T\Delta S$. Other parameters such as n, Ka, ΔS, and ΔH were obtained directly from multi injection mode of ITC at a constant temperature.

5.2.7. Zeta Potential Measurement

Zeta potential (ξ) of native and aggregated insulin and their co-incubated samples with PAPAP and APPPA were measured using with a Malvern Zetasizer Nano-ZS. A suspension of above-incubated solutions of different concentrations was dissolved in 5 mM Tris-HCl (pH 7.4) and transferred into 1 mL zeta potential cuvette (DTS1060, Malvern). Apparent zeta potential

(mV) of all protein solutions both in presence and absence of inhibitors were analyzed with Zetasizer software (version 7.11, Malvern).

5.2.8. Atomic Force Microscopy Study

To monitor the morphology, pristine solutions of native and aggregated insulin, APPPA, PAPAP and their coincubated insulin were dissolved in 10mM Tris-HCL (pH 7.4) and diluted 100 times before 10 μL of each sample was mounted onto the freshly cleaned glass slide. Then the slide was dried at room temperature under argon flow. Images were recorded on a Bruker, Innova AFM with non-contact tapping mode using a large scanner and analyzed with WSxM 5.0 Develop 8.0 software.

5.3. Results

In chapter 4, the modulatory behavior of this two perylenebisimide isomers were delineated toward amyloid-β aggregation. Mutual aggregation between perylene-protein and the interaction surface were the key features to develop a successful amyloid modulator. The isomer which was less aggregation prone was much more selective toward amyloid oligomer and no toxicity was observed in vitro MTT assay even at higher concentrations (0-100 μg/ml). These findings encourage us to check how they behave in presence of the other amyloid protein. This chapter details the insulin fibril formation in presence of PAPAP and APPPA by ThT assay, conformational modulation by CD spectrometer, binding kinetics by ITC measurements and finally the changes were visualized using atomic force microscopy. Moreover, the modulation strategy was discussed in detail and a structural relationship has been found based on photophysical properties of the perylenebisimide isomers.

5.3.1. Fibril formation by insulin

Fibrillation process in various proteins are commonly investigated through Thioflavin T (ThT) based fluorescence assay in which ThT delivers typical emission spectra at 482 nm after exciting buffer containing protein solutions at 450 nm.[34] The onset and maximum value of ThT fluorescence signal represent the lag phase and fibril quantity respectively. Figure 5.1 demonstrated the time evolution of insulin fibrillation based on ThT fluorescence values after incubation of insulin (~86 μM) at 37 °C under physiological pH 7.4 with stirring at 60 rpm. The ThT fluorescence curve represented a typical sigmoidal curve comprising three distinctive phase, initial lag phase, a succeeding growth phase followed by a plateau phase. Kinetic parameters such as lag phase duration and apparent rate constant (kapp) associated with

fibrillation were derived through the fitting of equation (Section 5.2.4 in materials and methods) to the ThT data and resulting time duration of lag phase was found to be as 3.87±0.12 h. The apparent rate constant for insulin fibrillation was calculated as 0.687 h^{-1} and reached a plateau within 12 h. The fibril formation was also established through atomic force microscopy images that showed a mesh of insulin fibrils (section 5.3.3) in control. The effect of two synthetic inhibitors, PAPAP and APPPA were investigated on insulin fibrillation with a final concentration of 8.6 μM as PAPAP showed a maximum reduction in ThT fluorescence intensities with this concentration and highlighted the strong inhibitory effect (Figure 5.1). Native insulin was incubated with varying concentrations of these inhibitors from 0.86 μM to 43 μM under same in vitro conditions at 37 °C with stirring at 60 rpm but ThT fluorescence intensity is almost reduced above 8.6 μM concentration of PAPAP and was not fitted to equation 1 for kinetic analysis, therefore we investigated the fibrillation inhibition of insulin with 8.6 μM of both inhibitors. Figure 5.1 illustrated the ThT fluorescence curve of fibrillation in presence of these two synthetic inhibitors with 8.6 μM of final concentrations. There is a substantial decrease in ThT fluorescence intensity that illustrated the quantitative reduction in the fibril formation in presence of both inhibitors. ThT reduction is more in presence of PAPAP as compared to APPPA and demonstrated its inhibitor efficiencies over APPPA. Kinetic analysis of insulin fibrillation has shown a maximum increase in the time duration of lag phase as 7.69±0.17 h in case of PAPAP while in the case of APPPA, it was approximately 6.58±0.13 h. Extended lag phase in PAPAP mediated fibrillation highlighted its efficient inhibitory property and delayed the nucleation process as compared to insulin fibrillation in absence of inhibitors. The kapp values for PAPAP and APPPA mediated inhibition of insulin fibrillation was calculated as 0.330 h^{-1} and 0.383 h^{-1} (Table 5.1) respectively which suggested their involvement in the suppression of fibrillation along with delaying the process. Subsequently, it was concluded that both compounds are a potent inhibitor and perform the efficacy through both ways, delaying, and suppression of the process. Figure 5.2 explained the increase in lag phase in presence of inhibitors and PAPAP mediated inhibition was superior to APPPA inhibition. Both the modulators helped to restore native insulin which was proved by a similar residual protein ThT assay (Figure 5.2b). Further to check the effects on preformed β-rich aggregates, we have performed ThT assay with the preformed insulin aggregates, similarly incubating with 8.6 μM of PAPAP and APPPA. PAPAP co-incubated aggregates resulted in a decrease in β-content compared to APPPA co-incubated and control insulin fibrillar aggregates as observed from ThT fluorescence profile (Figure A5.1).

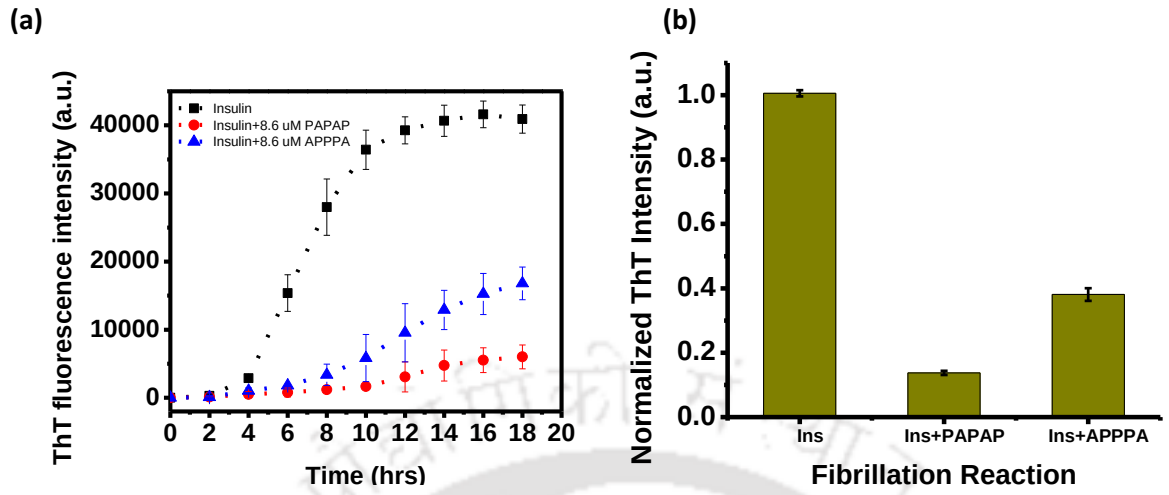

Figure 5.1. (a) Insulin fibrillation kinetics monitored through ThT fluorescence intensity with insulin amyloid fibrils. (b) Maximum ThT fluorescence intensity during the fibrillation in absence and presence of PAPAP and APPPA. ThT data are normalized with the maximum fluorescence intensity; error bar represents standard error of the minimum five different measurements.

Reaction	lag phase (h)	apparent rate (k_{app}/h^{-1})	Max. Intensity
Insulin	3.87±0.12	0.687	1.000
Insulin+PAPAP	7.69±0.17	0.330	0.139
Insulin+APPPA	6.58±0.13	0.383	0.410

Table 5.1. Kinetic parameters of insulin fibrillation in absence and presence of synthetic inhibitors, PAPAP and APPPA.

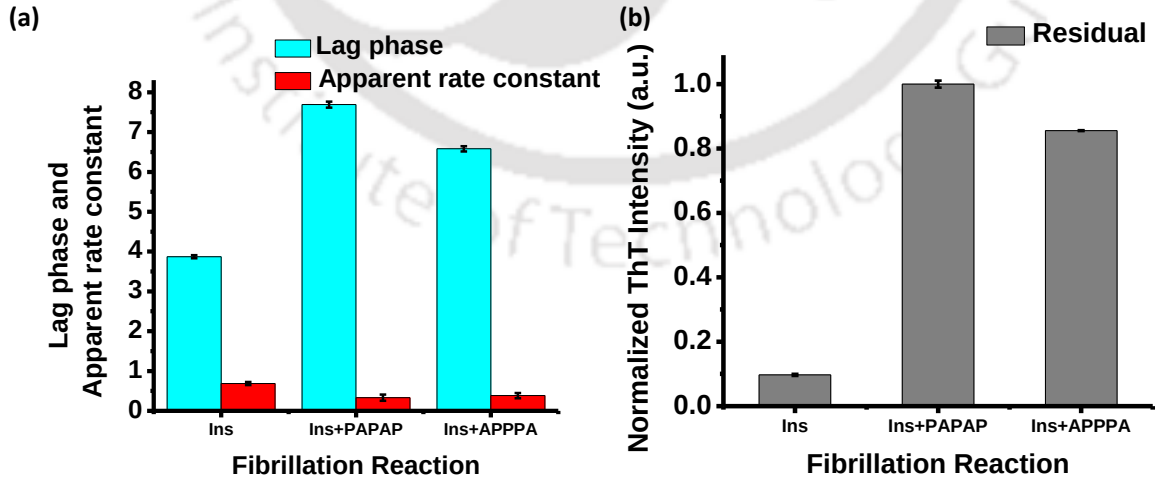

Figure 5.2. (a) Kinetic parameters lag phase and apparent rate constant (kapp) during insulin fibrillation in absence and presence of inhibitors (b) residual protein kinetics of insulin fibrillation in absence and presence of inhibitors.

5.3.2. Conformational restoration CD analysis

Time (hrs.)	Reaction	α-helix	β-sheet	β-turn	Random coil
0	HI	37	22.3	14.7	26
	HI+PAPAP	35.8	22	14.5	27.7
	HI+APPPA	36.7	22	14.6	26.7
4	HI	26.9	23.5	22.9	26.7
	HI+PAPAP	32.2	21.2	17	29.6
	HI+APPPA	28.1	22.2	22	27.7
8	HI	3.6	40.6	22	33.8
	HI+PAPAP	8.2	34.3	20.3	37.2
	HI+APPPA	5.9	37.6	20.6	35.9
12	HI	2.9	44.2	22.4	30.5
	HI+PAPAP	6.5	35.1	21.1	37.3
	HI+APPPA	5.2	36.9	22.2	35.7

Table 5.2. Percentage of α-helix, β-sheet, β-turn, and Random coil of incubated insulin (HI, 10 μM) both in presence and absence of inhibitors (PAPAP and APPPA, 8.6μM) in 5 mM Tris-HCl buffer, pH 7.4.

Far UV CD spectra were recorded in order to approve conformational modulation in the absence and presence of inhibitors (Figure 5.3). In CD spectra, 208 nm and 222 nm bands are characteristics for α-helix while 218 nm bands indicate β-sheet fraction in respective protein. It exhibited CD spectra highlighting the conversion of α-helix into the β-sheet like conformations (Figure 5.3a).[18,35] Changes in the protein secondary structures were studied in presence of both the inhibitors using CD spectrometer (Figure 5.3b and 5.3c) and the changes

in α and β fraction was carefully observed.In the present study, CD spectra of native insulin highlighted 37 and 22.2 % of α-helix and β-sheet fraction along with 14.7 and 26 % of β-turn and random coil respectively which is in good agreement with previous reports.36 PAPAP induced more reduction (~3.24 %) in α-helix of native insulin as compared to APPPA molecule (~0.81 %). Higher reduction in total α-helix proportion with PAPAP might be because of higher affinity to native insulin. (Table 5.2 and Figure A5.2).

Conformational modulation was also investigated in absence and presence of the inhibitors during the fibrillation that revealed ~92.2 %, ~82.4 % and ~85.9 % loss of α-helicity while ~98.2 %, ~57.4 % and ~65.5 % increase in a β-sheet fraction in control, PAPAP and APPPA mediated insulin fibrillation respectively. It was observed that presence of PAPAP at low concentration restore maximum α-helicity with a minimum β-sheet fraction in insulin during the fibrillation. (Figure A5.3) PAPAP also enhanced total fraction of the random coil as compared to control and APPPA mediated fibrillation which highlighted its potential anti-aggregation property. (Figure A5.4) Conclusively, CD analysis highlighted that PAPAP and APPPA both act as aggregation inhibitors and accomplished their modulating role through the reduction of α-helix into β-sheet along with increased random coil contents.

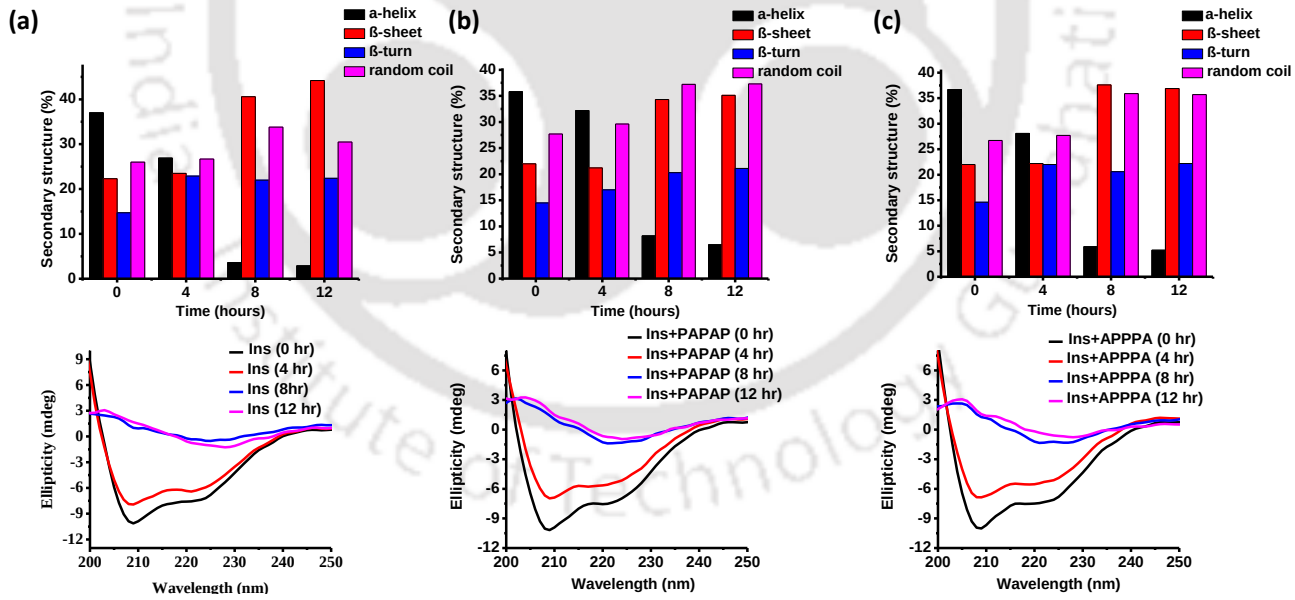

Figure 5.3. CD spectra and changes (bar diagram) in insulin secondary structure in (a) control as Native insulin, (b) coincubated with PAPAP, and (c) coincubated with APPPA with time (0-12 hrs) in 5 mM Tris-HCl buffer, pH 7.4. α-helix is denoted as a-helix and Protein concentration was 10 μM into 5 mM Tris-HCl buffer, pH 7.4

5.3.3. AFM analysis

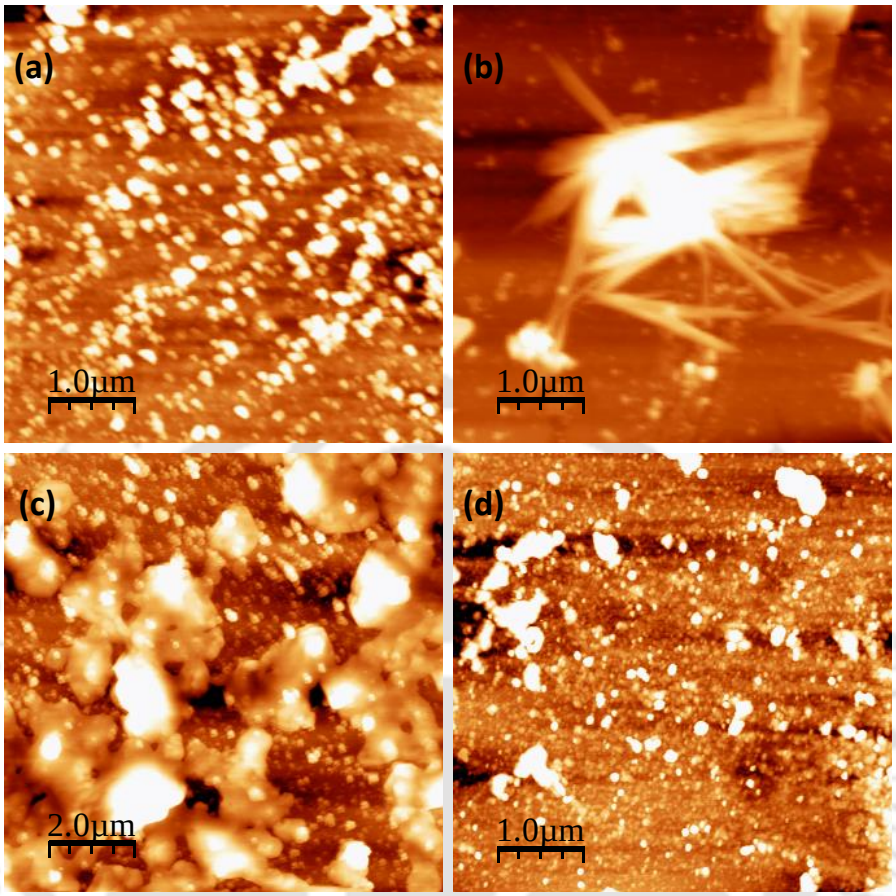

Figure 5.4. AFM images of control (a) native insulin monomers, (b) mature fibrils, and modulation (c) in presence of PAPAP, and (d) APPPA. All the samples were incubated at 37°C in Tris HCl buffer at pH 7.4. Images were taken after 72 hours of incubation. PAPAP and APPPA concentrations were 8.6 µM and insulin concentration was 86 µM.

Further to visualize the insulin aggregates in presence of modulators, fibrillization was confirmed by using atomic force microscopy (Figure 5.4). Insulin was incubated both in presence and absence of the modulators, PAPAP and APPPA for 72 hours to ensure fibril formation and the changes due to modulation. Native insulin monomers formed mature fibrils after 72 hours of incubation. Native insulin monomer presented a diameter of 200 nm and height of 12-16 nm as observed in topological image (Figure 5.4a, A5.5a and A5.5b). After 72 hours of incubation mature fibril was found to form with diameter 300-400 nm and ~25-35 nm in height (Figure 5.4b, A5.5c and A5.5d). PAPAP and APPPA co-incubated with insulin showed no fibril formation (Figure 5.4c and 5.4d). In presence of PAPAP, insulin oligomers (monomers and early aggregates) were blocked and thus restricted to come in contact with

other protein counterpart to form mature fibrils. PAPAP co-incubated insulin showed aggregates with diameter ~1μM and ~40-60 nm in height (Figure 5.4c, A5.5e and A5.5f). As attached phenyl ring of phenyl alanine was away from perylene core in case of PAPAP, it was more prone to aggregation and led to formation of larger aggregates compared to the other isomer, APPPA. On the other hand, APPPA co-incubated insulin resulted aggregates with diameter of 450 nm and ~20 nm in height (Figure 5.4d, A5.5g, and A5.5h). From AFM studies, it was revealed that PAPAP and APPPA was successfully inhibited insulin aggregation and stopped the fibril formation. More aggregation prone derivative resulted in a larger aggregates and better blocking surface toward early insulin aggregates.

5.3.4. Interaction analysis through ITC

Binding kinetics of these inhibitors with native insulin is decisive to understand the mechanistic insights of fibrillation inhibition mediated with PAPAP and APPPA (Figure 5.5 and Table 5.3).

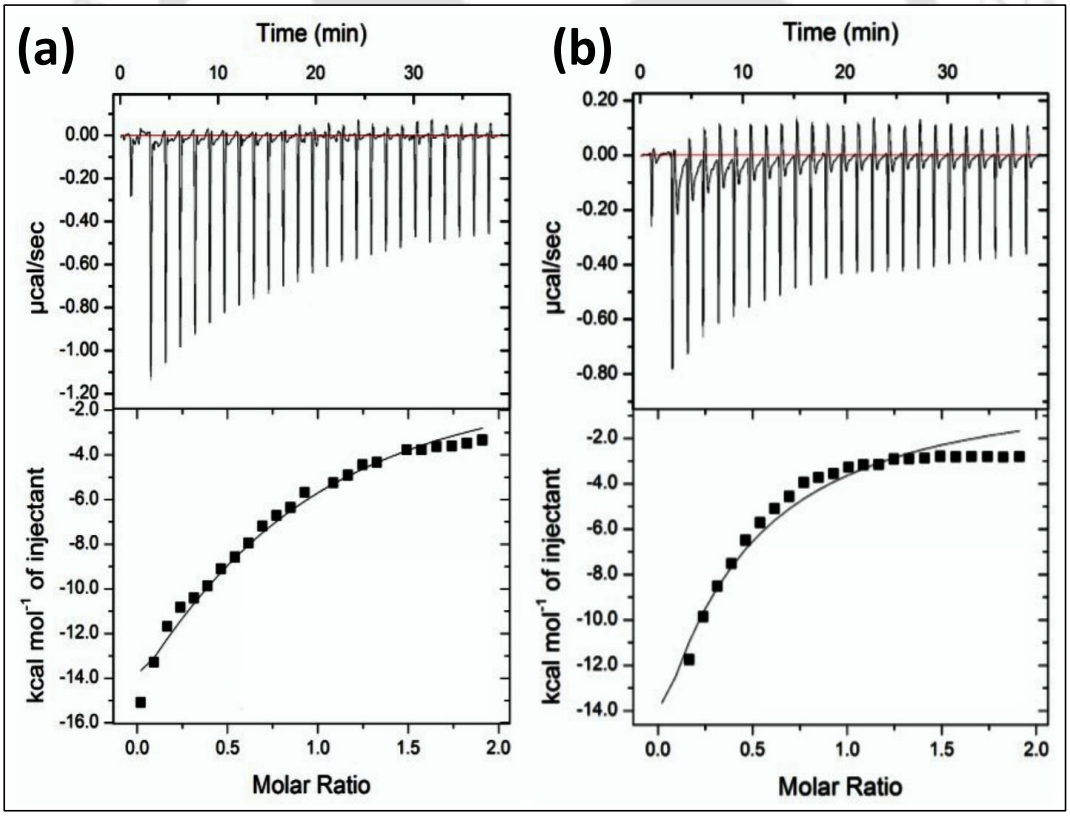

Figure 5.5. ITC thermogram of native insulin interaction with inhibitors PAPAP and APPPA at 37 °C.

Therefore, an ultrasensitive technique, isothermal titration calorimetry was applied for thermodynamic characterization of intermolecular interactions between native insulin and studied inhibitors. ITC is an efficient approach to study the binding affinity between two molecules in diverse in vitro conditions and typically offer binding stoichiometry (n), binding affinity (Ka), and total entropy change (ΔS) as well as total enthalpy change (ΔH) during the binding reaction. To assess the underlying association between protein and inhibitors as various potential interaction forces such as hydrophobic, electrostatic, hydrogen bonds and van der Waal's may involve in the interaction, therefore to dictate the driving force of corresponding interaction based on binding interaction and heat exchange among these substances. Both enthalpy change and entropy change were considered as driving factors for protein-ligand interaction. If ΔH<0, ΔS<0, the driving force is Van der Waal's and hydrogen bonding; if ΔH>0, ΔS>0, hydrophobic interaction is prevailing while ΔH<0, ΔS>0 infer the dominance of electrostatic forces. To rule out the electrostatic contribution at peptide-modulator interface, we have measured zeta potential of peptide aggregates in presence and absence of inhibitors in Tris-HCl buffer (Figure A5.6). We observed an increase in apparent zeta potential in case of co-incubated sample compared to pristine modulators. Briefly, ITC and zeta potential measurements revealed the predominance of Van der Waal's contribution toward perylene-insulin interaction.

Inhibitors	Stoichiometry (n)	K_b ($Mole^{-1}$)	ΔH ($kcal.mole^{-1}$)	ΔS ($cal.mol^{-1}k^{-1}$)	ΔG_{app} ($kcal.mole^{-1}$)
PAPAP	0.658±0.01	$1.92x10^4$±148	-13.83±0.15	-18.8	-5.82
APPPA	0.512±0.076	$2.79x10^3$ ± 119	-11.86±0.28	-25.35	-3.99

Table 5.3. Thermodynamic parameters of PAPAP and APPPA interaction with native insulin.

5.4. Discussion

Soluble oligomers of different sizes are formed during lag phase and are key for the fibrillization process. As obtained in far UV circular dichroism spectra, there was an increase in a β-sheet fraction when native insulin was incubated alone in the buffer. The increased exposure of aggregation-prone sections, which are protected in the parent protein, helps the nucleation and formation of final amyloid fibrils. The observed changes in presence of the modulators are due to inhibition of fibrillization caused by the trapping of early aggregates which occurred during lag phase. The effect of modulators was not only observed in

fibrillization but also on the prefibrillar aggregates as obtained in ThT profile of insulin fibril incubated with the modulators. The observed dual behavior proposes that the interaction with the perylene arises at the monomer and oligomer levels. Two factors control self-aggregation of the peptide, first the surface chemistry of modulator and the interaction with the hydrophobic core of the peptide which is responsible for the formation of pathological aggregates. Therefore, a stronger modulator–monomer interactions compared to the monomer–monomer interactions guide the oligomers to adsorb on the modulator surface will dissolve into monomers or oligomers of smaller size resulting in an increase in lag phase of the peptide fibrillation (Figure 5.1 and 5.2).[37] Based on the previous findings and to explore structurally efficient motifs that can detect and interact with amyloid oligomers, the perylenebisimide core was chosen as a preferred molecule with dipeptide tails. We have explored this isomers toward amyloid oligomer modulation in Aβ1-40 and real CSF samples. These π-conjugated chromophores of perylenebisimide are hydrophobic in nature and apparently, they are insoluble in aqueous media due to highly favorable π-stacking but the wise selection of di-peptide tentacles made it soluble in water and their mutual aggregation guided the fibrillation into an 'off-pathway'. Difference in di-peptide attachment to the perylene core led to distinct modes of aggregation as with normal Franck-Condon progression, A0→0/A0→1 becomes 1.5 to 0.7 and 1.5 to 1 in presence of water at a particular concentration of PAPAP and APPPA respectively (Figure A5.7).[34] This is further supported by their structural conformations optimized by Gaussian. PAPAP is more prone to aggregation as phenylalanine is not directly attached to the perylene core and thus hang on one side of the perylene plane allowing another perylene molecule to come close and available for π-stacking. But in case of APPPA, phenyl alanine is attached to perylene directly via amine end and thus to avoid steric hindrance phenyl rings are placed in a trans-fashion with respect to the perylene plane unlike in the case of PAPAP (Figure A5.8). As a result, both isomers show a distinct photophysical behavior in the aqueous environment. PAPAP is more aggregation-prone and thus hydrophobicity increases at the interface of small molecule-peptide interaction. For a smaller amyloid-like in case of amyloid-β, APPPA had a predominant role in modulating the early aggregates due to their structural similarity and as it was less aggregating in water, it could actually pass through the blood brain barrier compared to PAPAP. But in case of insulin, PAPAP dominates over APPPA due to favorable hydrophobic encounter as the nucleation progresses, the hydrophobicity of the peptide aggregates increases. To probe the electrostatic encounter, we measured the zeta potential of the peptide both in presence and absence of modulators. Both protein and the small molecule exhibit a

negatively charged surface. Initially, both co-aggregates show a zeta potential lower than their pristine values of both insulin and modulators. Further incubation leads to a higher increase in case of APPPA compared to PAPAP due to more probable electrostatic affection. Although the probability of available electrostatic encounter in both the modulators is same their individual self-aggregation creates a difference in hydrophobicity making PAPAP a selective modulator for insulin, unlike the other isomer which is selective toward amyloid-β. Overall, lag phase increases due to the presence of modulator which helps the protein to adsorb and interacts with its hydrophobic aromatic core due to its core and available hydrophobic tail of the modulators. The difference in their aggregation behavior makes them selective toward different structural amyloid via changing the protein secondary structures and most importantly shifting the pathogenic equilibrium toward the monomeric side.

5.5. Conclusion

Selective modulation of insulin fibrillization as well as preventing them from forming mature fibrils was achieved with two dipeptide linked perylenebisimide isomers (PAPAP and APPPA). Two factors are important for developing a selective amyloid modulator: first the surface chemistry and second the protein inherent hydrophobicity upon aggregation. Those factors control the specific interaction between amyloid and molecular modulators which lead to inhibition of self-aggregation of both events i.e., fibrillization of insulin and π-stacking of the perylenebisimide. These findings suggest that both the modulators interact with insulin at its monomeric and oligomeric stage selectively via specific non covalent interactions thereby stabilizing the lag phase and provide fundamental insights into the chemistry in peptide-based probes, therefore shifting the pathogenic aggregation to the opposite side. The more aggregation prone isomer produces a better hydrophobic encounter with insulin amyloid and thus acts as a better modulator compared to the other isomer. These results confirmed that insulin fibril regulation via selective noncovalent binding using peptide-based hydrophobic probes provide fundamental insights into the chemistry involved to understand amyloidosis mechanism and al-low the design of versatile materials containing biomolecules tagged to supramolecular cores.

References

(1) Selkoe, D.J. *Nature* **2003**, *426*, 900–904.

(2) Tycko, R.; Wickner, R. B. *Acc. Chem. Res.* **2013**, *46,* 1487–1496.

(3) Dikiy, I.; Eliezer, D. *Biochim. Biophys. Acta* **2012**, *1818*, 1013–1018.

(4) Sipe, J. D.; Benson, M. D.; J. N.; Ikeda, S.; Merlini, G.; Saraiva, M. J.; Westermark, P. *Amyloid* **2010**, *17*, 101–104.

(5) Oren, Z.; Shai, Y. *Biopolymers* **1998**, *47*, 451–463.

(6) Naiki, H.; Nagai, Y. *J. Biochem.* **2009**, *146*, 751–756.

(7) Chang, X.; Jorgensen, A. M.; Bardrum, P.; Led, J. J. *Biochemistry* **1997**, *36*, 9409–9422.

(8) Mayer, J. P.; Zhang, F.; DiMarchi, R. D. *Biopolymers* **2007**, *88*, 687–713.

(9) Ivanova, M. I.; Sievers, S. A.; Sawaya, M. R.; Wall, J. S.; Eisenberg, D. *Proc. Natl. Acad. Sci. U. S. A.* **2009**, *106*, 18990–18995.

(10) Whittingham, J. L.; Scott, D. J.; Chance, K.; Wilson, A.; Finch, J.; Brange, J.; Guy Dodson, G. *J. Mol. Biol.* **2002**, *318*, 479–490.

(11) Babenko, V.; Piejko, M.; Wójcik, S.; Mak, P.; Dzwolak, W. *Langmuir* **2013**, *29*, 5271–5278.

(12) Sluzky, V., Tamada, J. A.; Klibanov, A. M.; Langer, R. *Proc. Natl. Acad. Sci. U. S. A.* **1991**, *88*, 9377–9381.

(13) Nielsen, L.; Khurana, R.; Coats, A.; Frokjaer, S.; Brange, J.; Vyas, S.; Uversky, V. N.; Fink, A. L. Biochemistry **2001**, *40*, 6036–6046.

(14) Pandey, L. M.; Le Denmat, S.; Delabouglise, D.; Bruckert, F.; Pattanayek, S. K.; Weidenhaupt, M. *Colloids Surf. B* **2012**, *100*, 69–76.

(15) Erlkamp, M.; Grobelny, S.; Faraone, A.; Czeslik, C.; Winter, R. *J. Phys. Chem. B* **2014**, *118*, 3310–3316.

(16) Schlein, M. *AAPS J.* **2017**, *19,* 397–408.

(17) Krebs, M. R. H. MacPhee, C. E.; Miller, A. F.; Dunlop, I. E.; Dobson, C. M.; Donald, A. M. *Proc. Natl. Acad. Sci. U. S. A.* **2004**, *101*, 14420–14424.

(18) Kurouski, D.; Dukor, R. K.; Lu, X.; Nafie, L. A.; Lednev, I. K. *Biophys. J.* **2012**, *103*, 522–531.

(19) Amdursky, N., Gazit, E.; Rosenman, G. *Biochem. Biophys. Res. Commun.* **2012**, *419*, 232–237.

(20) Yoshihara, H.; Saito, J.; Tanabe, A.; Amada, T.; Asakura, T.; Kitagawa, K.; Asada, S. *J. Pharm. Sci.* **2016**, *105*, 1419–1426.

(21) Grudzielanek, S.; Velkova, A.; Shukla, A.; Smirnovas, V.; Tatarek-Nossol, M.; Rehage, H.; Kapurniotu, A.; Winter, R. *J. Mol. Biol.* **2007**, *370*, 372–384.

(22) Lorenzo, A.; Razzaboni, B.; Weir, G. C.; Yankner, B. A. *Nature* **1994**, *368*, 756–760.

(23) Gibson, T. J.; Murphy, R. M. *Protein Sci.* **2006**, *15*, 1133–1141.

(24) Mishra, N. K.; Joshi, K. B.; Verma, S. *Mol. Pharm.* **2013**, *10*, 3903–3912.

(25) Mishra, N. K.; Krishna Deepak, R. N. V.; Sankaramakrishnan, R.; Verma, S. *J. Phys. Chem. B* **2015**, *119*, 15395–15406.

(26) Zha, J.; Liu, X-m.; Zhu, J.; Liu, S-y.; Lu, S.; Xu, P-x.; Yu, X-l.; Rui-tian Liu, R-t. *Sci. Rep.* **2016**, *6:36631*, doi: 10.1038/srep36631.

(27) Choudhary, S., Kishore, N.; Hosur, R. V. *Sci. Rep.* **2015**, *5:17599*, doi: 10.1038/srep17599.

(28) Chowdhury, S. R., Agarwal, M.; Meher, N.; Muthuraj, B.; Iyer, P. K. *ACS Appl. Mater. Interfaces* **2016**, *8*, 13309–13319.

(29) Arora, A., Ha, C.; Park, C. B. *FEBS Lett.* **2004**, *564*, 121–125.

(30) Giger, K.; Vanam, R. P.; Seyrek, E.; Dubin, P. L. *Biomacromolecules* **2008**, *9*, 2338–2344.

(31) Härd, T.; Lendel, C. *J. Mol. Biol.* **2012**, *421*, 441–465.

(32) Siddiqi, M. K.; Alam, P.; Chaturvedi, S. K.; Nusrat, S.; Shahein, Y. E.; Khan, R. H. *Int. J. Biol. Macromolec.* **2017**, *95*, 713–718.

(33) Deckert-Gaudig, T.; Deckert, V. *Sci Rep.* **2016**, *6: 39622*, doi 10.1038/srep39622.

(34) Chowdhury, S. R.; Balaji, S. N.; Mondal, S.; Meher, N.; Trivedi, V.; Iyer, P. K. Manuscript Submitted (Chapter 4).

(35) Loksztejn, A.; Dzwolak, W. *J. Mol. Biol.* **2008**, *379*, 9–16.

(36) Hua, Q.-x.; Weiss, M. A. *J. Biol. Chem.* **2004**, *279*, 21449–21460.

(37) Cabaleiro-Lago, C.; Szczepankiewicz, O.; Linse, S. *Langmuir* **2012**, *28*, 1852–1857.

Appendix

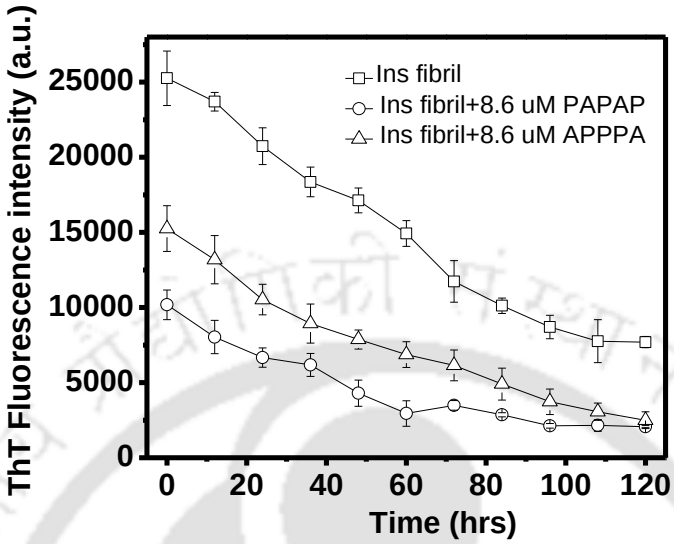

Figure A5.1. ThT fluorescence intensity modulation experiment. Preformed insulin fibers were incubated in presence and absence of inhibitors with ThT (20 μM) in 5 mM Tris-HCl at pH 7.4. ThT data are normalized with the maximum fluorescence intensity; error bar represents standard error of the minimum five different measurements.

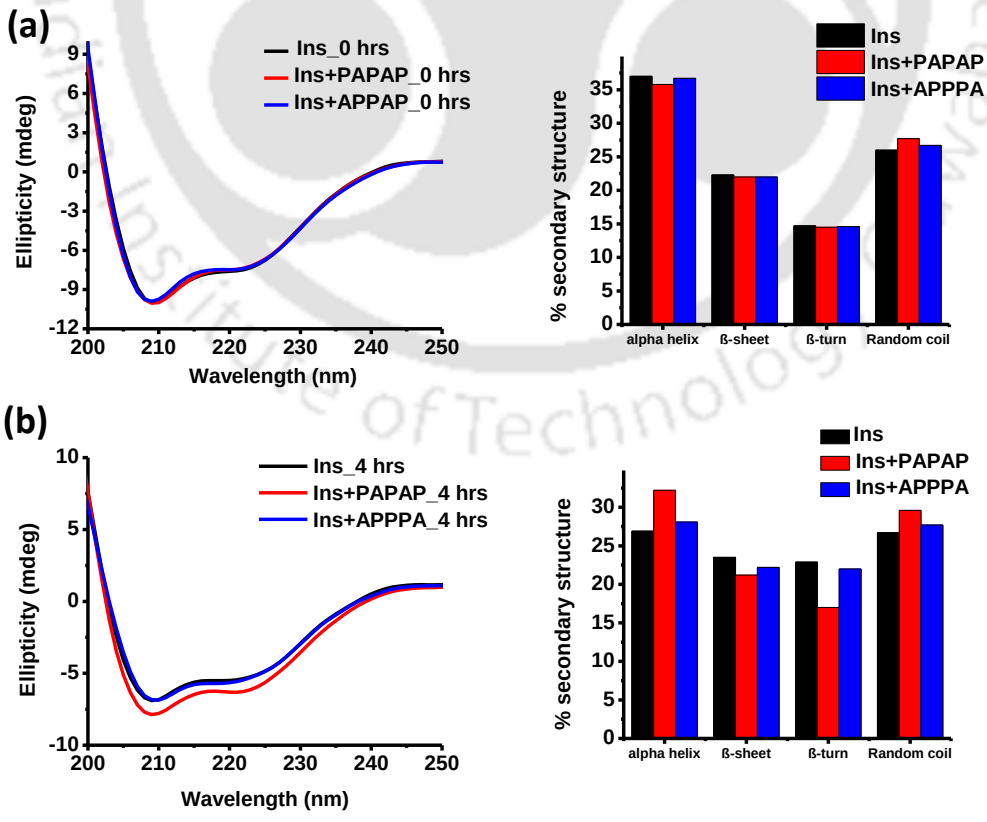

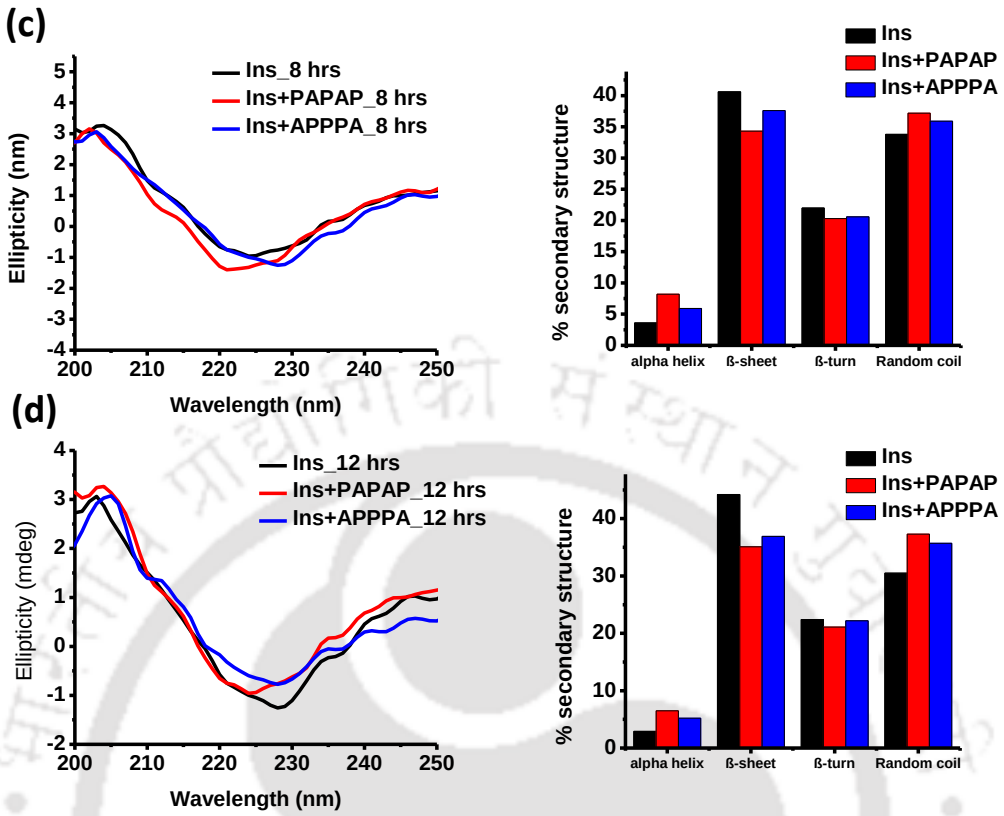

Figure A5.2. PAPAP and APPPA mediated conformational modulations in native insulin at time 0-12 hours (a-d). Samples were incubated in 5 mM Tris-HCl buffer, pH 7.4. Protein concentration was 10 μM and modulator concentration was 8.6 μM into 5 mM Tris-HCl buffer, pH 7.4.

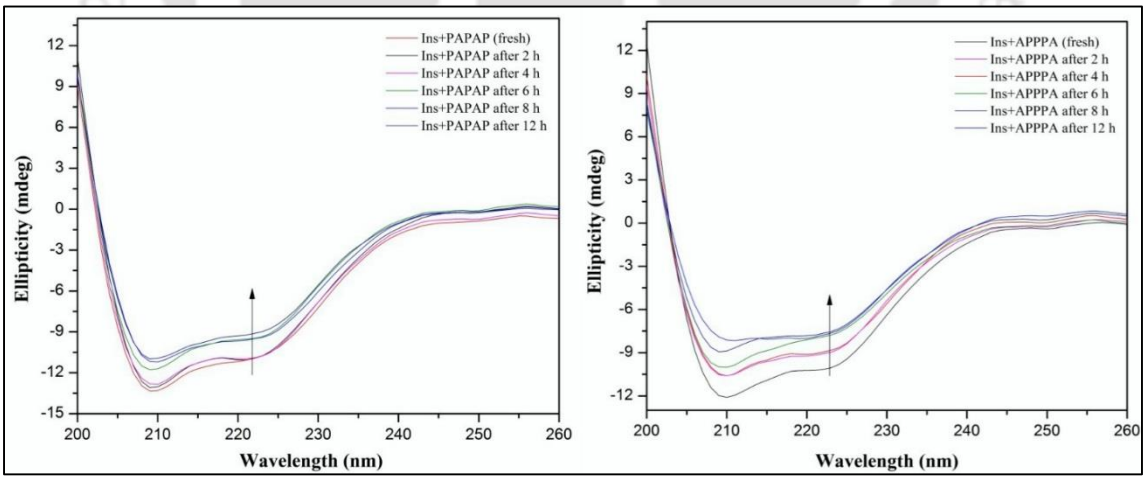

Figure A5.3. Conformational restoration at higher concentration (43.5 μM) of inhibitors. CD measurements were done in 5 mM Tris-HCl at pH 7.4.

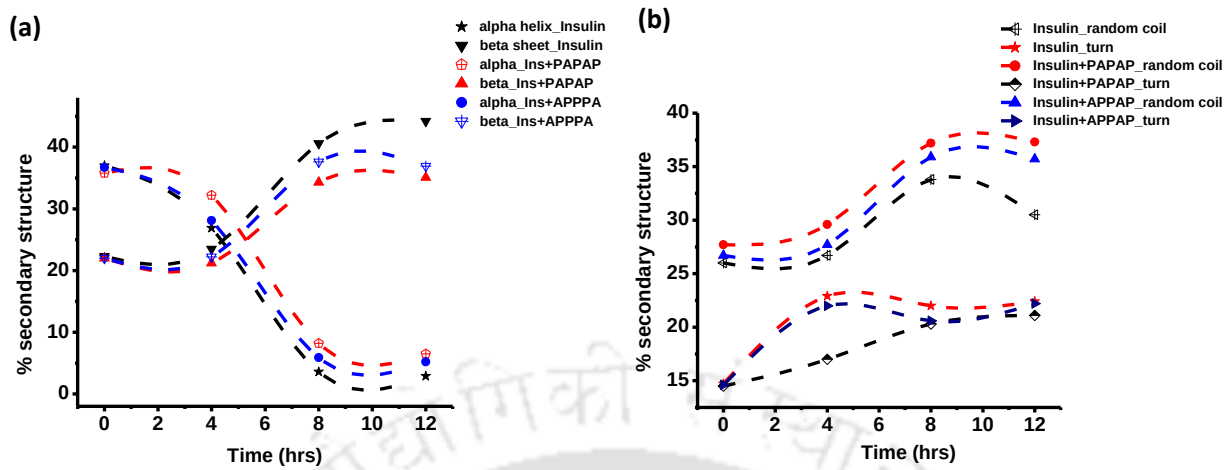

Figure A5.4. (a-b) Changes of secondary structures of insulin both in presence and absence of modulators.

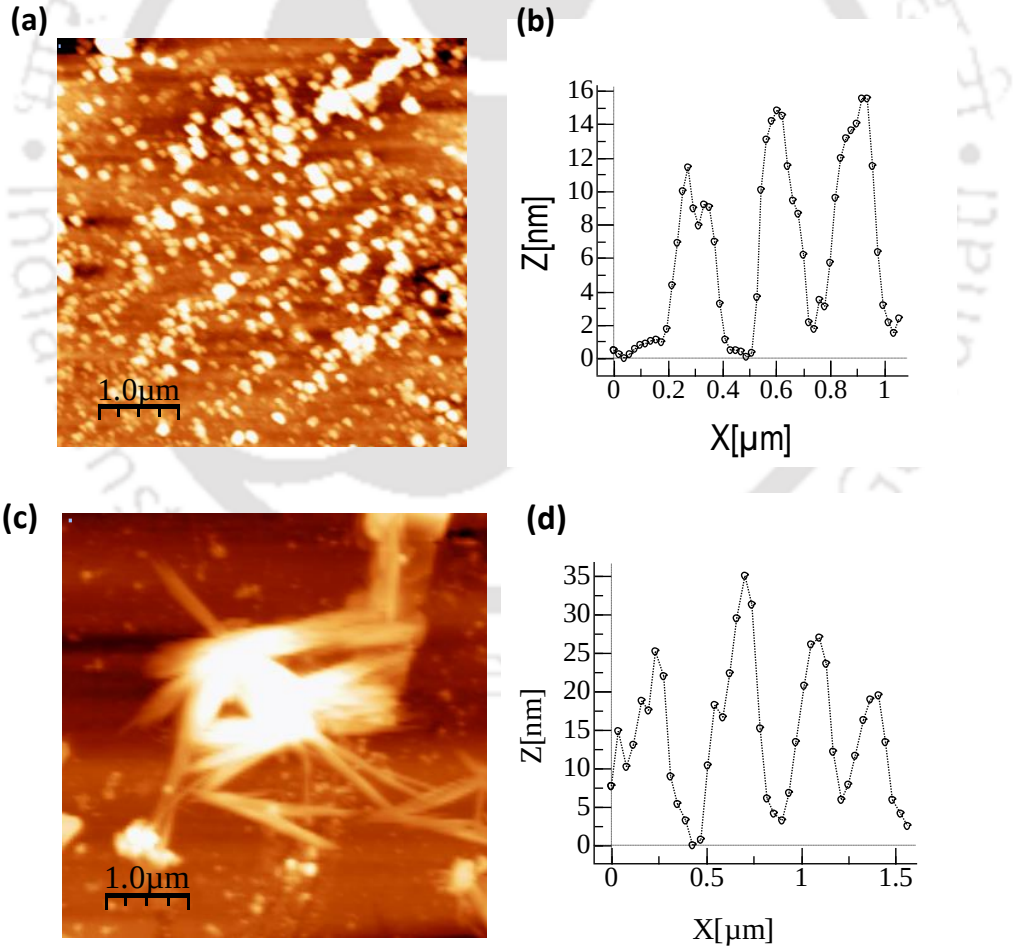

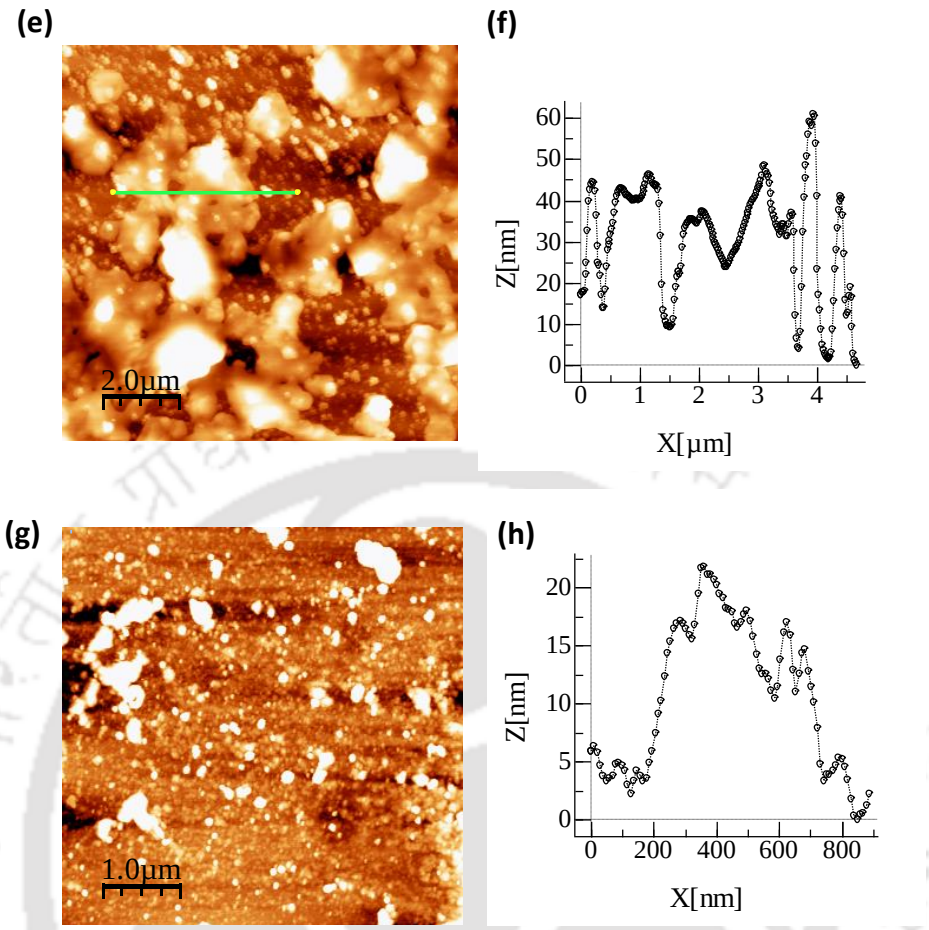

Figure A5.5. AFM images of control and co-incubated samples. (a) Morphology of native insulin monomers, (b) height profile of insulin monomers, (c) Morphology of mature fibrils, (d) height profile of insulin fibre, and modulation (e) Morphology of insulin aggregates in presence of PAPAP, (f) Height profile of the aggregates in presence of PAPAP, and (g) Morphology of insulin aggregates in presence of APPPA (h) height profile of the aggregates in presence of APPPA. All the samples were incubated at 37°C in Tris HCl buffer at pH 7.4.

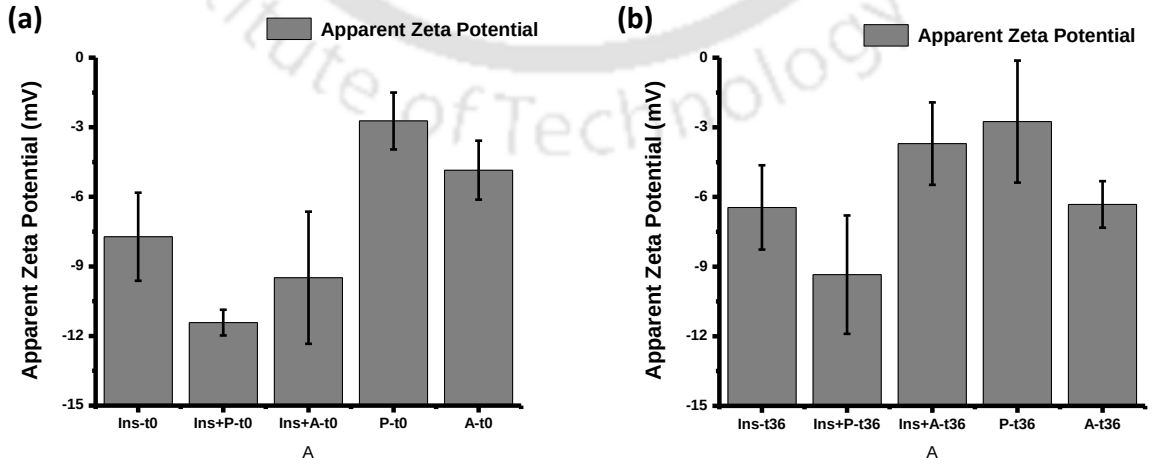

Figure A5.6. Apparent zeta potential of Insulin (86 μM) in presence and absence of PAPAP and APPPA (8.6 μM). Measurements were done in 5 mM Tris-HCl buffer at pH 7.4 and corrected by subtracting buffer spectra. Error bars represent the standard deviation of six measurements.

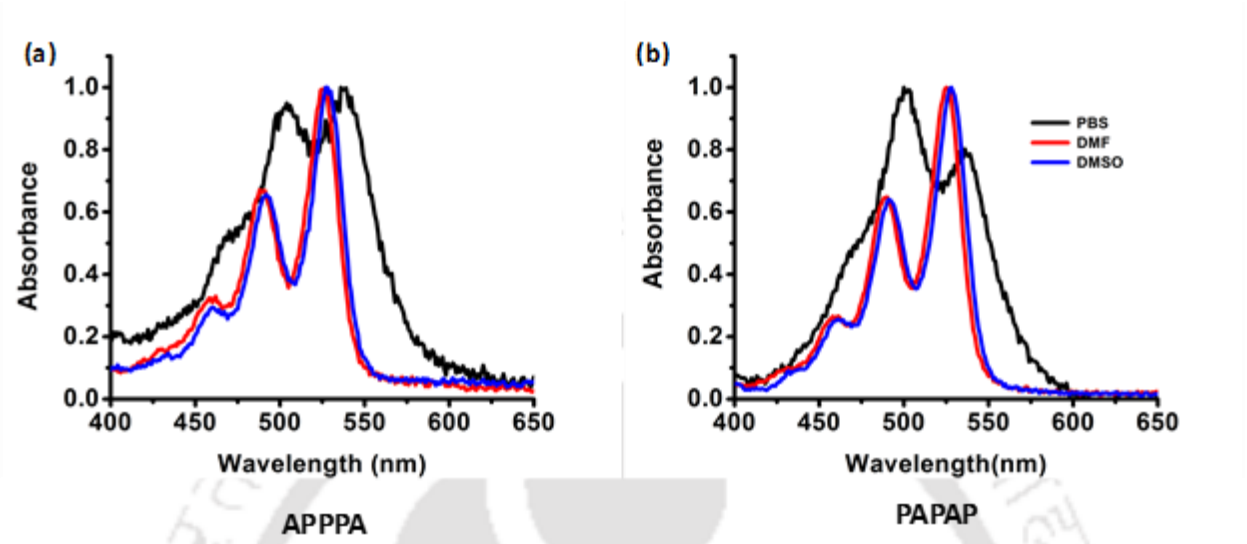

Figure A5.7. Normalized absorbance of (a) APPPA (5 μM) and (b) PAPAP (5 μM) in 10 mM PBS (pH7.4), DMF and DMSO.

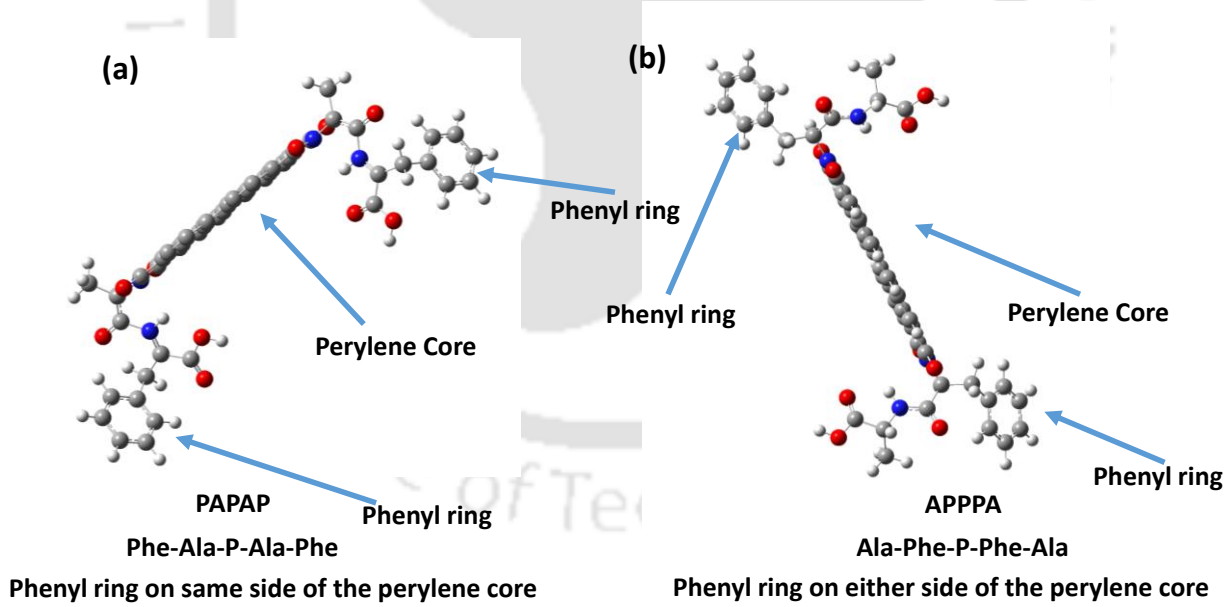

Figure A5.8. Optimized chemical structures of (a) PAPAP and (b) APPPA and the position of phenyl ring of the attached phenyl alanine in both isomers.

Future Aspects and Thesis Overview

Alzheimer's disease is genetically complex irreversible neurodegenerative disease in the brain. Multiple molecular mechanisms, interactive pathway contribute to slow progression and episodic memory decline and cognitive impairment at the final stage. To control this modern epidemic there is an urgent need for development of new therapies, diagnostic measures worldwide. Current Alzheimer's treatments temporarily boost the performance of chemicals that carry information from one cell to another but do not stop the cell death or disease progression. Developing treatments that can either stop or delay the progress is currently in progress. To date, only symptomatic treatments exist for this disease. Early detection will at least help us to make our ideas and plans work before the symptoms arise. Recent strategies include aim at plaques, keeping tau away from tangling, reducing inflammation, researching insulin resistance, studying heart and blood vessel health, and hormones proved beneficial in terms of protecting thinking and memory. But all of them are slow and painstaking processes and frustrating for those who are eagerly waiting for new options. Future Alzheimer's treatments may include a combination of medications as it progresses with downstream of several events in the brain. To date, biomarkers are directed toward prodromal stages of the disease. In order to achieve better treatment response, such biomarkers should enable an early prediction in terms of either diagnosis or monitoring disease progression with high sensitivity and specificity before clinical integration. A symptom-free stage must be not probabilistic rather measurable with high detection consistency, validity, and reproducibility. Intuitively, disease progression must be read using such biomarkers as pathophysiological changes occur well before the appearance of the disease symptoms. Thus these biomarkers can support and improve early detection. Clinically significant cognitive impairment starts to build up with pathophysiologic alterations in prodromal stage. The long clinically silent asymptomatic stage is still not detectable due to the unclear molecular mechanism. Aβ concentration in CSF and/or increased amyloid uptake, genetic susceptibility factors can be tailored as at-risk cohorts to predict the progression. A more advanced integrative global analysis is needed to complete the biochemical/pathological profile of any biological sample in order to detect prodromal stage. Identifying new potential markers (both genetic and molecular) may play a big role in future. But the use of this biomarkers are limited as the effect of gender, age, comorbidities are still not known. Finally, future early diagnosis of AD must be stage specific and will be able to identify the molecular mechanism in each individual and thereby enabling

personalized therapies. This can be achieved with a translational research worldwide including academia and industry by eliciting a microarray of multivariate biomarkers from several biological systems plus genetic risk profiles.

The following considerations have emerged that must be taken into account before developing future trials-

(1) To develop a successful disease modifying drugs, one must understand the relationship between Aβ, tau, and other critical factors including activation of astrocytes and microglia. Despite promising premises in each aspect, a large phase-III trials have failed to show positive effects on cognition.

(2) Most of the current treatments show benefits in mild AD and therefore they are effective only in certain disease phase. Therapeutic trials should, therefore, be carried out as early as possible during the course of the disease, which requires the identification of more accurate tools for early diagnosis. New criteria for AD diagnosis have engorged the early detection window depending on stages of the disease and incorporate biomarkers mechanistically related to disease pathology. Selection of these early biomarkers in executing outline of future examinations is profoundly desirable.

(3) Presently, the focus must shift from treatment to prevention. But in case of late onset AD detection is extremely difficult due to its heterogeneous nature in the clinical demonstration and underlying neuropathology. Improved tools are needed to detect neurodegeneration in patients with other diseases and syndromes and are at high AD risk. To identify subgroups with homogeneous biomarkers is a challenge and therefore these advancements are in high demand.

(4) To demonstrate a new development there must be surrogate measures in plenty. Surrogate biomarkers like CSF Aβ and tau, amyloid positron emission tomography, magnetic resonance imaging and the output must be well correlated with the existing clinical endpoints viz neuropsychological testing. Incorporating pathophysiological changes is the key along with amyloid accumulation triggering neuronal cell death.

(5) Extended development times delay effective therapies from reaching patients in need. The crucial question that comes in future developments is 'How much information is enough to proceed further in clinical trials?' Population upgrading with risk factors, sensitive clinical demonstration compared to existing trial, adaptive dose dependent results, and biomarkers

needs to be considered as means of shortening lengthy phase studies and creating an interface opportunity between phase trials.

(6) Effects on the brain with combined medications. 'How brain plasticity would react in presence of drug molecules?' An answer to this question may take time but definitely will disclose some interesting facts about human brain and its evolution against dementia.

At present, there is no preventive prescription available unlike in the case of other neurological disorders. The need for an early diagnosis is increasing due to an increase in modern population aging. Primitive success on early identification may result in an influx in the clinical setting which could result in increasing demands on the already restricted resources. Developments of much more consistent, high quality, multimodal, long-term care will be required to handle the pressing need. Thus it requires immediate improvements in strategy, structure, accessibility, and quality to tackle the imminent situation. Demands of each patient need to be tailored skillfully in terms of caregiving, appropriate drug therapy, and prevention of comorbidity. Important goals are achieving stabilization of psychological and social situation along with proper medication. A vast improvement in future medical care infrastructure for public means along with much more flexible and innovative care models are in high demand. A general awareness of geriatric and caregivers concepts need to be tailored to specific needs. Future care should be organized with sophisticated care models to overcome the fragmented ones along with enough qualified nurses and physician assistants for taking on medical tasks in delegation by specialists. Successful innovative models must reach to patients and their caregivers in need.

In this thesis, I have focused on small molecule and polymer based luminescent materials on amyloid aggregation in order to modulate amyloid aggregates with an additional feature of self-indication. Mutual aggregation between amyloid and modulator becomes predominant compared to self-aggregation due to oligo-blocking and/or formation of co-aggregates. An overview of my observations (Scheme 6) was also presented in this final chapter. Briefly, in second chapter PF-HQ showed an amyloid surface motif and hence, due to this similar interacting interface, it showed an excellent in vitro inhibition of amyloid aggregation by forming polymer-protein co-aggregates. Further, this polymeric nanoparticle showed excellent dual emission in aqueous and as well as organic solvent and thus utilized in multi-color bio-imaging and drug delivery for cancer treatment. But unfortunately, these polymer nanoparticles were not able to cross blood brain barrier (BBB) due to its hydrophobic nature. To overcome this, in the next chapter, a polymeric conjugate using polyfluorene (PF-DPA) and

chitosan was developed. It can cross BBB and traps oligomers in Aβ and CSF. The similar interacting interface provided the adsorption and further inhibition to fibril formation. To achieve better optical correlation on protein aggregation, perylenebisimide isomers (PAPAP and APPPA) were designed with a hydrophobic dipeptide tail. As expected they showed a distinct aggregation pattern in presence of oligomers of Aβ and insulin amyloid. These observations were discussed in chapter four and five. Interestingly, less aggregation prone derivative (APPPA) was able to cross BBB more proficiently and found efficient in modulating oligomers in Aβ and CSF whereas the other sibling, PAPAP was consistent with insulin amyloid. These findings may not directly involve in clinical trials but definitely, provide guidance taking molecules to clinical trials in order to achieve early diagnosis and prevention of neurodegeneration.

Thesis Overview

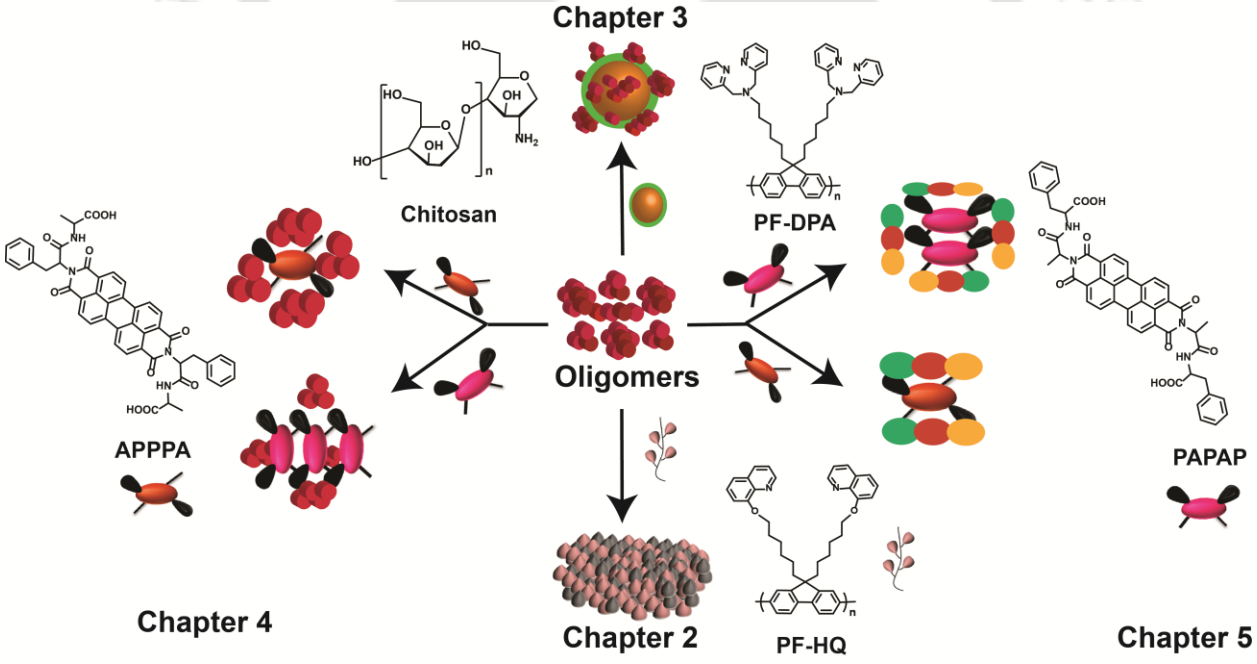

Thesis overview: Development of polymer and small molecule based luminescent Aβ modulator. PF-HQ was also utilized as multi-color bio-imaging and drug delivery for cancer treatment.

Publications

1. **Chowdhury, S. R.**; Mondal, S.; Iyer, P. K. Blocking Oligomeric Insulin Amyloid Fibrillation via Perylenebisimides Containing Dipeptide Tentacles. (Manuscript Under Communication)
2. **Chowdhury, S. R.**; Mondal, S.; Balaji, S. N.; Trivedi, V.; Iyer, P. K. Remarkably Efficient Blood-Brain Barrier Crossing Polyfluorene-Chitosan Nanoparticle Selectively Tweaks Amyloid Oligomer in CSF and Aβ1-40. (Manuscript Under Communication)
3. **Chowdhury, S. R.**; Balaji, S. N.; Mondal, S.; Meher, N.; Trivedi, V.; Iyer, P. K. Modulating Early Stage Amyloid Aggregates by Dipeptide Linked Perylenebisimides: Structure Activity Relationship, Inhibition of fibril formation in Human CSF and Aβ1-40. (Manuscript Under Communication)
4. Mondal, S.; **Chowdhury, S. R.**; Iyer, P. K. Small molecule and Polymer Conjugate: An Efficient Strategy to Modulate Amyloid Aggregates and cross BBB. (In preparation)
5. Mondal, S.; Kumar, V.; **Chowdhury, S. R.**; Kumar, S.; Iyer, P. K. Trapping Toxic Amyloid Oligomers by Gold Nanoparticle Based Ultrafast Antiaggregation Agents in Human Cerebrospinal Fluid: An Insight into Nano-Bio Interface. (Manuscript Under Preparation)
6. **Chowdhury, S. R**.; Mukherjee, S.; Das, S.; Patra, C. R.; Iyer, P. K. Multifunctional (3-in-1) cancer theranostics applications of hydroxyquinoline appended polyfluorene nanoparticles. *Chem. Sci.* **2017**, *8*, 7566-7575.
7. Muthuraj, B.; Mukherjee, S.; **Chowdhury, S. R**.; Patra, C. R.; Iyer, P. K. An efficient strategy to assemble water soluble histidine-perylene diimide and graphene oxide for the detection of PPi in physiological conditions and in vitro. *Biosens. Bioelectron.* **2017**, *89*, 636-644. (This work is highlighted in Atlas of Science).
8. Meher, N; **Chowdhury, S. R**.; Iyer, P. K. Aggregation induced emission enhancement and growth of naphthalimide nanoribbons via J-aggregation: Insight into disaggregation induced unfolding and detection of ferritin at nanomolar level. *J. Mater. Chem. B* **2016**, *4*, 6023-6031.
9. **Chowdhury, S. R**.; Agarwal, M.; Meher, N.; Muthuraj, B; Iyer, P. K. Modulation of Amyloid Aggregates into Nontoxic Coaggregates by Hydroxyquinoline Appended Polyfluorene. *ACS Appl. Mater. Interfaces* **2016**, *8*, 13309-13319.
10. Muthuraj, B.; **Chowdhury, S. R**.; Mukherjee, S.; Patra, C. R.; Iyer, P. K. Aggregation deaggregation influenced selective and sensitive detection of Cu^{2+} and ATP by histidine functionalized water-soluble fluorescent perylene diimide under physiological conditions and in living cells. *RSC Adv.* **2015**, *5*, 28211-28218.
11. Muthuraj, B.; **Chowdhury, S. R**.; Iyer, P. K. Modulation of Amyloid-β Fibrils into Mature Micro Rod-shaped Structure by Histidine Functionalized Water-soluble Perylene Diimide. *ACS Appl. Mater. Interfaces* **2015**, 7, 21226-21234.

Book Chapter

12. Malik, A. H.; Hussain, S.; **Chowdhury, S. R**.; Iyer, P. K. Conjugate polymer for disease diagnosis and theranostic medicine. Book Chapter. Wiley (In print)

Conferences

1. July 16-20, 2017: Summer School on Neuroimaging at IIIT-H.
2. 16-19 March, 2017: Poster presentation at Research Conclave at IIT Guwahati, India.
3. 3rd March, 2017: Oral presentation in the workshop on 'Innovation management and product commercialization' at IASST, Guwahati, India.
4. 19-23 Feb, 2017: Poster presentation at ABSMSNW-2017 at IIT BHU, Varanasi, India.
5. 3-5 Feb, 2017: Poster presentation at 20th National CRSI symposium at Gauhati University, Guwahati, India.
6. 17th January, 2017: Selected as a student presenter at ACS on Campus at IIT Guwahati.
7. 8-10th December, 2016: Poster presentation at FICS-2016 at IIT Guwahati, India.
8. 8-9 September, 2016: Oral presentation at NCRANNT at NEHU, Shillong, India.
9. 3-10 June, 2016: Poster presentation at GRC on 'Bioinspired Materials' at les Diablerets, Switzerland.
10. 25-26 April, 2016: Oral presentation at FCASI-2016 at University of Rajasthan, Jaipur, India.
11. 21-22 March, 2016: Participated in '2nd National workshop on MEMS/NEMS and Theranostic devices' at IIT Guwahati, India.
12. 5th March, 2016: Participated in Elsevier's Author Workshop, Gauhati University.
13. 8-11 December, 2015: Participated in ICANN-2015 held at IIT Guwahati.
14. 5 December, 2014: Participated in RACBT-2014 held at IIT Guwahati.
15. 4-6 March, 2014: Participated in the workshop on Electron Microscopy at NEHU Shillong.
16. 6-8 Feb, 2014: Participated and presented Poster in ICCB-2014 held at IICT Hyderabad.
17. 1-3 December, 2013: Participated in ICANN-2013 held at IIT Guwahati.
18. 15th November, 2013: Participated in the workshop on "Sensors and its application" at IASST Guwahati.

Vitae

Sayan Roy Chowdhury was born in West Bengal, India. He obtained his Bachelor of Science from St. Xavier's College, Kolkata and completed Master of Science in Chemistry from University of Delhi, India. Under the supervision of Prof. Parameswar Krishnan Iyer, he started his research career at the Department of Chemistry, IIT Guwahati – with the development of luminescent conjugate materials for amyloid aggregation inhibitors and cancer theranostic applications. His current research interests are conjugate materials and finding their applications as targeting toxic amyloid oligomers. He is also interested in designing multivalent probes with unprecedented affinity and selectivity toward a number of medically important protein aggregates responsible for neurodegenerative diseases.